University of Central Florida
STARS

Electronic Theses and Dissertations, 2004-2019

2011

Fine-scale Structures In Saturn's Rings Waves, Wakes And Ghosts

Kevin Baille
University of Central Florida

Part of the Astrophysics and Astronomy Commons, and the Physics Commons
Find similar works at: https://stars.library.ucf.edu/etd
University of Central Florida Libraries http://library.ucf.edu

This Doctoral Dissertation (Open Access) is brought to you for free and open access by STARS. It has been accepted for inclusion in Electronic Theses and Dissertations, 2004-2019 by an authorized administrator of STARS. For more information, please contact STARS@ucf.edu.

STARS Citation

Baille, Kevin, "Fine-scale Structures In Saturn's Rings Waves, Wakes And Ghosts" (2011). *Electronic Theses and Dissertations, 2004-2019*. 1897.
https://stars.library.ucf.edu/etd/1897

Showcase of Text, Archives, Research & Scholarship

FINE-SCALE STRUCTURES IN SATURN'S RINGS: WAVES, WAKES AND GHOSTS

by

KÉVIN BAILLIÉ
M.S. Observatoire de Paris - Université Paris VI Pierre et Marie Curie, 2005
M.S. Ecole Supérieure de Physique et de Chimie Industrielles de la Ville de Paris, 2005

A dissertation submitted in fulfillment of the requirements
for the degree of Doctor of Philosophy
in the Department of Physics - Planetary Science Track
in the College of Sciences
at the University of Central Florida
Orlando, Florida

Summer Term
2011

Major Professor:
Joshua Edwards Colwell

ABSTRACT

The Cassini mission provided wonderful tools to explore Saturn, its satellites and its rings system. The UVIS instrument allowed stellar occultation observations of structures in the rings with the best resolution available (around 10 meters depending on geometry and navigation), bringing our understanding of the physics of the rings to the next level. In particular, we have been able to observe, dissect, model and test the interactions between the satellites and the rings.

We first looked at kilometer-wide structures generated by resonances with satellites orbiting outside the main rings. The observation of structures in the C ring and their association with a few new resonances allowed us to estimate some constraints on the physical characteristics of the rings. However, most of our observed structures could not be explained with simple resonances with external satellites and some other mechanism has to be involved. We located four density waves associated with the Mimas 4:1, the Atlas 2:1, the Mimas 6:2 and the Pandora 4:2 Inner Lindblad Resonances and one bending wave excited by the Titan -1:0 Inner Vertical Resonance. We could estimate a range of surface mass density from 0.22 (±0.03) to 1.42 (±0.21) g cm^{-2} and mass extinction coefficient from 0.13 (±0.03) to 0.28 (±0.06) cm^{2} g^{-1}. These mass extinction coefficient values are higher than those found in the A ring (0.01 – 0.02 cm^{2} g^{-1}) and in the Cassini Division (0.07 – 0.12 cm^{2} g^{-1} from

Colwell et al. (2009), implying smaller particle sizes in the C ring. We can therefore imagine that the particles composing these different rings have either different origins or that their size distributions are not primordial and have evolved differently. We also estimate the mass of the C ring to be between 3.7 ($\pm$0.9) $\times 10^{16}$ kg and 7.9 ($\pm$2.0) $\times 10^{16}$ kg, equivalent to a moon of 28.0 ($\pm$2.3) km to 36.2 ($\pm$3.0) km radius (a little larger than Pan or Atlas) with a density comparable to the two moons (400 kg m^{-3}). From the wave damping length and the ring viscosity, we also estimate the vertical thickness of the C ring to be between 1.9 ($\pm$0.4) m and 5.6 ($\pm$1.4) m, which is consistent with the vertical thickness of the Cassini Division (2 – 20 m) from Tiscareno et al. (2007) and Colwell et al. (2009). Conducting similar analysis in the A, B rings and in the Cassini Division, we were able to estimate consistent masses with previous works for the these rings.

We then investigated possible interactions between the rings and potential embedded satellites. Looking for satellite footprints, we estimated the possibility that some observed features in the Huygens Ringlet could be wakes of an embedded moon in the Huygens gap. We discredited the idea that these structures could actually be satellite wakes by estimating the possible position of such a satellite.

Finally, we observed a whole population of narrow and clear holes in the C ring and the Cassini Division. Modeling these holes as depletion zones opened by the interaction of a moonlet inside the disk material (this signature is called a "propeller"), we could estimate a distribution of the meter-sized to house-sized objects in these rings. Similar objects, though an order of magnitude larger, have been visually identified in the A ring. In the C ring,

we have signatures of boulders which sizes are estimated between 1.5 and 14.5 m, whereas similar measures in the Cassini Division provide moonlet sizes between 0.36 and 58.1 m. Using numerical simulations for the propeller formation, we estimate that our observed moonlets belong to a population of bigger particles than the one we thought was composing the rings: Zebker et al. (1985) described the ring particles population as following a power-law size distribution with cumulative index around 1.75 in the Cassini Division and 2.1 in the C ring. We believe propeller boulders follow a power-law with a cumulative index of 0.6 in the C ring and 0.8 in the Cassini Division.

The question of whether these boulders are young, ephemeral and accreted inside the Roche limit or long-lived and maybe formed outisde by fragmentation of a larger body before migrating inward in the disk, remains a mystery. Accretion and fragmentation process are not yet well constrained and we can hope that Cassini extended mission will still provide a lot of information about it.

ACKNOWLEDGMENTS

All along my PhD, I have benefited from discussions and help from many people. In the first place, I would like to thank Josh for the opportunity he gave me and also for his support, his patience and his priceless advice for my professional career. I am also extremely grateful to Sébastien Charnoz, whose support never failed me, for all the unvaluable discussions and advice he has provided me over the last 6 years.

I would also like to thank committee members Yanga Fernández and Robert Peale, together with reviewers Larry Esposito and Philippe Thébault who helped me improving my presentation and writing skills. I also benefited from great interactions with Larry Esposito and Miodrag Sremčević as part of the Cassini-UVIS team and with Jack Lissauer and Mark Lewis as part of the "Rings" community. I am thankful to the UCF Planetary Science group and the Physics Department; in particular to the Colwell group and my officemates Tracy, Akbar and Eric whose presence turned this office in a place full of life.

I would like to thank my parents who supported my choices, and my sisters Gaëlle who reminded me regularly that research can be awesome even when it does not save lives and Jill for giving me motivation and support anytime I had to fly back to Orlando. I would

also like to thank Sandrine for her constant support, for listening to my complaints about my research and to my joys about it also, and for reminding me to go to sleep when she was waking up.

My gratitude also goes to Anne-Marie for helping me find my marks in Orlando; to Rohit and Nicolas who showed me the way; to Chandana, Hani, Rémy le destructureur d'intemporalité, Catherine and Charlotte who allowed me to step out of my research sometimes and reconnect with reality; to Cédric, Dom and Érica for welcoming me back in France when I visited; and to Olivier, Barbecue and the company in which we have always believed. Finally, I'd like to thank Yann for all of the above, for the motivation he always gave me and for the decompressing bretonnesques, nanardesques and heroestroisesques necessary moments.

TABLE OF CONTENTS

LIST OF FIGURES . . . . **xv**

LIST OF TABLES . . . . **xliii**

CHAPTER 1 INTRODUCTION **1**

1.1 The Beginning of Modern Astronomy 1

1.2 Saturn's Satellites 4

1.2.1 Moonlets Located inside the Roche Limit 6

1.2.2 The Main Satellites 7

1.2.3 The Irregular Satellites 8

1.2.4 Possible Origins 9

1.3 Saturn's Rings 11

1.3.1 From Galileo to Voyager 11

1.3.2 Composition 17

1.3.3 Origins 20

1.3.4 A Huge Diversity of Rings 23

1.3.5 The Main Rings 26

1.3.6 The Diffuse Rings 33

1.3.7 A Huge Variety of Structures 34

1.3.8 Other Flat Systems 42

1.3.8.1 The Physics of the Disks 42

1.3.8.2 The Other Planetary Rings 43

1.3.8.3 Towards Bigger Disks 49

1.4 Cassini UVIS Data 52

1.4.1 The Cassini Spacecraft 52

1.4.2 The UVIS High Speed Photometer 53

1.4.3 Stellar Occultations Data 57

1.5 General Questions 65

1.6 Points Addressed in this Manuscript 65

CHAPTER 2 WAVES IN THE C RING 67

2.1 Introduction 67

2.2 Observations 70

2.3 Wavelet Analysis 75

2.3.1 Wavelet Transform 75

2.3.2 Ringlet Signatures . . . 80

2.3.3 Waves Near Known Resonances . . . 82

2.3.4 Other Wavelike Signatures . . . 100

2.3.4.1 Outward Propagating Signatures . . . 100

2.3.4.2 Inward Propagating Signatures . . . 109

2.3.4.3 Other Signatures . . . 118

2.3.5 Surface Mass Density Model . . . 119

2.4 Results . . . 124

2.4.1 Determination of Theoretical Resonance Locations . . . 125

2.4.2 Resonances in the C Ring . . . 128

2.4.3 Resonance Strengths . . . 138

2.4.3.1 Inner Lindblad Resonances . . . 138

2.4.3.2 Other Resonances . . . 141

2.4.4 Wave Dispersion Relation . . . 144

2.5 Discussion . . . 145

2.5.1 Potential Resonance Association . . . 145

2.5.2 Resonance Association Verification . . . 146

2.5.3 Surface Mass Density and Mass Extinction Coefficient Measurements 149

2.6 Conclusions . . . 155

CHAPTER 3 WAVES IN THE B RING AND THE CASSINI DIVISION 157

3.1 Introduction 157

3.2 Observations 158

3.3 Resonances 158

3.4 Results 162

  3.4.1 B Ring Resonances 162

  3.4.2 Cassini Division Resonances 169

  3.4.3 Associated Waves 180

3.5 Discussions and Conclusions 180

CHAPTER 4 SATELLITE WAKES 183

4.1 Introduction 183

4.2 Observations 185

4.3 Satellite Wakes 197

4.4 Results 200

4.5 Discussions and Conclusions 201

CHAPTER 5 GHOSTS IN THE RINGS 203

5.1 Introduction 203

5.2 Observations 205

- 5.2.1 Cassini UVIS Data 205
- 5.2.2 Ghosts Identification 208
  - 5.2.2.1 Detection and Identification Criteria 208
  - 5.2.2.2 Chance Detection 216

5.3 Forming Ghosts 220

- 5.3.1 The Propeller Model 220
- 5.3.2 Numerical Simulations 228
  - 5.3.2.1 The Numerical Code 228
  - 5.3.2.2 Forming S-Shaped Depletion Zone 228
  - 5.3.2.3 Parameters 229
    - 5.3.2.3.1 Time Steps 229
    - 5.3.2.3.2 Particle Population 230
    - 5.3.2.3.3 Forcings 234

5.4 Results 236

- 5.4.1 Quantitative Results 236
  - 5.4.1.1 Observational Results 236
  - 5.4.1.2 Removing the Resolution Bias 239
- 5.4.2 Qualitative Results 242
  - 5.4.2.1 Boulder Radius 242

5.4.2.2 Particle Radii 246

5.5 Discussion 247

5.6 Conclusions and Perspectives 255

5.6.1 Conclusions 255

5.6.2 Perspectives 256

CHAPTER 6 CONCLUSIONS 257

6.1 Conclusions and Discussion 257

6.2 Perspectives 260

6.2.1 Saturn's Rings 260

6.2.2 Other Disks 262

APPENDIX THE NUMERICAL CODE 265

REFERENCES 269

LIST OF FIGURES

1.1 Image: NASA/JPL/Space Science Institute. Mozaic image of Saturn occulting the Sun, thus revealing very faint rings around the planet. The white arrow points at the Earth, visible through the rings on the left of Saturn. . . 4

1.2 Image: NASA/JPL/Space Science Institute. Cassini captured 6 moons in front of the A and F rings: Pan and Daphnis are inside the Encke and Keeler gaps of the A ring. Atlas is orbiting between the A ring and the F ring. Janus and Epimetheus are sharing common orbits a little farther and Enceladus is feeding the E ring. 5

1.3 Image: NASA/JPL. Saturn's principal satellites. Objects are presented in increasing distance away from Saturn. 6

1.4 Mass distance distribution of Saturn small satellites. External edges of the rings are shown with vertical dashed lines. Smaller satellites present a different trend (blue) than bigger ones (red). From Charnoz et al. (2010). 10

1.5 These drawings from Huygens's *Systema Saturnium* of 1659 illustrate the variety of perceptions of Saturn that resulted from the interplay of its changing orientations, improvements in telescopes, and new interpretations of its physical nature. The observers were: I, Galileo (1610), who in 1616 drew Saturn much like IX; II, Scheiner (1614); III, Riccioli (1641 or 1643); IV-VII, Hevel (theoretical forms); VIII and IX, Riccioli (1648-1650); X, Divini (1646-1648); XI, Fontana (1638); XII, Biancani (1616); Gassendi (1638-1639); XIII, Fontana and others at Rome (1644, 1645). From Alexander (1962). In the lower diagram, Huygens showed how the axial tilts of both Earth and Saturn combine with their orbital motions around the Sun to produce the cyclical pattern of change in Saturn's appearance. 12

1.6 In 1675, Cassini reported that a "dark line" divided the ring into two parts, "the inner of which was brighter that the outer one". He made this drawing in 1676, apparently showing the outer ring to be narrower than the inner ring. From Alexander (1962). 13

1.7 Image: NASA/JPL. An artist's concept of Saturn, its rings and major icy moons—from Mimas to Rhea. 14

1.8 Image: NASA/Space Telescope Science Institute. Saturn Ring-Plane Crossing: on May 22, 1995, Saturn was observed edge-on from the Hubble Space Telescope, clearly showing evidence of some of its satellites. The boxes around the western portion of the rings (on the right) indicate the area in which the faint light from the rings has been enhanced through image processing to make the rings more visible. 16

1.9 ISS mosaic (NASA/JPL/Space Science Institute) and UVIS stellar occultation data showing the A, B, C rings and Cassini Division (CD) at approximately 10 km radial resolution. The F ring is visible in the ISS mosaic beyond the outer edge of the A ring. The images were taken from an elevation of 4° above the illuminated (southern) face of the rings, so optically thick regions appear brighter than optically thin regions. From Colwell et al. (2009b). 25

1.10 UVIS occultation profile and ISS image (NASA/JPL/Space Science Institute) of the C ring. The image is from above the unilluminated face of the rings with a radial resolution of $\sim$ 6 km/pixel. The occultation data are shown at 10 km resolution. From Colwell et al. (2009b). 27

1.11 Cassini RSS occultation profile of the C ring. Unlike the A and B rings, the measured normal optical depth of the C ring is insensitive to viewing geometry. Prominent features are labeled (G for Gaps and P for Plateaus). From Colwell et al. (2009b). 28

1.12 UVIS occultation profile (α Leonis, rev. 9) and ISS image (NASA/JPL/Space Science Institute) of the Cassini Division. The transition from the Cassini Division to the A ring at the outer edge of the Cassini Division ramp is much more pronounced in optical depth than in the image. The image is from above the unilluminated face of the rings with a radial resolution of $\sim$ 6 km/pixel. The occultation data are shown at 10 km resolution. From Colwell et al. (2009b). 30

1.13 Normal optical depth profile of the Cassini Division obtained from UVIS stellar occultations. The Huygens gap is close to the inner edge of the Cassini Division. From Colwell et al. (2009b). 31

1.14 Image: NASA/JPL/Space Science Institute. Cassini ISS images revealing Pan orbiting in the Encke gap. The narrow ringlet co-orbiting with Pan is also visible, together with wakes just outside the Encke gap. 35

1.15 Image: NASA/JPL/Space Science Institute. The Encke gap (320 km wide) imaged by Cassini at Saturn Orbit Insertion showing dusty ringlets, a wavy inner edge recently perturbed by the satellite Pan (roughly five image widths upstream of the inner edge, or down in this view of the south face of the rings), and satellite wakes. Density waves are also visible, indicated here by the inner Lindblad resonances that launch them. Streamlines near the edge of a gap are deflected by the embedded moon, creating a wavy edge and satellite wakes, due to the moon Pan, within the ring. From Colwell et al. (2009b). . 36

1.16 Schematic diagrams of the coplanar particle paths that give rise to trailing spiral density waves near a resonance with an exterior satellite. (a) The two-armed spiral density wave associated with the 2:1 (m=2) inner Lindblad resonance. (b) The seven-armed spiral density wave associated with the 7:6 (m=7) inner Lindblad resonances. The pattern rotates with the angular velocity of the satellite and propagates outward from the exact resonance (denoted by the dashed circle). Figure and caption from Murray and Dermott (1999), p. 493, Figure 10.11. 37

1.17 Schematic diagrams showing an oblique view of the three-dimensional particle paths that give rise to trailing spiral bending waves near a resonance with an exterior satellite. (a) The two-armed spiral density wave associated with the 3:1 (m=2) inner vertical resonance. (b) The four-armed spiral bending wave associated with the 5:3 (m=4) inner vertical resonances. The pattern rotates with the angular velocity of the satellite and propagates inward from the exact resonance (denoted by the dashed curve). Figure and caption from Murray and Dermott (1999), p. 493, Figure 10.12. 38

1.18 Numerical simulation of self-gravity wakes in the rings. Saturn's direction is towards the bottom. Enough 20-cm radius particles were added to simulate a 0.5 optical depth. 40

1.19 Propellers as seen in selected Cassini images. The moonlets are at the center of the features. Figure from Tiscareno et al. (2010b). 41

1.20 Scaled giant planet ring systems. The dashed line shows the synchronous orbit. The dotted line is the Roche limit for a satellite with a density of 1000 $kg\ m^{-3}$. From Grün et al. (2001). 44

1.21 Image: NASA/JPL/Cornell University. Jupiter's ring system is shown here with the positions of the small moons that are embedded in the rings. 45

1.22 Image: NASA/Space Telescope Science Institute. Uranus and its rings. . . . 47

1.23 Image: NASA/JPL/Univ. of Arizona. Two exposures with Neptune blacked out (center) were used to make this image of the ring system of Neptune by Voyager 2. These images were made from a pair of 10-minute exposures while the Sun was behind Neptune, and faint ring particles were being lit from the back. 48

1.24 β Pictoris debris disks as seen from the Hubble Space Telescope (up) and from the European Southern Observatory (lower left). AU Microscopii's debris disk as observed from the Hubble Space Telescope (lower right) shows also light polarization. In all these observations, the star was occulted to enable observations of the disks. 50

1.25 Artist concept of an accretion disk orbiting a white dwarf star in a binary system. Credit: P. Marenfeld and NOAO/AURA/NSF 51

1.26 Image: K. Baillié, A. de Beauffort, J. Fontdecaba-Baig, and J. Desmars. Spiral galaxies M51 and M104 (in the Messier catalog) imaged from the 120-cm telescope at Observatoire de Haute-Provence. 52

1.27 Image: NASA/JPL. The Cassini spacecraft and the embarked instruments, including the UVIS telescope on the left side. 54

1.28 Image: NASA/JPL. Cassini mission journey from the Earth to the insertion in Saturn's orbit seven years later. 55

1.29 J. E. Westfall observations of a stellar occultation of Saturn's rings in 1957. From M. S. Brobov, "Physical Properties of Saturn's Rings", in *Surfaces and Interiors of Planets and Satellites*, 1970. 58

2.1 Photon counts from the occultation of β Centauri (Rev 75) showing structure 32, propagating inward (left) and of α Virginis (Rev 34) showing feature 6 propagating outward (right). 74

2.2 WWZ wavelet power profile for two reference theoretical signals: a step function (left) and a Dirac signal (right). The bottom panel presents the simulated data that were analyzed to produce these power transforms. 78

2.3 WWZ wavelet power profile for the Mimas 5:3 IVR bending wave (r_V = 131923 km), computed from individual occultation profile of α Virginis, rev. 34 (left) and β Centauri, rev. 105 (right). 79

2.4 WWZ wavelet power profile of embedded ringlet ER1 computed from 62 individual occultation profiles. Lower panel shows the β Centauri, rev. 85 occultation profile. Embedded ringlets produce this characteristic triangular profile in the power contour plots. 83

2.5 Co-added WWZ wavelet power profile of embedded ringlet ER2, computed from individual occultation profiles. Lower panel shows the α Virginis, rev. 34 occultation profile. A clear triangular shape is visible as the resulting signature of embedded ringlet ER2. 84

2.6 Co-added WWZ wavelet power profile of embedded ringlet ER8, computed from individual occultation profiles. Lower panel shows the β Centauri, rev. 85 occultation profile. The double peaks, characteristic of ER8, present clear signatures. 85

2.7 Co-added WWZ wavelet power profile of embedded ringlet ER17, computed from individual occultation profiles. Lower panel shows the α Virginis, rev. 30 occultation profile. A clear triangular shape is visible as the resulting signature of embedded ringlet ER17. 86

2.8 Co-added WWZ wavelet power profile of embedded ringlet ER18, computed from individual occultation profiles. Lower panel shows the β Centauri, rev. 104 occultation profile. Two peaks, separated by 0.8 km, are visible on the occultation profile. 87

2.9 WWZ wavelet power profile around the Mimas 4:1 inner Lindblad resonance ($r_L = 74891.9$ km, marked by the vertical dashed line), computed from β Centauri, rev. 75 individual occultation profile. The possible superposition with a ringlet structure is disturbing our perception of the direction of propagation. The asterisk locates the position of the observed wave source. 90

2.10 WWZ wavelet power profile of wave 12, computed from α Virginis, rev. 34 individual occultation profile. Titan -1:0 nodal resonance at 77511.3 km (vertical dashed line) excites an outward propagating wave. The asterisk locates the position of the observed wave source. 91

2.11 WWZ wavelet power profile of wave 33, computed from α Virginis, rev. 34 (left) and β Centauri, rev. 105 (right) individual occultation profiles. The Atlas 2:1 ILR (at 87646.5 km - vertical dashed line) has a greater torque than the Pan 2:1 ILR which does not seem to excite a wave at 85105 km. The asterisks locate the positions of the observed wave sources. Profiles of this wave consistently show a dispersion that places the wave source several km interior to the wave feature and the theoretical location of the Atlas 2:1 ILR. 92

2.12 Co-added WWZ wavelet power profile of waves 36 and 37, computed from co-added wavelet profiles. Mimas 6:2 ILR is at 89883.3 km and Pandora 4:2 ILR is at 89894.0 km, pointed by the vertical dashed lines. Lower panel shows the β Centauri, rev. 85 occultation profile. The almost 3:2 corotation resonance between Mimas and Pandora explains the proximity of these two waves. The asterisks locate the positions of the observed wave sources with uncertainties lower than 1 km. 94

2.13 WWZ wavelet power profile of feature 20, computed from β Centauri, rev. 104 individual occultation profile. Pan 4:2 ILR is at 84814.5 km (vertical dashed line). The relatively long distance between the Pan 4:2 ILR and the wave (about the same distance as the length of the wave itsself) together with a very low torque value for this resonance and an inconsistent wave source location from the feature invalidate the possibility of an association. Wave source location is outside the range of this figure, at 84775 ± 8 km. 97

2.14 WWZ wavelet power profile of structure 22, computed from β Centauri, rev. 89 individual occultation profile. Pan 2:1 ILR is at 85105.8 km (vertical dashed line). No obvious direction of propagatiom can be determined from diverse occultations. Wave source location is outside the range of this figure, at 84989 ± 20 km. 98

2.15 WWZ wavelet power profile of feature 40, computed from β Centauri, rev. 81 individual occultation profile. Tethys 6:1 ILR is at 90279.6 km (vertical dashed line). Its calculated strength is very low, suggesting that this is a chance association (Tiscareno et al., 2007). Wave source location is outside the range of this figure, at 90238.5 ± 2.5 km. 99

2.16 WWZ wavelet power profile of structures 3 and 4, computed from α Virginis, rev. 30 individual occultation profile. 101

2.17 Photon count rates of feature 6, computed from β Centauri, rev. 85 (top) and α Virginis, rev. 34 (bottom) individual occultation profiles. Feature 6 is clearly propagating outward though it is more prominent in the low-B incidence angle α Virginis occultation. 102

2.18 WWZ wavelet power profile computed from β Centauri, rev. 85 individual occultation profile showing structures 7 and 8 coexisting at the same location. Figure 2.19 gives more details about the central region where structure 9 is located. 103

2.19 WWZ wavelet power profile computed from α Virginis, rev. 34 individual occultation profile showing feature 9, propagating inward. 104

2.20 WWZ wavelet power profile of structure 24, computed from ζ Orionis, rev. 47 individual occultation profile. Feature 24 is located between plateaus P5 and P6. 105

2.21 Individual occultation profiles of β Centauri, rev. 64 (upper panel) and α Virginis, rev. 30 (lower panel) showing feature 27, clearly propagating outward. 106

2.22 Co-added WWZ wavelet power profile of structure 28, computed from individual occultation profiles. Lower panel shows the β Centauri, rev. 89 occultation profile. Structure 28 is the most extended feature observed in the C ring, but there is no low order resonance in its vicinity. 108

2.23 WWZ wavelet power profile of structure 13, computed from individual occultation profiles of β Centauri, rev. 77 (left) and α Virginis, rev. 34 (right). Structure 13 is clearly propagating inward on both high incidence and low incidence occultations. 110

2.24 WWZ wavelet power profile of feature 15, computed from co-added wavelet profiles. Lower panel shows the ζ Orionis, rev. 47 occultation profile. 111

2.25 WWZ wavelet power profile of structure 17, computed from co-added wavelet profiles of high-incidence angle occultations (left) and low-incidence angle occultations (right). Lower panel show the β Centauri, rev. 85 occultation profile (left) and the α Virginis, rev. 34 occultation profile (right). 112

2.26 WWZ wavelet power profile of structure 16, computed from co-added wavelet profiles of high-incidence angle occultations (left) and low-incidence angle occultations (right). Lower panel show the β Centauri, rev. 85 occultation profile (left) and the α Virginis, rev. 34 occultation profile (right). Structure 16 is located just exterior to the embedded ringlet ER10. 113

2.27 WWZ wavelet power profile of structure 18 (left) and 19 (right), computed from individual occultation profile of ζ Orionis, rev. 47. 114

2.28 WWZ wavelet power profile of structure 23, computed from ζ Orionis, rev. 47 individual occultation profile. 115

2.29 Co-added WWZ wavelet power profile of structure 32, computed from individual occultation profiles. Lower panel shows the β Centauri, rev. 85 occultation profile. Structure 32 is coexisting with the embedded ringlet ER13 that spreads from 87180 km to 87210 km. 116

2.30 WWZ wavelet power profile of the different parts composing structure 38, computed from individual occultation profile of β Centauri, rev. 89 (upper left), β Centauri, rev. 64 (upper right), and β Centauri, rev. 104 Ingress (bottom).The variety of observed patterns and the local superposition of waves at different wavelengths suggest that this is not a simple bending wave. . . . 117

2.31 WWZ wavelet power profile of structure 11, computed from α Virginis, rev. 30 individual occultation profile. 119

2.32 WWZ wavelet power profile around Maxwell ringlet, computed from β Centauri, rev. 105 individual occultation profile. Though the structure is quite clear and prominent to the eye on the occultation profile, the wwz profile is distorted by the relative importance of the amplitude of the highest wavelengths, hiding smaller amplitudes at the presented scale. 120

2.33 WWZ wavelet power profile of Maxwell Ringlet, computed from β Centauri, rev. 64 individual occultation profile. Again, the feature is clear on the occultation profile, but the wwz profile is distorted by the relative importance of the amplitude of the highest wavelengths. 121

2.34 WWZ wavelet power profile of R4 ringlet, computed from β Centauri, rev. 105 individual occultation profile. The Prometheus 2:1 ILR position is represented by a vertical dashed line. 122

2.35 Locations of the observed wavelike structures in the C ring. New developments appear in red. We also represent the locations of the resonance that match both the position and the direction of propagation when available. 123

2.36 Normal optical depth of the C ring. Lindblad and vertical first, second and third order resonances positions with the synchronous orbit are represented together with the positions of the reported waves. 130

2.37 Normal optical depth of the C ring. Lindblad and vertical first, second and third order resonances positions with the core of the F ring are represented together with the positions of the reported waves. 131

2.38 Normal optical depth of the C ring. Lindblad and vertical first, second and third order resonances positions with the outer edge of the B ring are represented together with the positions of the reported waves. 132

2.39 Normal optical depth of the C ring. Lindblad and vertical first, second and third order resonances positions with the G1 gap are represented together with the positions of the reported waves. 133

2.40 Normal optical depth of the C ring. Lindblad and vertical first, second and third order resonances positions with the Colombo gap are represented together with the positions of the reported waves. 134

2.41 Normal optical depth of the C ring. Lindblad and vertical first, second and third order resonances positions with the Maxwell gap are represented together with the positions of the reported waves. 135

2.42 Normal optical depth of the C ring. Lindblad and vertical first, second and third order resonances positions with the Bond gap are represented together with the positions of the reported waves. 136

2.43 Normal optical depth of the C ring. Lindblad and vertical first, second and third order resonances positions with the Dawes gap are represented together with the positions of the reported waves. 137

2.44 Various responses of a disk near an inner Lindlad resonance (located at $x = 0$). (a) A disk dominated by self-gravity. The wave is launched at $x = 0$ and propagates to the right of the resonance, while remaining evanescent on the left side. (b) A self-gravity wave damped by viscosity. (c) A wave in a disk dominated by pressure. The propagating and evanescent sides are inverted with respect to the self-gravity case. (d) Response in a disk dominated by viscosity. The wave is now evanescent on both sides of the resonances. Figure and caption from Sicardy (2006). 142

2.45 Measured phases of the Prometheus 9:8 density wave at r = 129000 km with respect to the longitude relative to Prometheus for individual occultations. . 147

2.46 Mass extinction coefficient limit values. Actual mass extinction coefficient values, calculated at the associated resonance locations are displayed in blue while upper limits of mass extinction coefficient, estimated from κ $(m-1)$, are shown in red. 153

3.1 WWZ wavelet power profile computed from the α Virginis, rev. 34, occultation of the Mimas 4:2 ILR region. The lower panel shows the photon count rates. 164

3.2 Co-added WWZ wavelet power profile computed from individual occultation profiles of α Virginis and β Centauri occultations of the Janus 2:1 ILR. The lower panel shows the α Virginis, rev. 34 photon count rates. 165

3.3 WWZ wavelet power profile computed from the α Virginis, rev. 34, occultation of the Pandora 4:3 ILR region. The lower panel shows the photon count rates. 166

3.4 WWZ wavelet power profile computed from the α Virginis, rev. 34, occultation of the Janus 5:3 ILR region. The lower panel shows the photon count rates. 167

3.5 WWZ wavelet power profile computed from the α Virginis, rev. 30, occultation of the Janus 4:2 ILR region. The lower panel shows the photon count rates. 168

3.6 WWZ wavelet power profile computed from the α Virginis, rev. 34, occultation of the Prometheus 5:4 ILR region in the Barnard Gap. The lower panel shows the photon count rates. 170

3.7 WWZ wavelet power profile computed from the α Virginis, rev. 34, occultation of the Pandora 5:4 ILR region (inner A ring). The lower panel shows the photon count rates. 171

3.8 WWZ wavelet power profile computed from the α Virginis, rev. 34, occultation of the Janus 7:5 ILR region. The lower panel shows the photon count rates. 172

3.9 Co-added WWZ wavelet power profile computed from individual occultation profiles of α Virginis and β Centauri occultations of the Pan 7:6 ILR. The lower panel shows the α Virginis, rev. 34 photon count rates. 173

3.10 Co-added WWZ wavelet power profile computed from individual occultation profiles of α Virginis and β Centauri occultations of the Atlas 5:4 ILR. The lower panel shows the α Virginis, rev. 34 photon count rates. 174

3.11 Co-added WWZ wavelet power profile computed from individual occultation profiles of α Virginis and β Centauri occultations of the Pan 6:5 ILR. The lower panel shows the α Virginis, rev. 34 photon count rates. 175

3.12 Co-added WWZ wavelet power profile computed from individual occultation profiles of α Virginis and β Centauri occultations of the Pandora 9:7 ILR. The lower panel shows the α Virginis, rev. 34 photon count rates. 176

3.13 WWZ wavelet power profile computed from the α Virginis, rev. 34, occultation of the Prometheus 10:8 ILR region. The lower panel shows the photon count rates. 177

3.14 WWZ wavelet power profile computed from the α Virginis, rev. 34, occultation of the Prometheus 9:7 ILR region. The lower panel shows the photon count rates. 178

3.15 WWZ wavelet power profile computed from the α Virginis, rev. 34, occultation of the Atlas 6:5 ILR region. The lower panel shows the photon count rates. 179

4.1 Image: NASA/JPL/Space Science Institute. Cassini ISS images revealing Pan orbiting in the Encke gap. The narrow ringlet coorbiting with Pan is also visible, together with wakes just ouside the Encke gap. 184

4.2 Photon counts from the occultation of σ Sagitarii (Rev 11) showing the Encke gap region and wavy features inner and outer to the gap. 186

4.3 WWZ wavelet power profiles of the Cassini Division around the Encke gap from individual occultation profile of σ Sagitarii, rev 11. 187

4.4 WWZ wavelet power profile of the Huygens ringlet from individual occultation profile of κ Centauri, rev 35. Lower panel shows the corresponding occultation profile. 188

4.5 WWZ wavelet power profile of the Huygens ringlet from the occultation of α Arae, rev 63. Lower panel shows the corresponding occultation profile. . . . 189

4.6 WWZ wavelet power profile of the Huygens ringlet from the occultation of γ Cassiopeiae, rev. 64. The lower panel shows the actual structures in the photon counts. 190

4.7 WWZ wavelet power profile of the Huygens ringlet from the occultation of α Virginis, rev. 30. The intermediate panel shows the corresponding occultation profile and the lower panel zooms in to show the actual structures in the photon counts. 192

4.8 WWZ wavelet power profile of the Huygens ringlet from the occultation of γ Gruis, rev. 41. The intermediate panel shows the corresponding occultation profile and the lower panel zooms in to show the actual structures in the photon counts. 193

4.9 WWZ wavelet power profile of the Huygens ringlet from the occultation of σ Sagitarii, rev. 11. The intermediate panel shows the corresponding occultation profile and the lower panel zooms in to show the actual structures in the photon counts. 194

4.10 WWZ wavelet power profile of the Huygens ringlet from the occultation of δ Lupi, rev. 57. The intermediate panel shows the corresponding occultation profile and the lower panel zooms in to show the actual structures in the photon counts. 195

4.11 WWZ wavelet power profile of the Huygens ringlet from the occultation of α Virginis, rev. 116. The intermediate panel shows the corresponding occultation profile and the lower panel zooms in to show the actual structures in the photon counts. 196

4.12 Ring-satellite interaction. Since we are in the rotating frame with the moonlet, inner particles (down) are moving to the left and outer particles (up) are moving to the right. Each encountering particle receives a gravitational "kick" as it passes close to the moonlet, and then proceeds on a more eccentric orbit. The overall direction of rotation is toward the left and the planet is toward the bottom. The radial scale is highly expanded compared to the azimuthal scale. Based on Figure 1.1 from Showalter et al. (1986). 198

4.13 Satellite wakes. Uniformly spaced semimajor axes particles are followed in the rotating frame with the satellite. Radial scans in the generated pattern presents an increasing wavelength and a decreasing amplitude when the distance to the moonlet is increasing. Though the particles start oscillating in phase, the wavelength varies and causes the trajectories to pile-up a few periods downstream. The index m numbers the density oscillation periods, starting with $m = 0$ at the moonlet azimuthal position. Farther, the pattern of streamlines is modified by collisions and the wakes pattern fades. The radial scale is highly expanded compared to the azimuthal scale. Based on Figure 1.2 from Showalter et al. (1986). 199

4.14 Images: NASA/JPL/Space Science Institute. Cassini ISS images of the Encke gap. Pan's orbit leaves a narrow ringlet visible inside the Encke gap. Increasing wavelengths with radial distance from Pan's orbit are clearly visible. Azimuthal wavelengths appear one order of magnitude bigger than radial wavelengths as expected from Equations 4.1 and 4.2. 200

4.15 WWZ wavelet power profiles of the Cassini Division around the Encke gap from individual occultation profile of σ Sagitarii, rev 11. Lower panel shows the corresponding occultation profile. Black lines correspond to theoretical wavelength from Equation 4.1. 201

4.16 Wavelength with respect to the radial distance to the satellite are plotted for longitudes relative to the moon evenly spaced every 10°. 202

5.1 From Sremčević et al. (2007). Propellers as seen by Cassini NAC, with a 1-km/pixel resolution in radius and a 0.5-km/pixel resolution in azimuth. . . 204

5.2 Photon count rates of the occultation of α Virginis, rev. 34 showing the Cassini Division (left) and α Virginis, rev. 30 showing the Huygens Gap (right).207

5.3 Photon count rates in the Huygens ringlet from the occultation of α Virginis, rev. 116. The red cross identifies the position of the detected ghost. Its height matches the background level of one of the stars that compose the α Virginis binary. 208

5.4 Photon count rates in the Huygens ringlet from the occultation of α Arae, rev. 63. The red cross identifies the position of the detected ghost. Its height matches the background level of the star. 209

5.5 Photon count rates outside the Huygens Gap from the occultation of α Virginis, rev. 34. The red cross identifies the position of the detected ghost. Its height matches the background level of the star. 210

5.6 While Cassini UVIS is moving along the rings and a structure (edge, ringlet...) comes in between the target binary stars and the spacecraft, we will observe steps in the measured photon count rates. The heights of these steps are proportional to the brightness of the binary components and are additive when both components are unocculted. The radial widths of the steps are function of the apparent separation between the binary stars, as seen from the instrument. 211

5.7 Upper panels show raw photon count rates versus ring plane radius for the occultation of the binary star α Cru (Rev 100), ingress (left) and egress (right). We observe the two rate levels due to the binary star. The central peak matches the level of one of the stars. The three lower panels for each direction of occultation provide details about the detection process steps: smoothing, subtracting and filtering on optical depth levels. 212

5.8 Photon count rates of the Huygens ringlet from the occultation of α Arae, rev. 63. The corresponding smoothed data is shown in the second plot. After subtracting the smoothed data from the raw data, the third plot (c) identifies the exact position of isolated features that might be a potential ghost (the structure around 117831 km is flagged as a potential ghost). The optical depth is also represented (d). 214

5.9 Cumulative width distribution of the detected ghosts in number of data points. The zone at the left of the vertical dashed line delimits the structures that we consider as ghosts with a high confidence. Larger structures (wider than 8 data points) that can correspond to other phenomena are excluded from the following study. 216

5.10 Top panel shows the mean of the signal in black and the variance of the signal in grey. Second panel presents the absolute difference between the mean and the variance, while third panel extracts the regions that can be considered "Poisson-like". Last panel shows the corresponding optical depth of the rings. 218

5.11 Propeller-shaped depletion zones created around a central moonlet. Orbital direction is towards the right and the planet is towards the bottom. Figure from Tiscareno et al. (2008). 223

5.12 Primary lobes of the propellers created by the interaction of 20-cm radius particles with a 10-m radius boulder. Optical depth is 0.1 and Saturn's direction is towards the bottom. 225

5.13 The propeller model described by Equation 5.8. The coordinate system is a radius-azimuth grid, in which the direction toward Saturn is down (-r) and the orbital direction is to the right (+). From Tiscareno et al. (2008). 226

5.14 Credit: NASA/JPL/Space Science Institute. Four propellers were identified in two images taken from Saturn Orbit Insertion on July 1, 2004 with the narrow angle camera on-board Cassini. These propellers are located in the A ring. They are about 5 kilometers long overall and have a total radial extension around 300 meters. Images are reprojected: Saturn is up and orbital motion is toward left. 227

5.15 Propeller signature after 6 orbits for a 10-m radius boulder (represented in red in the center of the figure) and 20-cm radius ring particles. Enough particles were simulated to reach an optical depth of 0.1. Saturn's direction is towards the bottom. 230

5.16 Primary lobe of the propellers created by the interaction of 20-cm radius particles with a 10-m radius boulder. This zoom in is showing the primary trailing outer lobe of the depletion zone. Particles around this zone had a close encounter with the boulder less than one orbit ago. 231

5.17 Propeller signature for a 10-m radius boulder (represented in red). Particles radii are 20 cm (upper left), 40 cm (upper right), 60 cm (lower left) and 80 cm (lower right). In each case, the optical depth and the particle masses are kept constant. Saturn's direction is towards the bottom. 233

5.18 Propeller signature for a 10-m radius boulder (represented in red) and equivalent 20-cm radius ring particles (in agreement with results from Section 5.3.2.3.2, we consider 80-cm radius particles with a density of 13.3 $kg\ m^{-3}$). Enough particles were simulated to reach an optical depth of 0.1. Saturn's direction is towards the bottom. Upper figures do not consider collisional effects whereas lower figures do. Self-gravity is taken into account only in right figures. 235

5.19 Photon count rates from the occultation of κ Centauri, rev. 35 across the Huygens Ringlet (left). We measure the width of the isolated peak (here defined by two data points) by estimating the width at half-height of the interpolation of the data (16 m) - (right). 237

5.20 Cumulative distribution of the ghosts widths in the C ring and in the Cassini Division. Though figure clarity prevents us from displaying them, we estimate the relative uncertainty on our width measures to be about $1/N$, N being the number of points in the ghost. 238

5.21 Cumulative distribution of the modeled ghosts widths in the C ring (upper panel) and in the Cassini Division (lower panel) for an initial particle size distribution power-law index of 0.6 for the C ring and 0.8 for the Cassini Division. Due to the logarithmic scales, matching the last few scattered points is less important than matching the left part: statistics cannot be applied for such small numbers of the biggest particles. 243

5.22 Outer trailing propeller signature for a perturbing boulder (represented in red) in an environment of 20-cm particles (50-cm for the 50-m and 100-m boulders) providing an optical depth around 0.1. Saturn's direction is towards the bottom. The boulder is drawn to scale in red. From left to right and top to bottom, boulder radii are 1 m, 2 m, 5 m, 10 m, 20 m, 50 m and 100 m. The extended size of the 100-m boulder simulation required to adapt the number of particles and the density as detailed in Section 5.3.2.3.2: we considered 2-m particles with a density of 13.3 $kg\ m^{-3}$ in that case. 244

5.23 Propeller signature for a 10-m radius boulder (represented in red). For left to right and top to bottom, particles radii are 5 cm, 10 cm, 20 cm, 50 cm, 1 m and following a power-law distribution with an index $q = 2.75$ reflecting the estimated Cassini Division particle distribution, between 10 cm and 1 m in the lower right panel. Optical depth is 0.1. Saturn's direction is towards the bottom. Simulations involving 5-cm and 10-cm particles are too heavy and required being adapted as detailed in Section 5.3.2.3.2: we considered 40-cm particles instead with densities of 1.66 $kg\ m^{-3}$ in the first case and 13.3 $kg\ m^{-3}$ in the second one. 248

5.24 Cumulative particle size distribution for the C ring (red), Cassini Division (blue) and the A ring (green). Submeter particle populations from Zebker et al. (1985) are displayed with dashed lines while the source distribution estimated from the Monte-Carlo algorithm for suprameter particles is displayed in solid lines. 249

5.25 Photon count rates from the ζ Orionis, rev. 42 occultation showing the Blériot Propeller Object. We measure a width of 535 m. 254

6.1 Relative masses of Saturn's inner satellites and rings as a function of their distance to the planet center. The masses are represented by circles of radius proportional to the cubic root of the mass. 259

LIST OF TABLES

1.1 Particle size distributions from Voyager RSS and 28 Sgr occultations of Saturn's rings. 18

1.2 Saturn's rings locations and optical depths. 24

1.3 Cassini UVIS stellar occultations. 60

2.1 Cassini UVIS stellar occultations. 72

2.2 Ringlet signatures. 82

2.3 Observed wavelike structures in the C ring. 88

2.4 Potential moons. 109

2.5 Gravitational Harmonics. 124

2.6 Resonance types. 128

2.7 Strongest Inner Lindblad Resonances in the C ring. 143

2.8 C ring surface-mass densities. 150

2.9 C ring surface mass density constraints. 152

3.1 Strongest Inner Lindblad Resonances in the B ring. 159

3.2 Strongest Inner Lindblad Resonances in the Cassini Division. 161

3.3 Surface-mass densities. 180

5.1 Detected ghost rates and widths. 215

5.2 Reference gaps for the identification of cosmic rays. 217

5.3 Derived boulder radii. 239

5.4 Radial extension of the outer trailing primary lobe of the propeller signatures. 245

CHAPTER 1

INTRODUCTION

Planetary ring systems are excellent laboratories for the study of flat systems such as protoplanetary, circumstellar, accretion or debris disks and even galaxies. They present a huge variety of structures, compositions and properties that we are not even close to fully understanding. Saturn has been observed for centuries and most recently, huge progress has been made thanks to spatial exploration: the Pioneer 11 probe (1979), Voyager 1 (1980), Voyager 2 (1981) and Cassini (2004-present) have provided new information about Saturn's rings with ceaselessly increasing resolution.

1.1 The Beginning of Modern Astronomy

The closest planets were known since ancient times with diverse names. The present name of the sixth planet comes from the Roman god Saturn, who is the equivalent of Krónos (Κρόνος) for the Greeks. Krónos, son of Ouranós (Uranus, the Sky) and Gaia (the Earth), king of the Titans and father of Zeus (Jupiter), should not be mistaken for Khrónos (Χρόνος), the early Greek deity embodying Time and Destiny. If Saturn is now very famous for its ring system, this attribute has only been known for less than 400 years. Benefiting from the Dutch innovations in optics, Galileo Galilei started building his own telescopes and used them to observe the phases of the Moon and the lunar terminator, revealing mountains on the Moon's surface. He also observed the sun spots, the organization of stars in clusters, Jupiter's four main satellites (that he named Medicean satellites and that are now known as Galilean satellites) and the Saturnian system. The second largest planet of the solar system, Saturn (Figure 1.1), is the sixth one from the Sun, located at 9.5 astronomical units (AU). Its equatorial radius (60268 km) is fairly different from its polar radius (58232 km), making Saturn the most oblate planet in the solar system, as a result of its very fast rotation around its axis. Indeed, Saturn's day lasts 10 hours and 39 minutes, while a saturnian year lasts 29.5 terrestrial years. With a mass of 5.68×10^{26} kg, Saturn is also the only planet with a density lower than water (0.69 kg cm^{-3}). Its orbit is slightly eccentric ($e = 0.0560$) and inclined ($i = 2.488°$) and the rotation axis of the planet is inclined by 25.3° to its orbit plane. Its atmosphere is made of hydrogen, with small quantities of helium and methane. Saturn's foggy yellow color presents wide atmospheric bands, similar to Jupiter's. Close to the equator, winds can reach velocities around 500 m s^{-1}. Saturn's interior is thought to be similar to Jupiter's: a rocky core surrounded by a liquid metallic hydrogen layer with traces of different ices. The internal temperature is estimated to 12000 K in the core and Saturn irradiates more energy to space than it receives from the Sun. Saturn also presents a magnetic field a little weaker than the Earth's, probably due to electrical current within the metallic-hydrogen layer. Recent models involving planet migration in the proto-planetary disk have revised the scenario in which all the planets formed close to their current orbits. The "Nice model" (Morbidelli et al. (2005), Tsiganis et al. (2005) and Gomes et al. (2005)) suggested that Saturn and Jupiter might have formed close to their present orbits while Neptune and Uranus could have formed much closer to the Sun in the early solar system (respectively around 12 and 15 AU) than they are now (30.1 and 19.2 AU): due to planet migration Jupiter could have eventually crossed its 2:1 Inner Lindblad Resonance with Saturn and generated a brutal reorganization of the solar system bodies. In particular, Neptune and Uranus would have been pushed outward in the solar system and could have switched their orbits, and the perturbation of the orbits of the small bodies could have triggered what is known as the Late Heavy Bombardment from analysis of the history of cratering on the Moon (Hartmann et al., 2000). This dramatic increase in the small bodies flux in the solar system occurred around 700 million years after the formation of the solar system 4.7 billion years ago, and is believed to have lasted around 10 million years. Charnoz et al. (2009) revisited the formation scenarios of Saturn's rings in the light of the "Nice model" and suggested that the Late Heavy Bombardment would be a favourable moment to form them by increasing the cometary flux in the solar system. Saturn is unique in the solar system from a variety of point of views including but not limited to the diversity of its ring system and satellite system. Figure 1.1 shows the beauty of these rings.

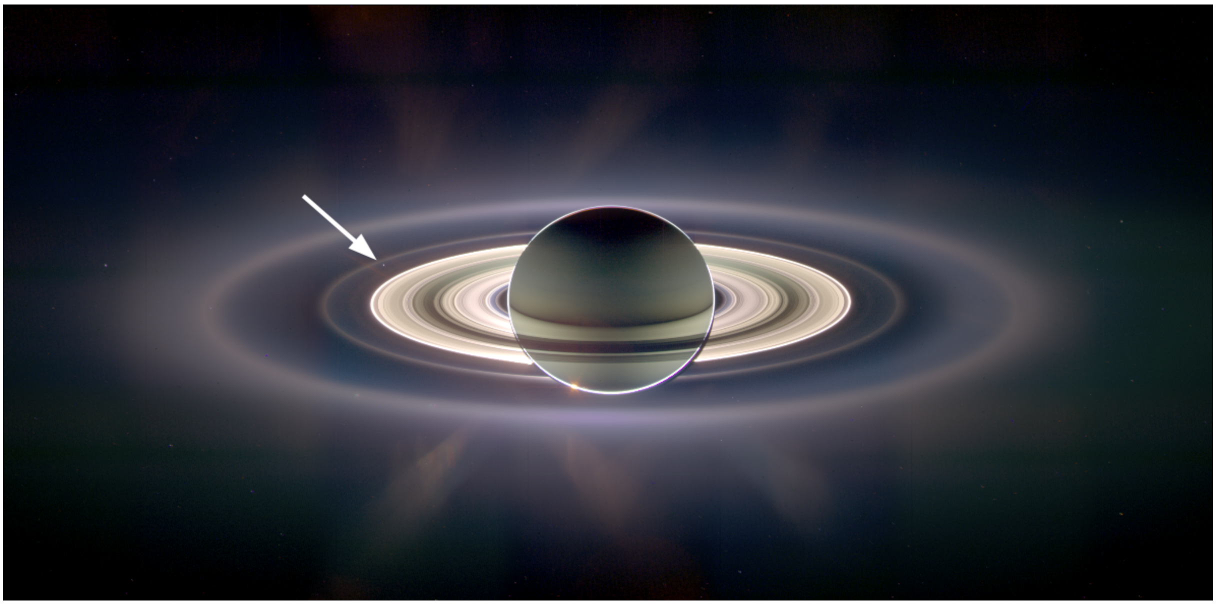

Figure 1.1: Image: NASA/JPL/Space Science Institute. Mozaic image of Saturn occulting the Sun, thus revealing very faint rings around the planet. The white arrow points at the Earth, visible through the rings on the left of Saturn.

1.2 Saturn's Satellites

Saturn presents a great variety of satellites (Figure 1.2).

Size diversity is also huge (Figure 1.3), ranging from tiny moonlets less than 1 kilometer in size up to Titan (2576 km in radius). Saturn has more than 60 moons with confirmed orbits, thirteen of which have diameters larger than 50 kilometers. Titan, larger than Mercury, is the second largest moon in the Solar System, and the only one that has a significant atmosphere. Enceladus is also very particular with its gas and dust jets at the poles.

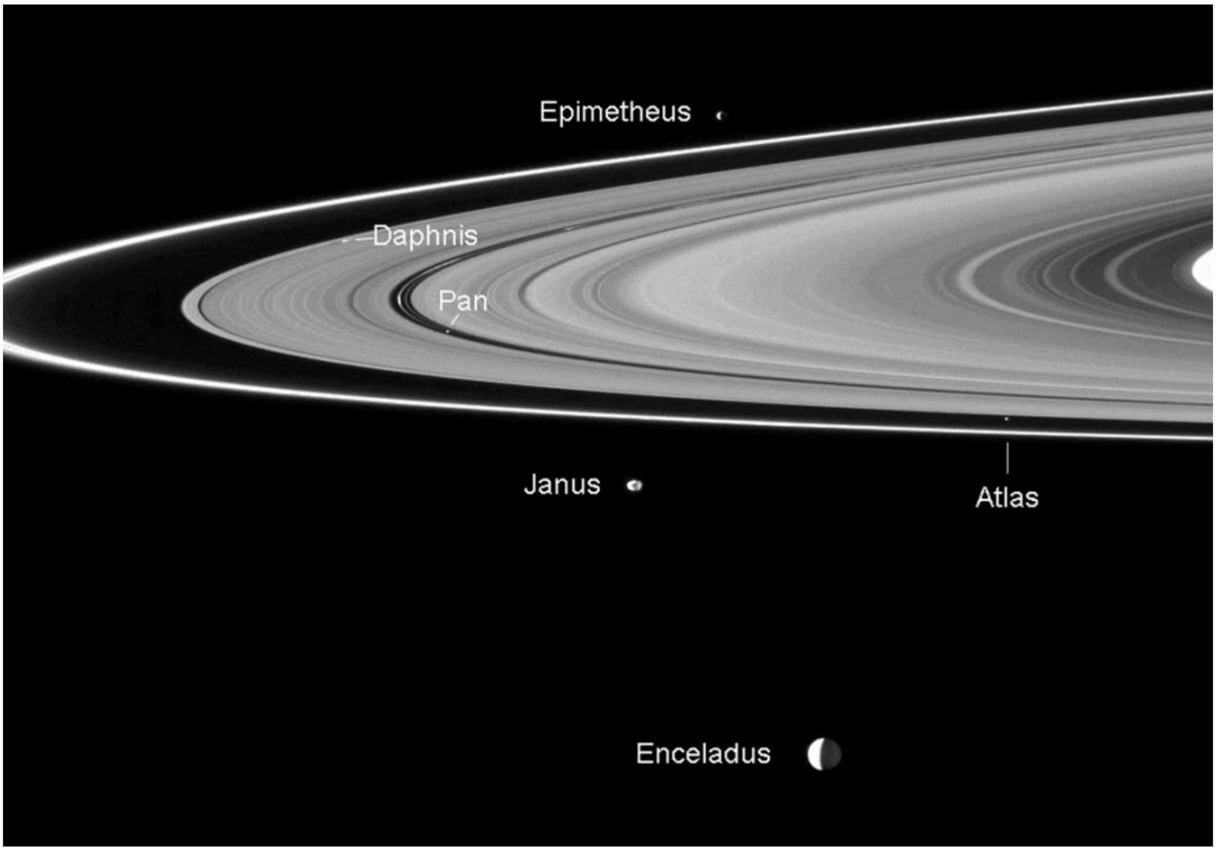

Figure 1.2: Image: NASA/JPL/Space Science Institute. Cassini captured 6 moons in front of the A and F rings: Pan and Daphnis are inside the Encke and Keeler gaps of the A ring. Atlas is orbiting between the A ring and the F ring. Janus and Epimetheus are sharing common orbits a little farther and Enceladus is feeding the E ring.

Saturn's regular satellites have prograde orbits not greatly inclined to the Saturn's equatorial plane. These include the major satellites (Mimas, Enceladus, Tethys, Dione, Rhea, Titan and Iapetus), small moons which are in Trojan orbits with larger moons (Telesto, Calypso, Helene and Polydeuces), two mutually co-orbital moons (Janus and Epimetheus), two moons which are shepherding the F Ring (Prometheus and Pandora), Pan and Daphnis

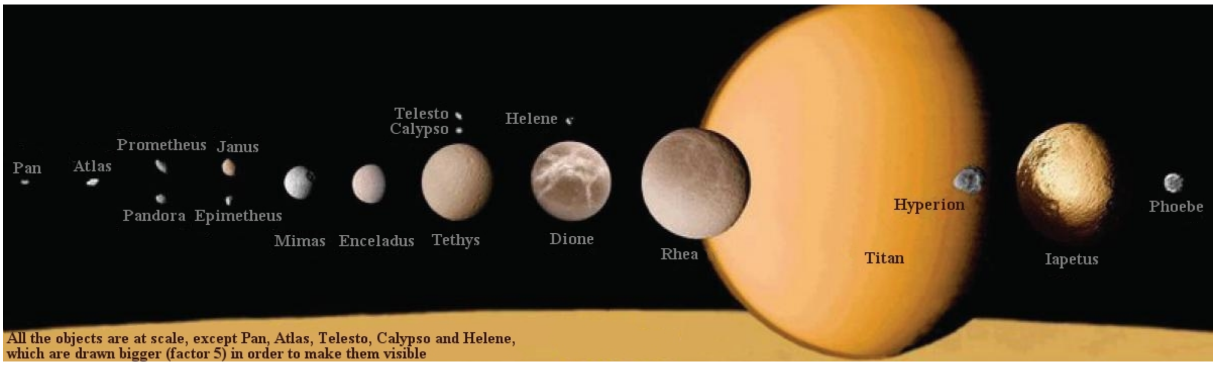
Pan
Atlas
Prometheus
Janus
Pandora
Epimetheus
Mimas
Enceladus
Telesto
Calypso
Tethys
Helene
Dione
Rhea
Titan
Hyperion
Iapetus
Phoebe

All the objects are at scale, except Pan, Atlas, Telesto, Calypso and Helene, which are drawn bigger (factor 5) in order to make them visible

Figure 1.3: Image: NASA/JPL. Saturn's principal satellites. Objects are presented in increasing distance away from Saturn.

which orbit within the Encke and Keeler gaps inside the rings respectively, the relatively large Hyperion, locked in a resonance with Titan and finally, Methone, Anthe and Pallene which orbit between Mimas and Enceladus. The irregular satellites, which are much farther from Saturn, have higher inclinations, and can be either prograde or retrograde. They probably were captured debris (Phoebe is the most obvious example).

1.2.1 Moonlets Located inside the Roche Limit

Recent observations established the existence of several moonlets in the A and B ring. A 300 m-moonlet was found 480 km inner to the B ring outer edge in 2009 while loads of propellers, with radii of tens to hundreds of meters, were observed in the A ring (Tiscareno et al. (2008, 2010b) and Lewis and Stewart (2009)). These objects are not big enough to open a stable gap on their orbit but create significant structures in the rings. Pan (28.4

km wide) and Daphnis (7.8 km wide) orbiting in the Encke gap and Keeler gap respectively could constitute the upper range of size of such a population since they opened a stable gap on their trajectory. Outside the main rings, Prometheus and Pandora belong to the class of shepherding satellites: the interaction of a satellite and a disk tends to push each one away from each other, and therefore, Prometheus (inner to the F ring) and Pandora (outer to the F ring) tend to confine the F ring (Goldreich and Tremaine, 1980). To a certain extent, Pan and Daphnis are also shepherding the edges of their neighbor rings. Another type of shepherding can occur when resonances with farther satellites confine ring edges (Goldreich and Tremaine, 1978b) as it is the case for the outer edge of the A ring in 7:6 inner Lindblad resonance with Janus and Epimetheus and for the outer edge of the B ring in 2:1 inner Lindblad resonance with Mimas (Porco et al., 1984a; Spitale et al., 2008). Finally, at the extreme limit of the Roche limit, Janus and Epimetheus are co-orbital satellites, swapping their orbits every 4 years (Lissauer et al. (1985) and Spitale et al. (2006)).

1.2.2 The Main Satellites

This category contains all the big satellites between Mimas and Iapetus. They are orbiting in Saturn's equatorial plane. Most of them present important craters, such as Mimas or Tethys. Going away from Mimas and the planet, we then find Enceladus which is the smallest geologically active object of the solar system. Volcanic plumes release vapor and dust on its orbit, feeding the E ring (Spahn et al., 2006; Porco et al., 2006). The very small km-sized moons Methone, Anthe and Pallene form the Alkyonides group. We then find Tethys and its two Trojans Telesto and Calypso (co-orbiting bodies trapped in the Lagrangian L4 and L5 points). Dione also has two Trojans: Helene and Polydeuces. Rhea, the second largest satellite of Saturn was briefly suspected to have rings (Jones et al., 2008) until Tiscareno et al. (2010a) invalidated that theory using Cassini images. Titan orbits more than 1 million kilometers away from Saturn. Bigger than Mercury, Titan has a dense atmosphere, rich in nitrogen with traces of methane. It also has a unique set of methane lakes. Hyperion is in resonance 4:3 with Titan but is much smaller and presents a very high porosity, coupled with an irregular shape that makes its rotation unpredictable. Iapetus completes the list of the main and regular satellites.

1.2.3 The Irregular Satellites

The 38 other farther satellites are distributed in 3 subcategories based on their orbital characteristics: the Inuits and the Gallics, prograde, and the retrograde Norses. Their orbits are mainly more inclined than the regular satellites. Only a few of them are bigger than 10 km. However, Phoebe is approximately 214 km wide and it is believed that it is a Kuiper Belt Object captured by Saturn (Jewitt and Haghighipour, 2007).

1.2.4 Possible Origins

Charnoz et al. (2010) suggested a correlation between satellite sizes and their distance to Saturn (Figure 1.4). If the largest satellites could be as old as the solar system, smaller ones (up to a few tens of kilometers) located close to the Roche limit could be younger. In this second population of satellites, it appears that their size is increasing with the distance to Saturn. In addition, these moons have a lower density and irregular shapes.

Salmon et al. (2010) showed that some material of the A ring could cross the Roche limit under the influence of viscous spreading. This material could then accrete and form satellites with similar sizes and densities to the actual satellites. The equatorial ridges of these satellites (Charnoz et al., 2007) could be the proof that accretion actually played a role.

The main satellites, on the contrary, probably formed at the same time as the planet in the accretion disk. Numerical simulations from Mosqueira and Estrada (2003a,b) showed that such formations in Saturn sub-nebula can happen in a very short time (about a hundred years). Canup and Ward (2006b) showed that this process involves a competition between satellite growth from the gas flux and their destruction in the planet after migration in the sub-nebula disk. As a consequence, the ratio of the total satellite mass over the planet mass has to tend to 10^{-4}, which is the observed trend in the giant planets. Not only will these satellites have resonances with ring particles but they also present resonances with other satellites as it is the case for Mimas-Tethys (4:2), Enceladus-Dione (2:1) or Titan-Hyperion

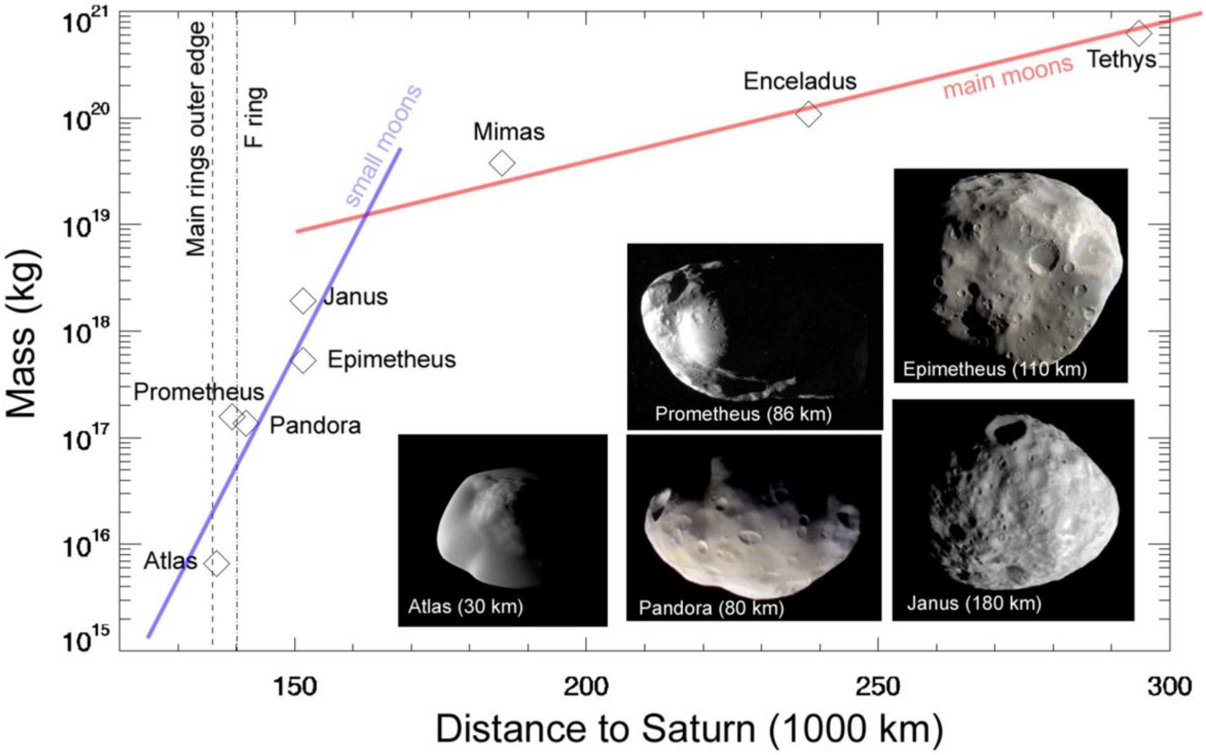

Figure 1.4: Mass distance distribution of Saturn small satellites. External edges of the rings are shown with vertical dashed lines. Smaller satellites present a different trend (blue) than bigger ones (red). From Charnoz et al. (2010).

(4:3). In addition to the apparent sorting of satellite masses with respect to their distance to Saturn, we can clearly identify two populations, suggesting possible different origins: the small moons orbiting within the Roche limit (up to Janus and Epimetheus) and the main satellites (from Mimas to Tethys at least).

1.3 Saturn's Rings

1.3.1 From Galileo to Voyager

In 1610, Galileo Galilei observed what he believed to be two satellites orbiting around Saturn. Two years later, he observed changes in that system: the two satellites were missing. He then wrote "Has Saturn, perhaps, devoured his own children?", referring to the mythology and the fact that Krónos was supposed to have eaten his children. We now know that rings were actually observed at different angle but it was not before 1654 that Christiaan Huygens suggested the existence of rings in order to justify the different observations (Figure 1.5).

Planetary rings origins are constrained by actual observations of an inner ring region and an outer satellite region. Indeed rings are located inside the Roche limit (below which tidal forces disrupt a body that is only submitted to its own self-gravitation). Some formation scenarios suggest that rings were formed at the same time the planet was while some others consider that rings result of the later destruction of a body orbiting Saturn. The following history is taken from Colwell et al. (2009b). Saturn was long considered to be the only planet hosting rings since Christiaan Huygens identified the rings system in Saturn's equatorial plane in 1654. Next, Jean-Dominique Cassini discovered the eponymous Cassini Division in 1675 (Figure 1.6).

Giuseppe Campani also observed in 1664 that the inner half of the disk was brighter than the outer half. Later observations by William Herschel confirmed in 1791 that the

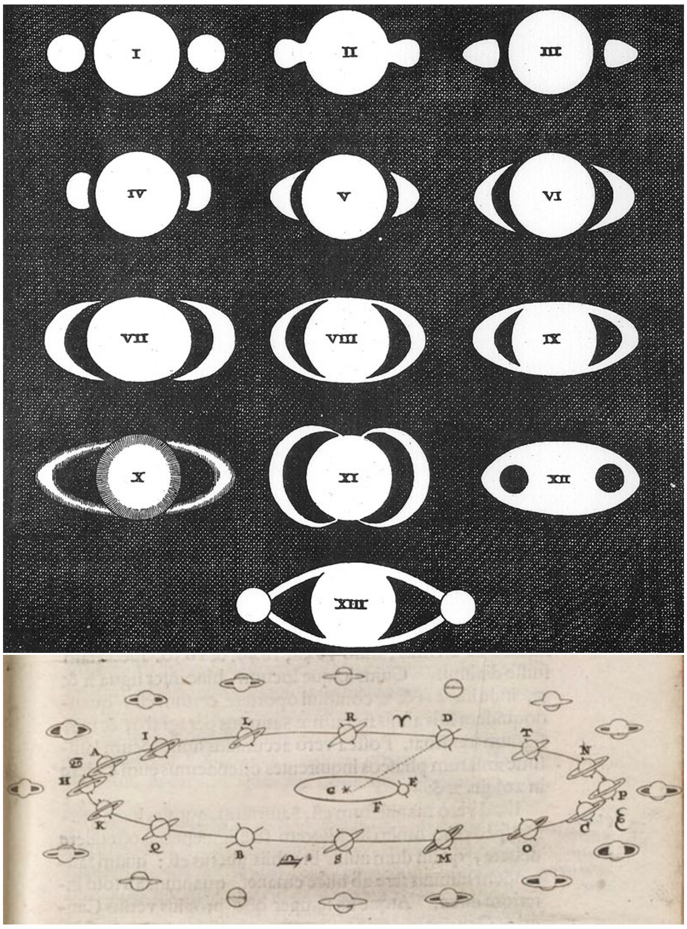

Figure 1.5: These drawings from Huygens's *Systema Saturnium* of 1659 illustrate the variety of perceptions of Saturn that resulted from the interplay of its changing orientations, improvements in telescopes, and new interpretations of its physical nature. The observers were: I, Galileo (1610), who in 1616 drew Saturn much like IX; II, Scheiner (1614); III, Riccioli (1641 or 1643); IV-VII, Hevel (theoretical forms); VIII and IX, Riccioli (1648-1650); X, Divini (1646-1648); XI, Fontana (1638); XII, Biancani (1616); Gassendi (1638-1639); XIII, Fontana and others at Rome (1644, 1645). From Alexander (1962). In the lower diagram, Huygens showed how the axial tilts of both Earth and Saturn combine with their orbital motions around the Sun to produce the cyclical pattern of change in Saturn's appearance.

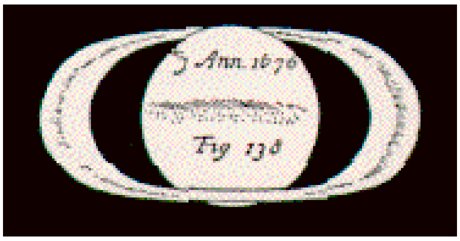

Figure 1.6: In 1675, Cassini reported that a "dark line" divided the ring into two parts, "the inner of which was brighter that the outer one". He made this drawing in 1676, apparently showing the outer ring to be narrower than the inner ring. From Alexander (1962).

Cassini Division appeared identical on both sides of the rings, proving that it was in fact a gap and not just a dark marking. In the XVIII$^{\text{th}}$ century, Pierre-Simon de Laplace worried about the structure and composition of the rings and proved that a solid ring would not be stable. Finally, James Clerk Maxwell described the rings as solid particles in independent differential rotation around the planet in 1859 (Maxwell, 1859), which would be verified by Edward Keeler's spectroscopic measures of radial velocities. Henri Poincaré then suggested the importance of collisional processes between ring particles in order to explain the flatness of the rings. Collisions were later studied numerically by Brahic (1974, 1975) and a systematic study of ring-satellites interactions was conducted by Goldreich and Tremaine (1980). The Encke Gap was named by James Keeler in 1888 after Johann Encke noticed irregularities in the A ring in 1837. Meanwhile, William and George Bond, and William Dawes independently discovered the C ring in 1850. In 1866, Daniel Kirkwood suggested that the Cassini Division is caused by a resonance with one of Saturn's moons. Goldreich and Tremaine (1978a) applied the theory of Lindblad resonances in spiral galaxies (Shu (1970a,b)) to describe spiral waves in the rings. Three new rings (D, F and G) and new ring-shepherding moons were discovered after the Pioneer and Voyager encounters with Saturn (Greenberg and Brahic, 1984). Figure 1.7 summarizes the rings names and locations, and average optical depth. Based on that last parameter, we would define the "main rings" as the ones with the highest optical depths (the A, B, C and F rings and the Cassini Division). The fainter rings would be referred to as the "diffuse rings". Stellar and radio occultations provided higher resolution information on the rings structures: Esposito et al. (1987) cataloged 216 features based on the Voyager 2 δ Scorpii stellar occultation. Subsequently, ring structure was probed by widespread Earth-based observations of a stellar occultation in 1989 (French and Nicholson, 2000).

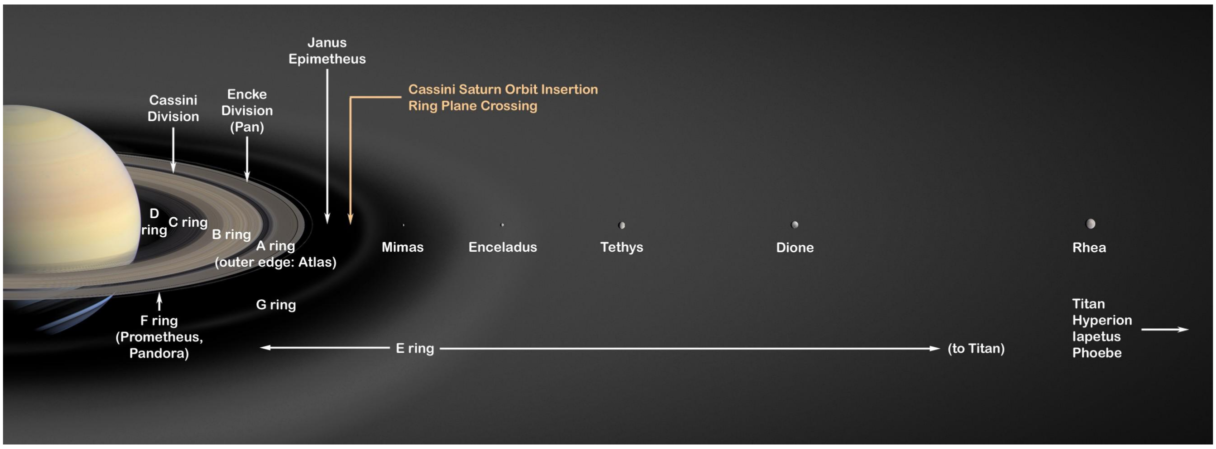
Janus
Epimetheus
Cassini Saturn Orbit Insertion
Ring Plane Crossing
Cassini
Division
Encke
Division
(Pan)
D
ring
C ring
B ring
A ring
(outer edge: Atlas)
Mimas
Enceladus
Tethys
Dione
Rhea
F ring
(Prometheus,
Pandora)
G ring
E ring
(to Titan)
Titan
Hyperion
Iapetus
Phoebe

Figure 1.7: Image: NASA/JPL. An artist's concept of Saturn, its rings and major icy moons—from Mimas to Rhea.

While Cassini was on its way to Saturn, numerous observations were conducted using the Hubble Space Telescope (HST). As the Earth passes through Saturn's ring plane about every

15 years, the HST was able to observe the 1995 Ring-Plane Crossing and imaged Saturn's ring system edge-on (Figure 1.8). Dones et al. (1996) and McGhee et al. (2001) could improve the astrometry knowledge of Saturn's satellites thanks to images of the Ring-Plane Crossing.

The HST also enabled clear observations of the B ring spokes by McGhee and French (2002) and McGhee et al. (2004, 2005). The opposition effect, a surge of brightness that can be observed when the planet is directly illuminated from behind the observer, was consecutively studied from HST images by French et al. (1998) and Poulet et al. (2002) who suggested that coherent backscattering was the principal cause of the opposition surge at very small phase angles, and by Salo et al. (2005) who attributed the opposition effect to mutual shadowing in the B ring. Cuzzi et al. (2002) focused on the radial color variations of the rings in order to model their composition. Bradley et al. (2010) also studied this effect using Cassini UVIS data. As Nicholson (1997) observed an azimuthal brightness asymmetry in the Ring-Plane Crossing from HST images, French et al. (2000) suggested that gravitational instabilities could play in key role in generating this asymmetry. The HST also enabled studies of the G ring by French et al. (1997) and Lissauer and French (2000), of the magnetosphere-ionosphere by Hansen et al. (2004) who coupled HST measurements of the Saturn aurora with Cassini data of the solar wind upstream from Saturn, and of the atmosphere and stratospheric haze of the planet by Muñoz et al. (2004). Finally, with the arrival of the Cassini orbiter in 2004, a new era in planetary exploration began.

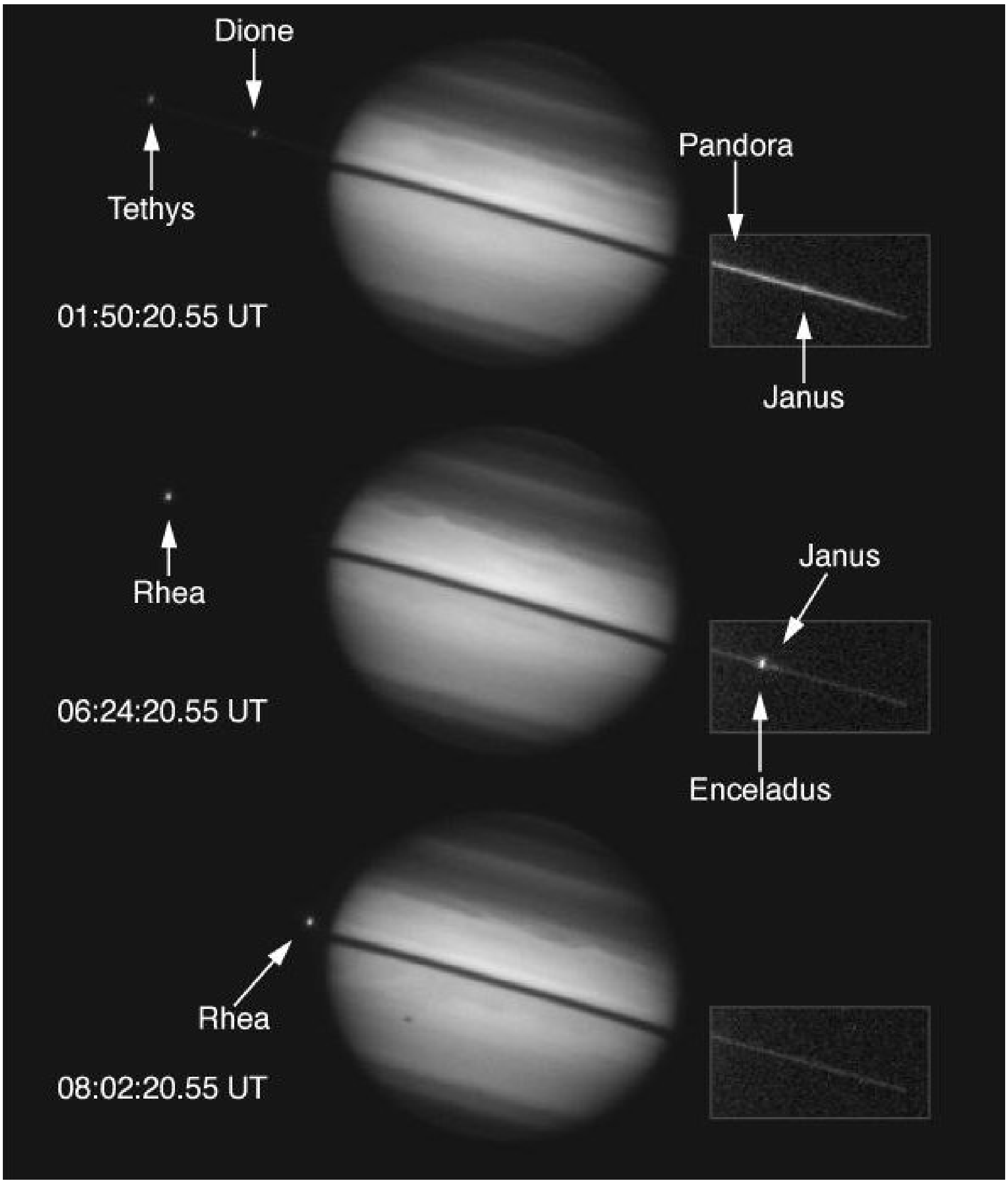
Dione
Tethys
Pandora
Janus
01:50:20.55 UT
Rhea
Janus
Enceladus
06:24:20.55 UT
Rhea
08:02:20.55 UT

Figure 1.8: Image: NASA/Space Telescope Science Institute. Saturn Ring-Plane Crossing: on May 22, 1995, Saturn was observed edge-on from the Hubble Space Telescope, clearly showing evidence of some of its satellites. The boxes around the western portion of the rings (on the right) indicate the area in which the faint light from the rings has been enhanced through image processing to make the rings more visible.

1.3.2 Composition

We can count on three complementary major sources of information about the particle sizes in Saturn's rings (see Cuzzi et al. (2009) for a complete review). Voyager 1 radio occultation (RSS) provided the first precise data in 1980 (Zebker et al., 1985), while the ground-based stellar occultation of 28 Sagitarii (28 Sgr) in 1989 improved the particle size distribution knowledge (French and Nicholson, 2000). Finally, Cassini radio occultation measures of differential optical depths (Marouf et al., 2008) provided the most recent parameters for the particle sizes.

Particle size distribution are regularly modeled by power-laws:

$$n(a)\mathrm{d}a = n_0 a^{-q}\mathrm{d}a \tag{1.1}$$

where a is the particle radius, $n(a)$ the number of particles with a radius equal to a, n_0 is a normalization factor and q is the differential power-law index.

For comparison, the destruction of a glacial boulder with a hammer usually provides a particle size distribution with an index of 3.4 (Hartmann, 1969; Dohnanyi, 1969, 1972). Parameters derived from Voyager RSS and 28 Sgr occultations are provided in Table 1.1.

Table 1.1: Particle size distributions from Voyager RSS and 28 Sgr occultations of Saturn's rings.

Ring region (R_{Saturn})	Radius range (km)	q	$a_{min}(cm)$	a_{max} (m)
Voyager RSS radio occultation[1].				
C1.35	78430–84460	3.11	0.1	4.5
C1.51	90640–91970	3.05	0.1	2.4–5.3
CD2.01	120910–122010	2.79	0.1	7.5
A2.10	125490–127900	2.70	0.1	5.4
A2.12	125490–130310	2.74	0.1	5.0
A2.14	127900–130310	2.75	0.1	6.3
A2.19	130860–133270	2.93	0.1	11.2
A2.24	133930–136350	3.03	0.1	8.9
28 Sagitarii occultation[2].				
C ring	74490–91983	3.1	1	10
B ring	91183–117516	2.75	30	20
Cassini Division	117516–122053	2.75	0.1	20
Inner A ring	122053–133423	2.75	30	20
Outer A ring	133745–136774	2.9	1	20

[1] From Zebker et al. (1985). The distribution parameters are inferred from inversion of the near-forward scattered 3.6-cm wavelength signal for $a > 1$ m, and of the modeling of both the 3.6-cm and the 13-cm wavelengths differential extinction as a power-law distribution over 0.1 cm< a <1 m. $a_{min} = 0.1$ cm is assumed for all regions.

[2] From French and Nicholson (2000). The distribution parameters are inferred from comparison of the strength and shape of profiles of the observed near-forward scattered stellar flux at 0.9, 2.1, and 3.9 μm wavelengths with theoretical predictions based on a power-law size distribution model, assumed uniform for each region.

Caption from Cuzzi et al. (2009).

In addition, Cassini results mainly comforted these results. However, values for a_{min} were estimated with an increased confidence: Cassini measured $q = 3.2$ in the C ring, where $a_{min} = 0.4$ mm and $a_{max} = 4.5$ m. From these results, it appeared that the distribution parameters were pretty uniform in the C ring, while the B ring was clearly showing some inconsistencies between the inner B1 region on one hand and the other B2, B3 and B4 regions on the other hand where $q < 2.7$. The Cassini Division also showed some differences between the main part and the Cassini Division ramp that was found to be closer to the inner A ring parameters. The A ring also presents some variations: either q has to increase with increasing radius or a_{min} has to decrease.

Larger particles, though sometimes not large enough to be called moonlets, have been detected in the A ring (Tiscareno et al., 2006; Sremčević et al., 2007; Tiscareno et al., 2008) as well as in the C ring and the Cassini Division (see Chapter 5 of the present manuscript). These boulders are big enough to create local disturbances but are still not able to open permanent gaps on their orbits. In the A ring, these boulders can reach a few hundreds of meters while they will be one order of magnitude smaller in the C ring and in the Cassini Division. Similar signatures are also visible in the B ring but have not yet been analyzed and are more likely to be associated with troughs generated by self-gravity-wakes. Whether they are longlived or transient remains an open question, as well as the question of their origins: were these boulders created by fragmentation or accretion? We will address that question in our Chapter 5.

Ring particles are mainly composed of water ice, pure at 99%, predominantly in crystalline form, with an outer regolith layer of dust. They present a reddish color at wavelengths shorter than 500 nm, though they do not appear to contain any macro-component that would strongly absorb in near-UV and blue wavelengths (see Poulet et al. (2003) for a complete review of the ring particles composition). It is also established that they do not contain any CO_2, CH_4 or other C-H bound. In addition, no silicates could be traced in the rings. The quest for the UV absorber is currently suggesting that reddening could be due to either micro-organic compounds such as Polycyclic Aromatic Hydrocarbons or nanohematite (Clark et al., 2008, 2009). Though no trend could be positively identified, it is clear from variations of ring color, particle albedo and water ice band depth, that the composition of the particles varies with the surface mass density and/or the optical depth. The C ring and the Cassini Division appear to show stronger correlations with optical depth variations than the A and B rings.

1.3.3 Origins

Esposito and Colwell (1989) estimated the lifetime of Uranian dust particles between 100 and 1000 years, suggesting that diffuse rings could be persistently fed in dust material by hypothetical moonlet belts. However, though this can be applied to Jupiter, Uranus and Neptune's diffuse rings, this process cannot generate such dense and massive rings as Saturn's. Four main formation scenarios are commonly proposed for the formation of Saturn's main rings.

Remnants of Saturn Sub-nebula:

A planetary embryo is surrounded by gas that collapses to form a disk (the energy is dissipated while the angular momentum is conserved): the sub-nebula. While energy is dissipated by radiation, the sub-nebula will cool down and contract before being accreted by the planet. The energy dissipation being no longer compensated, the planet will contract and reach its final radius. Pollack et al. (1977) believed that this could have happened to Saturn: the planet surface could have been located at the position of the B ring, thus creating an abrupt edge that would later be maintained by Mimas as Goldreich and Tremaine (1978a) showed. Then, if silicates condensed earlier than water ice, they could be eliminated by gas drag, accreting on the planet, and assuming that ice condensation could happen just before the sub-nebula dissipated, only ice particles would remain. The cooling time scale being much more important for Jupiter, the ice particles would probably not condense before the total dissipation of the sub-nebula. On the contrary, the cooling time scales are much shorter for Uranus and Neptune and therefore everything is likely to condense and be accreted in the planet by gas drag.

Tidal Disruption of Comets:

Comet composition is very close to that of ring particles. Therefore, the disruption of one or several comets in the Roche zone of the planet could provide the right material for the rings' formation. Fragments would form a ring around 120000 km away from the planet and would then spread viscously. However, considering either one big comet (around 200 km wide) or several smaller comets, the present population and flux of Centaurs in the solar system would not be able to generate such massive rings (Dones, 1991). Finally, the uniqueness of Saturn's rings would not be explained.

Catastrophic Impact between a Satellite and a Comet:

A catastrophic impact on a satellite would be able to generate the rings if this impact happened already within the Roche zone. Rather than creating a satellite there, it is more likely that the satellite would be created outside the Roche zone and then brought in either by gas drag or by type I migration (Ward, 1986) depending on its size. However, given the cometary flux in the solar system, a 150-km radius satellite would have a lifetime of the order of the solar system age.

In the last two scenarios, the cometary flux is a priori insufficient, unless considering that these scenarios could have happened during the Late Heavy Bombardment (Charnoz et al., 2009) that occurred around 700 million years after the solar system formation and lasted for about 10 million years. This period, possibly explained by the "Nice model" was the scene of a more intense flux of objects from the Kuiper Belt, also responsible for an sudden increase in crater impacts on the Moon at this period. However, though this coincidence increases the cometary flux and allows these formation scenarios, dense rings formation would be more likely to happen around the other giant planets than Saturn, therefore weakening the probabilities of these scenarios.

Tidal Disruption of a Titan-sized satellite:

Canup (2010) estimated that Saturn could have had more than one big satellite earlier, similarly to Jupiter. Assuming the loss of a differentiated Titan-sized satellite that would spiral into the planet, numerical models show that the tidal removal of mass from the icy upper layers of that satellite could generate a whole dense rings system with the actual observed composition. The core of such a satellite would be lost to collide with the planet after inward migration. The created rings would be more massive than currently but might lose mass in the process of forming icy moonlets at the outer edge, possibly compatible with the population of moons observed in the neighborhood of Saturn's Roche zone.

1.3.4 A Huge Diversity of Rings

Saturn's rings present a great diversity in observations, particle size, thickness, structures, densities and physical properties. Table 1.2 summarizes the various rings locations.

Table 1.2: Saturn's rings locations and optical depths.

Ring Name	Ring Plane Radius (km)	Optical Depth	Named After
D Ring	66900–74510	$< 10^{-5}$	
C Ring	74658–92000	0.1	
B Ring	92000–117580	0.4–2.5	
Cassini Division	117580–122170	0.1	Giovanni Cassini
A Ring	122170–136775	0.4–1.0	
Roche Division	136775–139380	~ 0	Édouard Roche
F Ring	140180	0.01–0.2	
Janus/Epimetheus Ring*	149000–154000	$< 10^{-5}$	Janus and Epimetheus
G Ring	166000–175000	$< 10^{-5}$	
Methone Ring Arc*	194230	$< 10^{-5}$	Methone
Anthe Ring Arc*	197665	$< 10^{-5}$	Anthe
Pallene Ring*	211000 – 213500	$< 10^{-5}$	Pallene
E Ring	180000–480000	$< 10^{-5}$	
Phoebe Ring	$\sim$ 4000000 –13000000	$< 10^{-5}$	Phoebe

Optical depth ranges are provided when an average value is not representative or uncertain. Rings with optical depths higher than 0.01 are considered "main rings" while fainter rings constitute the "diffuse rings". * denotes non-official names.

Observing the rings using stellar occultations, we can extract the normal optical depth τ_n, reflecting the amount of the star light that is occulted by the rings. If I is the instrument-measured photon counts, I_0 the star brightness in free space, B the appropriate background contribution for the interval of data being processed and θ the geometric viewing angle between the instrument line of sight to the star and the ring plane normal, then the normal optical depth is given by Equation 1.2.

$$\tau_n = ln\left(\frac{I_0}{I - B}\right)\cos\theta \tag{1.2}$$

The rings can be represented by their normal optical depth profile, which is presented scaled with an ISS image in Figure 1.9.

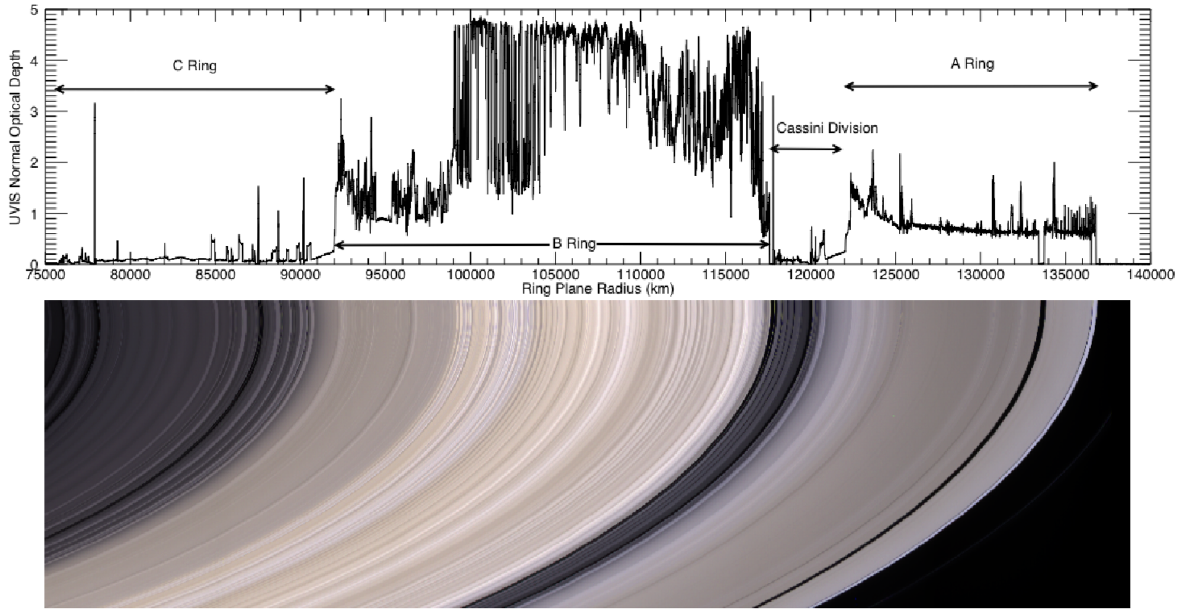

Figure 1.9: ISS mosaic (NASA/JPL/Space Science Institute) and UVIS stellar occultation data showing the A, B, C rings and Cassini Division (CD) at approximately 10 km radial resolution. The F ring is visible in the ISS mosaic beyond the outer edge of the A ring. The images were taken from an elevation of 4° above the illuminated (southern) face of the rings, so optically thick regions appear brighter than optically thin regions. From Colwell et al. (2009b).

Main rings (A, B, C, F) are very distinct from tenuous rings (D, E, G). The Cassini Division between the A and B rings has many similarities with the C ring. The Roche Division, separating the A and F rings, contains tenuous material more like the D and G rings. Overall the dense rings have typical optical depths greater than 0.1 and are predominantly composed of particles larger than 1 cm while the dusty rings have optical depths of 10^{-3} and lower. The F ring, torn quite literally between the regime of moons and rings, has a dense and complex core embedded in a broad sheet of dust.

1.3.5 The Main Rings

The main rings start almost at the planet surface and reach the Roche limit. From inside out, we will describe the C, B rings, the Cassini Division and the A ring. This overview of the main rings is abstracted from the review in Colwell et al. (2009b).

The C Ring: Figure 1.10 presents an occultation profile and an ISS (Imaging Science Subsystem) image of the C ring. Main ringlets and gaps are presented. Details are given in Colwell et al. (2009b) and reproduced in Figure 1.11.

The C ring presents a variety of gaps (regions of more diffuse material characterized by higher photon counts from the star and therefore lower optical depth), plateaus (higher optical depth regions) and ringlets (narrow high optical depth region that can be embedded in a gap).

All identified gaps, plateaus and ringlets in the C ring are referenced in Nicholson et al. (1990) and French et al. (1993). It has long been recognized that there are many similarities, both in particle properties and structure, between the C ring and the Cassini Division. From the structural viewpoint, the most obvious similarity is in their optical depth, which averages around 0.1 for both regions and only rarely exceeds 0.5. For comparison, the optical depth

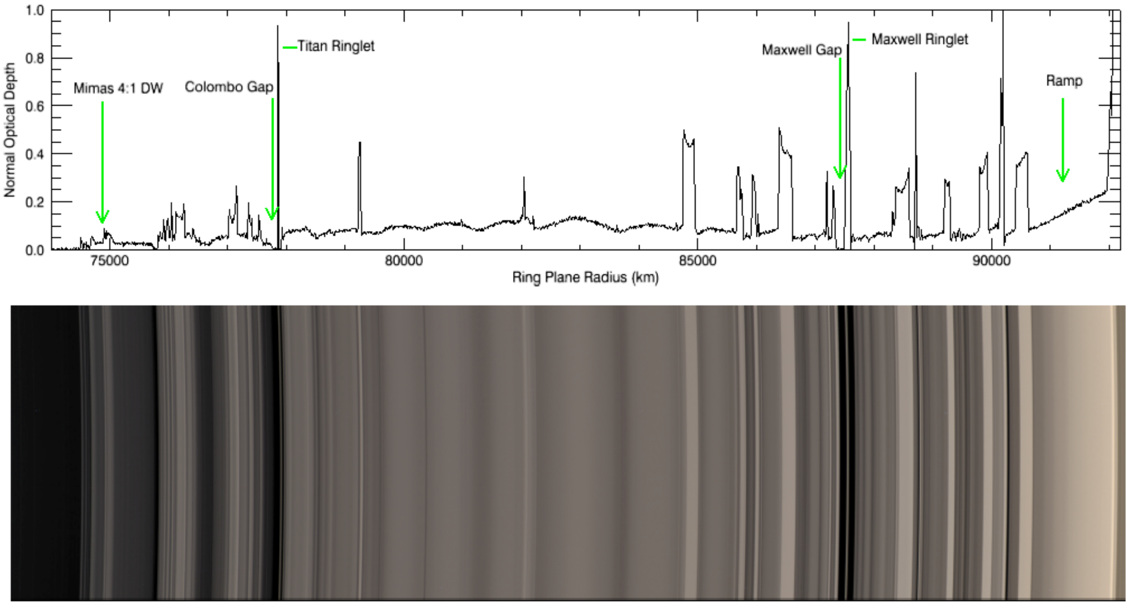

Figure 1.10: UVIS occultation profile and ISS image (NASA/JPL/Space Science Institute) of the C ring. The image is from above the unilluminated face of the rings with a radial resolution of $\sim$ 6 km/pixel. The occultation data are shown at 10 km resolution. From Colwell et al. (2009b).

averages $\sim$ 0.5 in the A ring, and is larger than this almost everywhere in the B ring. Another similarity is the number of narrow gaps within these two regions: 5 in the C ring and 8 in the Cassini Division (no gap is observed in the B ring, and only 2 in the A ring).

The B Ring: The abrupt B ring edge opens on the Cassini Division. This ring is the brightest, with an optical depth reaching 10 times the C ring values, up to 1.84 in average close to its exterior edge, which lies near the Mimas 2:1 inner Lindblad resonance (Porco et al., 1984a; Spitale et al., 2008). The Visual and Infrared Mapping Spectrometer (VIMS)

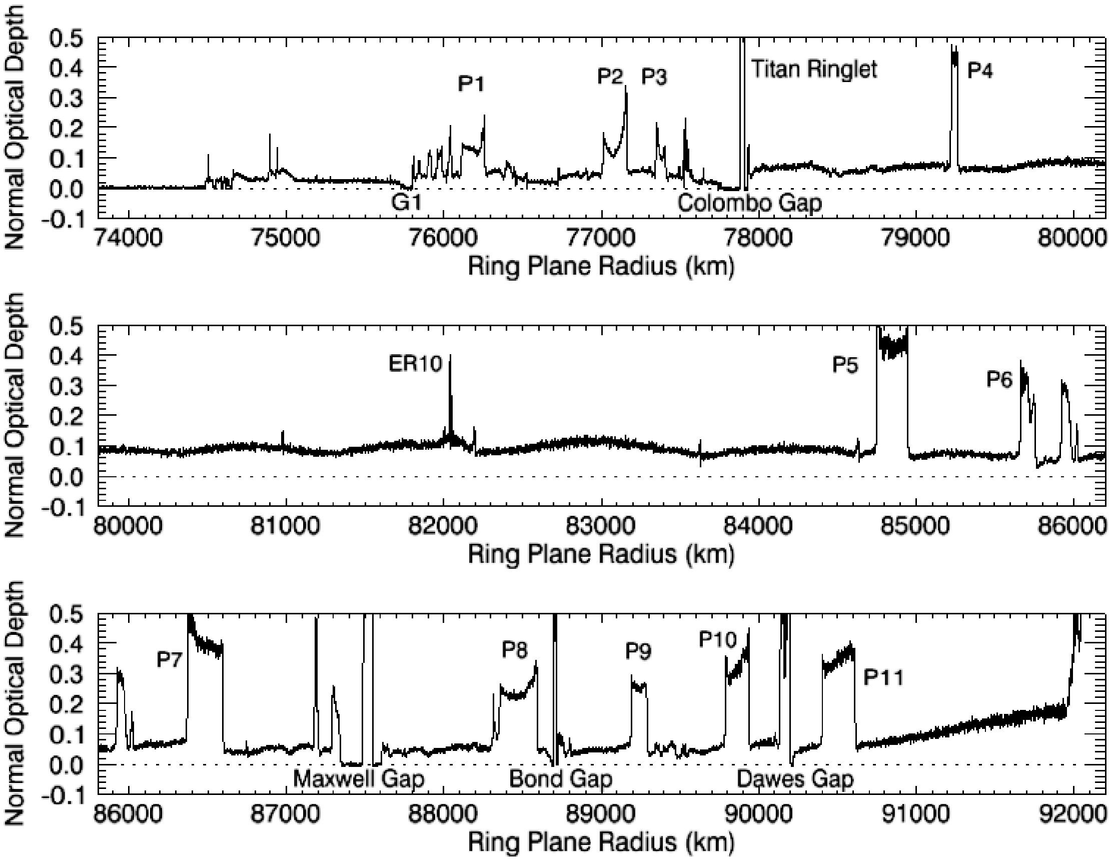

Figure 1.11: Cassini RSS occultation profile of the C ring. Unlike the A and B rings, the measured normal optical depth of the C ring is insensitive to viewing geometry. Prominent features are labeled (G for Gaps and P for Plateaus). From Colwell et al. (2009b).

confirmed the presence of azimuthally symmetric ($m = 2$ and $m = 1$) patterns of the B ring edge (Hedman et al., 2010). Esposito et al. (1983) estimated a lower value of the mass of the B ring about 50 times the C ring's mass while Esposito et al. (2008), based on Cassini data, estimated that the B ring could be 4 to 5 times more massive than initially expected. Numerical work from Robbins et al. (2010) showed that the A and B ring optical depth observations cannot be related linearly to the mass of the rings due to the piling of particles in the self-gravity wakes following the "granola-bar" model from Colwell et al. (2007). Though the estimate of the A ring mass is fairly precise ($0.5 - 0.7 \times 10^{19}$ kg), the B ring mass is estimated between 4×10^{19} kg and 7×10^{19} kg, confirming the revised estimates from Esposito et al. (2008).

The B ring density waves are analyzed in Chapter 3.

The Cassini Division: It has long been recognized that there are many similarities, both in particle properties and structure, between the C ring and the Cassini Division. Figure 1.12 presents an optical depth profile of the Cassini Division showing its numerous gaps and ringlets. Details about the Huygens Gap are given in Figure 1.13.

The Huygens Gap separates the B ring, whose outer edge is defined by the strong Mimas 2:1 inner Lindblad resonance, from the Cassini Division. It is the broadest gap in Saturn's rings and it is home to two narrow ringlets and one dusty ringlet, the latter discovered in Cassini images. The prominent Huygens ringlet was recorded in many Voyager images and occultation data sets and is both non-circular and variable in width.

Second only to the Huygens Gap in the Cassini Division is the Laplace Gap (or Outer Rift), with a width of ~ 240 km. This gap is also home to both sharp-edged and diffuse ringlets. Two narrow gaps, the Bessel Gap and Barnard Gap, with widths of 10 km and 13 km respectively, bracket a moderately opaque ringlet (R11). This 59-km wide ringlet, referred to as the 1.994 R_S ringlet by Nicholson et al. (1990), is also suspected to be non-circular. Its outer edge, which varies by at least 3 km in radius, falls close to the Prometheus 5:4 ILR

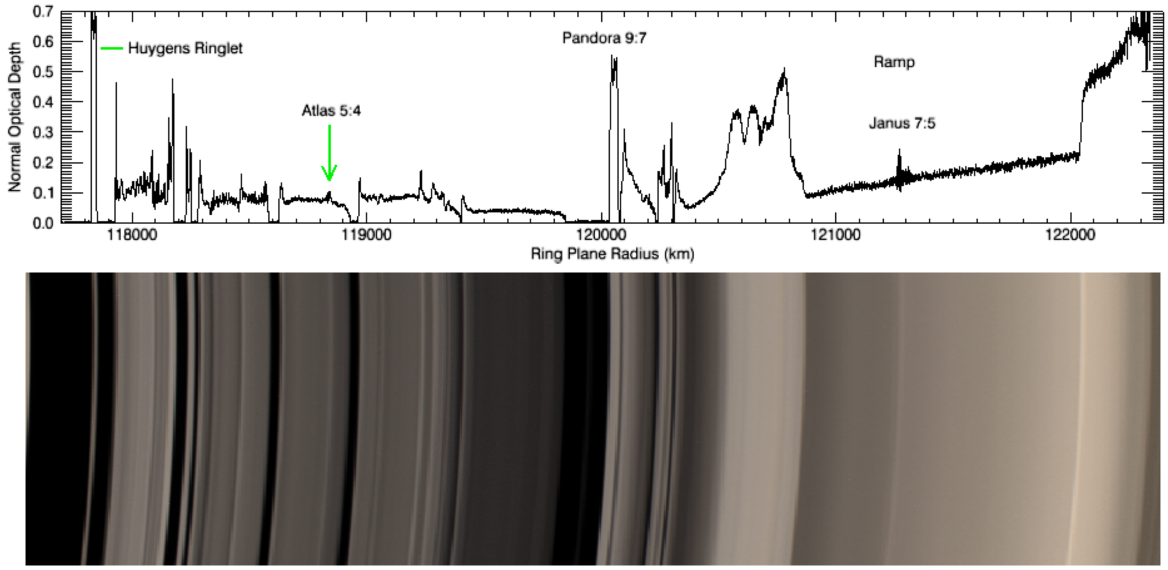

Figure 1.12: UVIS occultation profile (α Leonis, rev. 9) and ISS image (NASA/JPL/Space Science Institute) of the Cassini Division. The transition from the Cassini Division to the A ring at the outer edge of the Cassini Division ramp is much more pronounced in optical depth than in the image. The image is from above the unilluminated face of the rings with a radial resolution of $\sim$ 6 km/pixel. The occultation data are shown at 10 km resolution. From Colwell et al. (2009b).

at 120,304 km. Outside 120,400 km, the Cassini Division takes on a very different aspect, with no gaps and smoothly-varying optical depth. This region is dominated by a curious, broad feature with three distinct optical depth maxima (ER17, also referred to as the “Triple Band”). Completing the Cassini Division is a gradual, monotonic increase in optical depth towards the inner edge of the A ring at 122,050 km. This feature is often referred to as the “Cassini Division ramp”, and with a width of $\sim$ 1150 km is very similar to the ramp at

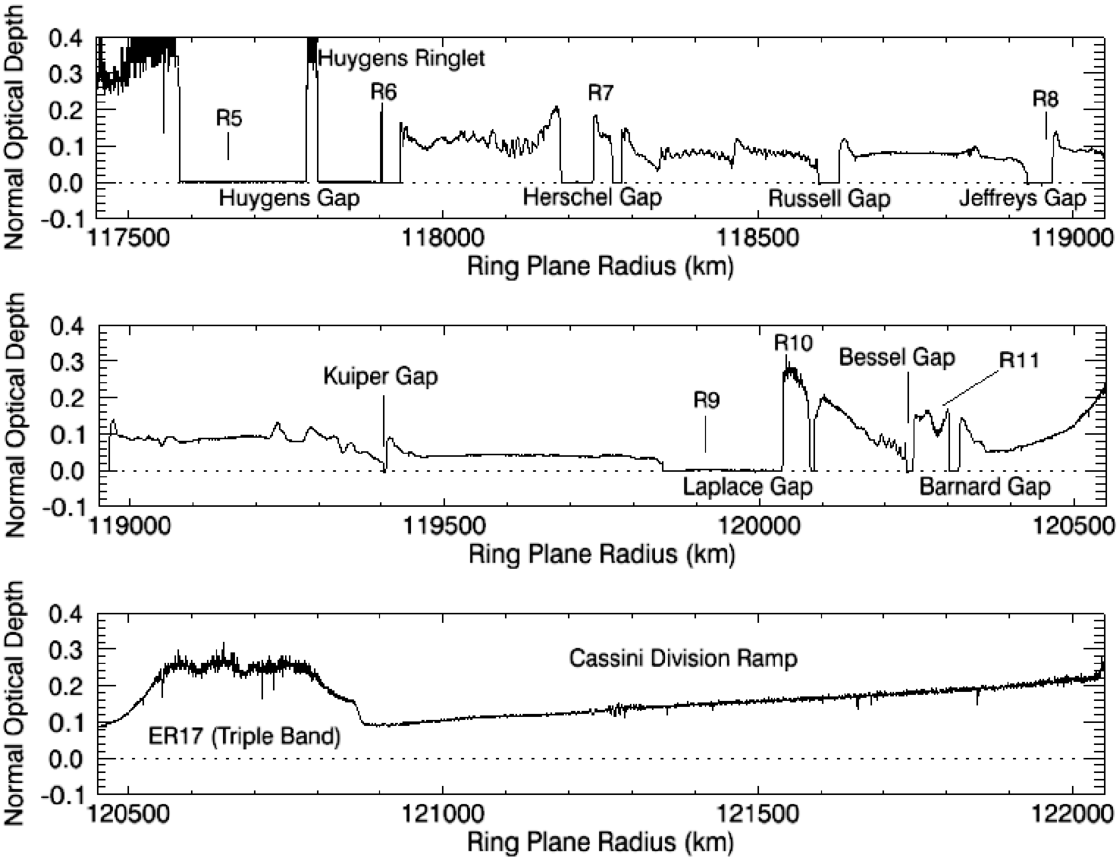

Figure 1.13: Normal optical depth profile of the Cassini Division obtained from UVIS stellar occultations. The Huygens gap is close to the inner edge of the Cassini Division. From Colwell et al. (2009b).

the outer edge of the C ring. Ballistic transport processes provide a successful model for the morphology of these ramps by assymetric absorption of meteoroid ejecta (Durisen et al., 1989, 1992).

Cassini-VIMS spacecraft observed stellar occultations providing accurate positions of the gaps and ringlets in the Cassini Division. Hedman et al. (2010) found some common patterns in the shapes of most of the gap edges: the outer edges appeared mostly circular while the inner edges are eccentric. Chapter 3 provides a detailed analysis of the density waves observed in the Cassini Division.

The A Ring: The A ring is very bright and has an optical depth varying between 0.15 in the regions of more diffuse material and 1.0 in the nearly opaque self-gravity wakes regions (Colwell et al., 2006; Hedman et al., 2007c), for a mass between 0.5 and 0.7×10^{19} kg (Robbins et al., 2010). Two main gaps, the Encke gap (325 km wide) and the Keeler gap (45 km wide) are hosting the satellites Pan (28 km wide) and Daphnis (7.8 km wide) respectively.

The F Ring: External to the main rings, the F ring is a showcase of accretion and disruption at the edges of Saturn's Roche zone. It is shaped by its two shepherding satellites Prometheus and Pandora. Goldreich and Tremaine (1979) described the interactions between a satellite and a disk and showed that they will tend to push each other away. Therefore, an inner and an outer satellites together can have a confining effect. The same shepherding situation occurs with Uranus'ϵ ring and the satellites Cordelia and Ophelia. The F ring is only a few hundreds of kilometers wide and presents various structures such as strands, kinks and clumps described by Showalter et al. (1986), Murray and Giuliatti Winter (1996) and Murray et al. (1997). With Cassini observations, new models were built to explain the four concentric strands observed in Voyager data as a core from which spiral strands are attached (Murray et al., 2005; Charnoz et al., 2005). Embedded moonlets have also been identified and described by Esposito et al. (2008) and Meinke et al. (2011).

1.3.6 The Diffuse Rings

The exploration of faint rings has been recently allowed by the use of space probes such as Voyager 1, 2 and Cassini.

The D Ring: Though located in the main rings system, the D ring is closer to the faint rings by its characteristics. This ring is the closest to the planet and has a very low optical depth. Marley and Porco (1993) analyzed some ringlets embedded in the D ring, observed from the Voyager missions. The Cassini spacecraft observed some significant changes in the D ring structure (Hedman et al., 2007a), 25 years later: in particular, the brightest ringlet was found 200 km inner to its first known position from Voyager 2. It was also observed to be wider (250 km) and more diffuse than it used to be (40 km). Cassini also found evidence of new ringlets and estimated that the particles of the D ring are mainly dust material between 1 and 100 microns in size. Hedman et al. (2007a) also report the changes in the wavelength of a periodic structure close to the outer edge of the D ring: ground based occultation observation of the star GSC5249-01240 showed a wavelength of about 60 km in 1995 that became about 30 km in Cassini high-resolution images. They interpreted this structure "as a periodic vertical corrugation in the D ring produced by differential nodal regression of an initially inclined ring" which formation could be due to a cometary or meteroid impact in early 1984.

The G Ring: The G ring is located 26000 km outer to the F ring and is 9000 km wide. It is composed of dust and has an optical depth around 10^{-6} (Esposito, 2002). This ring presents some azimuthal asymmetry: a 250-km wide arc of matter containing meter-sized particles. Hedman et al. (2007b) described how the 8:7 inner Lindblad resonance with Mimas is responsible for this confinement and suggested that these meter-sized particles could come from bigger satellites.

The E Ring: The E ring is located 5000 km farther than the G ring and spreads over 300000 km. Showalter et al. (1991) measured an optical depth of 1.5×10^{-5}. Its particles are composed of dirty water ice with possibly traces of silicates and other molecular compounds (Hillier et al., 2007). Enceladus geological activity at its south pole is responsible for the ejection of plumes of micron-sized icy particles feeding the E ring.

1.3.7 A Huge Variety of Structures

In addition to the gaps, plateaus, ringlets and other peaks and troughs in optical depth, the rings are the scene of a huge variety of organized structures, most of which are related to an interaction between the ring particles and a satellite. Rings interactions with satellites are very important as shown in Figure 1.14. Recent planetary missions provided us with high-resolution tools to observe the rings and allowed the discoveries of satellites orbiting within the rings.

These rings-satellites interactions can be of various types and shape the ring material in different kinds of waves. The A ring presents numbers of wavelike-structures, mainly excited by low order Lindblad resonances with external satellites. The Encke gap that separates the

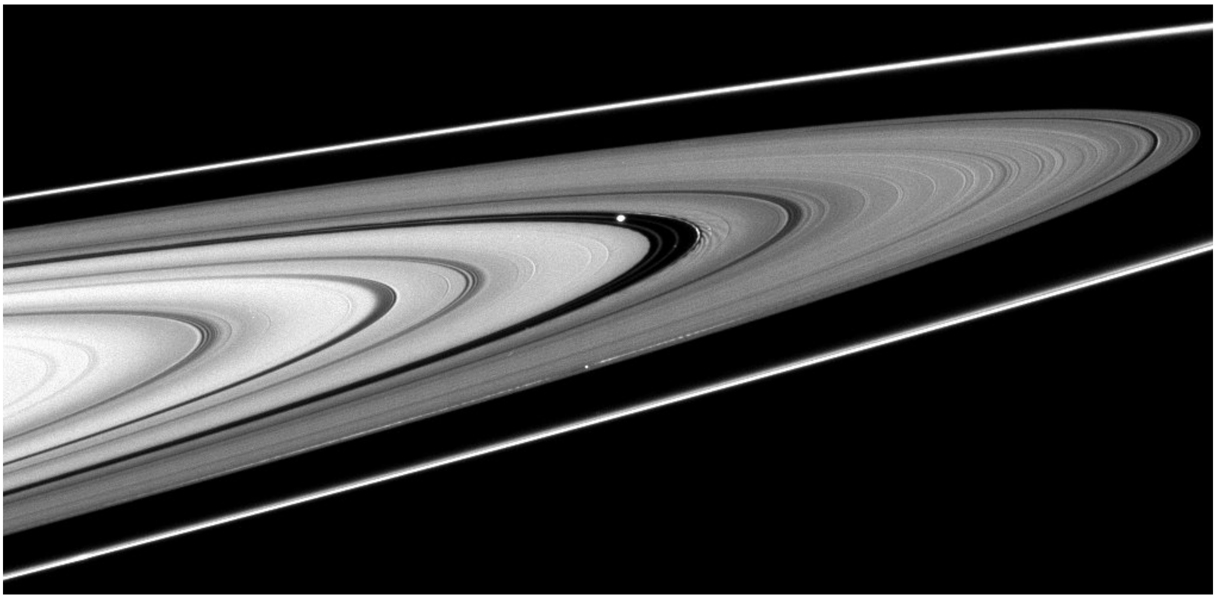

Figure 1.14: Image: NASA/JPL/Space Science Institute. Cassini ISS images revealing Pan orbiting in the Encke gap. The narrow ringlet co-orbiting with Pan is also visible, together with wakes just outside the Encke gap.

A ring hosts the satellite Pan that sculpts the edges of the gap. Figure 1.15 shows evidence of density waves triggered by first order inner Lindblad resonances with Prometheus and Pandora and of satellite wakes created by the recent passage of Pan in the Encke gap.

Spiral Density Waves:

Inner Lindblad resonances excite spiral density waves, mainly propagating outward in the rings. Though details about density waves will be given in the following chapters, Figure 1.16 explains the formation of a spiral density wave.

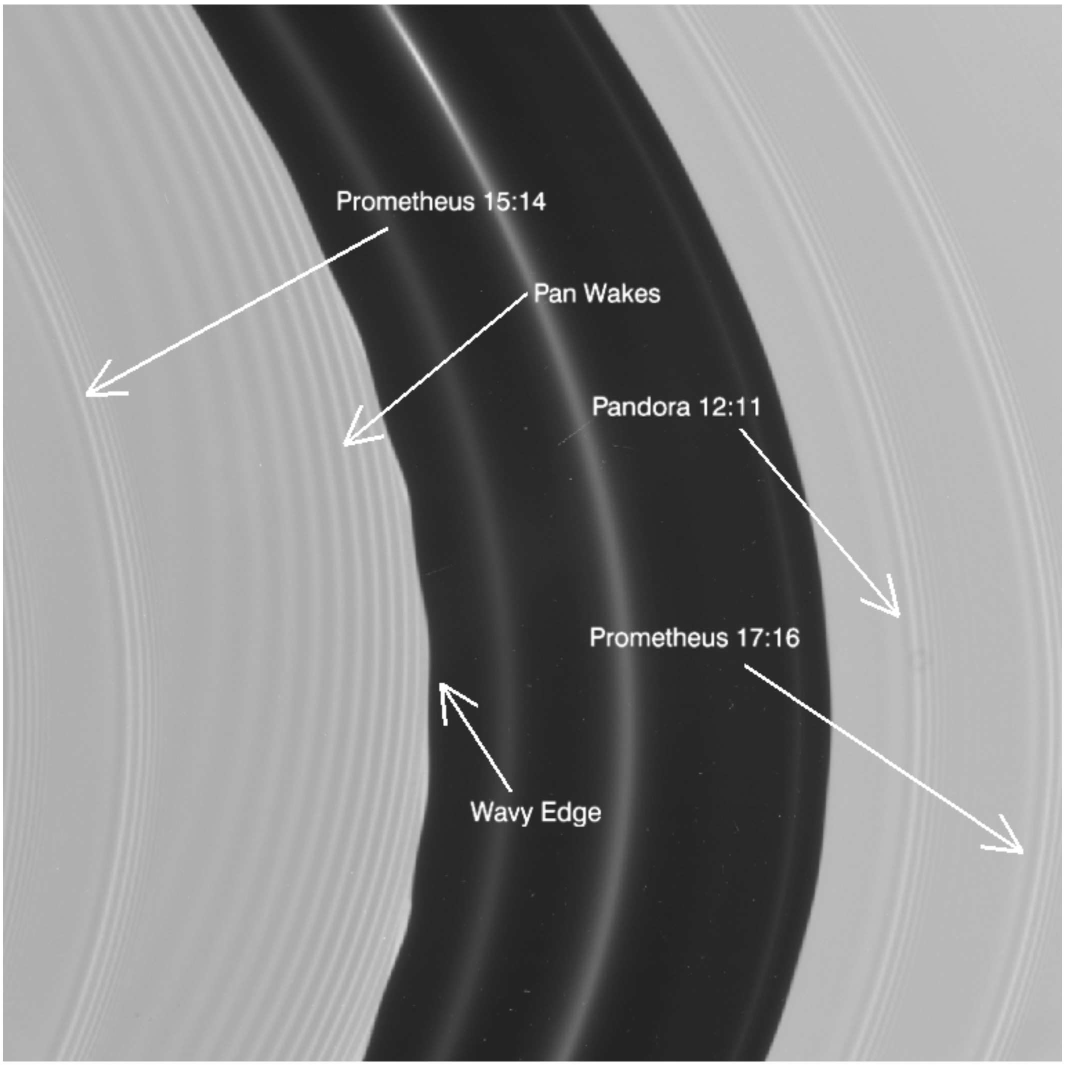
Prometheus 15:14
Pan Wakes
Pandora 12:11
Prometheus 17:16
Wavy Edge

Figure 1.15: Image: NASA/JPL/Space Science Institute. The Encke gap (320 km wide) imaged by Cassini at Saturn Orbit Insertion showing dusty ringlets, a wavy inner edge recently perturbed by the satellite Pan (roughly five image widths upstream of the inner edge, or down in this view of the south face of the rings), and satellite wakes. Density waves are also visible, indicated here by the inner Lindblad resonances that launch them. Streamlines near the edge of a gap are deflected by the embedded moon, creating a wavy edge and satellite wakes, due to the moon Pan, within the ring. From Colwell et al. (2009b).

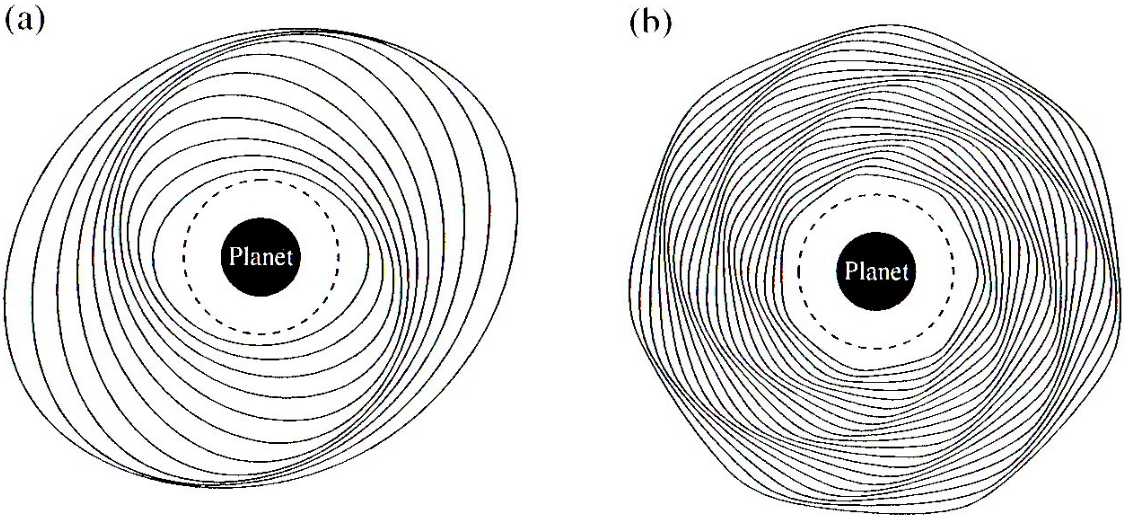

Figure 1.16: Schematic diagrams of the coplanar particle paths that give rise to trailing spiral density waves near a resonance with an exterior satellite. (a) The two-armed spiral density wave associated with the 2:1 (m=2) inner Lindblad resonance. (b) The seven-armed spiral density wave associated with the 7:6 (m=7) inner Lindblad resonances. The pattern rotates with the angular velocity of the satellite and propagates outward from the exact resonance (denoted by the dashed circle). Figure and caption from Murray and Dermott (1999), p. 493, Figure 10.11.

Spiral Bending Waves:

Figure 1.17 presents the formation of a spiral bending wave, excited by an inner vertical resonance with an external satellite. The 3-dimension structures are characteristic of these waves.

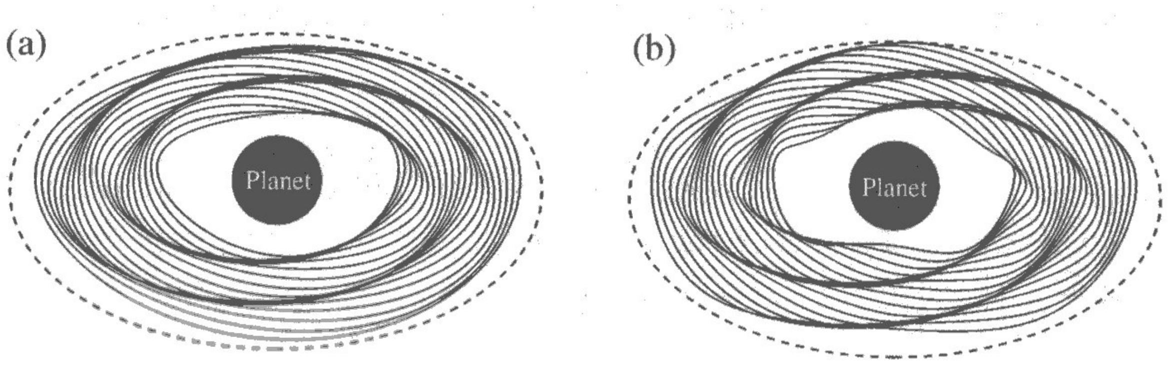

Figure 1.17: Schematic diagrams showing an oblique view of the three-dimensional particle paths that give rise to trailing spiral bending waves near a resonance with an exterior satellite. (a) The two-armed spiral density wave associated with the 3:1 (m=2) inner vertical resonance. (b) The four-armed spiral bending wave associated with the 5:3 (m=4) inner vertical resonances. The pattern rotates with the angular velocity of the satellite and propagates inward from the exact resonance (denoted by the dashed curve). Figure and caption from Murray and Dermott (1999), p. 493, Figure 10.12.

Self-gravity Wakes:

Particles throughout the A and B rings cluster into strands or self-gravity wakes tens of meters across that are in equilibrium between gravitational accretion and Keplerian shear (Figure 1.18). As Colwell et al. (2009b) said, "the A ring contains unseen embedded moonlets that reveal their presence through the "propeller"-shaped structures that form around them [(Figure 1.19 from] Tiscareno et al. (2010b)). [...] Here we identify a moonlet as an individual object that opens an azimuthally limited gap but, unlike the embedded moons Pan and Daphnis, does not clear a continuous gap in the ring. It is not yet clear whether or not these moonlets simply represent the largest members of the general particle size distribution in the rings.".

Satellite Wakes and Propellers:

The Hill sphere (Hayashi et al., 1977) of a boulder of mass M_{boulder} and of semi-major axis a_{boulder} is the region in which its attraction dominates Saturn's attraction. The radius of this sphere is $r_H = a_{boulder}\left(\frac{M_{\text{boulder}}}{3(M_{\text{Saturn}}+M_{\text{boulder}})}\right)^{1/3}$, where M_{Saturn} is Saturn's mass. The most recent numerical simulations (Tiscareno et al., 2008; Lewis and Stewart, 2009; Tiscareno et al., 2010b) used numerical integration of the classical Hill problem (massless test particles orbiting a large central body and deflected in the vicinity of a perturbing mass) in order to recreate propeller signatures. Particles with a semi-major axis difference Δa with the boulder less than 2 r_H follow horseshoe orbits. Farther particles are still perturbed and receive a kick in eccentricity that follows $1/(\Delta a)^2$. In addition, the phases of these particles' orbits are roughly aligned (Showalter and Burns, 1982). These now-eccentric particles will leave an open space on the outer trailing side and inner leading side of the boulder. Such a primary depletion zone has a radial extension of a few Hill radii while its azimuthal extension can be much larger. After a few orbits, the oldest and farthest depletion zones are destroyed by the combined effects of collisions and inter-particle gravitational forces provoking either

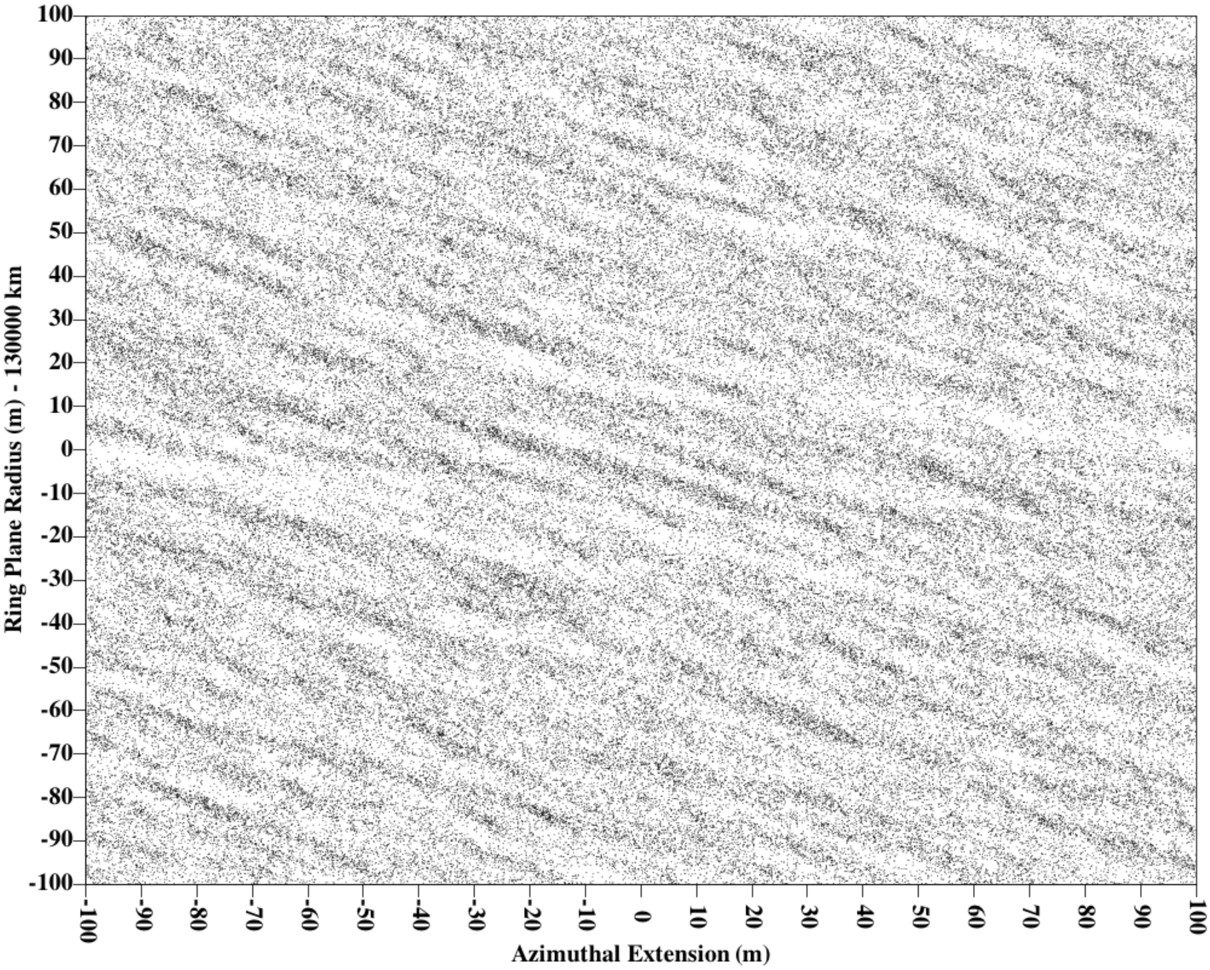

Figure 1.18: Numerical simulation of self-gravity wakes in the rings. Saturn's direction is towards the bottom. Enough 20-cm radius particles were added to simulate a 0.5 optical depth.

a damping of the eccentricity, a randomizing of the phases or a scattering of the eccentric particles in the depletion zones. The compression of the streamlines creates the satellite wakes. With the combined effects of collisions and self-gravity, the eccentricities of the wake particles will decrease and the structures will vanish, although some persist for multiple synodic periods. The recent detection of propellers in the A ring (Figure 1.19) brought the question whether the bright S-shape of the propeller signature was due to the outer edge of the depletion zones or rather to the boulder wakes. From numerical tests on various boulder and particle sizes, it appears that the primary depletion zone extensions are not subject to particle size variations as long as they remain at least three times smaller (assuming the same density for the particles and the boulder) than the boulder (Lewis and Stewart, 2009). In addition, we notice that both radial and azimuthal extensions of the primary lobe seem to grow linearly with the boulder radius, validating the previous estimates from Sremčević et al. (2002) and Tiscareno et al. (2008) stating that $\Delta r = (3.2 \pm 0.4)\, r_H$. However, previous work from Spahn and Sremčević (2000) and Sremčević et al. (2002) calculated that the azimuthal extension grew as the cube of the Hill radius of the boulder.

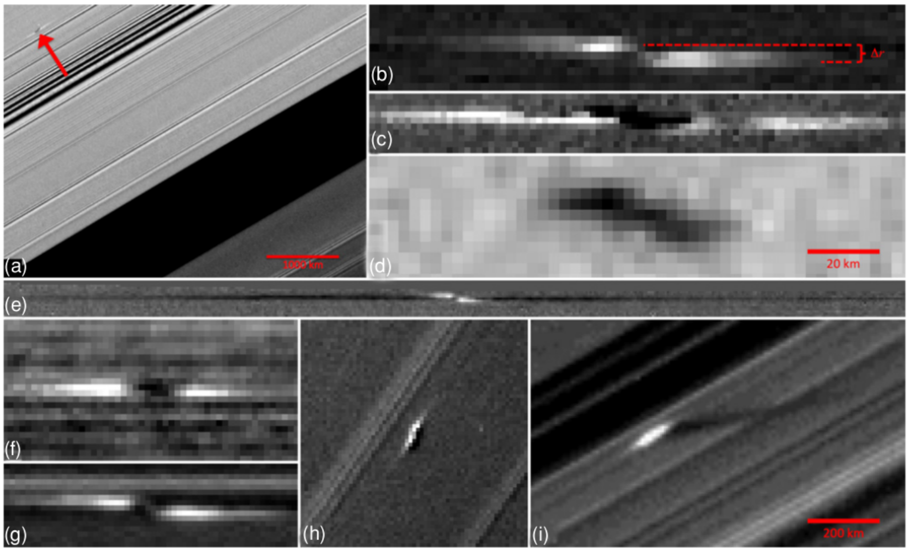

Figure 1.19: Propellers as seen in selected Cassini images. The moonlets are at the center of the features. Figure from Tiscareno et al. (2010b).

1.3.8 Other Flat Systems

1.3.8.1 The Physics of the Disks

In absence of damping, two main forces will rule a rotating gravitating system: centrifugal forces and gravitational attraction. Centrifugal forces will compensate gravitation but only in the perpendicular direction to the rotation axis, therefore flattening the system. Other forces could intervene, preventing the system from flattening such as radiative pressure in stars or a large dispersion of velocities in elliptical galaxies. In addition, the keplerian shear generates collisions, leading to a transfer of angular momentum from the inside to the outside and therefore to a spreading of the disk (Brahic, 1977). Microscopic particles can also be affected by the Poynting-Robertson drag, the radiation pressure or the Lorentz forces: these effects should not be neglected in the diffuse rings.

Rings are composed of individual particles but show collective effects: the physics of the rings is at the crossroad of solid mechanics and continuous medium physics. Indeed, we can consider the disk as a spreading fluid where the transfer of angular momentum and the dissipation of energy will be represented by a viscosity parameter. Thus, an increase of the viscosity translates in an increase of angular momentum transfer towards the outer regions, and then in a spreading of the disk.

A body orbiting around another one more massive will feel a differential gravitational potential between its closest point to the central body and its center. When this difference exceeds the internal cohesion forces, the secondary body will break. These differential tidal forces are stronger when the distance between the two bodies is lower. The Roche limit is the location where the second body will break. For a satellite with a density ρ and a central planet with a density ρ_{P} and a radius R_{P}, the Roche limit is given by $R_{\mathrm{Roche}} = \alpha\ R_{\mathrm{P}}\ \left(\frac{\rho_{\mathrm{P}}}{\rho}\right)^{1/3}$, where α is a factor representing the cohesion forces of the satellite. α is typically between 2.456 and 2.52 for icy satellites, which provide the following range for the Roche Limit between 135435 km and 138964 km away from the planet center. The Roche zone depends on the way to model internal forces but we can consider that it separates the inner zone where particles dominate and the outer zone where larger moonlets will be predominant: because of their location inside the Roche zone, the particles cannot stably agglomerate and the rings survive.

1.3.8.2 The Other Planetary Rings

Saturn is not the only planet in the solar system to have rings. Though less massive and dense, the other giant planets rings are also very original and surprising. Figure 1.20 summarizes the fours giant planet rings systems. They are scaled to the planets radius to allow comparisons.

Jupiter:

Jupiter's ring system was first observed by Voyager in 1979 (Smith et al., 1979), before being explored by Galileo in the 1990's. Showalter et al. (1987) described Jupiter's diffuse rings

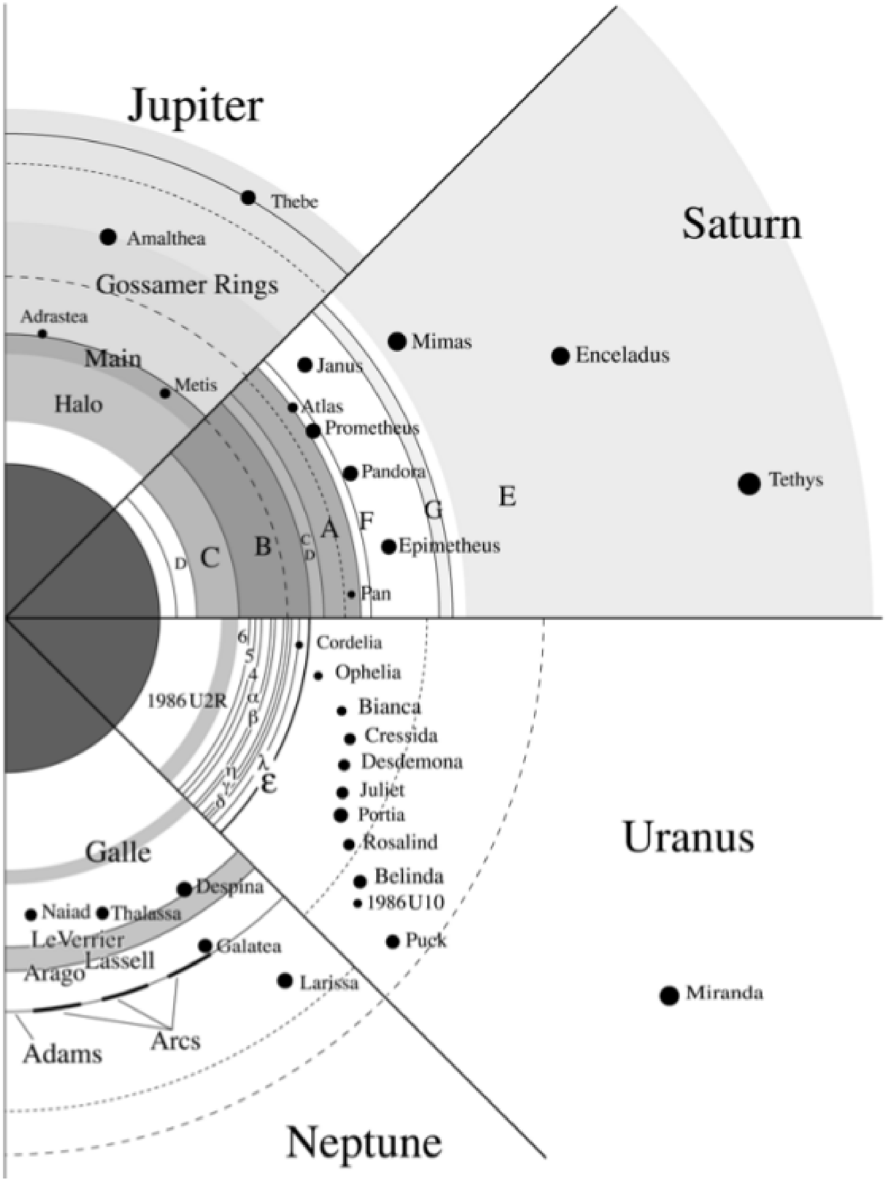
Jupiter
Thebe
Amalthea
Gossamer Rings
Adrastea
Main
Metis
Halo
Saturn
Mimas
Enceladus
Janus
Atlas
Prometheus
Pandora
Tethys
E
G
F
A
C
D
B
C
D
Epimetheus
Pan
Cordelia
Ophelia
Bianca
Cressida
Desdemona
Juliet
Portia
Rosalind
Belinda
1986U10
Puck
6
5
4
α
β
η
γ
δ
λ
ε
1986U2R
Uranus
Miranda
Galle
Despina
Naiad
Thalassa
LeVerrier
Lassell
Arago
Galatea
Larissa
Adams
Arcs
Neptune

Figure 1.20: Scaled giant planet ring systems. The dashed line shows the synchronous orbit. The dotted line is the Roche limit for a satellite with a density of 1000 $kg\ m^{-3}$. From Grün et al. (2001).

as composed of 100-microns dust particles and Ockert-Bell et al. (1999) described the rings system shown in Figure 1.21.

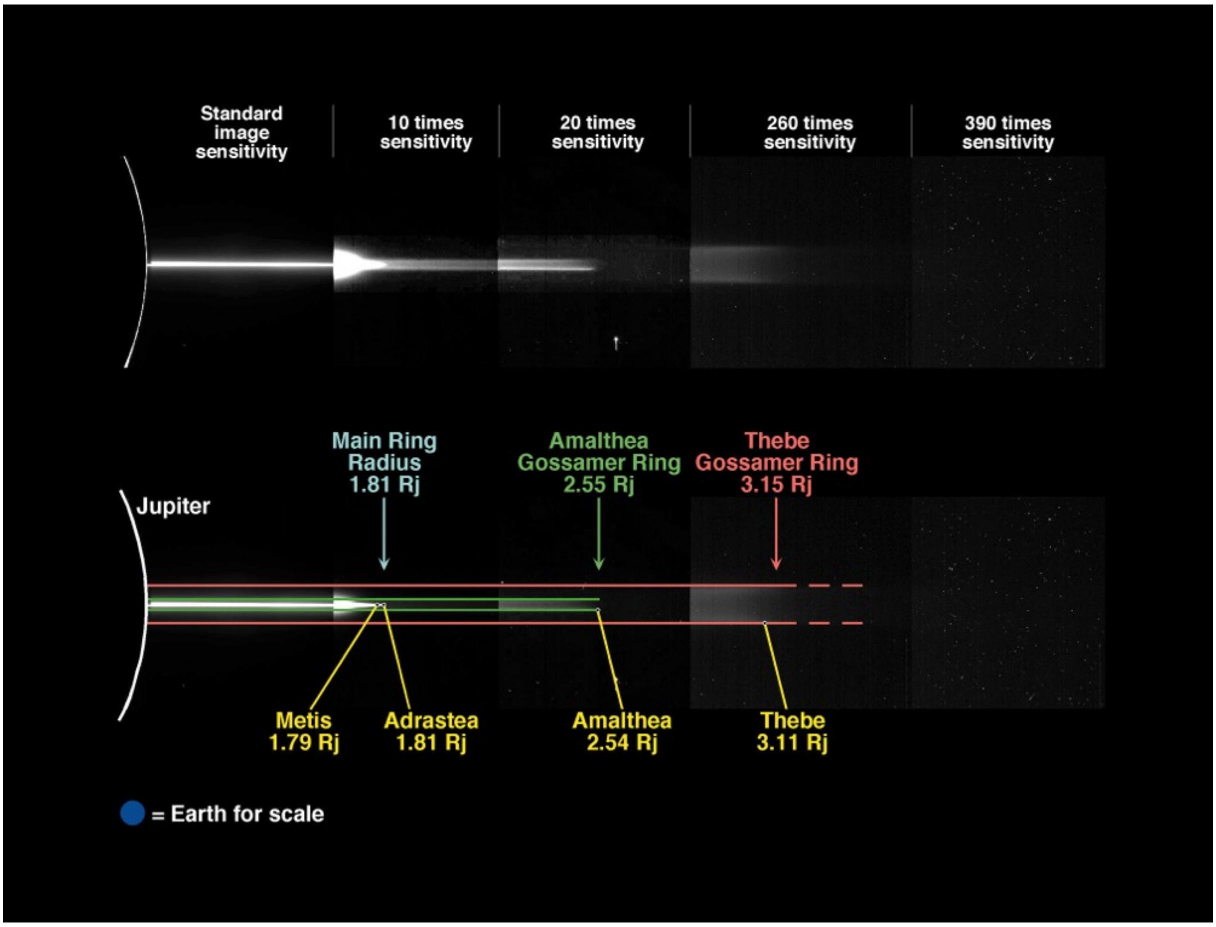
Standard image sensitivity
10 times sensitivity
20 times sensitivity
260 times sensitivity
390 times sensitivity
Main Ring Radius 1.81 Rj
Amalthea Gossamer Ring 2.55 Rj
Thebe Gossamer Ring 3.15 Rj
Jupiter
Metis 1.79 Rj
Adrastea 1.81 Rj
Amalthea 2.54 Rj
Thebe 3.11 Rj
● = Earth for scale

Figure 1.21: Image: NASA/JPL/Cornell University. Jupiter's ring system is shown here with the positions of the small moons that are embedded in the rings.

The innermost and thickest ring, usually described as a torus, is a halo that spreads between the planet and the main ring. This main ring is more flat and narrow and its outer edge is fixed by the moon Adrastea's orbit. This ring may be fed by particles knocked off

Adrastea and Metis. Farther, the Gossamer rings might be fed as well by the larger moons Thebe and Amalthea. Due to these satellite inclinations, the Gossamer rings are thicker. A more diffuse extension of the Gossamer rings spreads beyond Thebe's orbit.

Uranus:

The occultation of the star SAO 158687 by Uranus was followed from ground and air by not less than 5 observatories and the Kuiper Airborne Observatory (telescope mounted on a plane). From this complementarity of data, this occultation allowed to identify a total of nine rings surrounding the giant planet. Elliot et al. (1977) and Millis and Wasserman (1978) reported these discoveries. The Voyager 2 flyby in 1986 brought evidence of two new rings (Smith et al., 1986) before two other ones were discovered in 2006 from the Hubble Space Telescope observations (Figure 1.22) by Showalter and Lissauer (2006). The two last ones are quite similar to Saturn's E and G rings: wider and diffuse with an optical depth around 10^{-6}. Most of these rings are very narrow and composed of dust and centimeter-sized particles. However, the ϵ ring is larger (20 - 96 km) and more eccentric, with an optical depth between 0.5 and 2.5. This ring might contain basketball-size to house-size particles, and probably no dust. Miner et al. (2007) showed that Uranus' rings could contain carbon and not water ice, probably extracted from methane by the action of the magnetosphere.

Neptune:

After the successful stellar occultation by Uranus that revealed its rings, another stellar occultation allowed to identify Neptune's rings in July 1984 (rings were suspected before but observations were not consistent). William Hubbard and André Brahic observed a series of

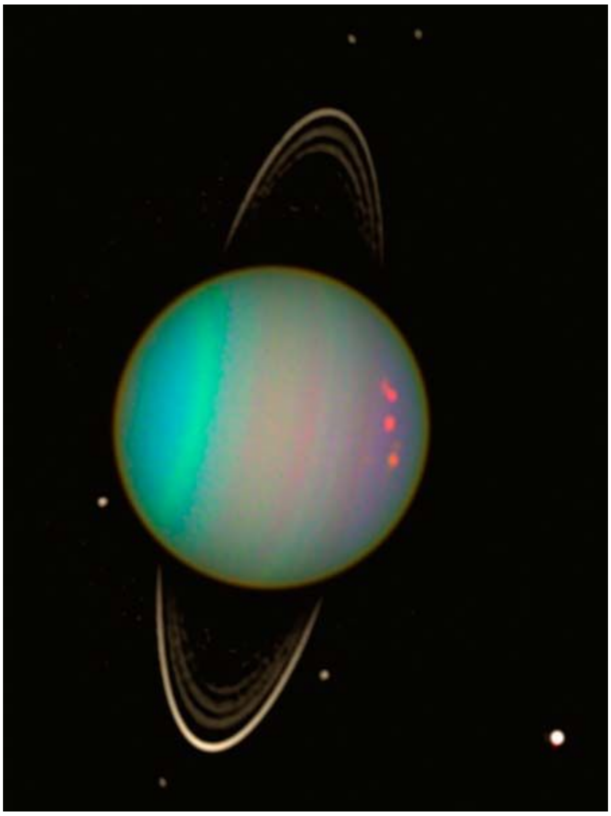

Figure 1.22: Image: NASA/Space Telescope Science Institute. Uranus and its rings.

secondary occultations in the neighborhood of the planet (Hubbard et al., 1985). These rings were confirmed in 1989 by the Voyager 2 flyby. Figure 1.23 shows the rings while the planet is hidden. Five rings, named Galle, Le Verrier, Lassell, Arago and Adams (in order of distance to the planet) were identified. Le Verrier and Adams are narrow and bright with an optical depth around 0.1, while the others are more diffuse with optical depths around 10^{-4}. Colwell et al. (1990) estimated that they are mainly made of dust. Like Uranus' rings, Neptune's would be composed of carbon rather than water ice, explaining their low reflectivity. Adams presents five arcs of material showing optical depths around 1. However, these arcs are the scene of short-time evolutions: Liberté almost disappeared in 2003 and some azimuthal positions do not match previous observations. The idea of such a fast evolution supports the idea that the arcs might be rather young.

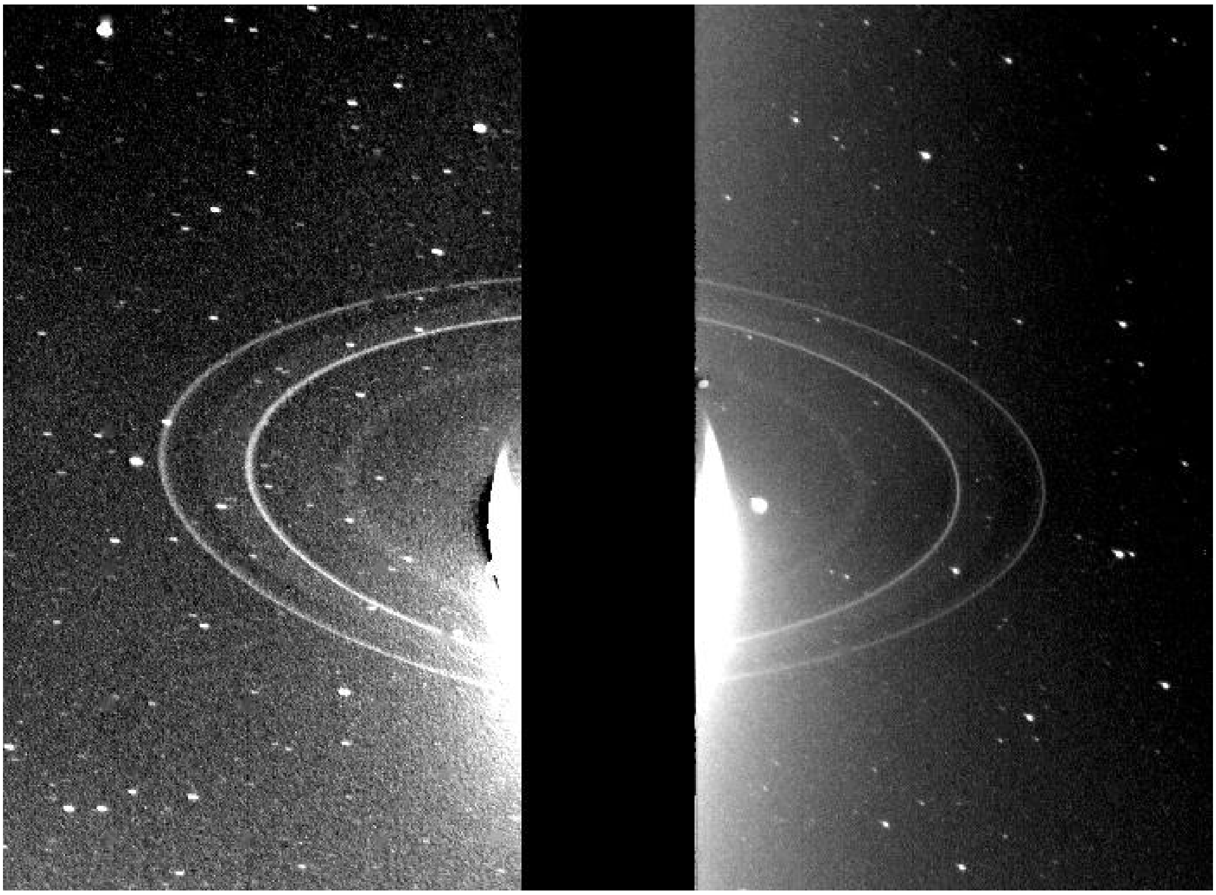

Figure 1.23: Image: NASA/JPL/Univ. of Arizona. Two exposures with Neptune blacked out (center) were used to make this image of the ring system of Neptune by Voyager 2. These images were made from a pair of 10-minute exposures while the Sun was behind Neptune, and faint ring particles were being lit from the back.

1.3.8.3 Towards Bigger Disks

The planetary rings are reachable laboratories for understanding farther and bigger structures.

Protoplanetary Disks:

According to the standard stellar formation model, a molecular cloud can form a star while the rest of the material will collapse in a disk around the star. As the disk cools down, the gas will condense in dust and bigger particles that will start interacting together: occasionally, accretion can lead to the formation of proto-planets. As the gas is accreted in the star, only dust and planetesimals will remain in the disk, that will therefore become a "debris disk". Such a disk has been observed around β Pictoris in 1984, τ Ceti or AU Microscopii more recently. β Pictoris (1.24) is the most famous example of a debris disk and for diverse exotic reasons. First, its circumstellar disk appears to be asymmetrical (Larwood and Kalas, 2001) and to contain an exoplanet. In addition, it appears to have a secondary disk, also asymmetrical and inclined by 5° (Golimowski et al., 2006), probably due to a massive planet on an inclined orbit. This planet would feed the second disk by deflecting material from the first one. Planetesimals in this system also appear to contain more carbon than the terrestrial planets of our solar system. The first disk could have been created from the debris of a binary companion during a close encounter with a nearby star (Kalas et al., 2000). This encounter could have happenened between 100000 and 350000 years ago (Kalas et al., 2001): this disk would therefore be very young. In addition, it is much larger than our solar system, reaching up to 1800 AU on one side and 1450 AU on the other.

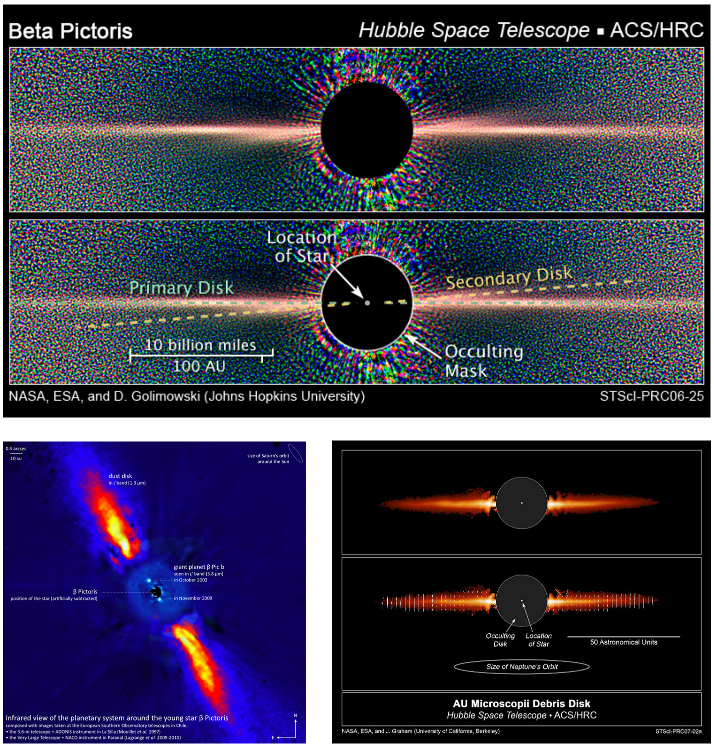
Beta Pictoris

Hubble Space Telescope ▪ ACS/HRC

NASA, ESA, and D. Golimowski (Johns Hopkins University)

STScI-PRC06-25

Infrared view of the planetary system around the young star β Pictoris

composed with images taken at the European Southern Observatory telescopes in Chile:

- the 3.6-m telescope + ADONIS instrument in La Silla (Mouillet *et al.* 1997)
- the Very Large Telescope + NACO instrument in Paranal (Lagrange *et al.* 2009-2010)

AU Microscopii Debris Disk

Hubble Space Telescope • ACS/HRC

NASA, ESA, and J. Graham (University of California, Berkeley)

STScI-PRC07-02a

Location of Star
Primary Disk
Secondary Disk
10 billion miles
100 AU
Occulting Mask
0.5 arcsec
10 AU
size of Saturn's orbit around the Sun
dust disk
in J band (1.3 μm)
giant planet β Pic b
seen in L′ band (3.8 μm)
in October 2003
β Pictoris
position of the star (artificially subtracted)
in November 2009
N
E
Occulting Disk
Location of Star
50 Astronomical Units
Size of Neptune's Orbit

Figure 1.24: β Pictoris debris disks as seen from the Hubble Space Telescope (up) and from the European Southern Observatory (lower left). AU Microscopii's debris disk as observed from the Hubble Space Telescope (lower right) shows also light polarization. In all these observations, the star was occulted to enable observations of the disks.

Accretion Disks:

Diffuse material orbiting a compact body will spiral inward towards it (Figure 1.25) and emit important electromagnetic radiations as the gravitational forces compress it. Depending on the central body, the wavelength of that radiation varies: accretion disks around proto-stars will emit in the infrared while neutron stars and black holes will emit in the X domain. An accretion disk can reach a distance of a hundred astronomical units from the star.

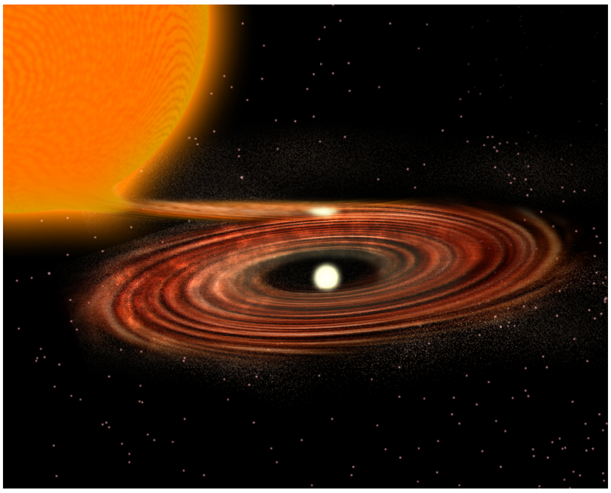

Figure 1.25: Artist concept of an accretion disk orbiting a white dwarf star in a binary system. Credit: P. Marenfeld and NOAO/AURA/NSF

Spiral Galaxies:

Spiral galaxies are the largest visible flat structures. Their diameter can reach up to 300000 light years. Shu (1970a,b) explained how the propagation of density waves can shape spiral arms in these structures. Figure 1.26 presents two spiral galaxies seen from above and edge on. A non-negligible fraction of the mass of galaxies is due to dark matter.

Lots of disk structures can be found in the universe. However, heating processes in accretion disks prevent to compare these disks with planetary rings. Collisions are also very different between all these structures (estimated 10000 times more important in rings than proto-planetary disks) together with thickness, age, accretion or mass ratios. Planetary disks

Figure 1.26: Image: K. Baillié, A. de Beauffort, J. Fontdecaba-Baig, and J. Desmars. Spiral galaxies M51 and M104 (in the Messier catalog) imaged from the 120-cm telescope at Observatoire de Haute-Provence.

are therefore very interesting laboratories for other flat systems, though it is necessary to be very careful while extrapolating rings conclusions to other systems.

1.4 Cassini UVIS Data

1.4.1 The Cassini Spacecraft

The Cassini spacecraft (Figure 1.27) has a great variety of instruments. Among them, three different ones can observe high-resolution occultations of the rings:

- UVIS: UltraViolet Imaging Spectrograph which observes occultations of ultraviolet stars,
- VIMS: Visual and Infrared Mapping Spectrometer which observes occultations of infrared stars, and
- RSS: Radio Science Subsystem which transmits a coherent radio signal through the rings to the Earth.

Launched after the Voyager flybys, the Cassini-Huygens mission is the first space mission dedicated to Saturn's exploration. The American orbital module realized by NASA and its European companion, the Huygens probe, inserted in Saturn's orbit on July 1^{st}, 2004 after a 7 year-journey and 3.5 billion kilometers (Figure 1.28). The orbiter has collected numerous images and data about the planet, the satellites, the rings and other interests of the saturnian system. The Huygens probe dived into the atmosphere of Titan in January 2005 and landed on its surface, gathering data for a few hours all the way down to the surface and surviving there for a few more minutes in order to probe the crust of the satellite and send the data back to Earth.

1.4.2 The UVIS High Speed Photometer

The Cassini spacecraft's Ultraviolet Imaging Spectrograph (UVIS) includes a high-speed photometer (HSP) (details are provided in Esposito et al. (1998) and Esposito et al. (2004))

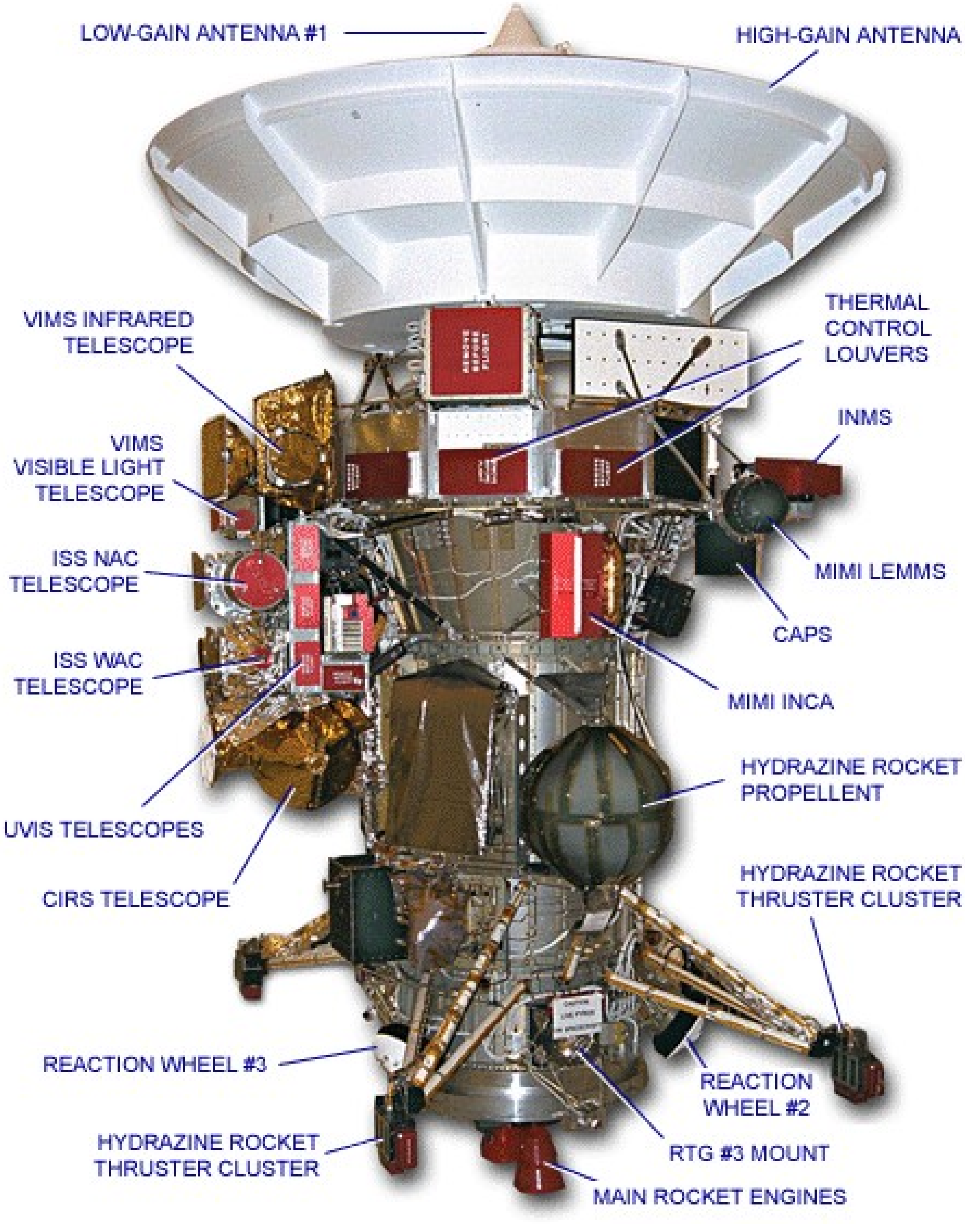
LOW-GAIN ANTENNA #1
HIGH-GAIN ANTENNA
VIMS INFRARED TELESCOPE
THERMAL CONTROL LOUVERS
INMS
VIMS VISIBLE LIGHT TELESCOPE
ISS NAC TELESCOPE
MIMI LEMMS
CAPS
ISS WAC TELESCOPE
MIMI INCA
HYDRAZINE ROCKET PROPELLENT
UVIS TELESCOPES
CIRS TELESCOPE
HYDRAZINE ROCKET THRUSTER CLUSTER
REACTION WHEEL #3
REACTION WHEEL #2
HYDRAZINE ROCKET THRUSTER CLUSTER
RTG #3 MOUNT
MAIN ROCKET ENGINES

Figure 1.27: Image: NASA/JPL. The Cassini spacecraft and the embarked instruments, including the UVIS telescope on the left side.

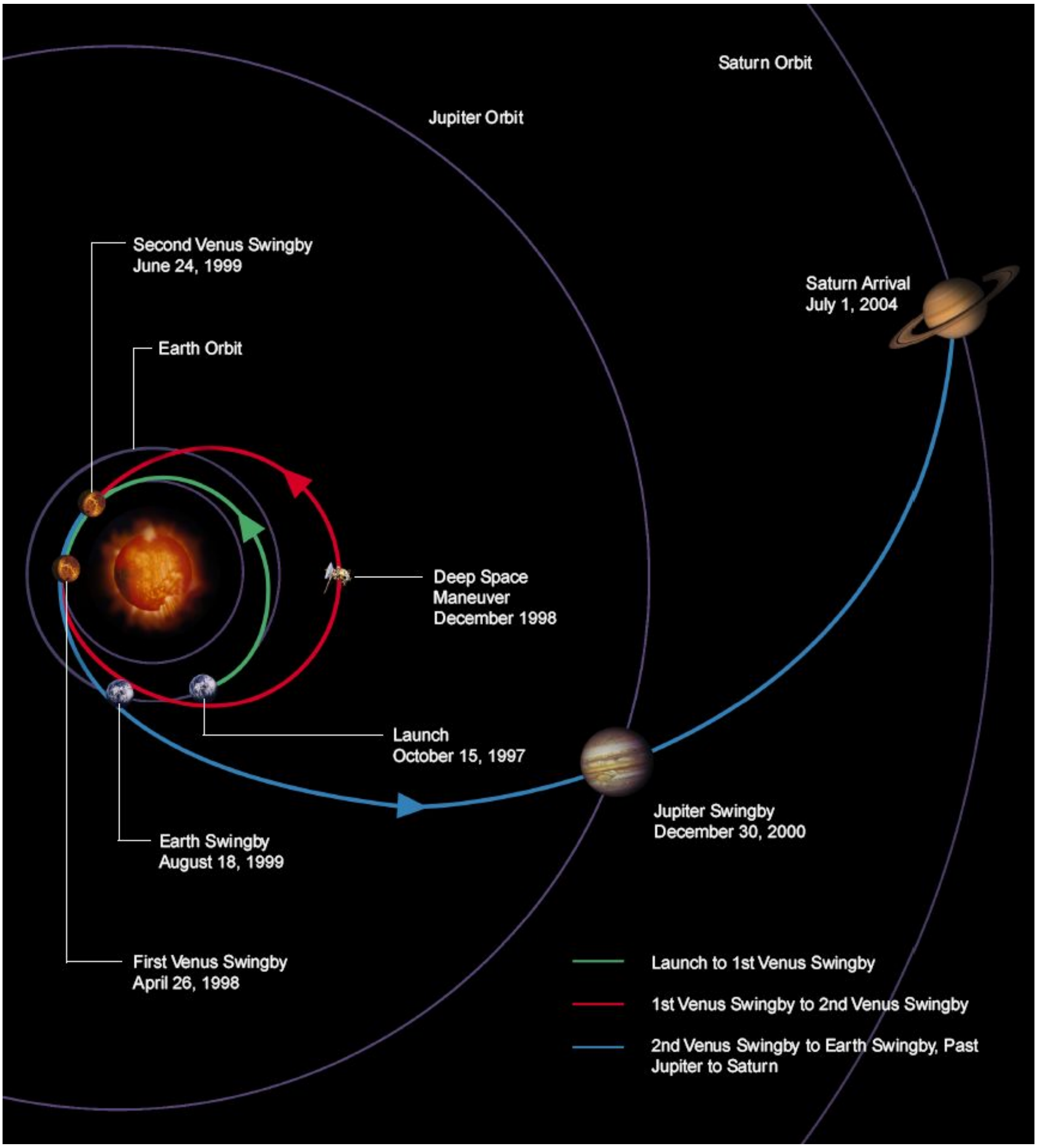
Saturn Orbit
Jupiter Orbit
Second Venus Swingby
June 24, 1999
Earth Orbit
Saturn Arrival
July 1, 2004
Deep Space
Maneuver
December 1998
Launch
October 15, 1997
Jupiter Swingby
December 30, 2000
Earth Swingby
August 18, 1999
First Venus Swingby
April 26, 1998
Launch to 1st Venus Swingby
1st Venus Swingby to 2nd Venus Swingby
2nd Venus Swingby to Earth Swingby, Past
Jupiter to Saturn

Figure 1.28: Image: NASA/JPL. Cassini mission journey from the Earth to the insertion in Saturn's orbit seven years later.

that has observed more than 100 stellar occultations by Saturn's rings. These observations provide measurements of ring structure that approaches the scale of the largest common ring particles (~ 5 m). The combination of multiple occultations at different viewing geometries enables reconstruction of the three-dimensional structure of the rings. In the case of the UVIS-HSP, this involves removal of the background (non-stellar) signal from the data and compensation for a drift in the instrument's sensitivity during the course of an occultation (Colwell et al., 2007).

The UVIS investigation has a broad range of scientific objectives encompassing the origin and evolution of the planets and their atmospheres, clouds and aerosols, magnetospheres, thermospheres and exospheres, satellite surfaces and their tenuous atmospheres, and ring structure, composition, and histories. UVIS-HSP has an integration time of 2.0 ms to observe stars occulted by the rings of Saturn. The spectral response of the HSP is limited at short wavelengths to about 115 nm by the MgF_2 detector window and at long wavelengths to about 190 nm by the work function of the CsI photocathode. The UVIS-HSP channel has been optimized to follow up on the Voyager investigations. The HSP field of view is 6 mrad * 6 mrad, large enough that no brightness modulations are expected from pointing variations. Occultations of the brightest stars (α Virginis, β Centauri, λ Scorpii, α Crucis) measured photon count rates higher than 1000 per integration period. This compares to the Voyager PPS observation of δ Scorpii of 39 counts every 10 ms (Esposito et al., 1983). Thus the Cassini UVIS HSP can probe structures five times narrower than Voyager, with 50 times the signal in each integration period. This high sensitivity and resolution was used to probe wakes, waves, and ring edges.

1.4.3 Stellar Occultations Data

Maurice Ainslie and John Knight, two British amateur astronomers observed the first reported stellar occultation of Saturn's rings in February 1917, reporting that the star brightness decreased to 25% in the A ring except in two locations when it doubled in brightness near the outer edge of the A ring (the Encke gap and the Keeler gap). On 28 April 1957, J. E. Westfall observed the 3.5-hour occultation of a star by the A and B rings (Figure 1.29). The apparent gaps near the outer edge of the A ring are likely to be the Keeler gap (the inner one) and the Encke gap (the broader, less distinct feature in the middle of the ring).

As detailed in the complete review from Esposito et al. (1998), "Voyager 1 and 2 made the closest investigations of Saturn's rings in 1980 and 1981. These missions provided images, spectra, and radio and stellar occultations as well as information on the ring environment. [...] The radio occultation, stellar occultation, and sequences of images each provided complete radial coverage of the ring system [...]. Conversely, the azimuthal coverage is more sketchy. [...] The Cassini mission provides the opportunity to measure the rings at high resolution in the radial, azimuthal, and vertical dimensions". Occultation tracks at multiple ring longitudes will likely reveal azimuthal asymmetries in the rings. These asymmetries may provide clues to the origin of the ring features and imply the presence of nearby per-

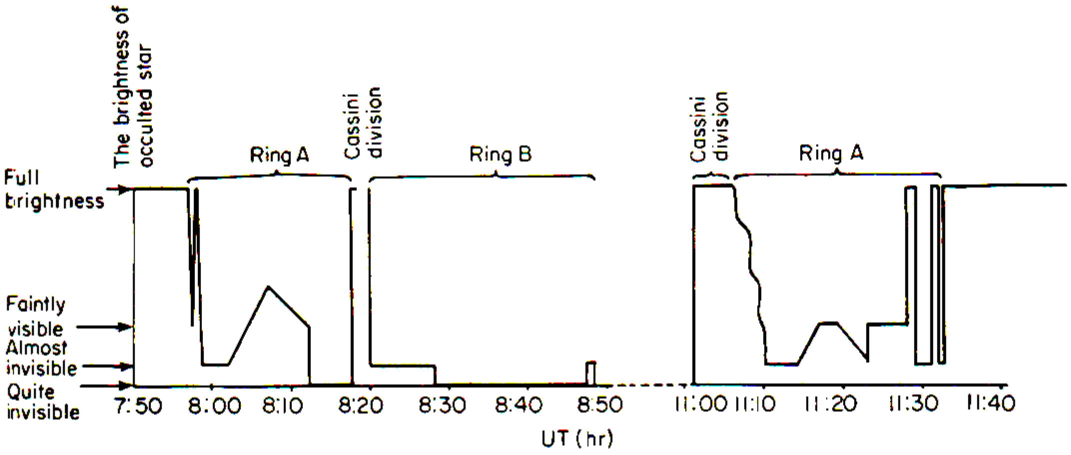

Figure 1.29: J. E. Westfall observations of a stellar occultation of Saturn's rings in 1957. From M. S. Brobov, "Physical Properties of Saturn's Rings", in *Surfaces and Interiors of Planets and Satellites*, 1970.

turbing satellites. Radial optical depth profiles have been generated from stellar occultation measurements (Colwell et al. (1990, 2010b)). During HSP observations of stellar occultations, the UVIS Far Ultraviolet channel (FUV) measures ring background brightness. These measurements provide information on the size distribution of small (micrometer-sized) dust particles in the rings during occultations by the shadowed rings. The abundance, size, and distribution of dust in the rings are useful diagnostics for the size distribution, velocity distribution, and surface properties of the larger ring particles, which act as sources and sinks of dust in the rings. Data on these larger particles are obtained from stellar occultations and combining UVIS reflectance data with images from the Cassini Imaging Science Subsystem (ISS) and Visual and Infrared Mapping Spectrometer (VIMS). The FUV data is also used to determine the magnitude of the ring background signal to be removed from the HSP occultation data. Because UVIS has the shortest wavelength of any of the remote sensing instruments, it is more sensitive to the smallest particles in the rings, with sizes as small as 0.01 to 0.1μm. The images at different UV wavelengths can be compared to camera images to determine the dust contribution and extend the size distribution. Characteristics of UVIS stellar occultations are provided in Table 1.3.

Table 1.3: Cassini UVIS stellar occultations.

Occultation Star (rev) side	Date (Year-Day)	|B| (°)	ϕ (°)	R (km)	Duration (s)	I_0 (Hz)
ξ2 Cet (A) E	2004-280	14.9	72.9-89.4	57,757-80,239	27197	1,300
ξ2 Cet (A) E	2004-281	14.9	98.8-103.8	108,956-135,650	26199	1,400
126 Tau (8) E	2005-139	21.1	130.2-88.8	70,380-141,390	31888	3,600
α Vir (8) I	2005-141	17.2	116.1-150.2	118,979-141,954	2546	479,000
α Vir (8) E	2005-141	17.2	116.1-82.2	118,979-141,704	2535	509,000
δ Aqr (8) E	2005-141	12.2	106.8-131.4	60,687-169,884	9871	700
α Leo (9) I	2005-159	9.5	68.0-10.7	114,150-204,718	6948	46,500
α Leo (9) E	2005-159	9.5	68.0-98.4	114,150-131,539	2663	43,200
126 Tau (10) I	2005-175	21.1	204.3-216.5	103,210-144,810	15898	4,100
σ Sgr (11) I	2005-195	29.1	221.9-248.8	85,987-146,929	5721	117,000
α Sco B (13) I	2005-232	32.2	155.0-208.4	101,173-155,751	6873	3,600
α Sco B (13) E	2005-232	32.2	155.1-105.8	101,173-146,576	6027	3,600
ζ Oph (26) E	2006-206	16.2	126.7-116.6	120,941-149,225	6611	28,000
λ Cet (28) I	2006-256	15.3	304.0-258.5	74,330-144,011	8901	2,500
α Sco B (29) I	2006-269	32.2	327.3-274.2	79,864-149,436	17154	3,500
ι Sco (29) E	2006-269	41.7	189.1-136.4	88,478-143,801	23518	285,000
α Vir (30) I	2006-285	17.2	266.2-219.8	64,022-151,545	4772	535,000
γ Lup (30) I	2006-286	47.4	157.1-185.9	83,062-94,587	7467	80,000
γ Lup (30) E	2006-286	47.4	157.1-102.7	83,062-141,044	18845	80,200
ϵ Mic (30) E	2006-292	31,0	189.1-174.6	97,363-140,210	16382	300*
μ Psa (31) I	2006-306	30.4	248.1-284.2	116,605-144,033	20599	800
μ Psa (31) E	2006-306	30.4	248.1-234.8	116,605-119,797	6691	700
γ Peg (32) I	2006-311	20.3	110.7-149.5	103,925-155,444	7712	75,000
γ Lup (32) E	2006-313	47.4	26.3-38.2	84,310-136,192	7046	74,200
α Ara (32) I	2006-314	54.4	280.9-276.5	61,333-139,786	15231	38,900
μ Psa (32) I	2006-318	30.4	248.1-282.6	118,450-143,457	19683	700
μ Psa (32) E	2006-318	30.4	248.1-245.2	118,450-118,607	1486	500
α Ara (33) I	2006-325	54.4	280.8-276.6	65,886-145,356	15461	38,700
α Vir (34) I	2006-337	17.2	282.1-220.9	74,536-153,654	4061	506,000
α Vir (34) E	2006-337	17.2	282.1-344.6	74,536-160,059	4281	516,000
η Lup (34) I	2006-337	51,0	325.0-286.1	106,848-135,360	10858	47,600
η Lup (34) E	2006-337	51,0	325.0-7.9	106,848-143,838	12513	46,300
κ Cen (35) E	2006-350	48.5	108.9-76.6	68,853-146,169	16765	47,100
α Ara (35) I	2006-351	54.4	221.2-252.0	64,857-130,424	22626	37,900
α Ara (35) E	2006-352	54.4	120.1-113.2	126,867-173,467	13891	37,900
γ Peg (36) I	2006-363	20.3	101.6-156.6	102,296-178,178	9939	73,000
γ Peg (36) E	2006-363	20.3	101.6-55.7	102,296-146,785	7172	70,100
δ Per (36) E	2006-364	54,0	68.3-65.7	66,531-140,886	8312	13,900

Occultation Star (rev) side	Date (Year-Day)	|B| (°)	ϕ (°)	R (km)	Duration (s)	I_0 (Hz)
κ Cen (36) I	2007-002	48.5	250.0-237.8	63,531-156,380	18341	44,200
ϵ Lup (36) E	2007-003	51,0	36.7-48.3	63,450-148,837	18431	33,300
α Ara (36) I	2007-005	54.4	3.2-311.6	70,897-113,954	24719	37,500
α Ara (36) E	2007-005	54.4	3.2-55.5	70,897-115,410	25228	35,700
γ Gru (37) I	2007-009	35.1	244.3-265.8	137,190-147,326	11069	7,300
γ Gru (37) E	2007-009	35.1	244.3-219.6	137,190-150,985	12999	6,800
δ Per (37) I	2007-015	54,0	281.1-258.2	60,054-142,584	11273	13,700
ϵ Lup (37) I	2007-020	51,0	324.8-284.8	99,479-129,588	17628	31,700
ϵ Lup (37) E	2007-020	51,0	324.8-10.9	99,479-142,934	21790	31,500
γ Ara (37) I	2007-022	61,0	245.6-251.2	121,471-147,952	7591	25,400
γ Ara (37) E	2007-022	61,0	142.5-117.2	80,500-155,599	22962	27,300
ϵ Psa (38) I	2007-027	23.7	255.1-299.3	82,195-114,638	8817	2,600
ϵ Psa (38) E	2007-027	23.7	255.1-239.1	82,195-85,527	2610	2,600
ψ Cen (38) I	2007-038	44.3	260.3-243.8	96,426-150,172	12338	1,100
γ Ara (38) I	2007-041	61,0	212.6-218.7	87,186-93,028	2860	24,400
ϵ Psa (39) I	2007-045	23.7	255.0-277.4	86,910-94,013	3534	2,500
ϵ Psa (39) E	2007-045	23.7	255.0-233.6	86,910-93,340	3357	2,300
δ Per (39) I	2007-049	54,0	284.1-257.8	55,505-143,284	13131	12,600
ξ Cen (39) I	2007-056	47.5	159.9-183.9	98,599-148,429	16186	13,200
θ Ara (40) I	2007-061	53.9	16.3-348.5	130,041-146,853	17211	15,300
θ Ara (40) E	2007-061	53.9	16.3-33.6	130,041-136,092	10120	15,000
γ Gru (40) E	2007-063	61,0	232.3-181.8	67,340-147,704	14990	7,500
β Psa (40) I	2007-063	29.2	269.5-288.1	119,978-142,564	4846	600
3 Cen (40) E	2007-073	39.3	39.4-37.8	110,987-147,354	7481	5,000
ψ Cen (40) I	2007-073	44.3	216.5-216.9	136,109-149,973	3736	2,500
θ Ara (41) E	2007-078	53.9	63.8-89.4	63,681-152,229	25676	12,100
β Sgr (41) I	2007-079	46.3	38.3-18.2	127,360-135,501	9616	2,700
β Sgr (41) E	2007-079	46.3	38.3-64.6	127,360-141,957	13040	2,900
γ Gru (41) I	2007-080	35.1	243.1-294.4	91,528-145,958	13345	8,100
γ Gru (41) E	2007-080	35.1	243.1-193.0	91,528-142,229	12781	7,800
δ Per (41) I	2007-082	54,0	232.8-240.6	49,260-149,746	10051	12,300
κ Cen (42) I	2007-092	48.5	141.6-178.0	114,712-142,152	27744	40,900
κ Cen (42) E	2007-092	48.5	141.6-115.3	114,712-127,824	18632	41,700
β Per (42) I	2007-098	47.4	227.8-230.8	84,461-149,674	5326	19,700
ζ Per (42) I	2007-098	38,0	328.0-318.1	132,811-134,700	1834	10,100
ζ Per (42) E	2007-098	38,0	328.0-344.0	132,811-137,957	3046	10,100
μ Sco (43) E	2007-112	43.4	155.8-162.1	117,000-123,000	4171	76,900
λ Sco (44) I	2007-129	41.7	211.1-244.4	69,544-141,063	19151	250,000
ζ Ori (47) E	2007-179	2.66	99.4-106.6	78,770-137,732	3890	175,000
α Sco (55) E	2008-003	32.2	49.6-68.0	115,023-142,164	7841	2,400

Occultation Star (rev) side	Date (Year-Day)	|B| (°)	ϕ (°)	R (km)	Duration (s)	I_0 (Hz)
ι Cen (56) E	2008-014	42.7	80.0-77.5	131,856-141,213	2880	853*
ν Cen (57) I (a)	2008-026	48,0	167.1-174.2	115,269-122,933	3740	38,300
ν Cen (57) I (b)	2008-026	48,0	142.2-146.3	104,915-105,173	1682	38,300
ν Cen (57) E	2008-026	48,0	142.2-133.8	104,915-106,010	3479	38,300
SAO205839 (57) I	2008-026	15.3	263.7-262.7	129,999-146,087	3331	11,200
ι Cen (57) E	2008-026	52.5	80.8-76.6	128,120-144,648	5072	945*
κ Cen (57) I	2008-026	48.5	238.4-239.3	139,320-146,914	1491	20,500
β Lup (57) I	2008-026	49.6	226.2-231.9	119,418-148,147	5906	71,200
δ Lup (57) I	2008-026	47,0	259.3-260.4	114,919-147,965	5805	48,300
γ Lup (57) I	2008-026	47.4	261.8-262.3	135,464-148,220	2141	54,200
γ Cnc (58) E	2008-040	21.3	227.9-189.4	77,203-160,536	9156	2,800
β Hya (60) I	2008-058	38.6	173.7-183.2	121,736-162,267	12341	1000
ζ Cen (60) I	2008-060	53.6	221.1-231.2	66,648-146,507	17320	107,000
δ Per (60) I	2008-062	54,0	283.9-274.5	54,975-146,216	7570	11,600
ζ Cen (62) E	2008-082	53.6	77.3-67.0	63,689-145,087	17831	107,000
α Ara (63) E	2008-092	54.4	95.8-112.3	73,261-141,566	8531	2,900
α Sex (63) I	2008-095	2.7	271.2-207.7	90,296-202,539	2958	500
α Sex (63) E	2008-095	2.7	271.2-337.4	90,296-223,667	3339	500
δ Cen (64) I	2008-100	55.6	117.2-127.9	131,696-133,946	5443	63,000
δ Cen (64) E	2008-100	55.6	117.2-107.9	131,696-133,387	4717	66,000
β Cen (64) E	2008-101	66.7	137.8-89.7	84,952-151,166	20690	600,000
γ Cas (64) I	2008-102	66.3	177.9-201.9	71,735-119,601	4411	103,000
ϵ Cen (65) I	2008-110	59.6	221.7-229.0	69,876-148,192	15730	130,000
α Ara (65) E	2008-111	54.4	110.4-112.9	125,009-143,844	2325	25,100
δ Cen (66) I	2008-119	55.6	117.4-142.4	130,072-143,054	13255	50,500
δ Cen (66) E	2008-119	55.6	117.4-110.6	130,072-130,974	3416	41,600
δ Cen (68) I	2008-137	55.6	201.9-203.4	124,551-150,366	4731	46,500
θ Hya (70) I	2008-156	1.4	89.5-17.9	126,499-401,041	3428	3,600
θ Hya (70) E	2008-156	1.4	89.5-160.3	126,499-384,109	3267	2,800
θ Hya (71) I	2008-163	1.4	89.5-23.2	124,439-310,043	2561	4,000
θ Hya (71) E	2008-163	1.4	89.5-153.9	124,439-287,654	2339	3,100
β Cen (75) I	2008-188	66.7	283.5-264.4	72,427-144,448	9611	592,000
γ Cnc (75) I	2008-190	21.3	79.8-24.1	71,827-130,700	10241	4,400
β Cen (77) I	2008-202	66.7	282.9-264.4	73,334-144,893	9481	583,000
β Cen (77) E	2008-203	66.7	34.6-54.4	73,267-143,444	10191	604,000
β Cen (78) E	2008-210	66.7	23.7-54.8	58,470-145,023	12731	572,000
α Ara (79) I	2008-217	54.4	49.5-354.2	94,195-157,552	10626	24,600
α Ara (79) E	2008-217	54.4	49.5-70.2	94,195-100,266	2874	24,600
β Cen (81) I	2008-231	66.7	294.4-267.6	72,829-151,692	12191	546,000
β Cen (85) I	2008-260	66.7	295.3-269.5	73,112-143,414	10991	531,000

Occultation Star (rev) side	Date (Year-Day)	|B| (°)	ϕ (°)	R (km)	Duration (s)	I_0 (Hz)
α Ara (85) I	2008-261	54.4	49.7-353.3	93,510-160,543	10917	25,100
α Ara (85) E	2008-261	54.4	49.7-106.4	93,510-157,485	10873	24,000
α Ara (86) I	2008-268	54.4	49.7-352.5	93,407-163,471	11220	22,400
α Ara (86) E	2008-268	54.4	49.7-107.2	93,407-160,105	11171	21,400
β Cen (89) I	2008-290	66.7	296.4-269.8	71,854-141,886	10931	500,000
α Ara (90) I	2008-298	54.4	49.7-352.7	92,106-160,553	10949	20,200
α Ara (90) E	2008-298	54.4	49.7-106.7	92,106-156,650	10812	20,000
α Cru (92) I	2008-312	68.2	125.0-181.6	77,557-155,730	20861	516,000
β Cen (92) E	2008-313	66.7	42.7-59.1	50,676-154,574	16180	463,000
θ Hya (94) I	2008-332	1.4	89.5-10.5	83,453-436,956	2994	1800*
θ Hya (94) E	2008-332	1.4	89.5-169.9	83,453-500,646	3446	1800*
β Cen (96) I	2008-343	66.7	288.6-264.8	72,456-155,341	12582	441,000
α Ara (96) I	2008-344	54.4	46.9-1.6	108,169-150,852	9900	19,800
α Ara (96) E	2008-344	54.4	46.9-94.2	108,169-155,151	10551	19,300
δ Cen (98) I	2008-359	55.6	209.3-212.0	55,447-153,103	14531	36,100
β Cru (98) I	2008-359	65.2	157.3-202.6	58,104-154,683	18080	279,000
α Ara (98) I	2008-360	54.4	42.3-357.4	110,536-154,532	12407	17,200
α Ara (98) E	2008-360	54.4	42.3-86.3	110,536-152,130	12024	17,200
α Cru (100) I	2009-012	68.2	124.2-164.8	114,050-149,157	14422	438,000
α Cru (100) E	2009-012	68.2	124.2-83.5	114,050-149,449	14508	418,000
γ Cas (100) E	2009-015	66.3	86.4-66.0	72,440-140,370	9611	56,000
β Cen (102) I	2009-031	66.7	250.7-248.3	73,243-143,508	10311	369,000
β Cen (104) I	2009-053	66.7	179.2-220.0	70,203-147,291	27000	365,000
β Cen (104) E	2009-053	66.7	134.8-94.7	68,934-131,988	15591	365,000
ϵ Cas (104) I	2009-058	69.9	154.5-198.7	111,694-154,568	15864	4,400
ϵ Cas (104) E	2009-058	69.9	154.5-111.7	111,694-151,532	15197	4,400
θ Hya (104) I	2009-062	1.4	89.3-3.0	66,876-1,051,956	5513	1000*
θ Hya (104) E	2009-062	1.4	89.3-172.5	66,876-561,578	2928	1000*
β Cen (105) I	2009-065	66.7	199.1-222.0	88,502- 158,713	14561	310,000
β Cen (105) E	2009-065	66.7	121.7-91.5	77,787-147,358	15341	301,000
α Ara (105) I	2009-066	54.4	39.2-343.9	93,917-163,844	19802	15,500
α Ara (105) E	2009-066	54.4	39.2-88.6	93,917-143,382	15969	17,000
ζ Cen (112) I	2009-163	53.6	236.6-241.2	71,486-143,214	16464	53,000
μ Cen (113) I	2009-177	48.7	236.2-240.6	75,975-155,785	16090	9,400
α Lup (113) I	2009-178	53.8	172.4-217.8	83,839-118,956	20269	26,400
α Lup (113) E	2009-178	53.8	172.4-160.9	83,839-85,541	4071	26,400
β Lup (114) I	2009-193	49.6	186.8-217.4	118,474-144,836	16090	24,000*
λ Sco (114) I	2009-195	41.7	219.6-259.1	110,857-148,227	31840	88,500
σ Sgr (114) I	2009-198	29.1	332.1-329.2	84,449-149,875	21040	33,300
μ Sgr (115) I	2009-212	24.9	44.1-27.4	90,967-94,935	10104	>200+

Occultation Star (rev) side	Date (Year-Day)	$\|B\|$ (°)	ϕ (°)	R (km)	Duration (s)	I_0 (Hz)
μ Sgr (115) E	2009-212	24.9	44.1-80.3	90,967-112,618	24707	>200+
β Per (116) I	2009-223	47.4	153.8-169.6	131,436-135,217	2294	2000*
β Per (116) E	2009-223	47.4	153.8-138.5	131,436-134,741	2206	2200*
α Vir (116) I	2009-223	17.2	245.2-241.9	103,059-144,566	3764	165,000
π4 Ori (117) E	2009-239	3.7	105.2-109.1	68,168-145,300	4811	3300
α Vir (124) E	2010-011	17.2	121.7-124.1	70,494-142,431	6011	165,000
β Lib (124) E	2010-011	15.8	236.9-221.5	115,071-123,509	2756	2900

Notes: Rev refers to the number of the orbit of Cassini around Saturn on which the observation occurred. Cassini revs are numbered 0, A, B, C, 3, 4, and consecutively thereafter. Ranges in ϕ and R are for the entire observation, and the range in ϕ is listed in the order corresponding to the range in R. In some cases, part of the occultation is obscured by the planet. The values listed here are for the full occultation, not just the part where the star is unobstructed. Durations indicate the time from the start of measurements to the last measurement, including gaps caused by data dropouts. *: Indicates occultations for which the background cannot be directly measured, and the values listed in the I_0 column are I_0+b for those occultations. +: Indicates occultations for which the stellar signal cannot be directly measured, and the values listed in the I_0 column are estimates from other occultations. I and E indicate ingress and egress occultations, respectively. Table and caption from Colwell et al. (2010b).

1.5 General Questions

We are not even close to fully understanding all the structures we observe in Saturn's rings. Whatever model is built to explain some of these structures, it will rely on our estimation of the physical characteristics of the rings. These properties are the rings heritage, traces that could lead us closer to understand when they formed, how they formed and why Saturn's rings are so different from the other giant planet rings. Understanding this system could help us understand the other astrophysical disks we described earlier.

1.6 Points Addressed in this Manuscript

Taking advantage of the highest resolution available in Saturn's rings observations, we first focused in regions of relatively low optical depth in the main rings: the C ring and the Cassini Division. Modeling the interactions between an exterior satellite in resonance and a disk allowed the estimation of some of the physical intrinsic properties of the rings: in particular, particle sizes and rings densities (Chapter 2). Chapter 3 proceeds with similar analysis in the B ring and in the Cassini Division. We then considered interactions of the rings particles with an embedded satellite and drew some conclusions about the possible presence of such a satellite in the Huygens gap (Chapter 4). Finally, we investigated the formation of such embedded moonlets and tried to detect smaller boulders in the C ring and the Cassini Division (Chapter 5). These observations allowed us to estimate some constraints on the upper part of the particle size distributions in these rings.

CHAPTER 2

WAVES IN THE C RING

2.1 Introduction

Many of Saturn's moons have low order inner Lindblad resonances (ILRs) located in Saturn's rings that excite outwardly propagating spiral density waves (Goldreich and Tremaine (1982) and Shu (1984)). Although some of these resonances coincide with obvious wavelike features in the rings, it is not the case in general. Most waves discovered in the C ring in Voyager data and reported by Rosen et al. (1991a,b) have no known resonance association. Identification of wavelike structures in the C ring can now be performed with enhanced confidence using Cassini data, especially occultation data provided by Cassini UVIS with a spatial resolution close to 20 m. By combining dozens of Cassini UVIS occultations, we have identified more than 30 waves in the C ring. We tentatively associate 3 of these waves (plus 2 others already known) with resonances, though a definitive association is complicated by uncertainties in the geometry of the occultations that are comparable to the wavelengths of many of the waves.

Many similar studies have been conducted on other parts of the rings and have mainly revealed longer waves than the ones we report here (Esposito et al. (1998), Spilker et al.

(2004), Tiscareno et al. (2007) and references therein). The UVIS stellar occultations can resolve wave structures with short wavelengths, and the large number of occultations boosts the signal to noise ratio making it possible to combine profiles to identify waves with small amplitudes. Identifying the resonance locations is crucial before making associations with observed wavelike features. If the wave can be positively identified as a density or bending wave associated with a specific resonance, the dispersion of the wave can be analyzed to constrain the surface mass density, σ, and mass extinction coefficient, $\kappa = \tau/\sigma$, where τ is the optical depth of the ring at the location of the wave. Rosen and Lissauer (1988) and Rosen et al. (1991b) provided estimates of the surface mass density in the C ring, together with constraints on the vertical thickness of the C ring (less than 2.5 m). Tiscareno et al. (2007) derived surface mass density and ring thickness from Cassini ISS data (10 – 15 m in the inner A ring and 3 – 4.5 m in the Cassini Division). Colwell et al. (2009a) also analyzed high resolution Cassini UVIS data to determine the surface mass density and vertical thickness of the Cassini Division (3 – 6 m). These ring properties lead to a better understanding of the composition and size distribution of particles in the rings. Earlier analyses of density waves in the A ring and the Cassini Division have shown that κ is nearly constant across the A ring and into the Cassini Division ramp (Tiscareno et al., 2007), and then jumps by a factor of ~ 4 in the main Cassini Division, indicating a different particle population there (Colwell et al., 2009a). Tiscareno et al. (2009) analyzed the Iapetus -1:0 nodal bending wave and showed that the mass extinction coefficient drops by a factor of 10 between the main Cassini

Division and the Cassini Division Ramp, and then jumps by a factor of 3 at the inner edge of the A ring.

The C ring shares similar optical depths and colors with the Cassini Division, however the strong satellite resonances are concentrated in the outer part of the ring system so that the same sort of systematic wave diagnostic applied there has not been possible in the C ring (or, for that matter, in the much more optically thick B ring). Here we show that the C ring has many wavelike structures throughout, and we identify several features not previously reported. Among them are what we believe to be density waves associated with the Mimas 4:1 ILR, Atlas 2:1 ILR, Mimas 6:2 ILR, and Pandora 4:2 ILR, and a bending wave associated with the Titan -1:0 nodal resonance (Rosen and Lissauer, 1988). The majority of the wave features' locations, however, do not correspond in location to strong resonances with the known external satellites. However, even in the absence of a resonance association, limits can be placed on both σ and κ from the measured dispersion of the wave within a multiplicative factor of the azimuthal parameter m, and by assuming that these features are in fact density or bending waves, depending on their direction of decreasing wavelength. In particular, we find $\sigma \geq 0.14$ g cm^{-2} and $\kappa \leq 0.63$ cm^2 g^{-1}. Besides these constraints, actual values of σ and κ were derived from resonance associations, defining a range of surface mass density from 0.22 ($\pm$0.03) to 1.42 ($\pm$0.21) g cm^{-2} and mass extinction coefficient from 0.13 ($\pm$0.03) to 0.28 ($\pm$0.06) cm^2 g^{-1}. These mass extinction coefficient values are higher than those found in the A ring (0.01 – 0.02 cm^2 g^{-1}) and in the Cassini Division (0.07 – 0.12 cm^2 g^{-1} from Colwell et al. (2009a)), implying smaller particle sizes in the C ring than either the A ring or the Cassini Division. We also estimate the mass of the C ring to be between 3.7 (±0.9) $\times 10^{16}$ kg and 7.9 (±2.0) $\times 10^{16}$ kg, equivalent to a moon of 28.0 (±2.3) km to 36.2 (±3.0) km radius (a little larger than Pan or Atlas) with a density comparable to the two moons (400 kg m^{-3}). From the wave damping length and the ring viscosity, we also estimate the vertical thickness of the C ring to be between 1.9 (±0.4) m and 5.6 (±1.4) m, which is consistent with the vertical thickness of the Cassini Division (2 – 20 m) from Tiscareno et al. (2007) and Colwell et al. (2009a).

In Section 2.2 we describe occultation data provided by Cassini UVIS instrument. Section 2.3 reviews the principles of our analysis and presents newly identified waves. In Section 2.4 we show possible correlations with satellite resonance locations, and in Section 2.5, we estimate resulting physical properties of the rings at these locations.

2.2 Observations

We selected 62 complete or partial stellar occultations of the rings observed with the High Speed Photometer (HSP) of the Cassini Ultraviolet Imaging Spectrograph (UVIS), (Esposito et al. (1998), Esposito et al. (2004) and Colwell et al. (2010b)). These occultations, detailed in Table 2.1, have integration periods of 1-2 ms that provide a spatial resolution in the ring plane of about 10–20 m, varying with the viewing geometry (which varies between occultations and also within a given occultation).

Occultations from 2007 and earlier are detailed in Colwell et al. (2007), and a description of calibration procedures applied to all occultations is presented in Colwell et al. (2010b), which documents viewing geometries and star brightnesses. While some stars like γ Grus (Rev 40) are relatively faint, others such as β Centauri (Rev 64, 75, 77, 78, 81, 85, 89, 92, 96, 102, 104, 105) produce photon count rates 10 to 100 times higher. In addition, some stars have very low incidence angles relative to the plane of the rings, which allow a better observation of structures inclined to the plane of the rings, such as bending waves.

Table 2.1: Cassini UVIS stellar occultations.

Occultation Star (rev) side	Date (Year-Day)	|B| (°)	ϕ (°)	R (km)	Duration (s)	I_0 (Hz)
ξ2 Cet (A) E	2004-280	14.9	72.9-89.4	57,757-80,239	27197	1,300
126 Tau (8) E	2005-139	21.1	130.2-88.8	70,380-141,390	31888	3,600
σ Sgr (11) I	2005-195	29.1	221.9-248.8	85,987-146,929	5721	117,000
λ Cet (28) I	2006-256	15.3	304.0-258.5	74,330-144,011	8901	2,500
α Sco B (29) I	2006-269	32.2	327.3-274.2	79,864-149,436	17154	3,500
α Vir (30) I	2006-285	17.2	266.2-219.8	64,022-151,545	4772	535,000
γ Lup (30) I	2006-286	47.4	157.1-185.9	83,062-94,587	7467	80,000
γ Lup (30) E	2006-286	47.4	157.1-102.7	83,062-141,044	18845	80,200
γ Lup (32) E	2006-313	47.4	26.3-38.2	84,310-136,192	7046	74,200
α Ara (32) I	2006-314	54.4	280.9-276.5	61,333-139,786	15231	38,900
α Ara (33) I	2006-325	54.4	280.8-276.6	65,886-145,356	15461	38,700
α Vir (34) I	2006-337	17.2	282.1-220.9	74,536-153,654	4061	506,000
α Vir (34) E	2006-337	17.2	282.1-344.6	74,536-160,059	4281	516,000
κ Cen (35) E	2006-350	48.5	108.9-76.6	68,853-146,169	16765	47,100
α Ara (35) I	2006-351	54.4	221.2-252.0	64,857-130,424	22626	37,900
δ Per (36) E	2006-364	54,0	68.3-65.7	66,531-140,886	8312	13,900
κ Cen (36) I	2007-002	48.5	250.0-237.8	63,531-156,380	18341	44,200
ϵ Lup (36) E	2007-003	51,0	36.7-48.3	63,450-148,837	18431	33,300
α Ara (36) I	2007-005	54.4	3.2-311.6	70,897-113,954	24719	37,500
α Ara (36) E	2007-005	54.4	3.2-55.5	70,897-115,410	25228	35,700
δ Per (37) I	2007-015	54,0	281.1-258.2	60,054-142,584	11273	13,700
γ Ara (37) E	2007-022	61,0	142.5-117.2	80,500-155,599	22962	27,300
γ Ara (38) I	2007-041	61,0	212.6-218.7	87,186-93,028	2860	24,400
ϵ Psa (39) I	2007-045	23.7	255.0-277.4	86,910-94,013	3534	2,500
ϵ Psa (39) E	2007-045	23.7	255.0-233.6	86,910-93,340	3357	2,300
δ Per (39) I	2007-049	54,0	284.1-257.8	55,505-143,284	13131	12,600
γ Gru (40) E	2007-063	61,0	232.3-181.8	67,340-147,704	14990	7,500
θ Ara (41) E	2007-078	53.9	63.8-89.4	63,681-152,229	25676	12,100
δ Per (41) I	2007-082	54,0	232.8-240.6	49,260-149,746	10051	12,300
β Per (42) I	2007-098	47.4	227.8-230.8	84,461-149,674	5326	19,700
ζ Ori (47) E	2007-179	2.66	99.4-106.6	78,770-137,732	3890	175,000
ζ Cen (60) I	2008-060	53.6	221.1-231.2	66,648-146,507	17320	107,000
δ Per (60) I	2008-062	54,0	283.9-274.5	54,975-146,216	7570	11,600
ζ Cen (62) E	2008-082	53.6	77.3-67.0	63,689-145,087	17831	107,000
α Ara (63) E	2008-092	54.4	95.8-112.3	73,261-141,566	8531	2,900
γ Cas (64) I	2008-102	66.3	177.9-201.9	71,735-119,601	4411	103,000
ϵ Cen (65) I	2008-110	59.6	221.7-229.0	69,876-148,192	15730	130,000
β Cen (75) I	2008-188	66.7	283.5-264.4	72,427-144,448	9611	592,000

Occultation Star (rev) side	Date (Year-Day)	$\lvert B \rvert$ (°)	ϕ (°)	R (km)	Duration (s)	I_0 (Hz)
β Cen (77) I	2008-202	66.7	282.9-264.4	73,334-144,893	9481	583,000
β Cen (77) E	2008-203	66.7	34.6-54.4	73,267-143,444	10191	604,000
β Cen (78) E	2008-210	66.7	23.7-54.8	58,470-145,023	12731	572,000
β Cen (81) I	2008-231	66.7	294.4-267.6	72,829-151,692	12191	546,000
β Cen (85) I	2008-260	66.7	295.3-269.5	73,112-143,414	10991	531,000
β Cen (89) I	2008-290	66.7	296.4-269.8	71,854-141,886	10931	500,000
α Cru (92) I	2008-312	68.2	125.0-181.6	77,557-155,730	20861	516,000
β Cen (92) E	2008-313	66.7	42.7-59.1	50,676-154,574	16180	463,000
β Cen (96) I	2008-343	66.7	288.6-264.8	72,456-155,341	12582	441,000
δ Cen (98) I	2008-359	55.6	209.3-212.0	55,447-153,103	14531	36,100
β Cru (98) I	2008-359	65.2	157.3-202.6	58,104-154,683	18080	279,000
γ Cas (100) E	2009-015	66.3	86.4-66.0	72,440-140,370	9611	56,000
β Cen (102) I	2009-031	66.7	250.7-248.3	73,243-143,508	10311	369,000
β Cen (104) I	2009-053	66.7	179.2-220.0	70,203-147,291	27000	365,000
β Cen (104) E	2009-053	66.7	134.8-94.7	68,934-131,988	15591	365,000
β Cen (105) I	2009-065	66.7	199.1-222.0	88,502- 158,713	14561	310,000
β Cen (105) E	2009-065	66.7	121.7-91.5	77,787-147,358	15341	301,000
ζ Cen (112) I	2009-163	53.6	236.6-241.2	71,486-143,214	16464	53,000
μ Cen (113) I	2009-177	48.7	236.2-240.6	75,975-155,785	16090	9,400
α Lup (113) I	2009-178	53.8	172.4-217.8	83,839-118,956	20269	26,400
α Lup (113) E	2009-178	53.8	172.4-160.9	83,839-85,541	4071	26,400
σ Sgr (114) I	2009-198	29.1	332.1-329.2	84,449-149,875	21040	33,300
μ Sgr (115) I	2009-212	24.9	44.1-27.4	90,967-94,935	10104	>200
μ Sgr (115) E	2009-212	24.9	44.1-80.3	90,967-112,618	24707	>200

Notes: Rev refers to the number of the orbit of Cassini around Saturn on which the observation occurred. Cassini revs are numbered 0, A, B, C, 3, 4, and consecutively thereafter. Ranges in ϕ and R are for the entire observation, and the range in ϕ is listed in the order corresponding to the range in R. In some cases, part of the occultation is obscured by the planet. The values listed here are for the full occultation, not just the part where the star is unobstructed. Durations indicate the time from the start of measurements to the last measurement, including gaps caused by data dropouts. I and E indicate ingress and egress occultations, respectively. Table and caption from Colwell et al. (2010b).

Direct measurements of the brightness of the occulted star are converted into an optical depth profile of the C ring. We can clearly identify gaps (regions of lowest optical depth), ringlets (peaks in optical depth) and plateau regions in the C ring. Thanks to the high resolution of UVIS data, we can distinguish small scale structures like wavelike features that are only a few kilometers in radial width and with wavelengths that are a fraction of a kilometer. Figure 2.1-a shows an inward propagating wave (the wavelength decreases when the ring plane radius is decreasing), whereas Figure 2.1-b shows, in contrast, an outward propagating wave (i.e. a decreasing wavelength while ring plane radius increases).

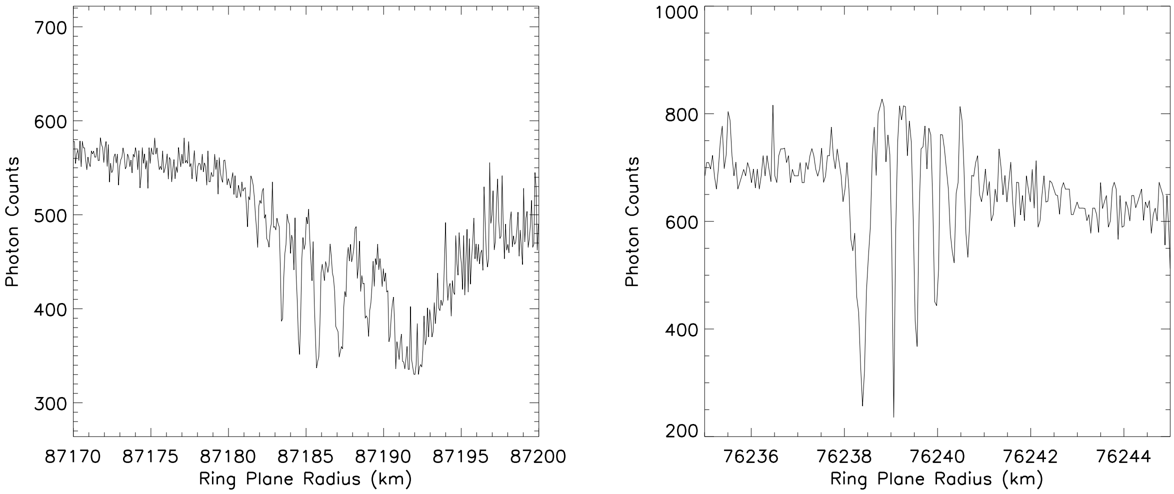

Figure 2.1: Photon counts from the occultation of β Centauri (Rev 75) showing structure 32, propagating inward (left) and of α Virginis (Rev 34) showing feature 6 propagating outward (right).

2.3 Wavelet Analysis

2.3.1 Wavelet Transform

While looking at the raw data reveals evidence of several wavelike features, a more systematic process can be applied to the whole C ring in order to detect these periodic signatures, especially when the environment (gaps and ringlets, for example) prevents the signature from being obvious in the raw data. To this end, following the method detailed in Colwell et al. (2009a), we computed for each occultation a weighted wavelet Z (WWZ) transform, which is based on a Morlet wavelet transform (Torrence and Compo, 1998) and which can handle data with uneven positional sampling (Foster, 1996), as used by Colwell et al. (2009a) for analysis of Cassini Division waves. The Morlet wavelet is a plane wave modulated by a Gaussian:

$$\Psi_0(t) = \pi^{-1/4}\ e^{i\omega_0 t} e^{-t^2/2}, \tag{2.1}$$

where t will be our non-dimensional radius parameter and ω_0 is a non-dimensional frequency set by the user. Wavelet analysis consists in translating and dilating the mother wavelet in order to generate the daughter wavelets that will be convolved with an input signal. We can define the daughter wavelet at a location r and for a spatial scale s as follows:

$$\Psi_{r,s}(r') = s^{-1/2}\ \pi^{-1/4}\ e^{\frac{i\omega_0(r'-r)}{s} - \frac{(r'-r)^2}{2s^2}}. \tag{2.2}$$

The continuous wavelet transform of an evenly sampled radial signal is given by:

$$T(r,s) = \int_{-\infty}^{\infty} x(r')\Psi^{*}_{r,s}(r')\mathrm{d}r', \tag{2.3}$$

where * denotes the complex conjugate.

The Fourier wavelength is given by:

$$\lambda_F = \frac{4\ \pi\ s}{\omega_0 + \sqrt{2 + \omega_0}} \tag{2.4}$$

and the wavenumber is $k = \frac{2\pi}{\lambda_F}$.

Then, we can define the wavelet energy spectrum

$$E_W(r,s) = |T(r,s)|^2, \tag{2.5}$$

and the wavelet phase

$$\phi_W(r,s) = \tan^{-1}\left(\frac{\mathrm{Im}(T(r,s))}{\mathrm{Re}(T(r,s))}\right). \tag{2.6}$$

For each subset of an occultation (typically 100 km in radial extent), we generate a wavelength power spectrum at each radial location (computed with 50 m resolution). Spatial wavelengths are distributed accross 100 logarithmically-spaced bins between 0.3 km and 8 km (with a few exceptions that include wavelength powers outside these boundaries). In the next figures, we will present WWZ wavelet power profiles, showing in the top panel the strength of spatial wavelength components as a function of ring plane radius, and in the bottom panel the corresponding raw data. The cone of significance on wavelet power profiles delimits regions that should not be trusted, due to the influence of the nearby artificial and arbitrary boundaries of the data subset. The width of this cone of influence is given by

$w(\lambda) = \frac{\sqrt{2}(\omega_0+\sqrt{2+\omega_0})}{4\pi}$. This cone of influence is not too relevant in our case since our data sets are much wider than the considered subsets. Therefore, resulting plots are cuts in wider processed sections, large enough to include at least twice the radial extent of the equivalent cone of significance.

In order to better analyze the results of the wavelet profiles, we generated the profiles for some basic reference signals. A sine signal will obviously result in a constant profile at the wavelength of the signal. Ascending or descending isolated ramps will not show any specific wavelength. But, dealing with step functions will radically change the profiles. In those cases we will find some power at wavelengths equal to the width of the step (Figure 2.2-a). This is confirmed for a more "Dirac"-like signal, that we can consider as a superposition of several step functions with decreasing width. Therefore, we expect to find a pattern of power at all wavelengths, centered on the Dirac peak location and with widths proportional to the wavelength. That would result in an inverted triangular shape on the wavelet profile (Figure 2.2-b).

Not all individual occultation profiles present clear wave structures at the locations of wave structures seen in other occultations, mainly due to low signal rates, occultation elevation angle or slight radial shifts coming from navigation errors. These effects can be compensated for by co-adding all the wavelet transforms; this has the effect of enhancing any true periodic signature in the data, while random fluctuations will tend to average out (Colwell et al., 2009a). Because each of the individual occultations has uncertainties in the absolute geometry of about 1 km due primarily to uncertainties in the spacecraft's position

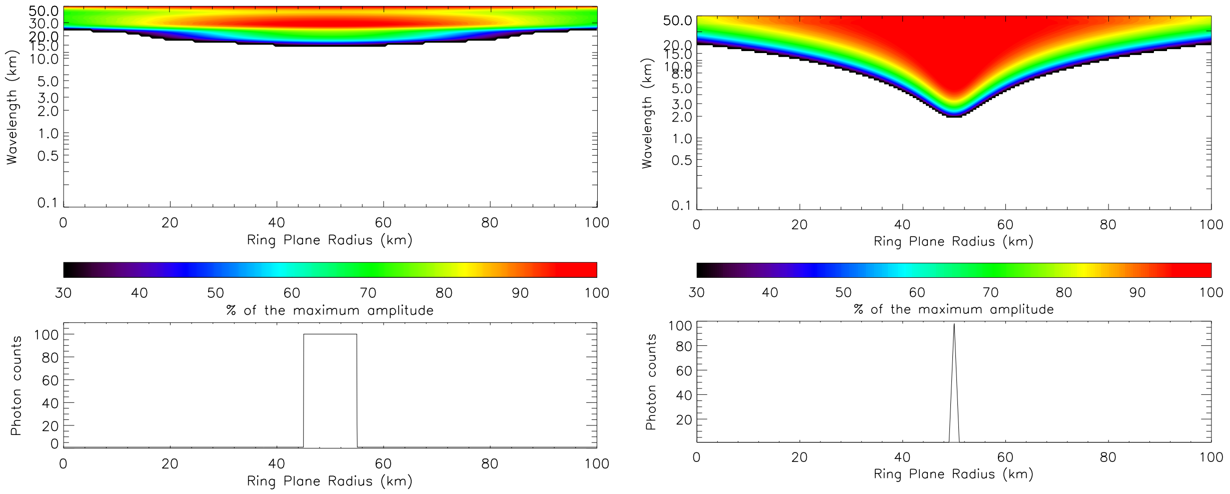

Figure 2.2: WWZ wavelet power profile for two reference theoretical signals: a step function (left) and a Dirac signal (right). The bottom panel presents the simulated data that were analyzed to produce these power transforms.

along its trajectory, the co-adding process tends to smear the wave signal over this same 1-km range. When structures that are in the rings are clearly shifted in ring plane radius, we used circular fiduciary features from French et al. (1993) to adjust the radial scale for those occultations. Nevertheless, those edge locations are not precise to better than 1 km, so we are left with a typical uncertainty in ring plane radius of 1 km.

We found that once a wave has been identified, the most precise information can be extracted from the occultations presenting the highest photon count rates (the 12 β Centauri, the α Virginis, rev. 30 and 34 and the ζ Orionis, rev. 47, occultations (Table 2.1)). The β Centauri occultations have a high elevation angle $B = 66^\circ$ relative to the ring plane and therefore allow us to identify the density wave positions particularly well, whereas the others have some of the lowest B angles permitting more accurate detection of the bending wave locations, as we can see in Figure 2.3: the Mimas 5:3 inner vertical resonance at 131923 km is clearly visible in the low elevation angle occultations whereas β Centauri occultations do not allow this wave to be observed systematically (but still sometimes as on the β Centauri, rev. 105 occultation).

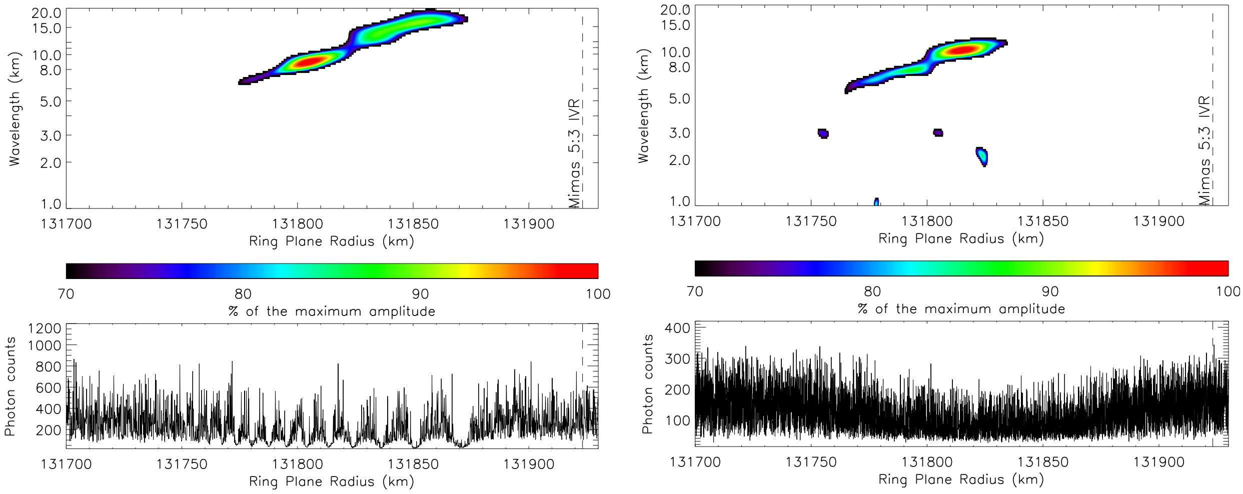

Figure 2.3: WWZ wavelet power profile for the Mimas 5:3 IVR bending wave ($r_V = 131923$ km), computed from individual occultation profile of α Virginis, rev. 34 (left) and β Centauri, rev. 105 (right).

Our WWZ analysis revealed the 10 waves reported by Rosen et al. (1991a) and Rosen et al. (1991b), the 12 additional waves reported by Colwell et al. (2009b) (including the Atlas 2:1 density wave at 87645 km (structure 33) visible in Figure 2.11), together with 18 previously unreported wavelike features, which appear to be propagating waves. We consider a wave to be potentially propagating if it exhibits a dispersion in wavelength (decreasing or increasing with distance from Saturn) analogous to density and bending waves.

In addition to 10 previously reported structures presenting a wavelength decreasing with radius, 11 previously known features with wavelength increasing with radius, and one last with no reported prefered direction of propagation, our new structures are divided in 12 new outward features, 5 new inward ones and one which direction of propagation is not clear. Occultation and wavelet profiles showing the propagation for selected structures are presented in Figures 2.4-2.33. As expected, outward features, more likely to be density waves are visible in both β Centauri and α Virginis occultations while inward structures, more likely to be bending waves, are only visible in αVirginis and ζ Orionis occultations.

2.3.2 Ringlet Signatures

We observe a great variety of wavelet power signatures: from clearly propagating waves to triangle-shaped signatures produced by narrow ringlets. Such signatures for which we cannot positively identify a propagating wave on individual occultation scans are listed in Table 2.2. For example, structure 1 of this Table is displayed in Figure 2.4: the location of this signature coincides with the Embedded Ringlet 1 reported by Colwell et al. (2009b). We cannot distinguish any propagating wave in any individual occultation at this radial position, and the signature is consistent with a possible triangle-shaped artifact as generated by the "Dirac" signal, modeling an embedded ringlet. Other examples are observed at the positions of other embedded ringlets such as ER2 (Figure 2.5) or ER8 (double peak) (Figure 2.6). Larger ringlets give larger wavelengths. But we also observe such patterns at two locations where embedded ringlets were not previously reported. Individual occultation profiles at these positions confirm the existence of new embedded ringlets (ER 17 (Figure 2.7) and ER 18 (Figure 2.8) of Table 2.2). In these cases, the ring structure signature is dominant over a possible propagating wave, but that does not exclude the possibility that these structures themselves can be due to satellite resonances. Finally, some other known ringlets coincide with the location of some waves reported here: ER7 is just 3 km exterior to the inward propagating feature 5 in Table 2.3, ER10 is 4 km interior to the inward propagating wave 16, ER13 is overlapping with inward propagating structure 32 and ER16 is also overlapping with inward propagating features 38 and 39, and coincides with the location of Mimas 3:1 ILR. We notice that most of the embedded ringlets coincide with a wavelike signature that cannot be explained by the shape of the ringlet alone. For those of the signatures that appear to be propagating, the direction is apparently inward. Despite this direction of propagation, which would suggest that they are bending waves if due to external satellites, these waves are very clear on β Centauri occultations ($B = 66.7^\circ$). This direction of propagation has been explained by Rosen and Lissauer (1988) and Nicholson et al. (2010), who give a detailed analysis of the Titan -1:0 nodal resonance that is an outward propagating bending wave, due to its negative pattern speed. We report only two potential resonance associations in the neighborhood of these ringlets: Pandora 2:1 ILR at 90165.4 km and Mimas 3:1 ILR at 90195.9 km are located inside ER16 and at its outer edge respectively.

Table 2.2: Ringlet signatures.

#	Position	Reference of existing Embedded Ringlet	Figure
1	74501-74513	ER1	2.4
2	74527-74544	ER17 (new) 1 km wide	2.7
3	75656-75674	ER2	2.5
4	75790	ER3	
5	75970	ER6	
6	76457-76459	ER18 (new) - 2 peaks - 1 km wide	2.8
7	77644-77662	ER8 (2 peaks)	2.6
8	90130-90200	ER16 (Mimas 3:1 ILR)	

Previous references are from Colwell et al. (2009b).

2.3.3 Waves Near Known Resonances

Most of the power wavelet signatures we observe may be related to propagating waves, and we could expect some of these waves to be associated with particular satellite resonances. The direction of propagation is not always obvious on every reported signature: we observe that the directions derived from decreasing amplitude may not always confirm the direction of decreasing wavelength away from the wave start point. We report the wavelike features

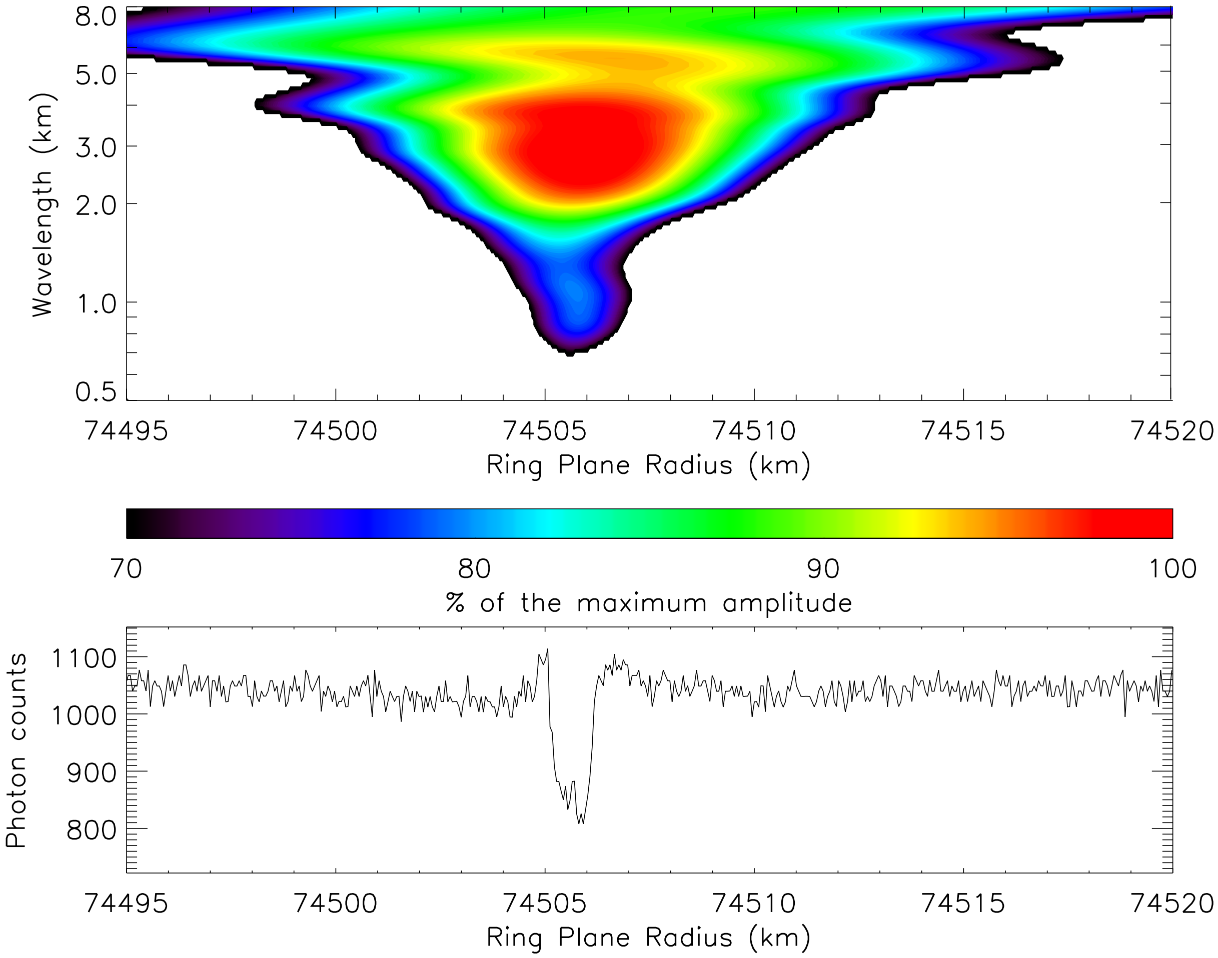

Figure 2.4: WWZ wavelet power profile of embedded ringlet ER1 computed from 62 individual occultation profiles. Lower panel shows the β Centauri, rev. 85 occultation profile. Embedded ringlets produce this characteristic triangular profile in the power contour plots.

in Table 2.3 with their radial extents as measured from the co-added wavelet profiles: we consider the borders of the structure to be delimited by the area where the wavelet power is higher than 85 % of the maximum power of the structure. We also mention potential previous references and possible resonance associations, together with wave starting locations from

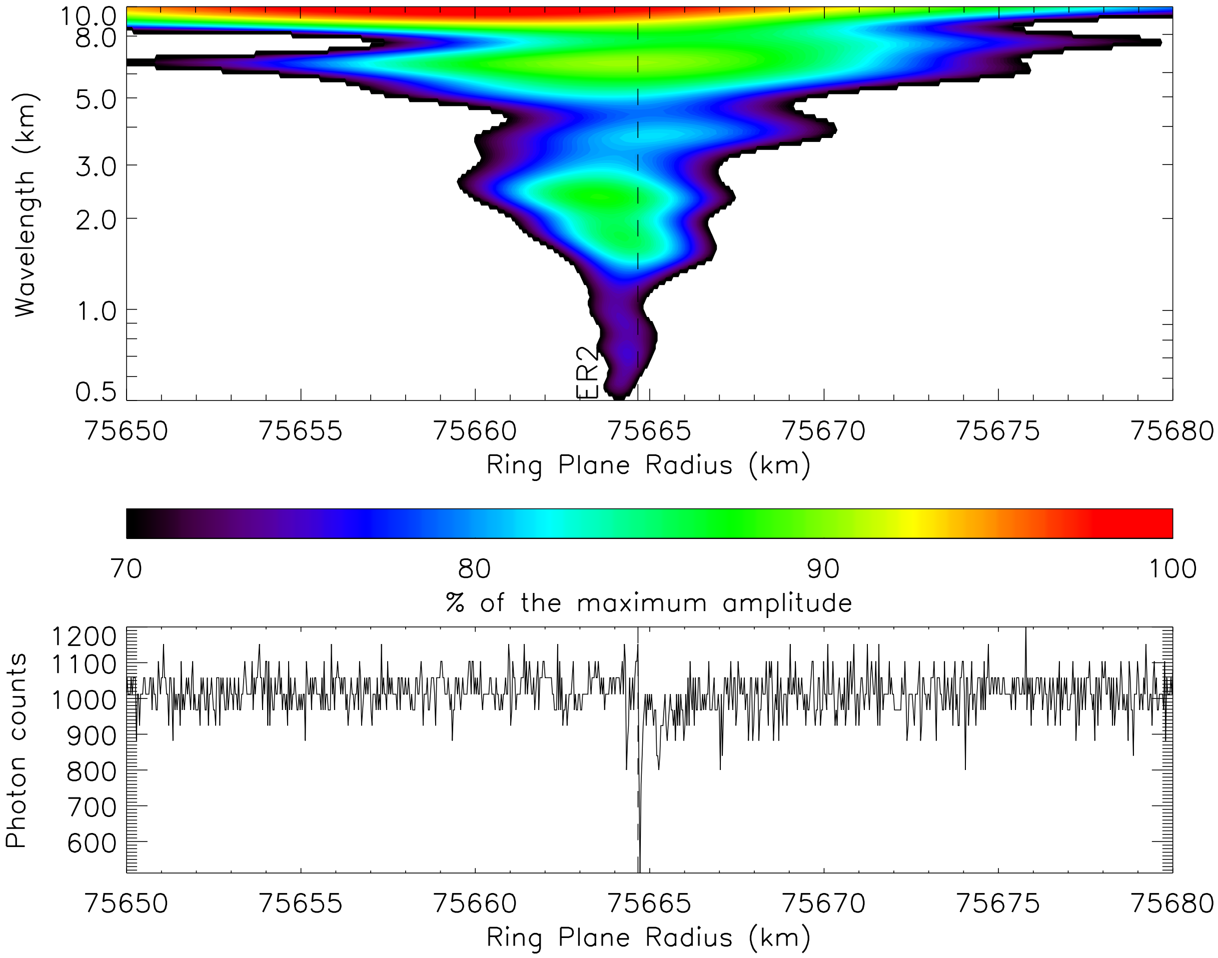

Figure 2.5: Co-added WWZ wavelet power profile of embedded ringlet ER2, computed from individual occultation profiles. Lower panel shows the α Virginis, rev. 34 occultation profile. A clear triangular shape is visible as the resulting signature of embedded ringlet ER2.

our data (for the structures that present an actual chance of being waves). Using the known dispersion relation for the wave, we can extrapolate the position where the wavelength of maximum power is expected to diverge: this position will be referred to as the wave source location and is determined with a precision of the order of a few kilometers, depending on

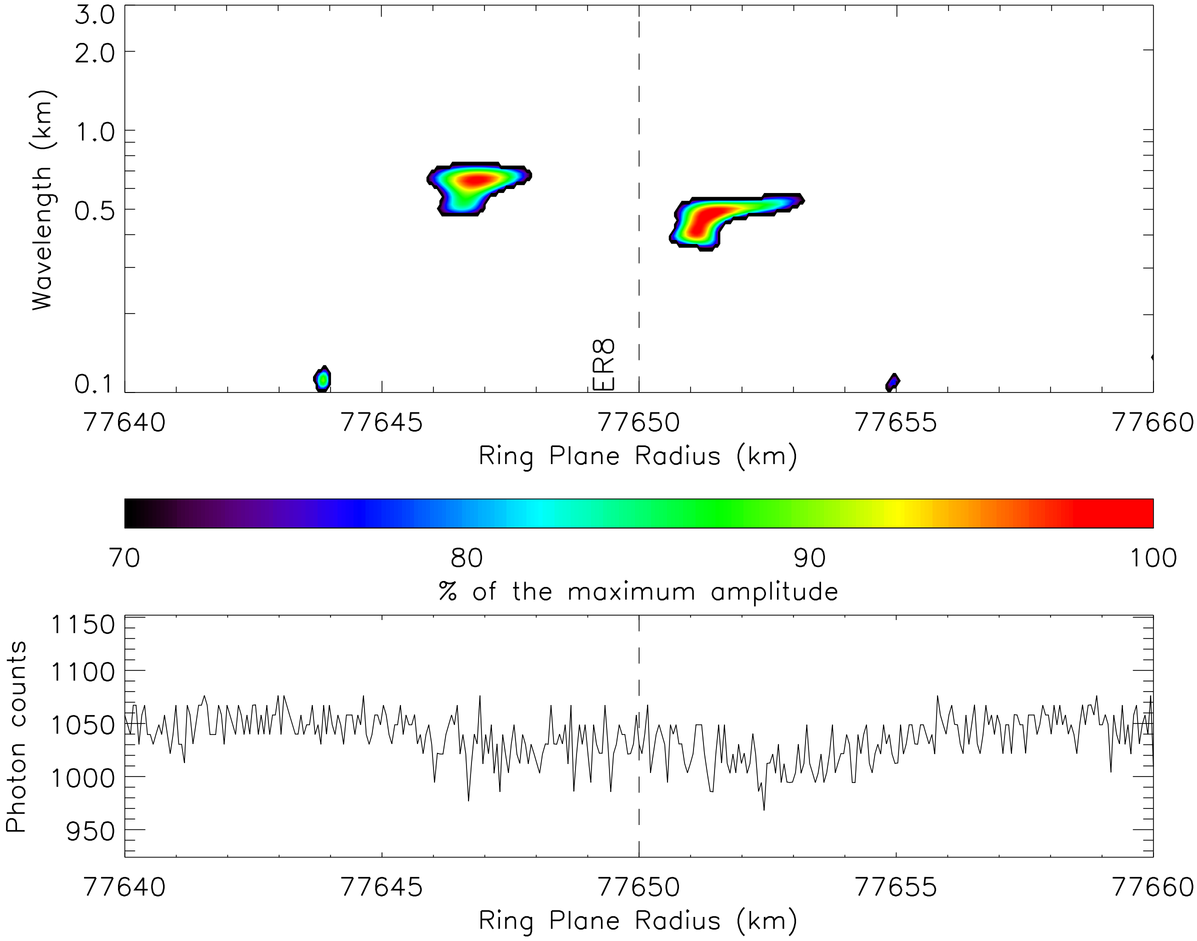

Figure 2.6: Co-added WWZ wavelet power profile of embedded ringlet ER8, computed from individual occultation profiles. Lower panel shows the β Centauri, rev. 85 occultation profile. The double peaks, characteristic of ER8, present clear signatures.

the precision of the wavelength fitting. The distance between these wave source locations and the theoretical resonance locations provides a good test of a resonance association with an observed wave. Details on particular waves are provided below.

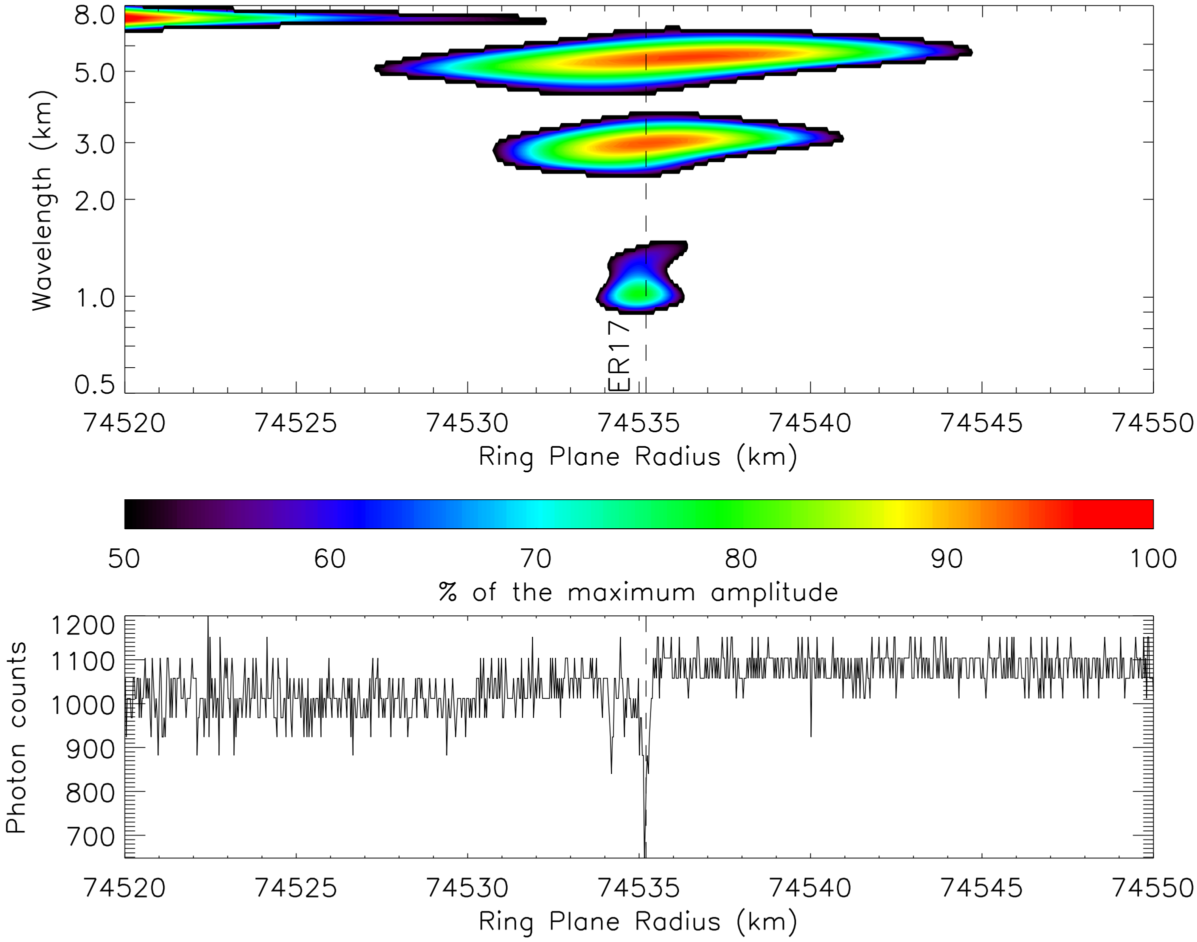

Figure 2.7: Co-added WWZ wavelet power profile of embedded ringlet ER17, computed from individual occultation profiles. Lower panel shows the α Virginis, rev. 30 occultation profile. A clear triangular shape is visible as the resulting signature of embedded ringlet ER17.

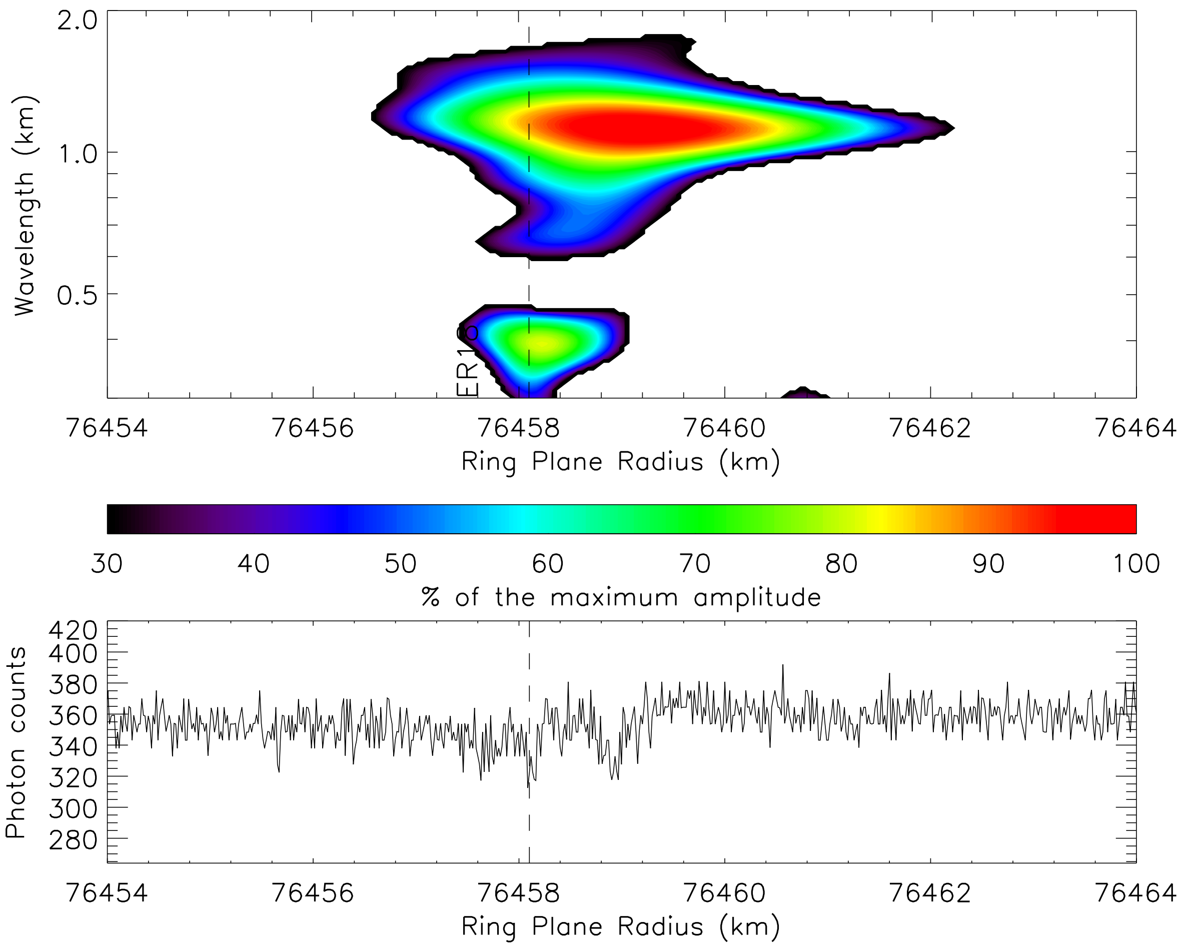

Figure 2.8: Co-added WWZ wavelet power profile of embedded ringlet ER18, computed from individual occultation profiles. Lower panel shows the β Centauri, rev. 104 occultation profile. Two peaks, separated by 0.8 km, are visible on the occultation profile.

Table 2.3: Observed wavelike structures in the C ring.

Feature ID (Figure)	Inner Edge (km)	Outer Edge (km)	Direction of Decreasing Wavelength	Previous Reference	Possible Resonance Association (order)	Theoretical Resonance Location (km)	Wave Source Location (km)
1	74666	74669	Outward	Colwell et al. (2009b)			
2 (2.9)	74891	74900	Outward	Rosen et al. (1991b) (a)	Mimas 4:1 ILR (3)	74891.8	74889.6 ± 1.5
3 (2.16)	74935	74939	Outward	Colwell et al. (2009b)			
4 (2.16)	74940	74946	Outward	Rosen et al. (1991b) (b)			
5	76013	76022	Inward	Colwell et al. (2009b)			
6 (2.17)	76238	76242	Outward	Colwell et al. (2009b)			
7 (2.18)	76380	76500	Inward				
8 (2.18)	76416	76472	Outward				
9 (2.19)	76432	76435	Inward	Colwell et al. (2009b)			
10	76521	76539	Inward				
11 (2.31)	76729	76732		Colwell et al. (2009b)			
12 (2.10)	77524	77544	Outward	Rosen et al. (1991b) (c)	Titan -1:0 IVR BW (3)	77511.3	77509.0 ± 4.5
13 (2.23)	80978	80988	Inward	Rosen et al. (1991b) (e)			
14	81018	81023	Outward				
15 (2.24)	82000	82009	Inward	Colwell et al. (2009b)			
16 (2.26)	82049	82061	Inward	Rosen et al. (1991b) (f)			
17 (2.25)	82196	82209	Inward	Rosen et al. (1991b) (g)			
18	83628	83633	Inward	Rosen et al. (1991b) (h)			
19	84632	84644	Inward	Rosen et al. (1991b) (i)			
20 (2.13)	84821	84829	Outward				
21	84857	84867	Outward				
22 (2.14)	85105	85117					
23 (2.28)	85440	85450	Inward	Rosen et al. (1991b) (j)			
24 (2.20)	85480	85491	Outward	Colwell et al. (2009b)			
25	85505	85514	Inward	Colwell et al. (2009b)			
26	85523	85533	Outward	Colwell et al. (2009b)			
27 (2.21)	85677	85690	Outward	Rosen et al. (1991b) (d)			
28 (2.22)	86400	86452	Outward				
29	86576	86582	Outward				
30	86584	86587	Outward				
31	86595	86601	Outward				
32 (2.29)	87183	87189	Inward	Colwell et al. (2009b)			
33 (2.11)	87645	87651	Outward	Colwell et al. (2009b)	Atlas 2:1 ILR (1)	87646.5	87633.4 ± 4.0
34 (2.34)	88704	88716	Inward				
35	88736	88754	Outward				
36 (2.12)	89889	89898	Outward		Mimas 6:2 ILR (4)	89883.3	89883.5 ± 2.0
37 (2.12)	89900	89911	Outward		Pandora 4:2 ILR (2)	89894.0	89891.9 ± 1.6
38 (2.30)	90143	90156	Inward				
39	90190	90210	Inward				
40 (2.15)	90279	90285	Outward				

For each wavelike feature observed in the C ring, we give the edge locations, the direction of propagation when possible, previous reference (Rosen et al. (1991b) or Colwell et al. (2009b)) and possible resonance association. Finally, we provide wave source locations with uncertainties taking into account both intra and inter occultation uncertainties. See Section 2.4.3.1 for further discussion of resonance associations.

Notes: ILR: Inner Lindblad Resonance, IVR: Inner Vertical Resonance, DW: Density Wave, BW: Bending Wave.

- Around 74891 km, we observe the superposition of a short propagating wave and a ringlet structure signature: the Mimas 4:1 inner Lindblad resonance (Figure 2.9). This feature was identified by Rosen et al. (1991a), who used it to provide a wave-derived estimate of the C ring surface mass density ($\sigma \sim 1 \pm 0.5$ g cm^{-2}), together with a lower bound on the C ring viscosity ($\nu \gtrsim 7.19 \times 10^{-5}$cm^2 sec^{-1}). We derive consistent value of the surface mass density in that vicinity: $\sigma = 0.58$ (± 0.09) g cm^{-2}.

- Wave 12, presented in Figure 2.10, matches the location of the Titan -1:0 nodal resonance, supposed to be located at 77511.3 km, as reported in Rosen et al. (1991a) and analysed in Rosen and Lissauer (1988). As we can see in Table 2.8, the resonant argument parameters prove that this resonance is an inner vertical resonance and therefore we expect to find a bending wave, even if it is propagating outward (since its pattern speed is negative). That vertical property is the reason why the wave is very clearly visible on the α Virginis, rev. 30, occultation. Yet, the amplitude associated with this resonance is one of the largest in the C ring (Rosen and Lissauer, 1988), allowing the wave to appear so clearly on some high-incidence angle occultations such as β Centauri occultations. Titan also has another resonance in the C ring: an apsidal 1:0 resonance around 77846 km, which would not result in a clear wave because it is located in the Colombo Gap but which could be the origin of that ringlet (Lissauer and Cuzzi, 1982).

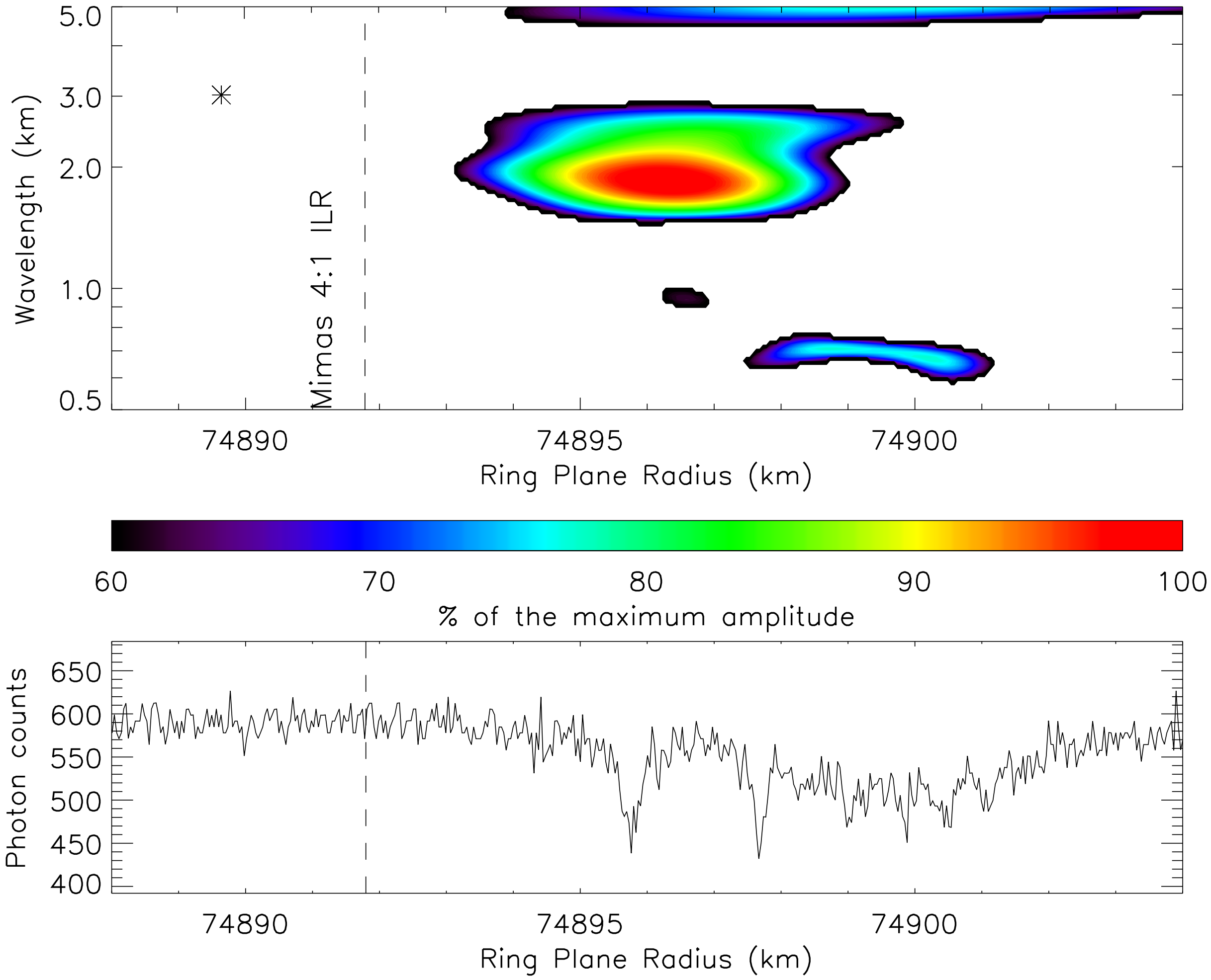

Figure 2.9: WWZ wavelet power profile around the Mimas 4:1 inner Lindblad resonance (r_L = 74891.9 km, marked by the vertical dashed line), computed from β Centauri, rev. 75 individual occultation profile. The possible superposition with a ringlet structure is disturbing our perception of the direction of propagation. The asterisk locates the position of the observed wave source.

- Wave 33 (Figure 2.11) appears to be associated with the Atlas 2:1 inner Lindblad resonance at 87646.5 km. However, the dispersion of wave 33 is smaller than expected for the location of the Atlas 2:1 ILR making this association tentative.

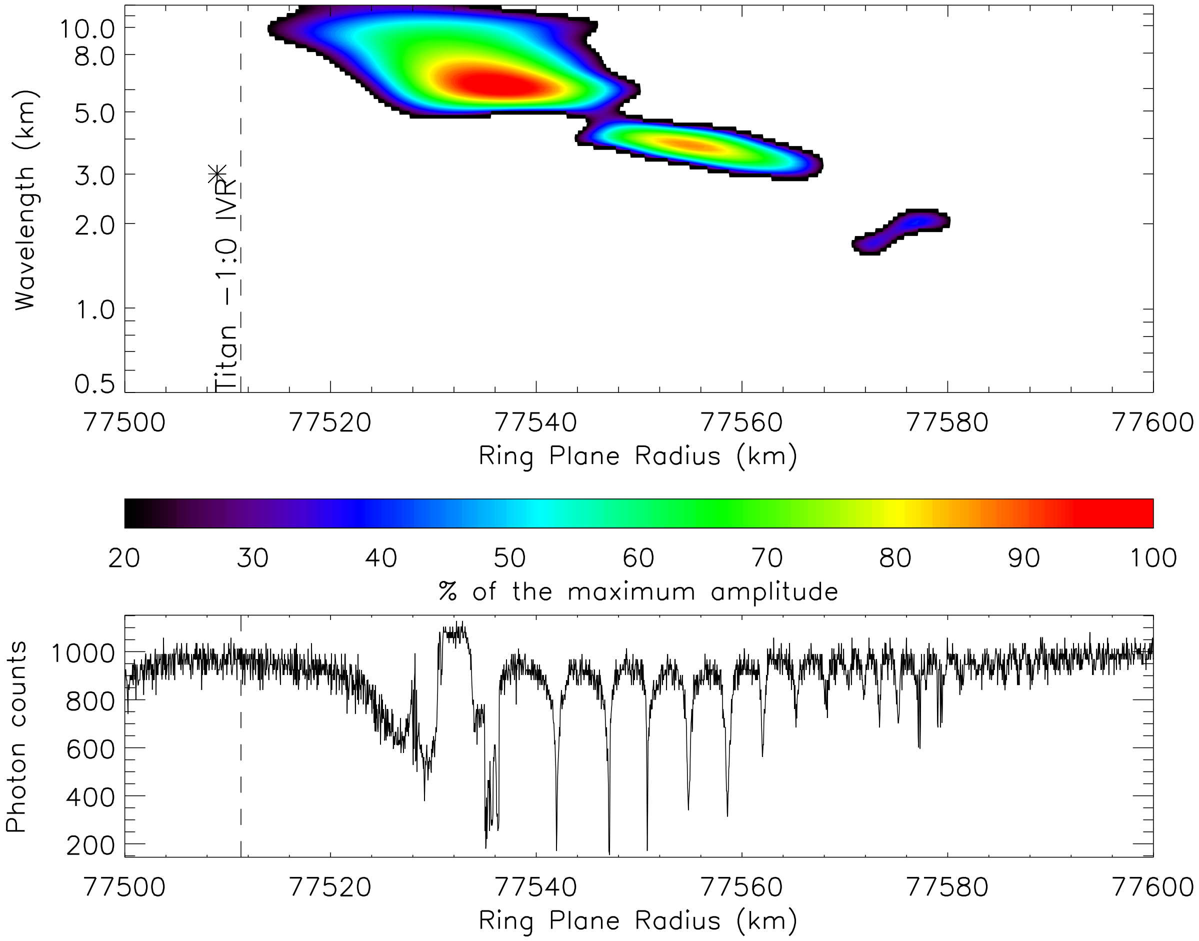

Figure 2.10: WWZ wavelet power profile of wave 12, computed from α Virginis, rev. 34 individual occultation profile. Titan -1:0 nodal resonance at 77511.3 km (vertical dashed line) excites an outward propagating wave. The asterisk locates the position of the observed wave source.

- Wave 36 and 37 are separated by only 10 km (Figure 2.12). These two waves are propagating outward and could be associated with resonances. Indeed, the 89889 km wavetrain matches the Mimas 6:2 inner Lindblad resonance at 89883.3 km while the

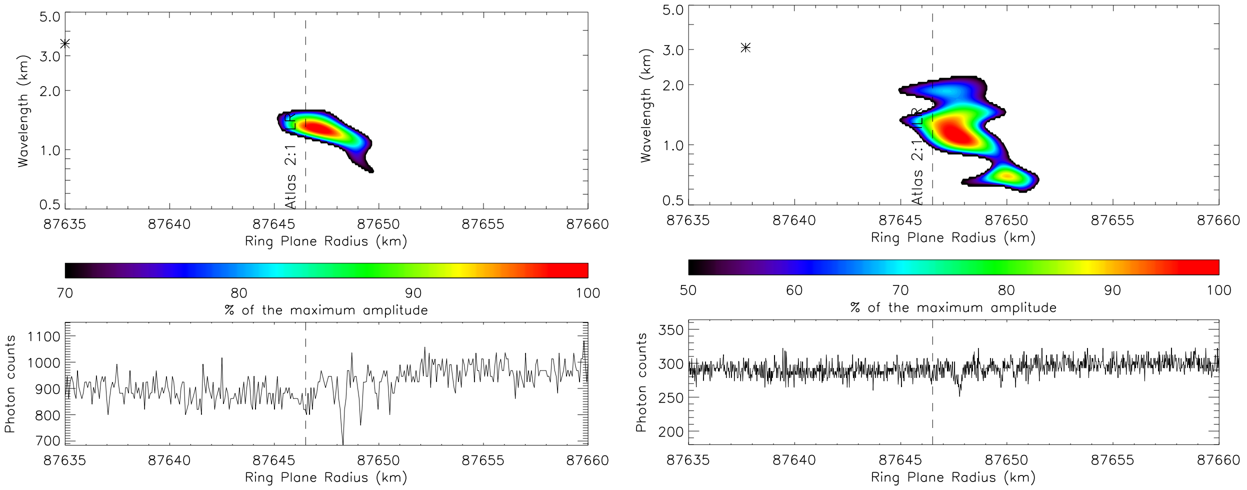

Figure 2.11: WWZ wavelet power profile of wave 33, computed from α Virginis, rev. 34 (left) and β Centauri, rev. 105 (right) individual occultation profiles. The Atlas 2:1 ILR (at 87646.5 km - vertical dashed line) has a greater torque than the Pan 2:1 ILR which does not seem to excite a wave at 85105 km. The asterisks locate the positions of the observed wave sources. Profiles of this wave consistently show a dispersion that places the wave source several km interior to the wave feature and the theoretical location of the Atlas 2:1 ILR.

89900 km wave fits the Pandora 4:2 inner Lindblad resonance which is located at 89894.0 km. The Mimas 3:1 ILR is supposed to be stronger than the Mimas 4:1 ILR and Mimas 6:2 ILR (Table 2.7). We would therefore expect to observe a clearer wave at its location around 90195 km. However, this location coincides with the outer edge of the embedded ringlet ER16 and with observed feature 39. However, this structure is not clearly propagating and we cannot derive physical properties of the ring from this feature. We could also expect to observe waves associated with the Pandora 2:1 ILR which is supposed to be stronger than the Pandora 4:2 ILR. That wave would actually be located at 90165 km, fitting the position of feature 38, close to the previously mentioned Mimas 3:1 ILR. Whether ER16 is created by this resonance or not, its presence prevents identification of any wave there. Pandora's orbit parameters being very similar to the ones of Prometheus, we can also expect to observe waves associated with Prometheus resonances. Feature 34 is actually very close to the Prometheus 2:1 ILR located at 88712.9 km, in the ringlet R4. We observe periodic features in R4 but could not estimate a direction of propagation for this signal. The Prometheus 4:2 ILR is also located close to a ringlet (inner edge of ER15) around 88298 km, while the Prometheus 4:2 IVR is at the outer edge of the Maxwell Ringlet (at 87589 km). The presence of these embedded ringlets at the locations of resonances is suggestive of a causal link, but we can only point out the associations here. Nevertheless, it strengthens our confidence in the identification of waves 36 and 37 with the Mimas 6:2 ILR and Pandora 4:2 ILR that the stronger first-order counterparts of those resonances do have ring features associated with them.

- The direction of propagation of feature 20 is not very clear, but appears to be outward from Figure 2.13. The Pan 4:2 inner Lindblad resonance at 84814.5 km could be a match for that structure, which is 7 km exterior. However, the length of that distance, compared to the length of the structure itself, raises the concern of a chance association.

In order to estimate the chance of a coincidental match between a wave location and a resonance location, we performed the following simple statistical test. We estimate the probability p that drawing Q random numbers for r between 74000 and 92000 km, N

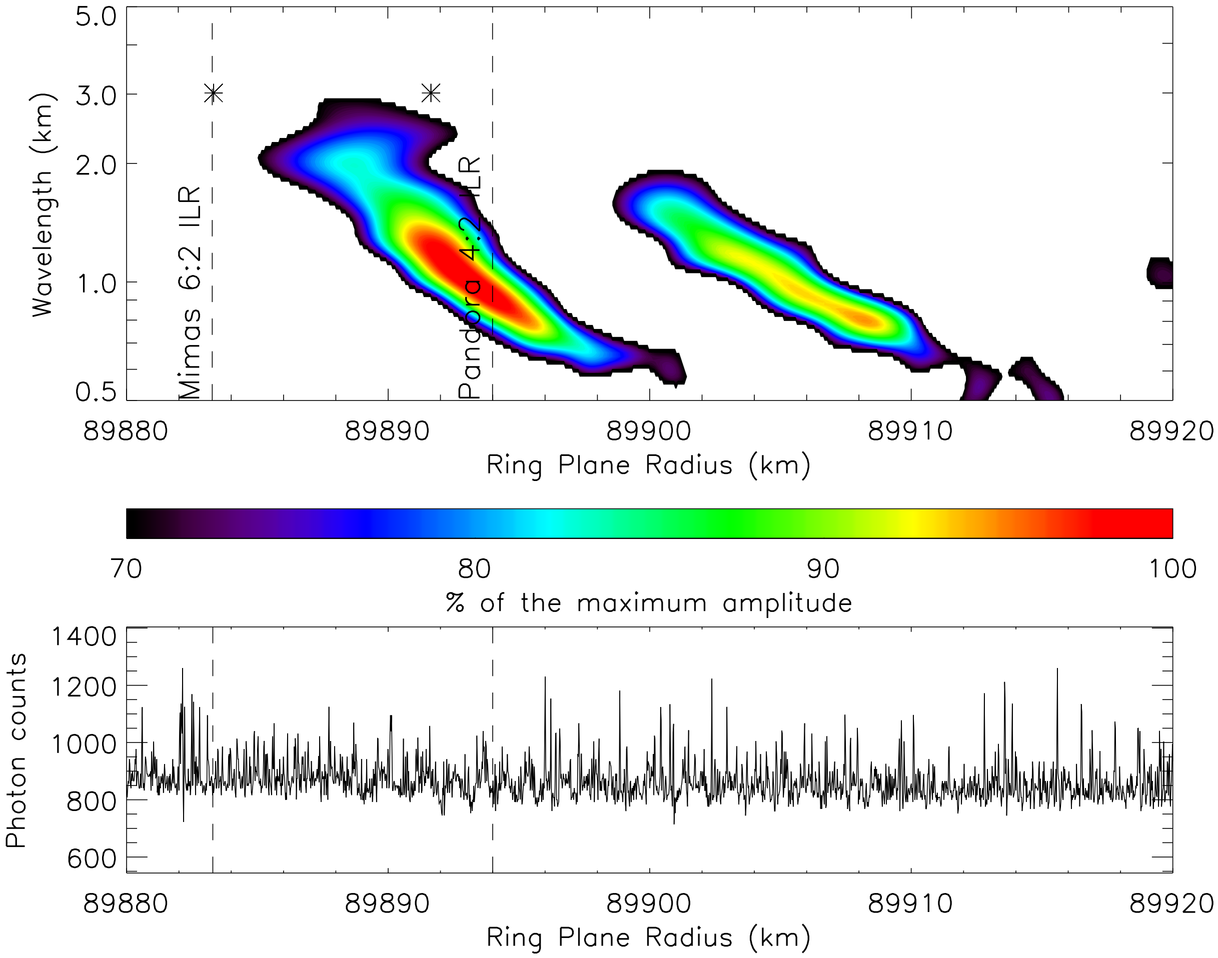

Figure 2.12: Co-added WWZ wavelet power profile of waves 36 and 37, computed from co-added wavelet profiles. Mimas 6:2 ILR is at 89883.3 km and Pandora 4:2 ILR is at 89894.0 km, pointed by the vertical dashed lines. Lower panel shows the β Centauri, rev. 85 occultation profile. The almost 3:2 corotation resonance between Mimas and Pandora explains the proximity of these two waves. The asterisks locate the positions of the observed wave sources with uncertainties lower than 1 km.

of them show up within X km of one of the W $\mathrm{n^{th}}$-order resonances. N is the number of waves we associate with $\mathrm{n^{th}}$-order resonances and X is the radial separation between the starting point of a wave and the theoretical location of an $\mathrm{n^{th}}$-order resonance that we associate with that wave. We uniformly pick Q random positions in the range of width L. Considering one isolated pick, the probability p' that one random position is within X km of a specific position is $p' = \frac{2X}{L}$. Considering one isolated pick, the probability $p"$ that one random position is within X km of W specific positions is $p" = Wp'$. Considering Q picks, the probability pp that exactly i of them are within X km of W specific positions is

$$pp(i) = C_Q^i p"^i (1 - p")^{(Q-i)} \tag{2.7}$$

Therefore, the probability p that at least N of them are within X km of W specific positions is

$$p = \sum_{i=N}^{Q} pp(i) \tag{2.8}$$

ie

$$p = \sum_{i=N}^{Q} C_Q^i \left(\frac{2WX}{L}\right)^i \left(1 - \frac{2WX}{L}\right)^{(Q-i)} \tag{2.9}$$

where $L = 92000 - 74000$ km and $Q = 40$

Concerning the possible association of the Pan 4:2 inner Lindblad resonance with feature 20, we measure a wave source location at 84775 ± 8 km (39.5 km interior to the resonance location). Our catalog of second-order inner Lindblad resonances in the C ring was narrowed to 14 potential resonances ($W = 14$). Therefore, the probability that a second-order inner Lindblad resonance will come within 39.5 km of one of the outward propagating waves is higher than 87%. This Pan 4:2 ILR association appears less reliable than the closer ones.

Besides, if that structure was really associated with the Pan 4:2 ILR, we should expect to see the Pan 2:1 ILR at 85105 km, but the corresponding observed feature 22 is located between the plateaus P5 and P6 (Figure 2.14), in a region of very diffuse material, similar to the region of the Atlas 2:1 ILR, and we cannot estimate a privileged direction of propagation. Therefore, this cannot constitute a proof of this association.

- Finally, Tiscareno et al. (2007) already rejected the possible association of feature 40 with the Tethys 6:1 inner Lindblad resonance at 90279.6 km (Figure 2.15). Besides, the estimated strength (torque) of the Tethys 6:1 ILR is much lower than for many resonances that do not excite waves. In addition, the measured wave source location for this feature is located at 90240 km. Then, we estimate the probability of finding such a fifth-order resonance by chance in a vicinity of 39.6 km around feature 40 to be about 1.

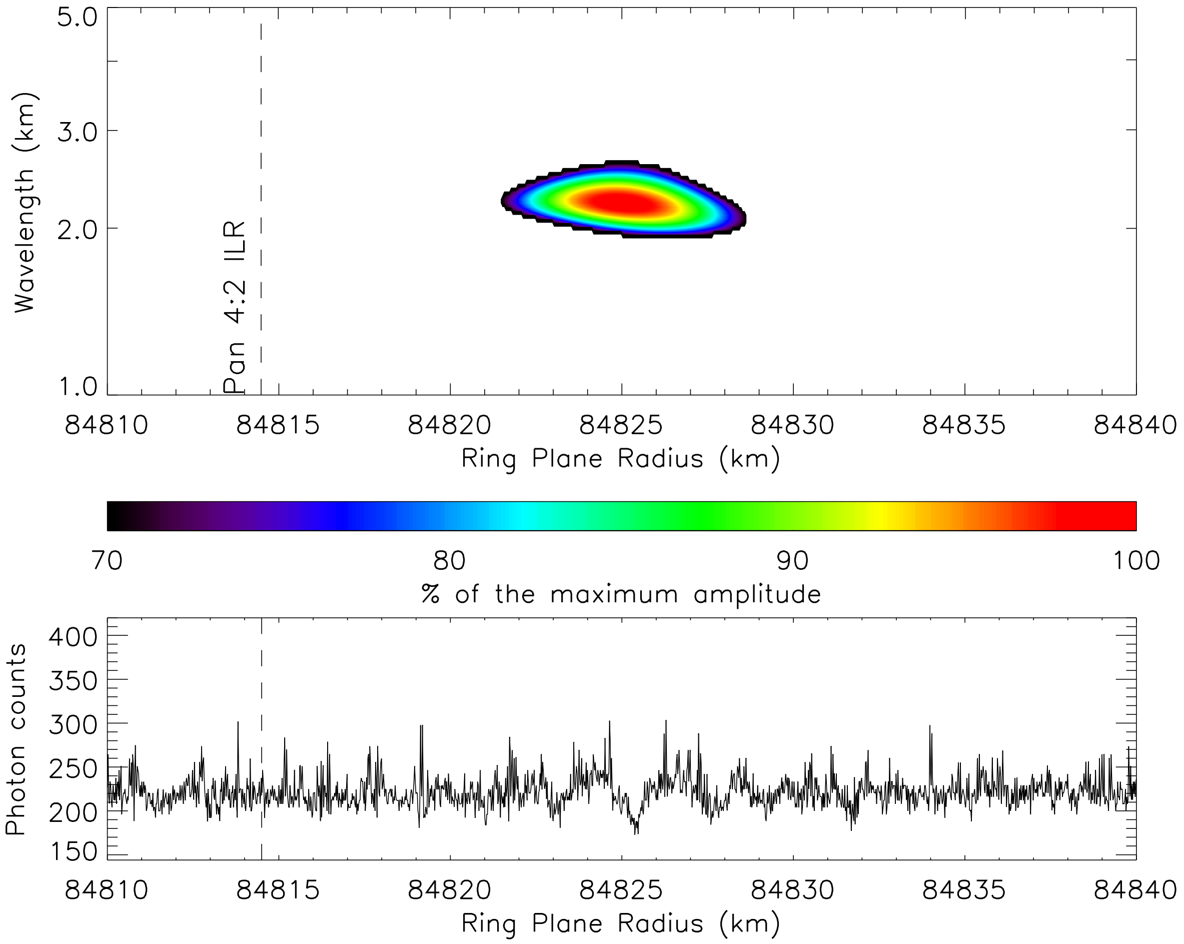

Figure 2.13: WWZ wavelet power profile of feature 20, computed from β Centauri, rev. 104 individual occultation profile. Pan 4:2 ILR is at 84814.5 km (vertical dashed line). The relatively long distance between the Pan 4:2 ILR and the wave (about the same distance as the length of the wave itsself) together with a very low torque value for this resonance and an inconsistent wave source location from the feature invalidate the possibility of an association. Wave source location is outside the range of this figure, at 84775 ± 8 km.

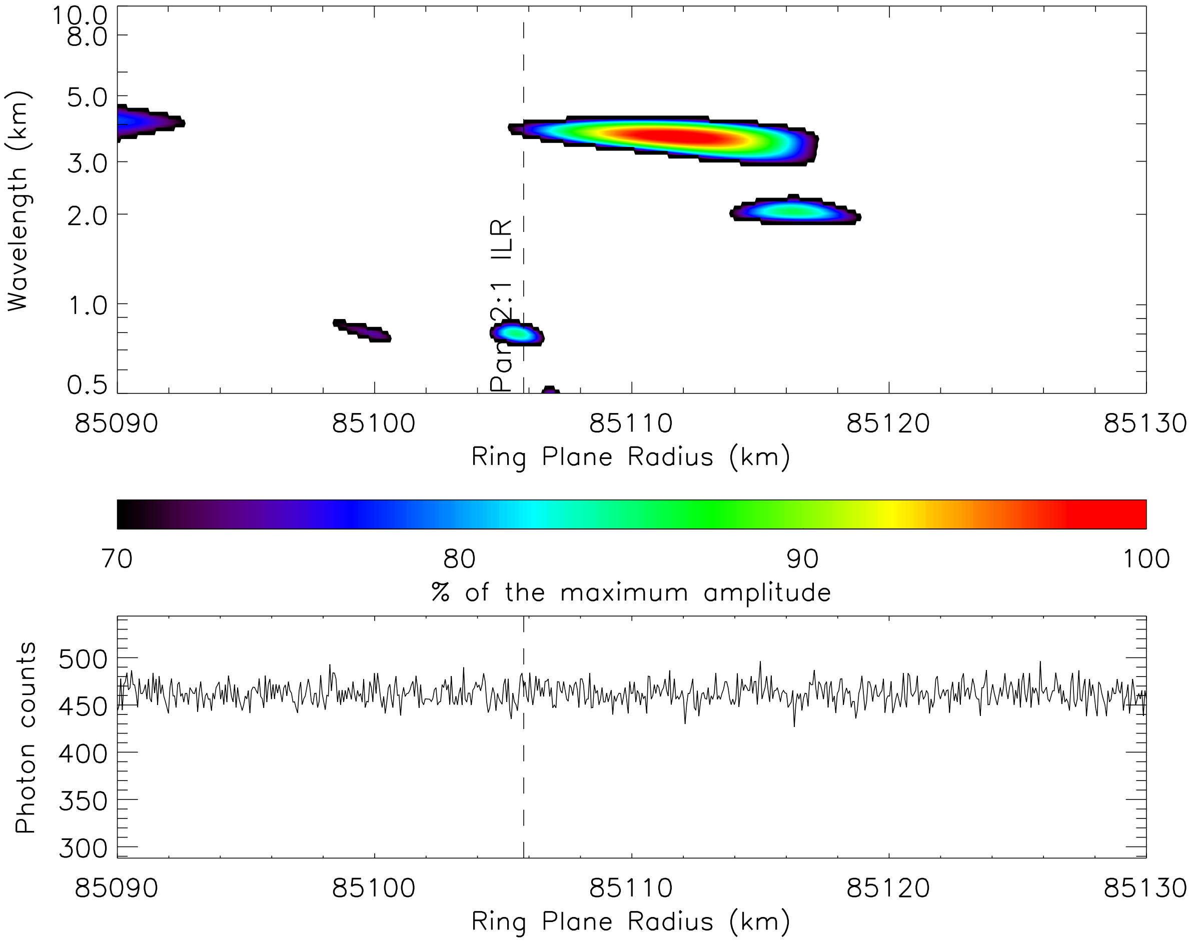

Figure 2.14: WWZ wavelet power profile of structure 22, computed from β Centauri, rev. 89 individual occultation profile. Pan 2:1 ILR is at 85105.8 km (vertical dashed line). No obvious direction of propagatiom can be determined from diverse occultations. Wave source location is outside the range of this figure, at 84989 ± 20 km.

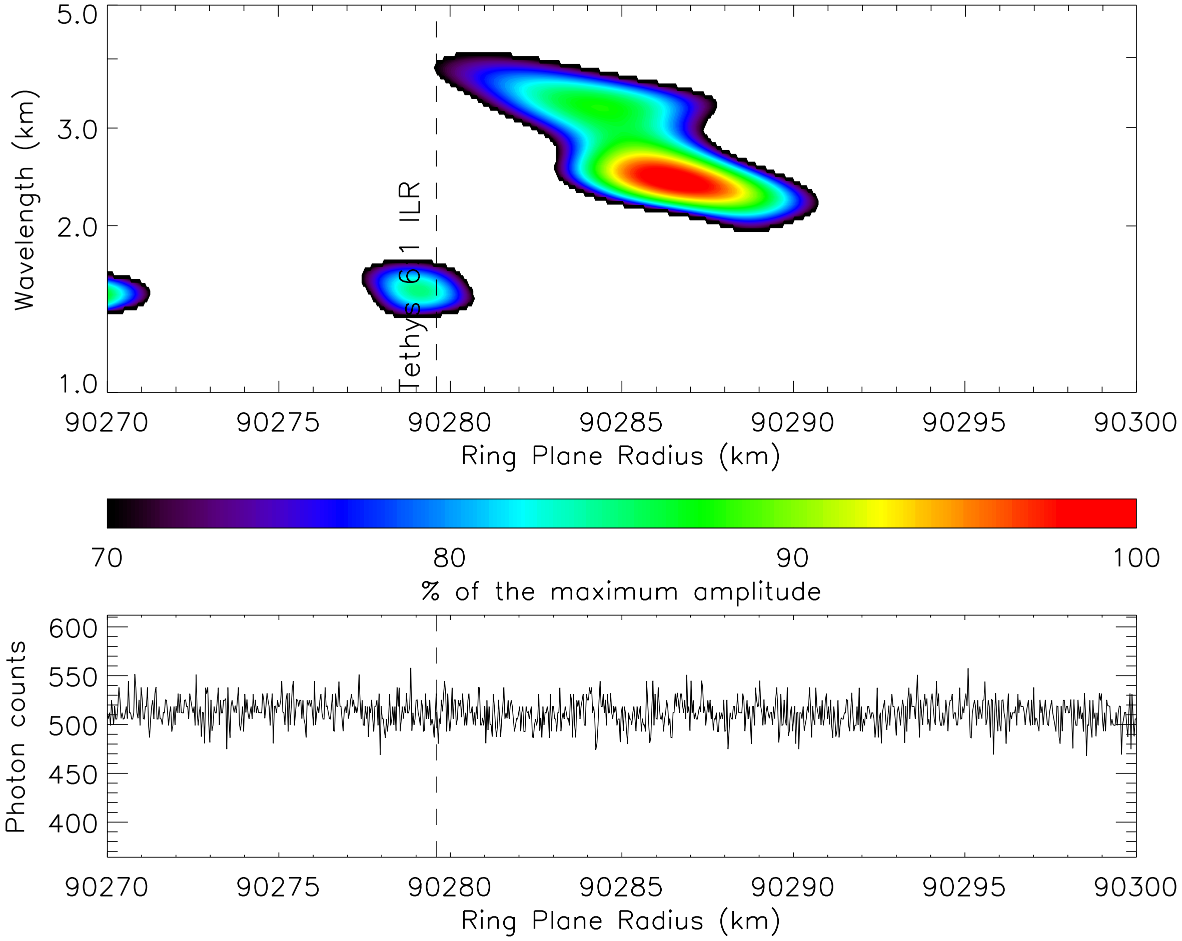

Figure 2.15: WWZ wavelet power profile of feature 40, computed from β Centauri, rev. 81 individual occultation profile. Tethys 6:1 ILR is at 90279.6 km (vertical dashed line). Its calculated strength is very low, suggesting that this is a chance association (Tiscareno et al., 2007). Wave source location is outside the range of this figure, at 90238.5 ± 2.5 km.

2.3.4 Other Wavelike Signatures

2.3.4.1 Outward Propagating Signatures

- Structures 3 and 4 are shown in Figure 2.16. A 4 km wide embedded ringlet appears in β Centauri occultations and seems to disturb the region but the α Virginis is very clear. As shown in Table 2.3, the inner structure has been reported by Colwell et al. (2009b), whereas the outer one was mentioned by Rosen et al. (1991a). Our resonance catalog (Table 2.7) indicates we should not expect many low order resonances at these locations in the C ring, and even the Daphnis 5:2 ILR at 74923 km is quite far from feature 3 (12 km interior).
- Sometimes, even outward propagating waves are more obvious on low incidence angle occultations, as is the case for structure 6 (Figure 2.17).
- Structures 7 and 8 (Figure 2.18) appear to be coexisting around the same location as feature 9 (Figure 2.19), though we cannot state that structures 7 and 8 are propagating like waves. Indeed, we observe a structure at wavelengths around 25 km (wavelike feature 7), then we see another one at a wavelength around 12 km (structure 8), and finally, we distinguish a clear inward feature at smaller wavelengths, around 1 km (structure 9).
- Structure 21 is easily visible in β Centauri occultations, and propagates outward.

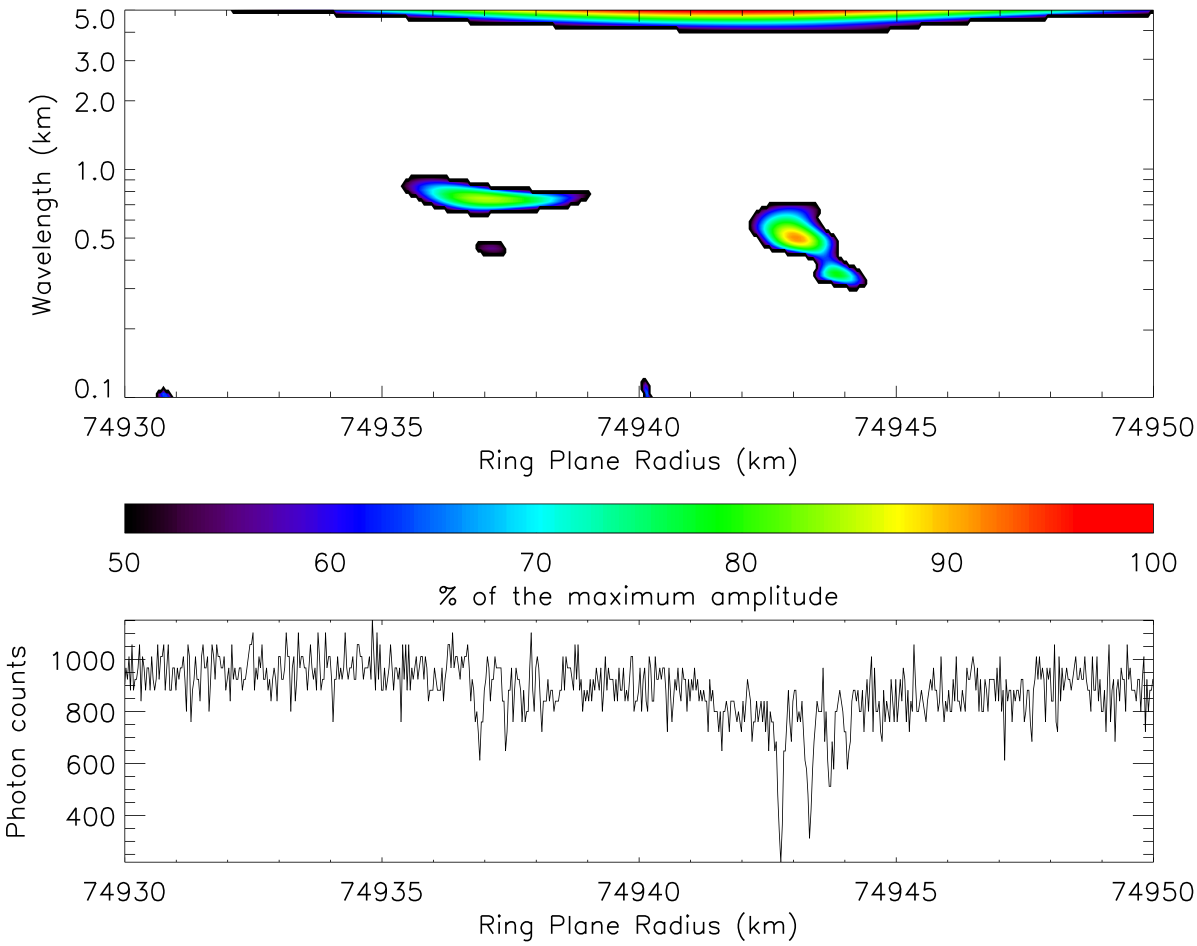

Figure 2.16: WWZ wavelet power profile of structures 3 and 4, computed from α Virginis, rev. 30 individual occultation profile.

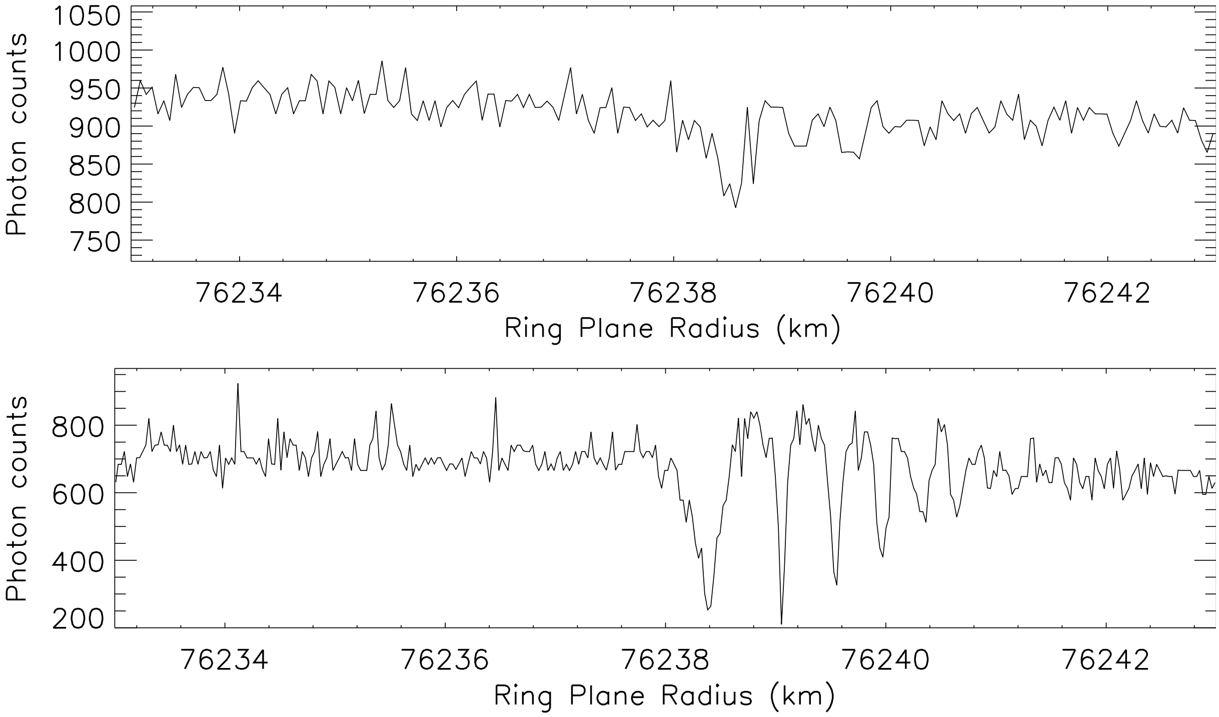

Figure 2.17: Photon count rates of feature 6, computed from β Centauri, rev. 85 (top) and α Virginis, rev. 34 (bottom) individual occultation profiles. Feature 6 is clearly propagating outward though it is more prominent in the low-B incidence angle α Virginis occultation.

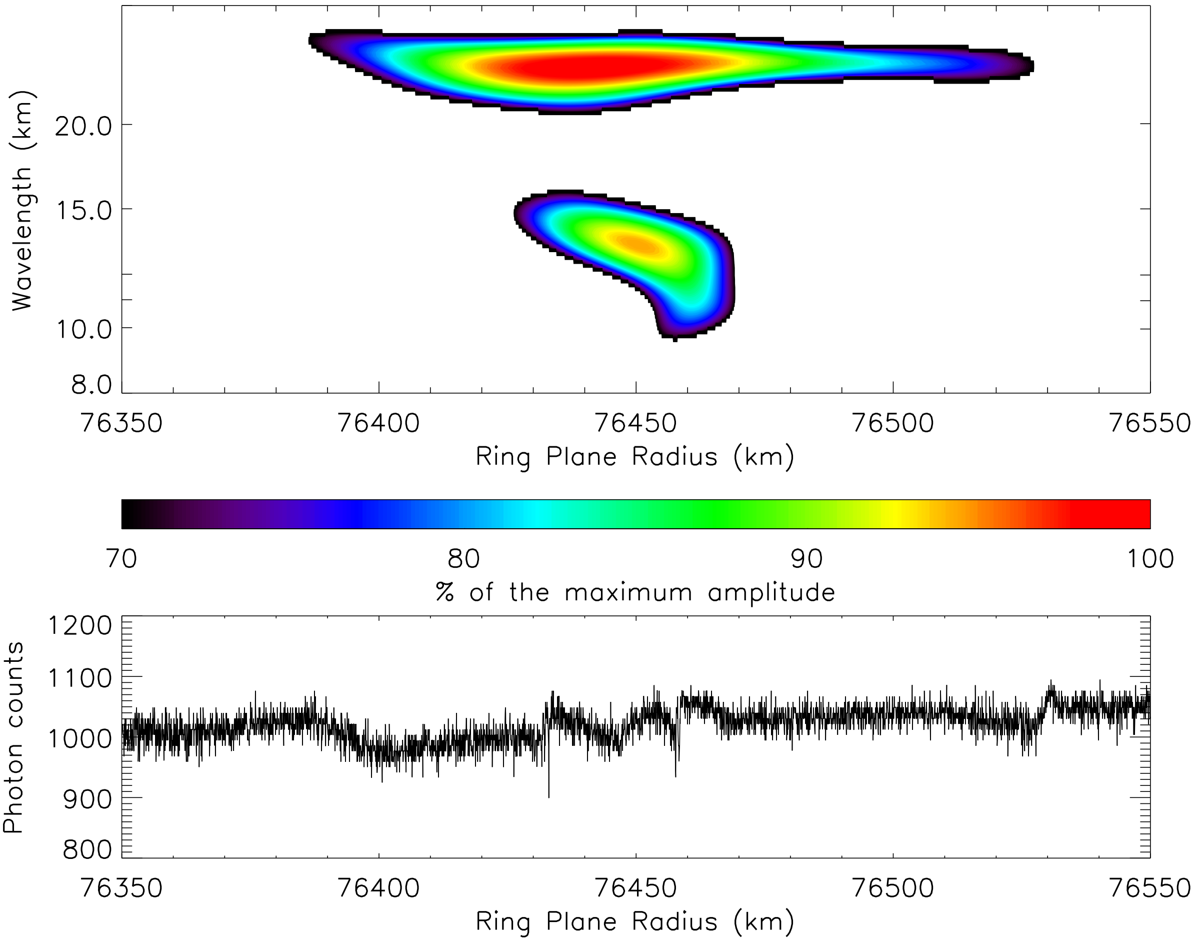

Figure 2.18: WWZ wavelet power profile computed from β Centauri, rev. 85 individual occultation profile showing structures 7 and 8 coexisting at the same location. Figure 2.19 gives more details about the central region where structure 9 is located.

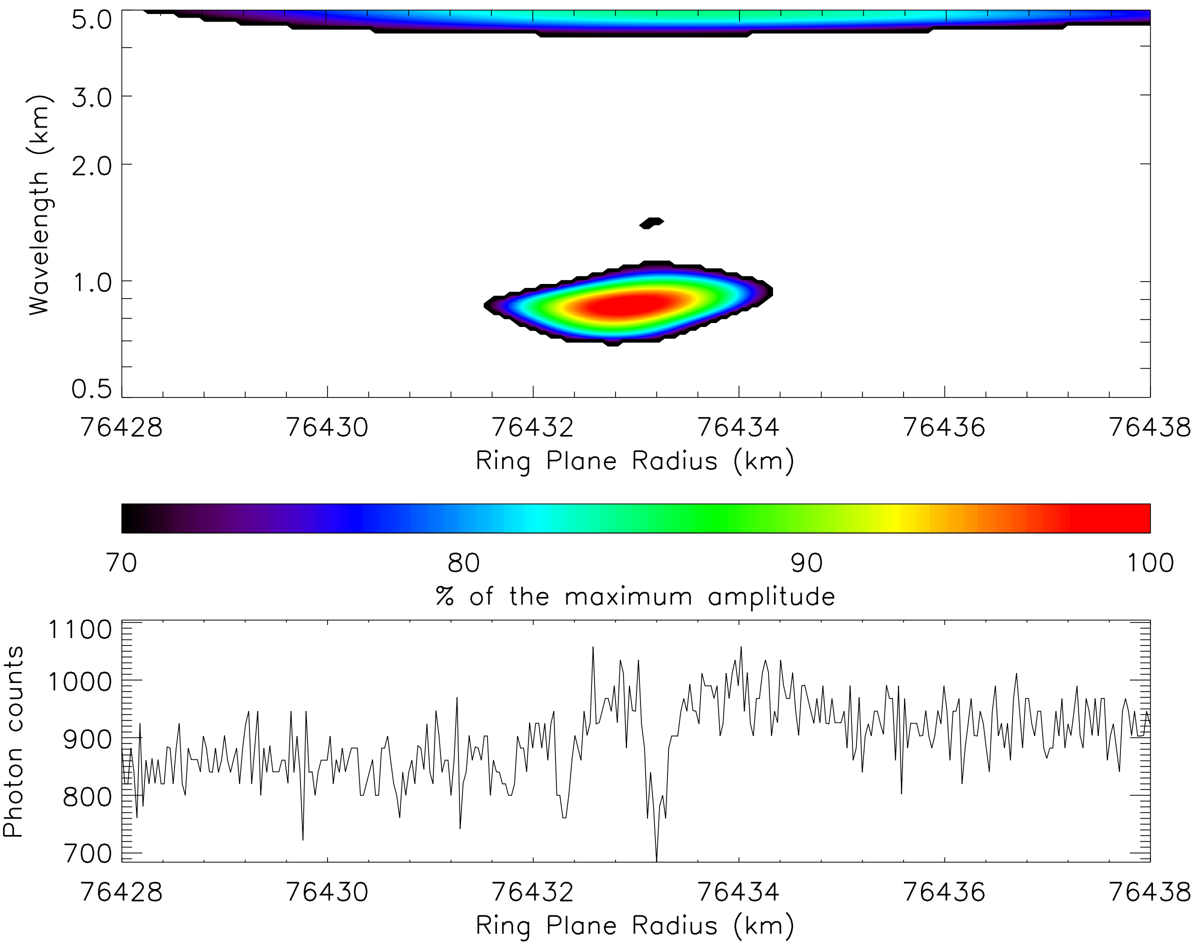

Figure 2.19: WWZ wavelet power profile computed from α Virginis, rev. 34 individual occultation profile showing feature 9, propagating inward.

- Structure 24 (Figure 2.20), from Colwell et al. (2009b), presents the peculiarity that it seems to propagate outward and yet it is only visible at low incidence angles, such as on ζ Orionis.

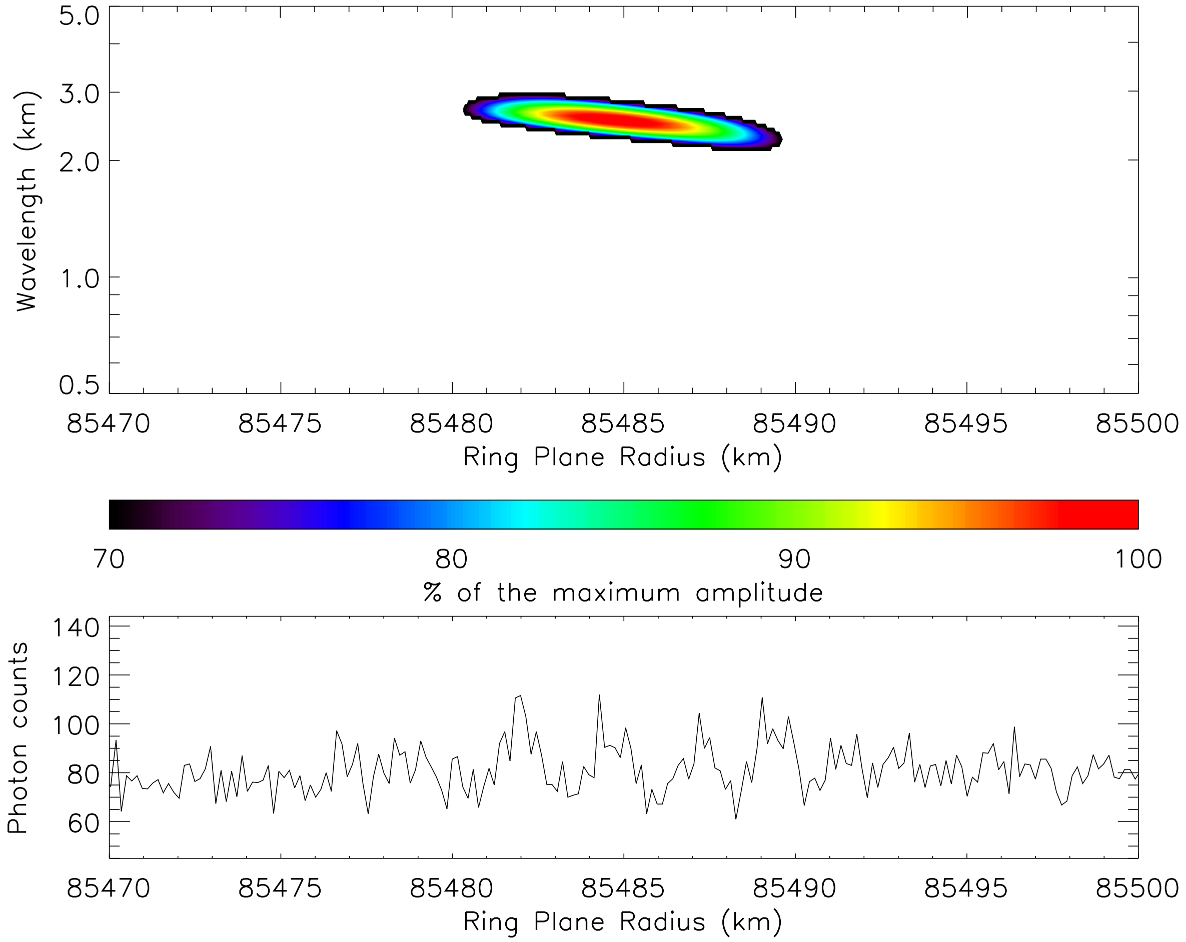

Figure 2.20: WWZ wavelet power profile of structure 24, computed from ζ Orionis, rev. 47 individual occultation profile. Feature 24 is located between plateaus P5 and P6.

- Structure 27 (Figure 2.21) is one of the most extended features that we observed in the C ring. This feature is clearly propagating outward. Yet, no low order inner Lindblad resonance could be found in this neighborhood.

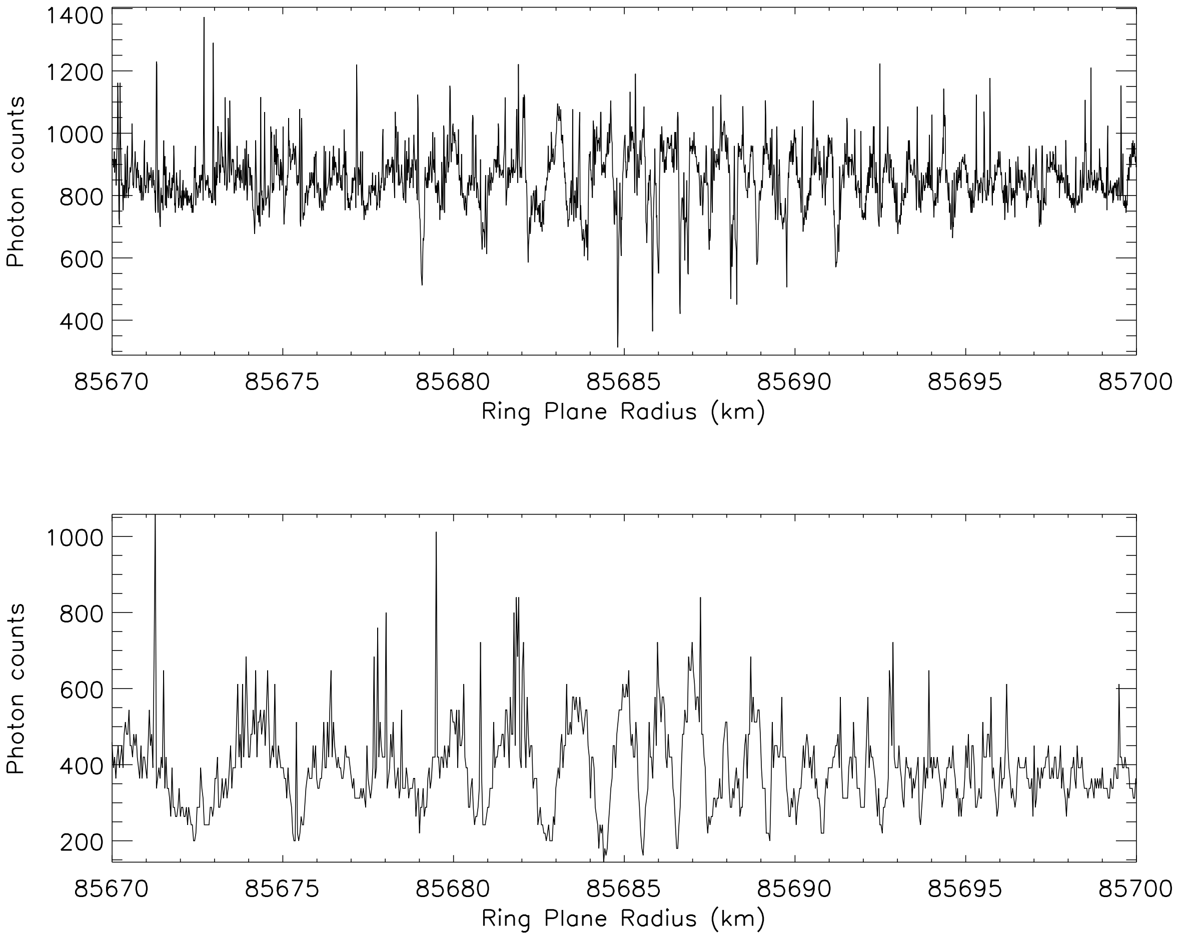

Figure 2.21: Individual occultation profiles of β Centauri, rev. 64 (upper panel) and α Virginis, rev. 30 (lower panel) showing feature 27, clearly propagating outward.

- Structure 28 (Figure 2.22) is certainly the second-most extended one that we found in the C ring, after the Titan -1:0 nodal resonance. This is a 52-km-long outward propagating wavetrain in the plateau P7 (Colwell et al., 2009b) at 86400 km. This feature is actually most prominent in UVIS occultations of stars at high incidence angle (large B angles, Table 2.1) suggesting that it is not a bending wave but instead represents variations in particle packing with radius like in a density wave. Yet, no low order resonance with any known moon is expected at the location of this wavetrain.

Assuming that structure 28 is corresponding to a density wave with an azimuthal parameter m, of order N, we can determine the position of a putative moon in order to create such a wave. Table 2.4 provides the semi-major axes of these moons. Considering the locations that are outside the main rings system, none matches the actual position of a satellite. Moons located in the A ring do not belong to the "propeller belts" as identified by Tiscareno et al. (2008) between 126750 km and 132000 km and therefore are less likely to exist without being already known. The B ring is obviously not hosting such a moon. We then explore the remaining possibility; that structure 28 would be a density wave excited by an 8:5 ILR with a moon located in the Huygens gap at 117636 km. This could coincide with the detection of 1 km-wavelength signatures in the Huygens ringlet: we indeed show in Chapter 4 that a moon located in the Huygens gap, within 200 km away from the Huygens ringlet, could generate wakes in this ringlet. However, a moon at 117636 km would also excite density waves associated with a 2:1 ILR at 75200.5 km and a 3:1 ILR at 90261.1 km in the C ring. The fact that such density waves are not observed invalidates this Huygens gap moon as the origin of structure 28.

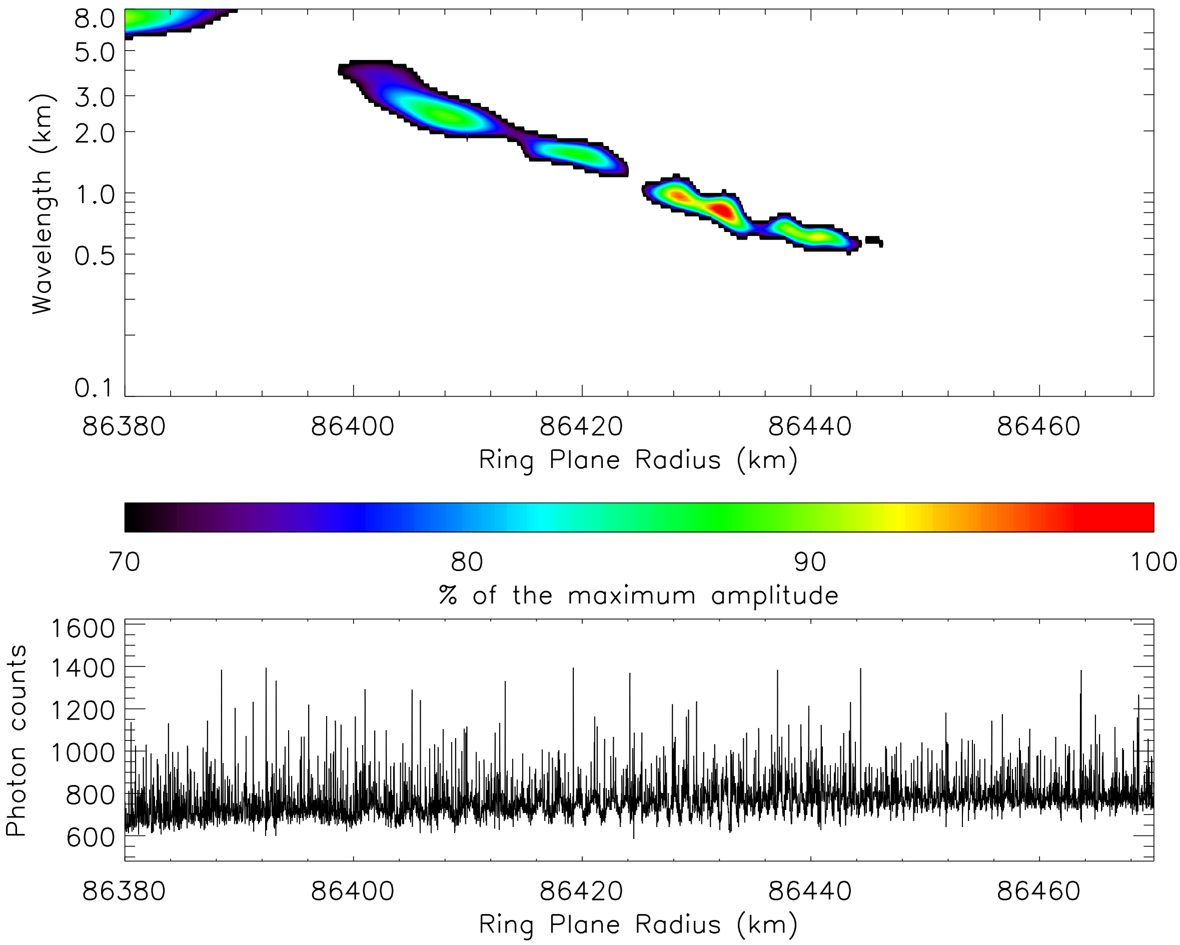

Figure 2.22: Co-added WWZ wavelet power profile of structure 28, computed from individual occultation profiles. Lower panel shows the β Centauri, rev. 89 occultation profile. Structure 28 is the most extended feature observed in the C ring, but there is no low order resonance in its vicinity.

Table 2.4: Potential moons.

	$N = 1$		$N = 2$		$N = 3$	
	ILR	a_{moon}	ILR	a_{moon}	ILR	a_{moon}
$m = 2$	2:1	135664	3:1	177535	4:1	215001
$m = 3$	3:2	112545	4:2	136123	5:2	157866
$m = 4$	4:3	104234	5:3	120764	6:3	136276
$m = 5$	5:4	99940	6:4	112691	7:4	124793
$m = 6$	6:5	97315	7:5	107700	8:5	117636
$m = 7$	7:6	95543	8:6	104306	9:6	112740

Positions of potential moons that would present an N^{th}-order resonance with an azimuthal parameter m generating a density wave at 86400 km. An uncertainty of 5 km has been estimated from the application of the same process in the determination of real moon loations, given the resonance position.

2.3.4.2 Inward Propagating Signatures

- Structure 13 (Figure 2.23) is clearly propagating inward both in the β Centauri and α Virginis occultations.

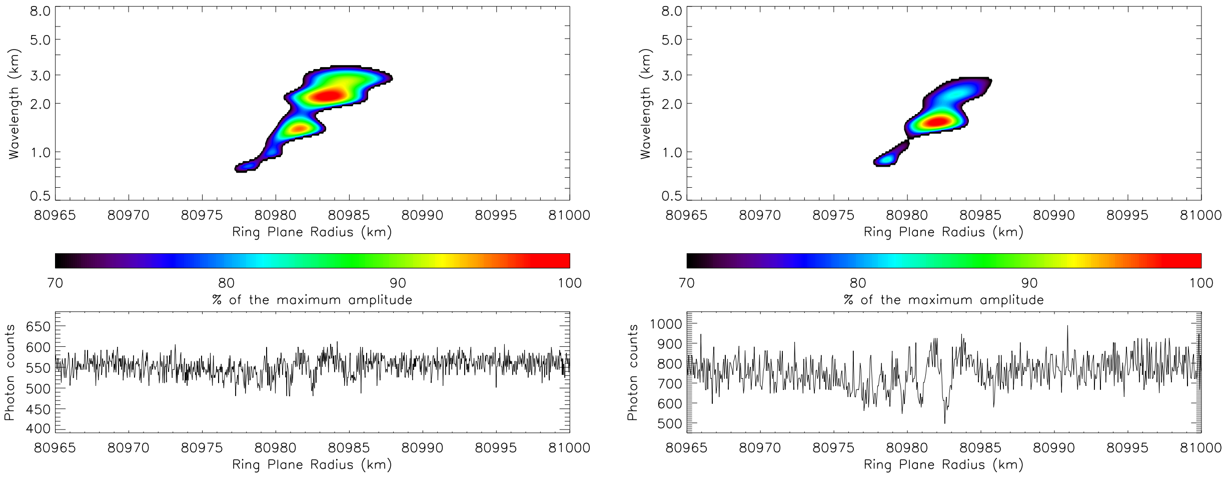

Figure 2.23: WWZ wavelet power profile of structure 13, computed from individual occultation profiles of β Centauri, rev. 77 (left) and α Virginis, rev. 34 (right). Structure 13 is clearly propagating inward on both high incidence and low incidence occultations.

- Structure 15 (Figure 2.24), from Colwell et al. (2009b), appears to propagate inward on every occultation; the wwz profile in Figure 2.24 shows the co-added wavelet profiles of all β Centauri occultations as well as the low-incidence-angle occultation ζ Orionis ($B = 2.66°$).

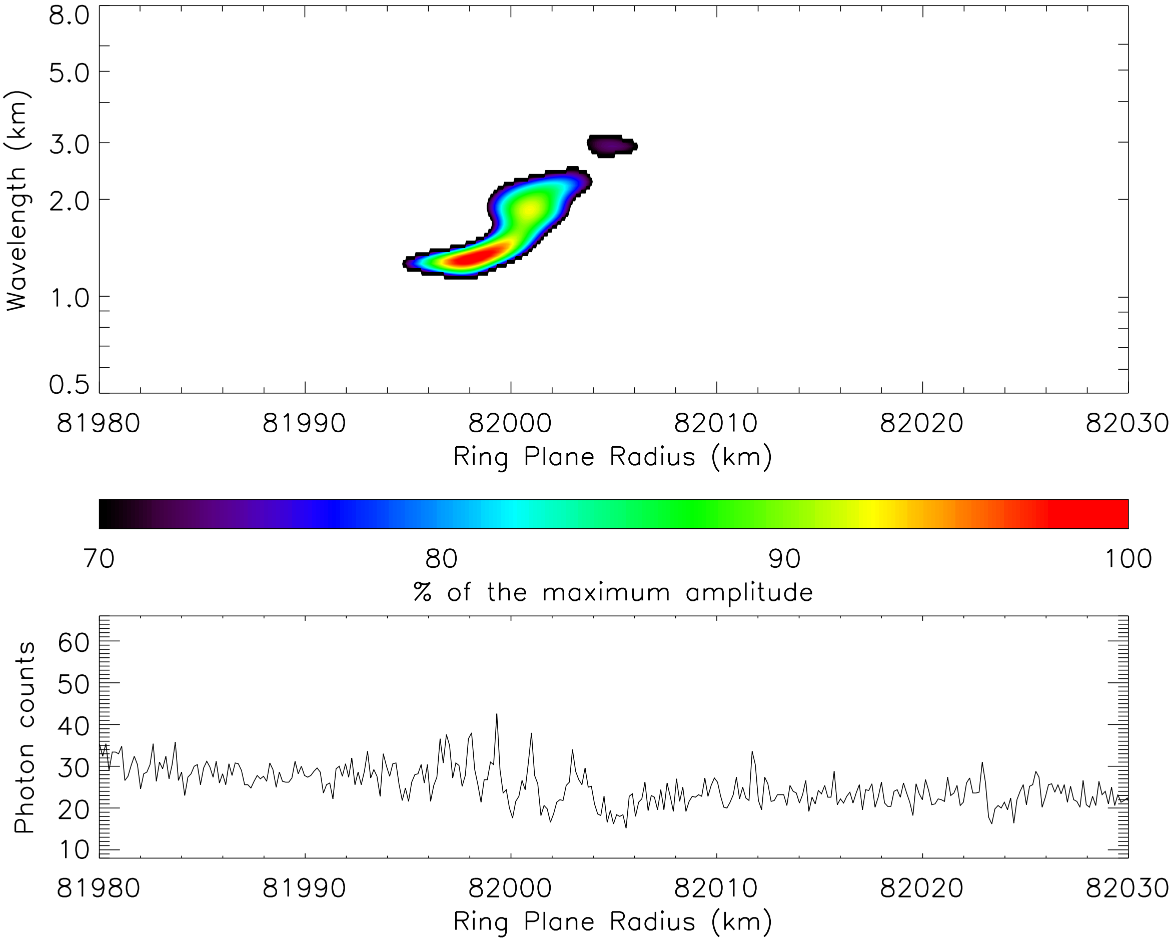

Figure 2.24: WWZ wavelet power profile of feature 15, computed from co-added wavelet profiles. Lower panel shows the ζ Orionis, rev. 47 occultation profile.

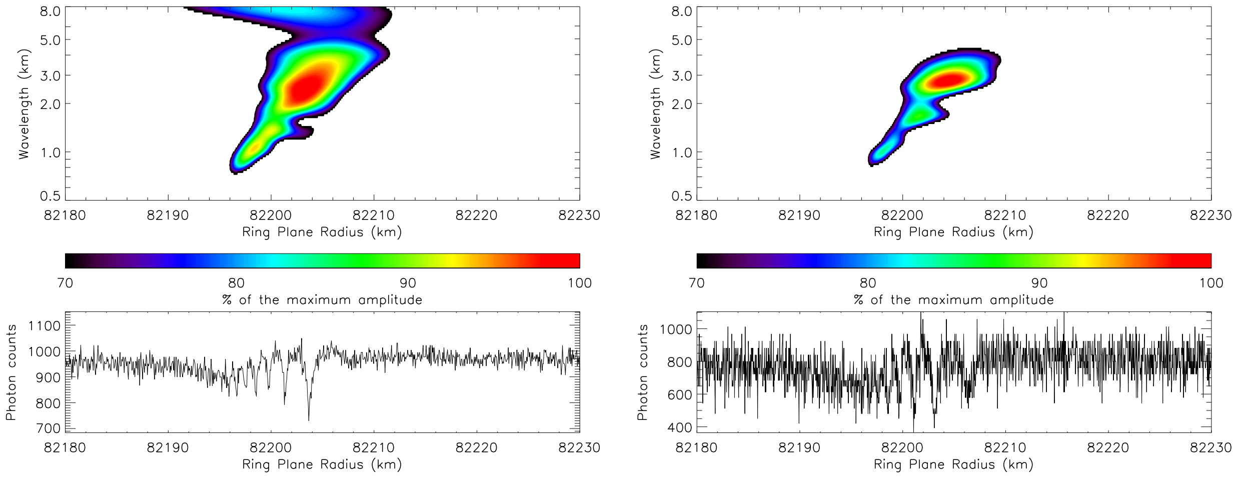

Figure 2.25: WWZ wavelet power profile of structure 17, computed from co-added wavelet profiles of high-incidence angle occultations (left) and low-incidence angle occultations (right). Lower panel show the β Centauri, rev. 85 occultation profile (left) and the α Virginis, rev. 34 occultation profile (right).

- Structures 16 and 17 (Figure 2.26 and 2.25), from Rosen et al. (1991a), also present inward propagation that is visible on both co-added profiles.

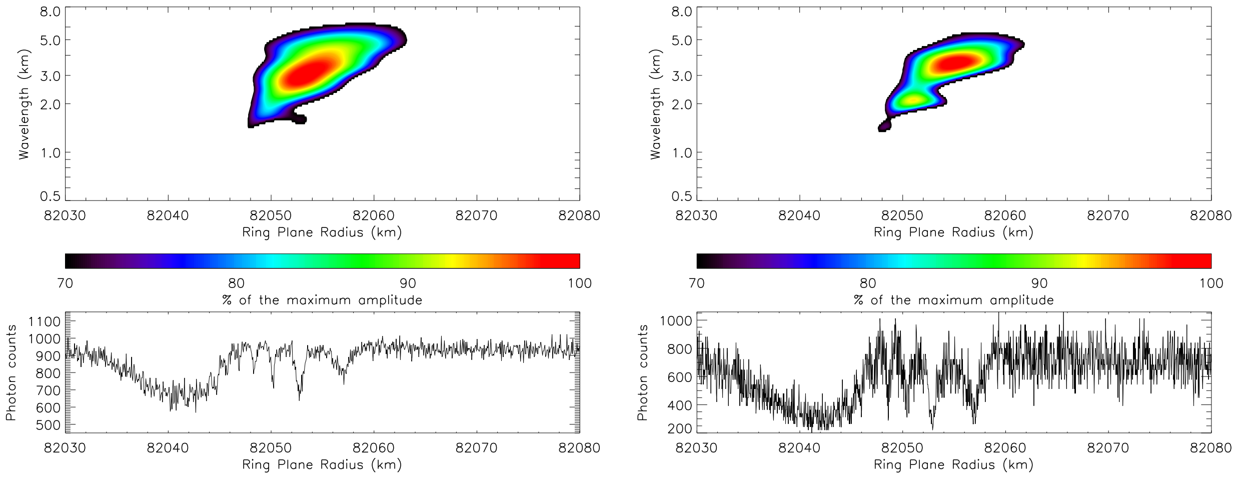

Figure 2.26: WWZ wavelet power profile of structure 16, computed from co-added wavelet profiles of high-incidence angle occultations (left) and low-incidence angle occultations (right). Lower panel show the β Centauri, rev. 85 occultation profile (left) and the α Virginis, rev. 34 occultation profile (right). Structure 16 is located just exterior to the embedded ringlet ER10.

- Structures 18 and 19 are very clearly propagating inward as shown on ζ Orionis occultation scans (Figure 2.27).

- Structure 23, reported by Rosen et al. (1991a), is only seen on the small incidence angle occultation ζ Orionis (Figure 2.28), validating the observed inward propagation.

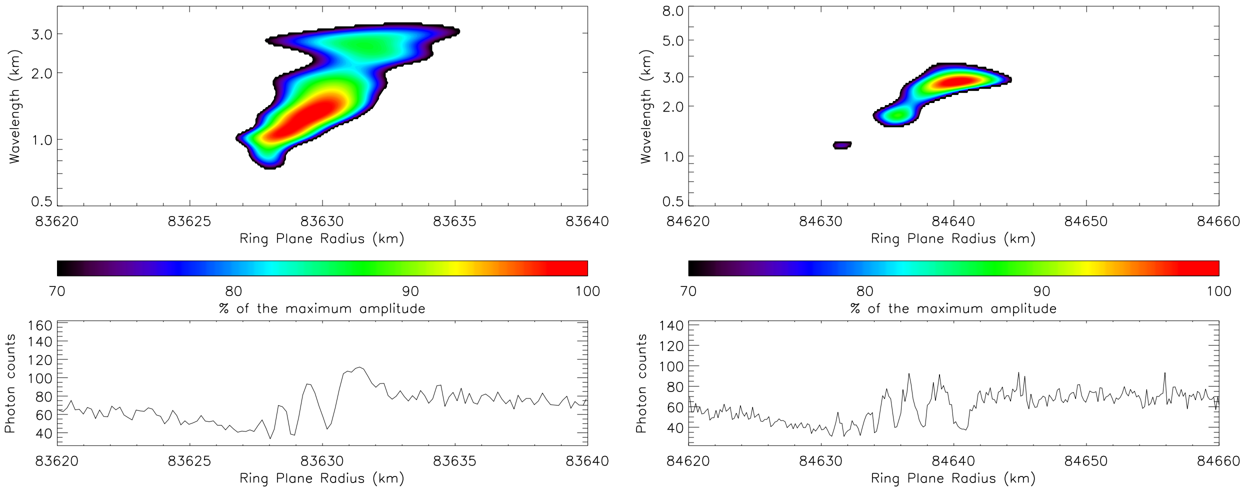

Figure 2.27: WWZ wavelet power profile of structure 18 (left) and 19 (right), computed from individual occultation profile of ζ Orionis, rev. 47.

- Structure 25 is with good reasons only seen on ζ Orionis because of the inward direction of propagation indicating it is a bending wave.

- Structure 32 (Figure 2.29) was reported by Colwell et al. (2009b) and propagates inward.

- Between 90130 km and 90200 km, we observe different features (gathered under structure 38) depending on the occultation (Figure 2.30).

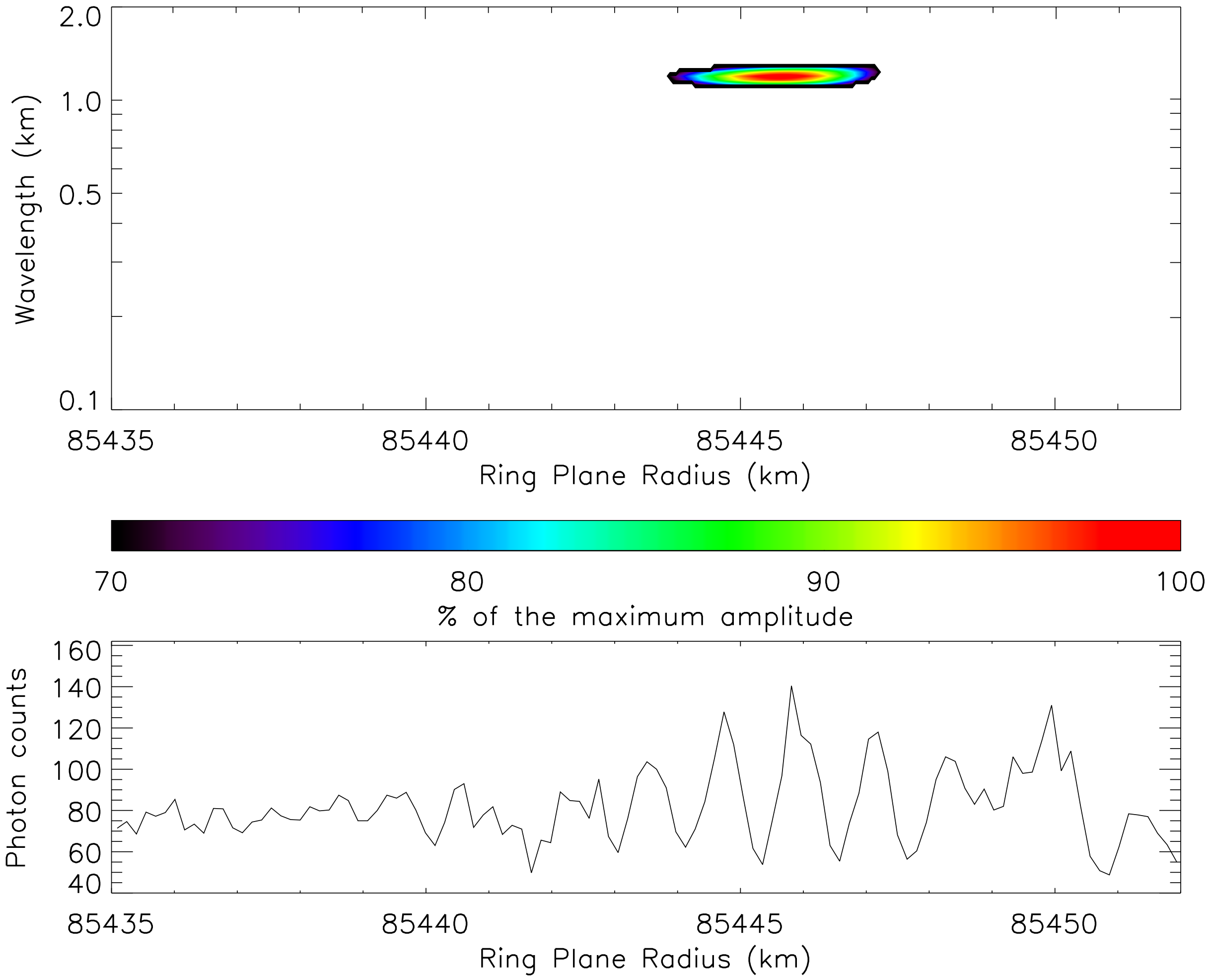

Figure 2.28: WWZ wavelet power profile of structure 23, computed from ζ Orionis, rev. 47 individual occultation profile.

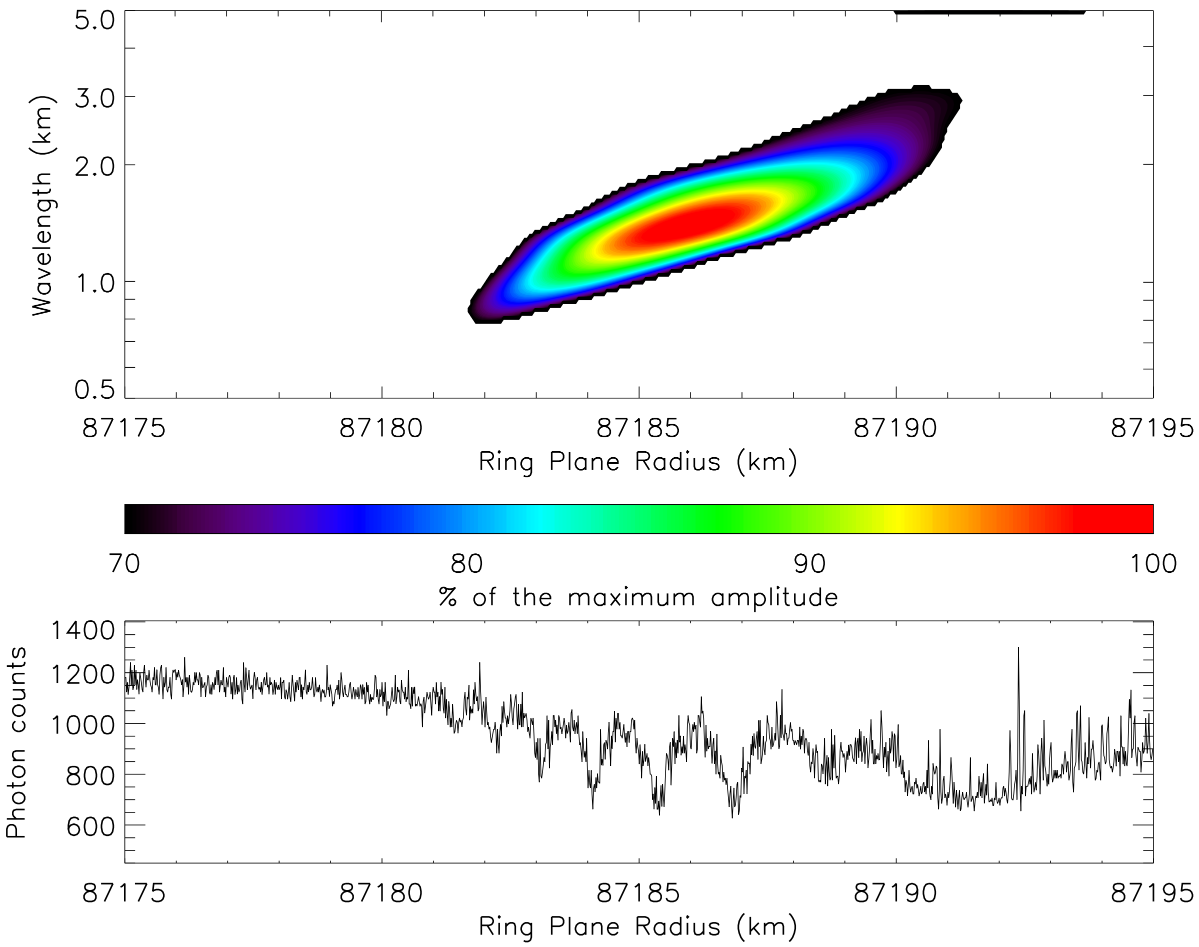

Figure 2.29: Co-added WWZ wavelet power profile of structure 32, computed from individual occultation profiles. Lower panel shows the β Centauri, rev. 85 occultation profile. Structure 32 is coexisting with the embedded ringlet ER13 that spreads from 87180 km to 87210 km.

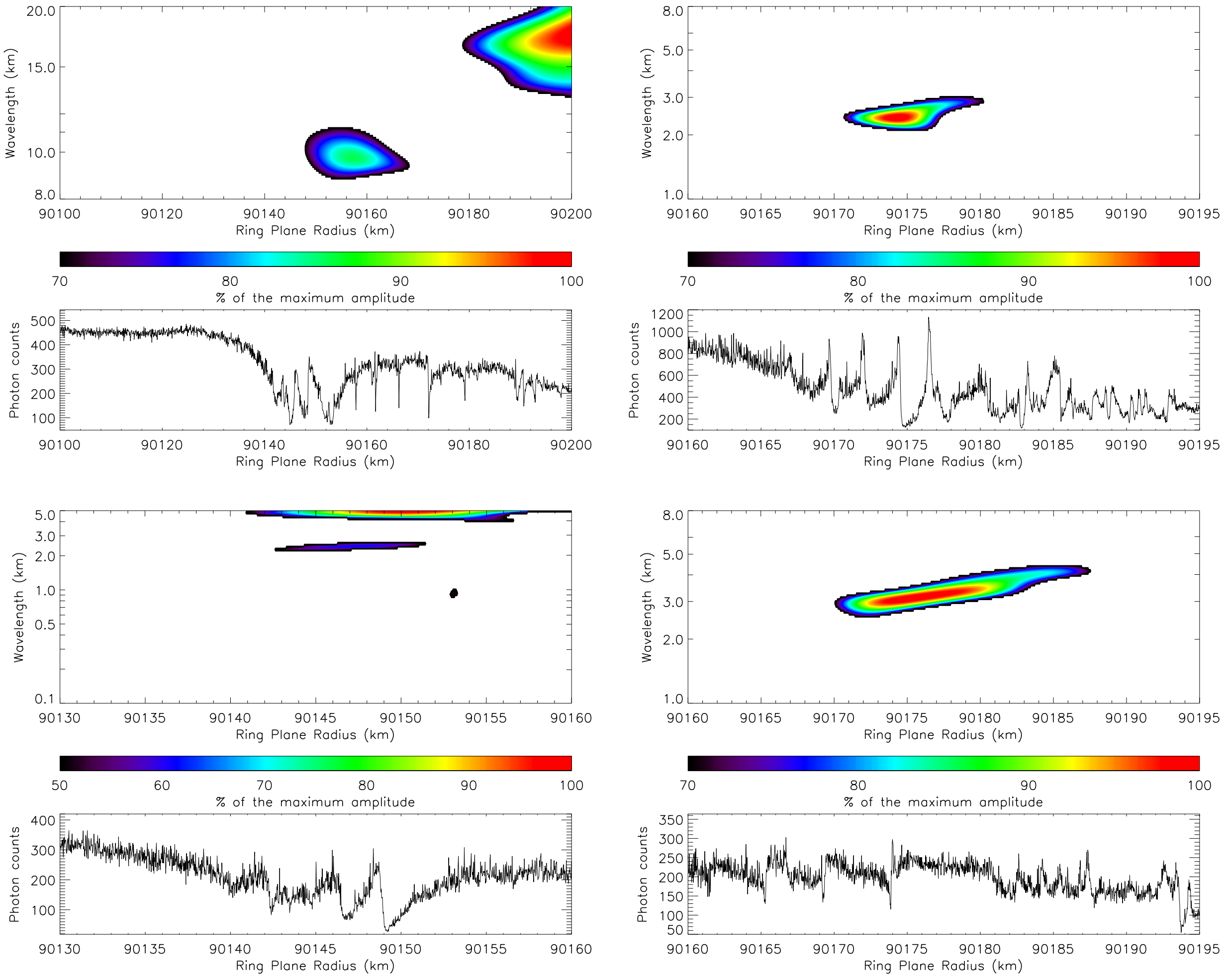

Figure 2.30: WWZ wavelet power profile of the different parts composing structure 38, computed from individual occultation profile of β Centauri, rev. 89 (upper left), β Centauri, rev. 64 (upper right), and β Centauri, rev. 104 Ingress (bottom).The variety of observed patterns and the local superposition of waves at different wavelengths suggest that this is not a simple bending wave.

2.3.4.3 Other Signatures

- Structure 11 was reported by Colwell et al. (2009b) as an inward propagating feature. It appears to be located at the position of a 6-km-wide embedded ringlet that generated a wavelike signature around 12 km, but we can extract an actual feature at shorter wavelengths (Figure 2.31). Although the amplitude of structure 11 decreases outward, the wavelength remains constant, and thus we cannot state the direction of propagation for that structure.

- We see an inward-propagating structure in the well-known eccentric Maxwell Ringlet at 87545 km (Figures 2.32 and 2.33). Not with the same regularity, we observe wavelike signatures in the R4 ringlet at 88700 km; Figure 2.34 presents what could be interpreted as an inward propagating structure. We also notice that the Prometheus 2:1 inner Lindblad resonance is located inside the R4 ringlet and that the Mimas 3:1 inner vertical resonance is located at 88728.3 km, which is farther from the expected position of the wave than for the other associations previously made.

clearpage

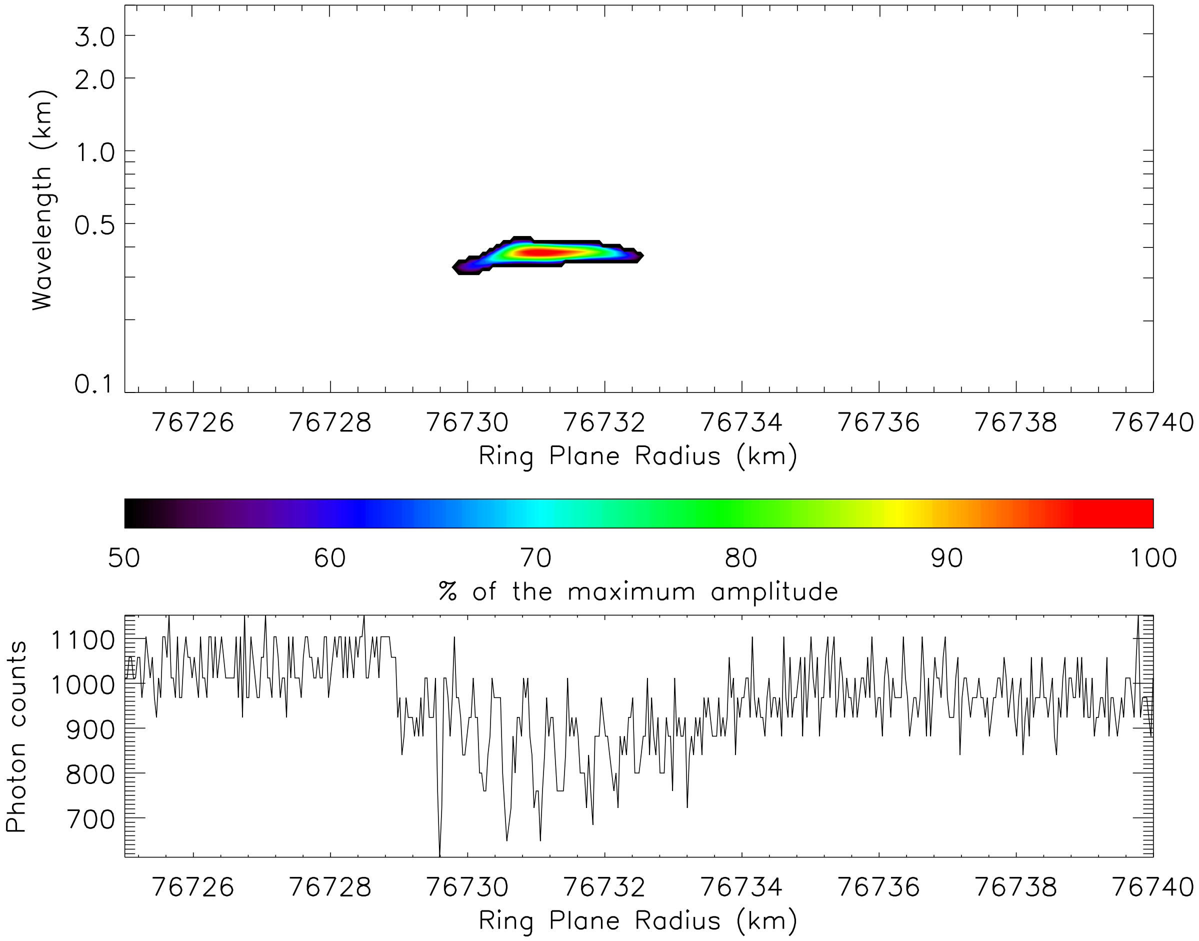

Figure 2.31: WWZ wavelet power profile of structure 11, computed from α Virginis, rev. 30 individual occultation profile.

2.3.5 Surface Mass Density Model

Most of these structures are narrower in radial extent than 13 km. Structure 27 (which is about 15 km wide) and structure 28 (with a width of about 52 km) are among the exceptions. These waves are not apparent in the Voyager radio and stellar occultations due to their small

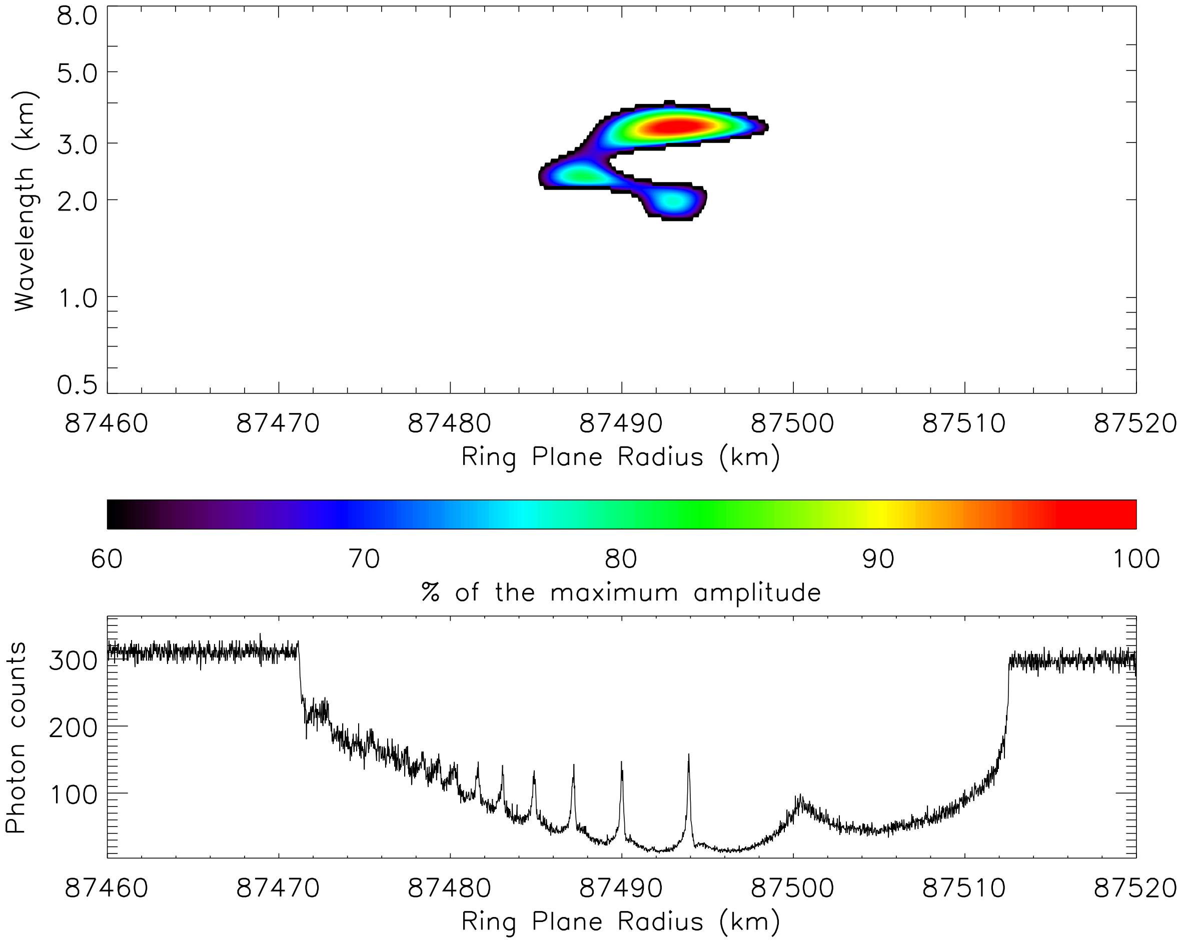

Figure 2.32: WWZ wavelet power profile around Maxwell ringlet, computed from β Centauri, rev. 105 individual occultation profile. Though the structure is quite clear and prominent to the eye on the occultation profile, the wwz profile is distorted by the relative importance of the amplitude of the highest wavelengths, hiding smaller amplitudes at the presented scale.

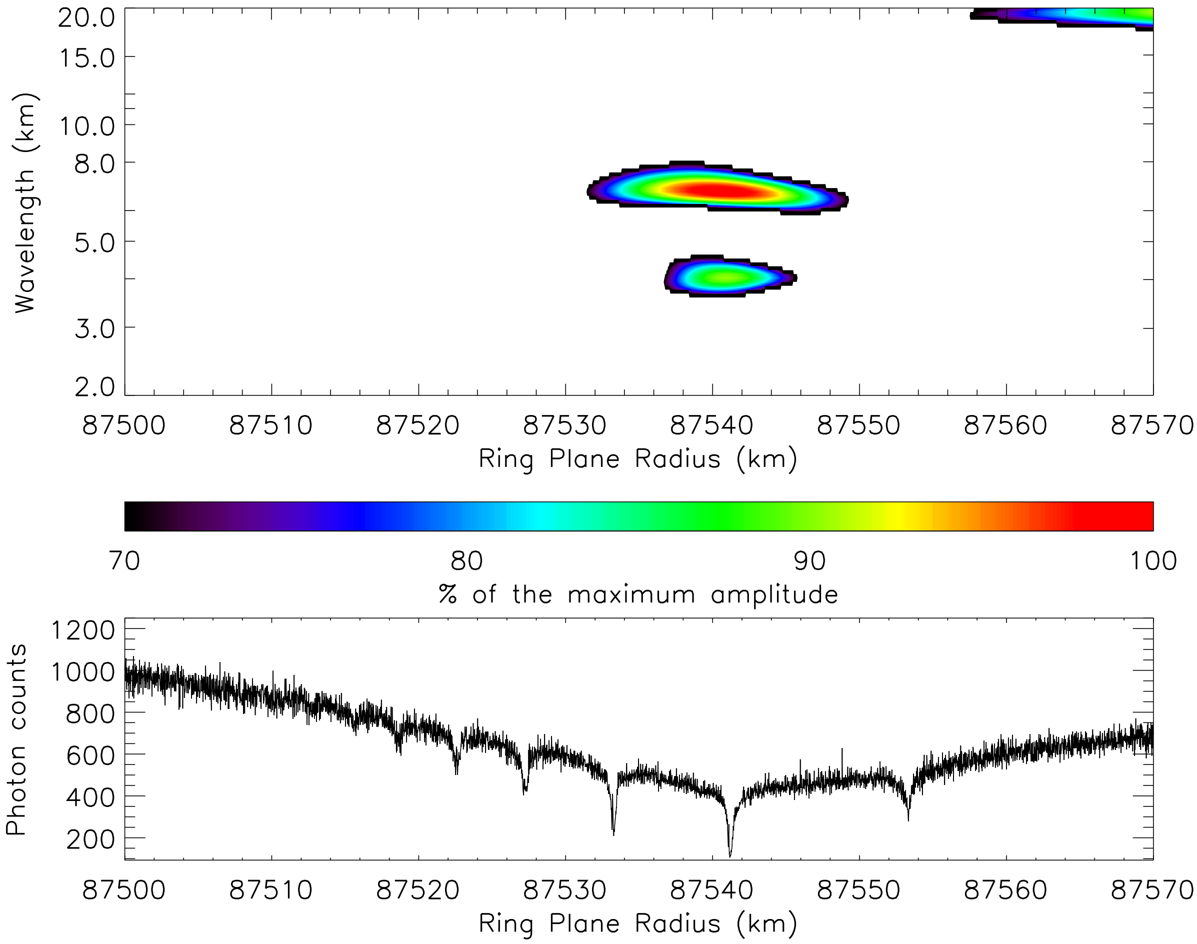

Figure 2.33: WWZ wavelet power profile of Maxwell Ringlet, computed from β Centauri, rev. 64 individual occultation profile. Again, the feature is clear on the occultation profile, but the wwz profile is distorted by the relative importance of the amplitude of the highest wavelengths.

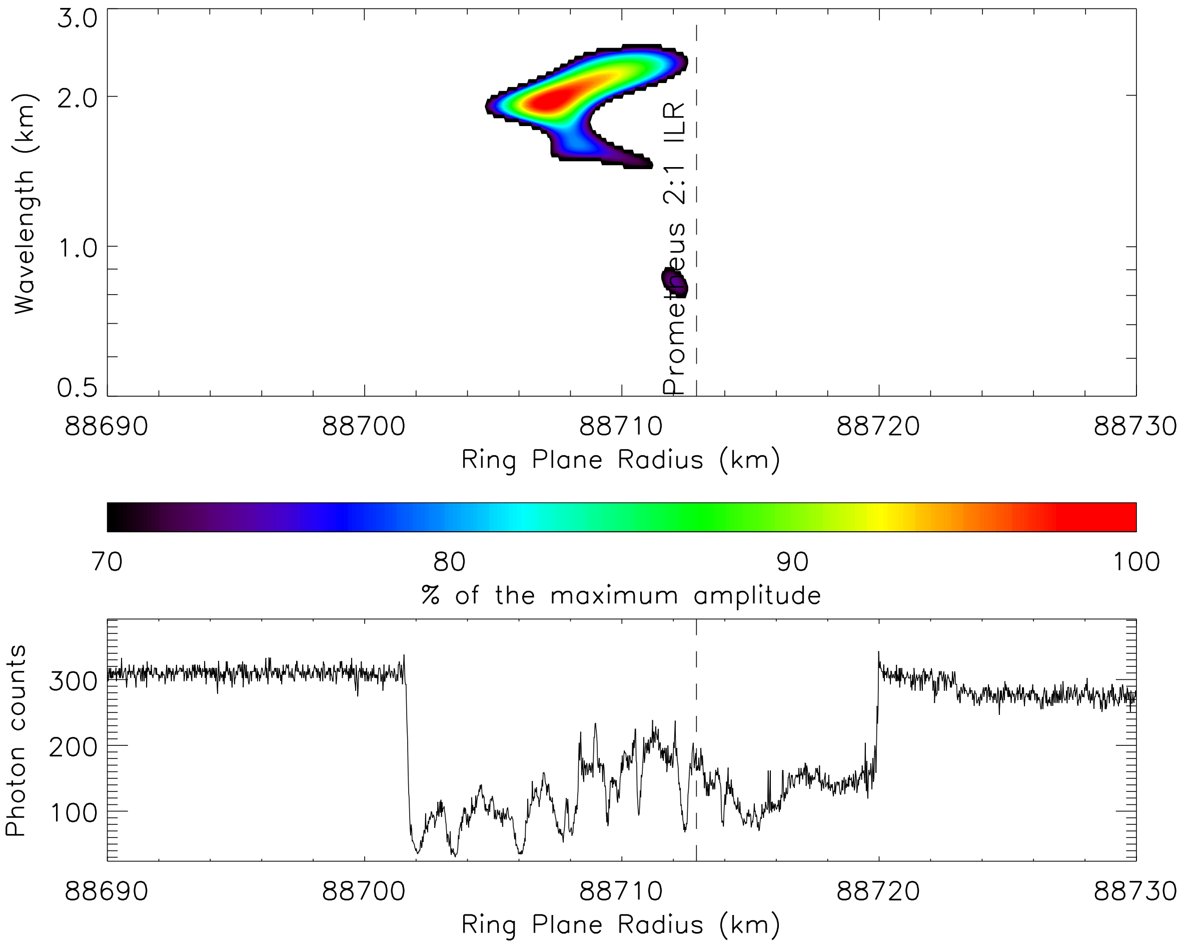

Figure 2.34: WWZ wavelet power profile of R4 ringlet, computed from β Centauri, rev. 105 individual occultation profile. The Prometheus 2:1 ILR position is represented by a vertical dashed line.

amplitude and short wavelength. These waves are detailed in Table 2.3 and can be located in the C ring in Figure 2.35.

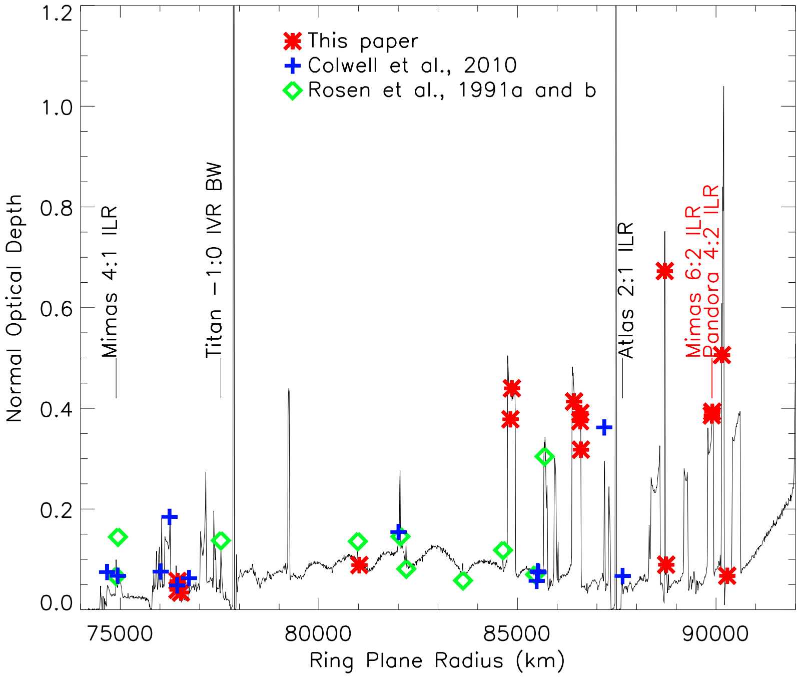

Figure 2.35: Locations of the observed wavelike structures in the C ring. New developments appear in red. We also represent the locations of the resonance that match both the position and the direction of propagation when available.

We next extract $\lambda(r)$, the wavelength of peak power as a function of r, from the co-added WWZ transforms. If the structure is a density wave or a bending wave, associated with a $p : q$ resonance, the dispersion of the wavelength is given by Equation 2.11, from Rosen et al. (1991a), where σ is the surface mass density, r_{LV} is the location of the resonance at the origin of the wave, m is a geometrical parameter representing the number of spiral arms

($m = q + 1$ for a Lindblad or vertical resonance), J_2 is the second gravitational harmonic (see Table 2.5), and $n(r)$ is the mean motion of a particle orbiting at radius r.

$$\begin{aligned} \mathcal{D}_{LV}(r) &= \left(3(m-1)n(r)^2 + J_2\left(\frac{R_{Saturn}}{r_{LV}}\right)^2\left(\frac{21}{2} - \frac{9}{2}(m-1)\right)n(r)^2\right) && (2.10) \\ \sigma &= \frac{|r - r_{LV}|\lambda}{4\pi^2 G r_{LV}}\,\mathcal{D}_{LV}(r) && (2.11) \end{aligned}$$

Table 2.5: Gravitational Harmonics.

Gravitational Harmonics	Value
J_2	$16290.71\ 10^{-6}$
J_4	$-935.83\ 10^{-6}$
J_6	$86.14\ 10^{-6}$
J_8	$-10.0\ 10^{-6}$

From Jacobson et al. (2006). $R^{eq}_{Saturn} = 60330$ km.

2.4 Results

We produced a map of resonances with the known external perturbers (Section 2.4.1) up to the eighth order, allowing us to identify potential associations between waves and resonances such as the Pandora 4:2 ILR (Section 2.3). A more definitive resonance association would be possible by showing that the phase of the wave in individual occultations matches the phase predicted for the corresponding resonance. This check on our resonance associations, as described below, is complicated by the uncertainty in the absolute radial scale that is comparable to the wavelength of the waves. Here we describe other tests based on resonance strength and observed resonance locations to check our tentative resonance associations.

2.4.1 Determination of Theoretical Resonance Locations

In order to identify the potential resonances that could generate the reported wavelike structures, we updated a resonance location list with a complete mapping of all possible resonances up to 8^{th} order with $j_1 \leq 50$ using converging routines based on Equations 2.12, 2.13 and 2.14. For a given particle with a semi-major axis a, Murray and Dermott (1999) provides the mean motion n, and the eccentricity and inclination frequency κ and ν:

$$n = \sqrt{\frac{GM}{a^3}\left(1+\frac{3}{2}J_2\left(\frac{R_S}{a}\right)^2-\frac{15}{8}J_4\left(\frac{R_S}{a}\right)^4+\frac{35}{16}J_6\left(\frac{R_S}{a}\right)^6-\frac{315}{128}J_8\left(\frac{R_S}{a}\right)^8\right)} \quad (2.12)$$

$$\kappa = \sqrt{\frac{GM}{a^3}\left(1-\frac{3}{2}J_2\left(\frac{R_S}{a}\right)^2+\frac{45}{8}J_4\left(\frac{R_S}{a}\right)^4-\frac{175}{16}J_6\left(\frac{R_S}{a}\right)^6+\frac{2205}{128}J_8\left(\frac{R_S}{a}\right)^8\right)} \quad (2.13)$$

$$\nu = \sqrt{\frac{GM}{a^3}\left(1+\frac{9}{2}J_2\left(\frac{R_S}{a}\right)^2-\frac{75}{8}J_4\left(\frac{R_S}{a}\right)^4+\frac{245}{16}J_6\left(\frac{R_S}{a}\right)^6-\frac{2835}{128}J_8\left(\frac{R_S}{a}\right)^8\right)} \quad (2.14)$$

The disturbing potential is the sum of a usual central potential and a disturbing potential:

$$U = -\frac{GM_{Saturn}}{r} - Gm_m\left(\frac{1}{|\vec{r}_m - \vec{r}|} - \frac{\vec{r}\,\vec{r}_m}{r_m^3}\right) \quad (2.15)$$

That last term has a direct part $\Re_d$ and an indirect part $\Re_i$ which can both be expressed as follows:

$$\Re = \sum_k A_k \cos(\Phi_k), \quad (2.16)$$

where Φ is the resonant argument and can be expressed as in Equation 2.17.

$$\Phi = j_1\lambda_s + j_2\lambda + j_3\varpi_s + j_4\varpi + j_5\Omega_s + j_6\Omega \quad (2.17)$$

where $\sum_{i=1}^{6} j_i = 0$, with j_i integers and $(j_5 + j_6)$ even, λ, ϖ and Ω are the mean longitude, the longitude of the pericenter and the longitude of the ascending node of a test particle and λ_s, ϖ_s and Ω_s are the mean longitude, the longitude of the pericenter and the longitude of the ascending node of the disturbing satellite. Finally, the azimuthal symmetry number m, mentioned above as the number of spiral arms, is defined mathematically by $m = j_1 + j_3 + j_5$ and we also define $k = -j_3$ and $p = -j_5$.

For cumulative effects, we consider the averaged disturbing function $< \Re >$. $< \Re >= 0$ unless $\Phi = 0$.

Using the mean motion n, the epicyclic frequency κ, the vertical frequency ν and the pattern speed Ω_P defined as follows, we can express the resonant conditions by Equation 2.22.

$$\begin{aligned} n &= \dot{\lambda} && (2.18) \\ \kappa &= n - \dot{\varpi} && (2.19) \\ \nu &= n - \dot{\Omega} && (2.20) \\ m\Omega_P &= mn_m - j_3\kappa_m - j_5\nu_m && (2.21) \\ m(\Omega_P - n) &= j_4\kappa + j_6\nu && (2.22) \end{aligned}$$

Depending on the combinations of the j_i parameters, we can access different types of resonance, as detailed in Table 2.6.

Table 2.6: Resonance types.

Resonance Type	j_3	j_4	j_5	j_6 [1]
Inner Lindblad Resonance	$\forall$[2]	-1	$\forall$	0
Outer Lindblad Resonance	$\forall$	1	$\forall$	0
Inner Vertical Resonance	$\forall$	0	$\forall$	-1
Outer Vertical Resonance	$\forall$	0	$\forall$	1
Corotation Eccentricity Resonance	$\forall$	0	0	0
Corotation Inclination Resonance	0	0	$\forall$	0

[1] $(j_5 + j_6)$ has to be even.

[2] For all.

2.4.2 Resonances in the C Ring

We computed the resonance locations with the highest precision available, and in particular with terms up to J_8 of the gravitational harmonics taken from Jacobson et al. (2006)[1] and Nicholson and Porco (1988) (see Table 2.5). The following satellites were considered (in distance order to Saturn): Pan, Daphnis, Atlas, Prometheus, Pandora, Janus, Epimetheus, Mimas, Methone, Pallene, Enceladus, Tethys, Polydeuces, Dione, Rhea, Titan, Hyperion,

---

[1] Jacobson et al. (2006)'s fit assumed a Saturn equatorial radius of 60330 km even if it was reestimated to 60268 km later by Seidelmann et al. (2007).

Iapetus and Phoebe. Semi-major axes of Saturn's satellites were taken from Jacobson et al. (2008). In order to check for other possible resonance sources, we also calculated resonances with the synchronous orbit and with the B ring outer edge.

For the synchronous orbit, we used the two periods identified by Kurth et al. (2008) in the magnetosphere rotation from early Cassini data: these periods of 10.80 hours and 10.59 hours are varying over the course of the Cassini mission. Hedman et al. (2009) related these to the observed periods of perturbations in the D ring and the Roche Division. However, the main low-order resonances with these forcing periods are the 3:2 ILRs located at 86020 and 87134 km, where we do not observe any particular structure.

Concerning the B ring outer edge forcing, Porco et al. (1984a) and Porco et al. (1984b) showed that the Mimas 2:1 inner Lindblad resonance is a source of perturbation of the B ring edge. Spitale and Porco (2010) recently described in detail the elements of this forced mode of the B ring edge together with three different free modes with wavenumbers 1, 2 and 3. By comparing the pattern of resonances from the B ring edge with the observed distribution of waves in the C ring, we can reject any association between B ring edge resonances and the waves reported here. Because the number of resonances can be unlimited if we go to sufficiently high order, in the next section we calculate resonance strengths to help identify associations between resonances and observed wave features. The resonance pattern corresponding to the synchronous orbit (Figure 2.36) clearly shows some inconsistencies with the observed waves in the C ring. Though the B ring edge 2:1 ILR are located between 75000 and 75150 km (Figure 2.38 shows the wavenumber-2 forced mode), the observed features appear uncorrelated with B ring edge resonances.

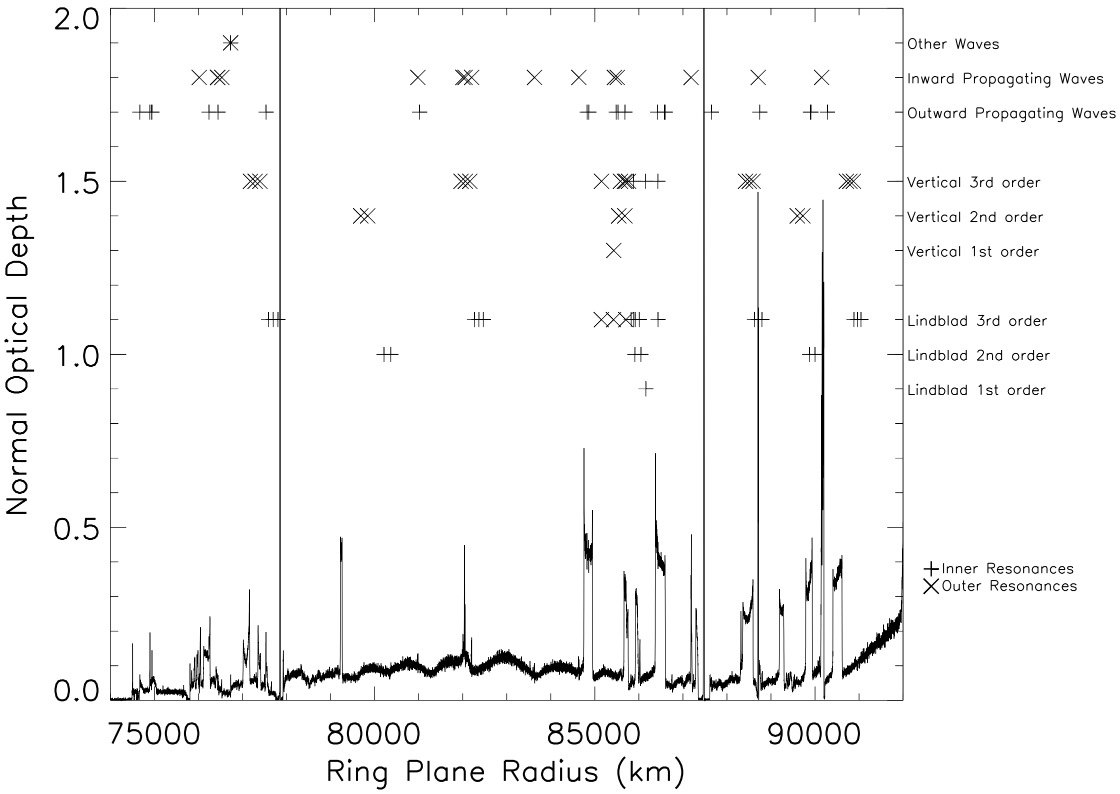

Figure 2.36: Normal optical depth of the C ring. Lindblad and vertical first, second and third order resonances positions with the synchronous orbit are represented together with the positions of the reported waves.

Finally, we investigate the possibility of moonlets orbiting in the C ring gaps (the G1 as referred to in Colwell et al. (2010b), Colombo, Maxwell, Bond and Dawes gaps) that could create low order resonances in the C ring. We find that any moonlet in one of these gaps

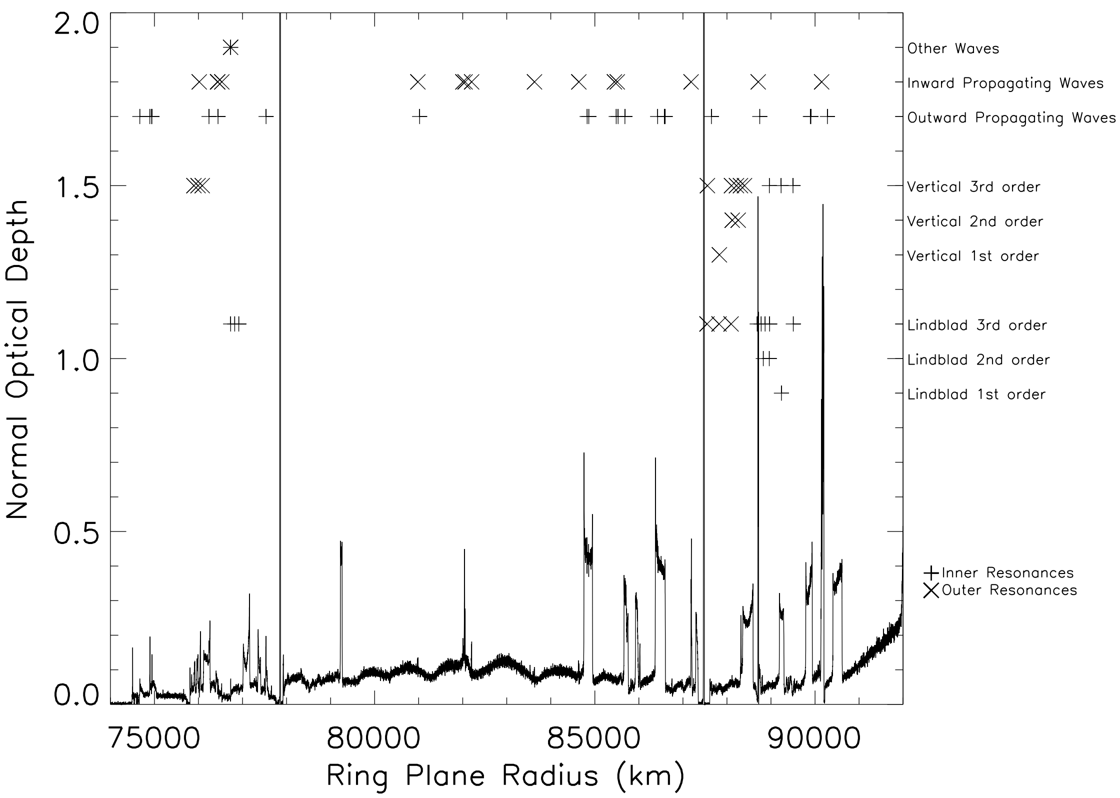

Figure 2.37: Normal optical depth of the C ring. Lindblad and vertical first, second and third order resonances positions with the core of the F ring are represented together with the positions of the reported waves.

should create a resonance pattern that would be inconsistent with the observed waves, or more precisely, inconsistent with the fact that no obvious wave is reported in regions where we should observe some waves of comparable strength with the few that are observed and might be due to such a moonlet. Figures 2.39, 2.40, 2.41, 2.42 and 2.43 show the absence

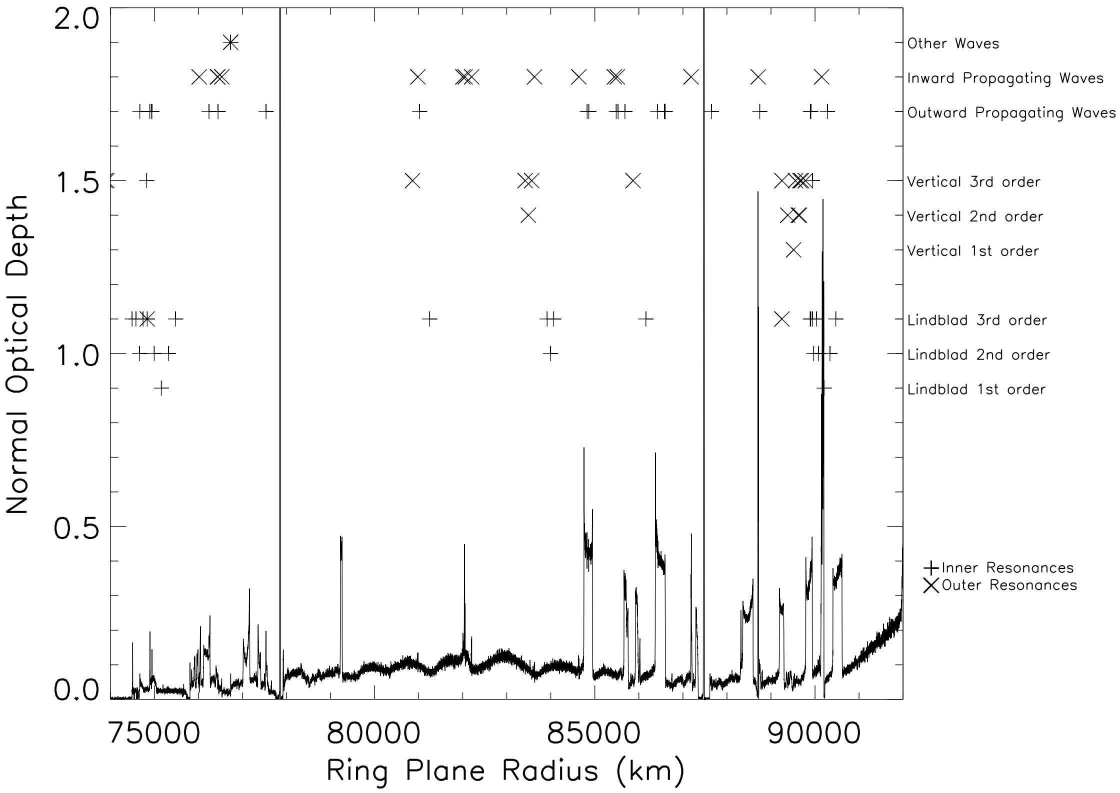

Figure 2.38: Normal optical depth of the C ring. Lindblad and vertical first, second and third order resonances positions with the outer edge of the B ring are represented together with the positions of the reported waves.

of waves at expected low order resonance locations with embedded moonlets in the C ring gaps.

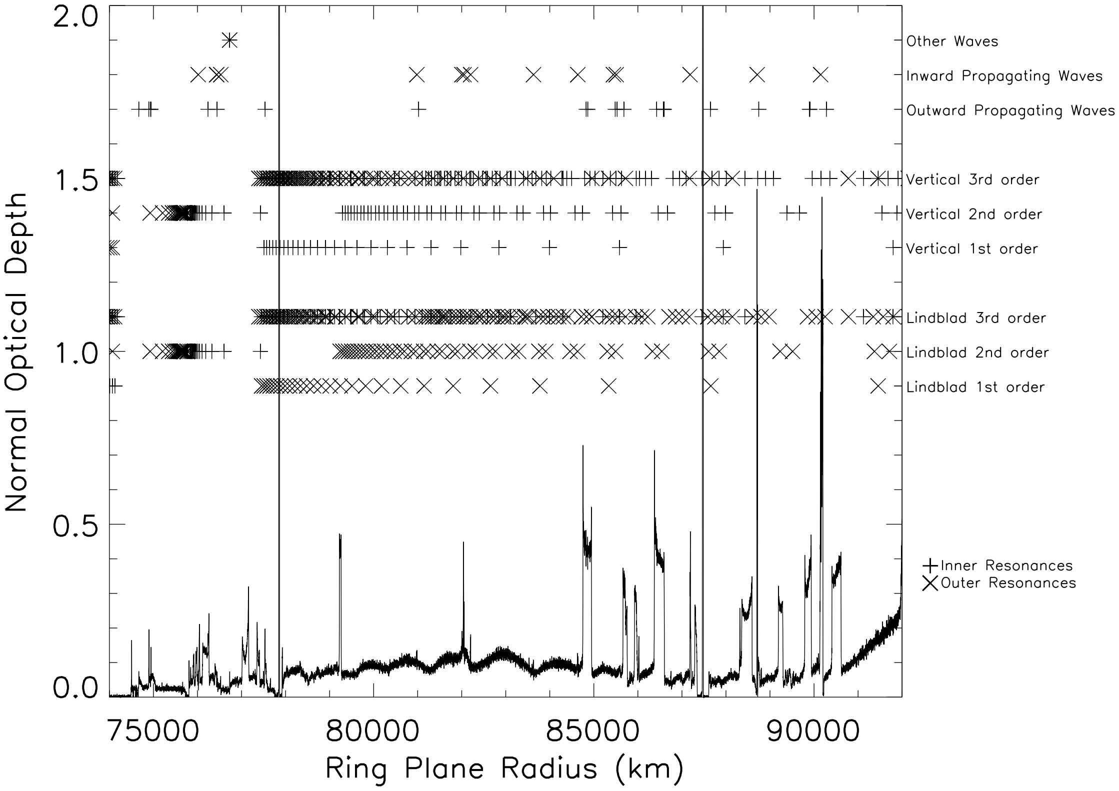

Figure 2.39: Normal optical depth of the C ring. Lindblad and vertical first, second and third order resonances positions with the G1 gap are represented together with the positions of the reported waves.

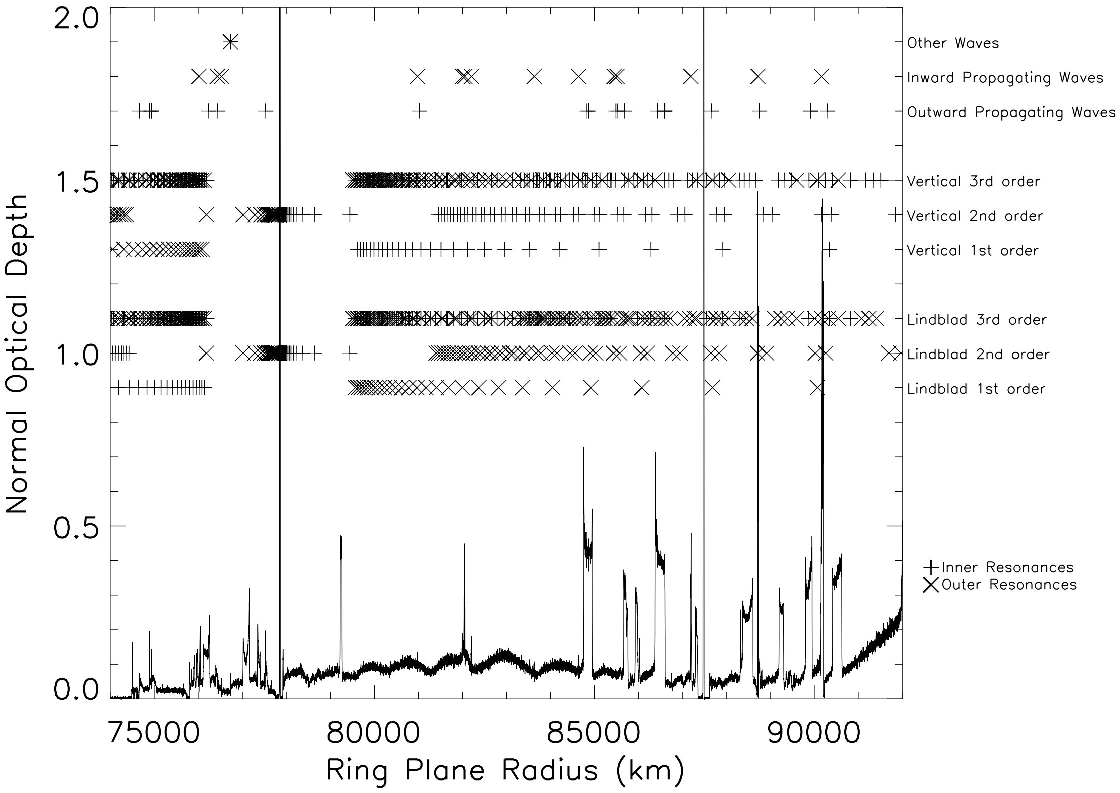

Figure 2.40: Normal optical depth of the C ring. Lindblad and vertical first, second and third order resonances positions with the Colombo gap are represented together with the positions of the reported waves.

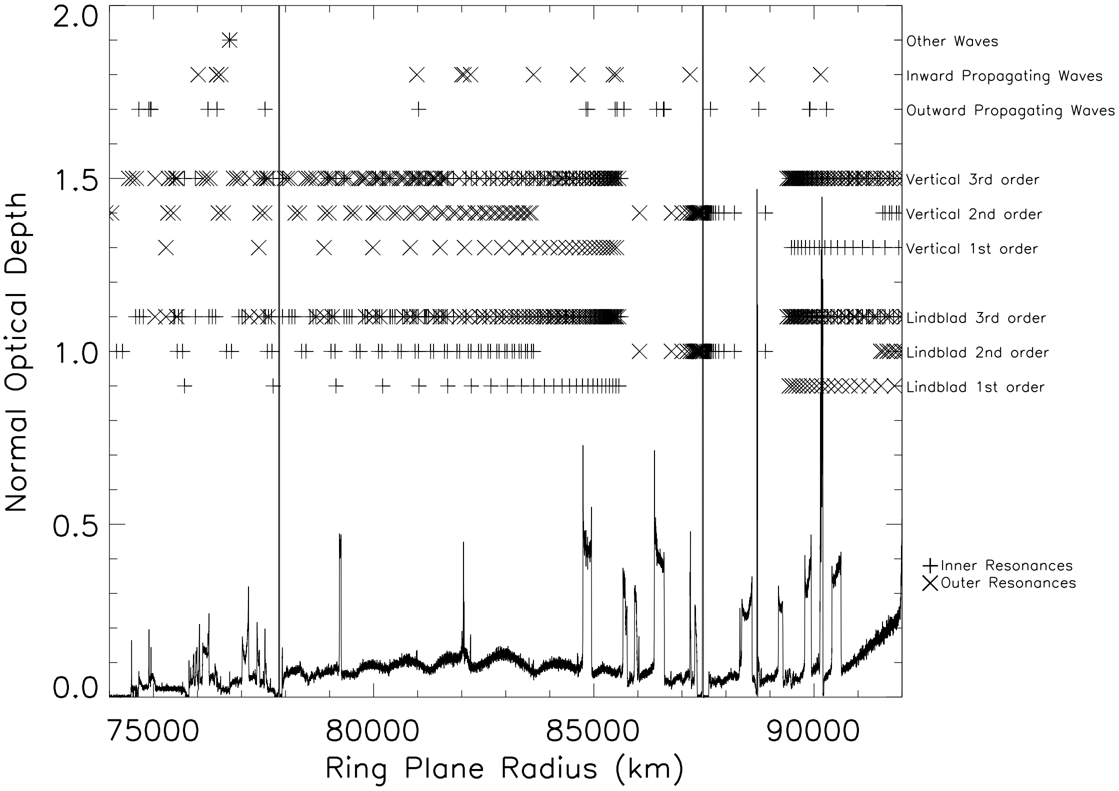

Figure 2.41: Normal optical depth of the C ring. Lindblad and vertical first, second and third order resonances positions with the Maxwell gap are represented together with the positions of the reported waves.

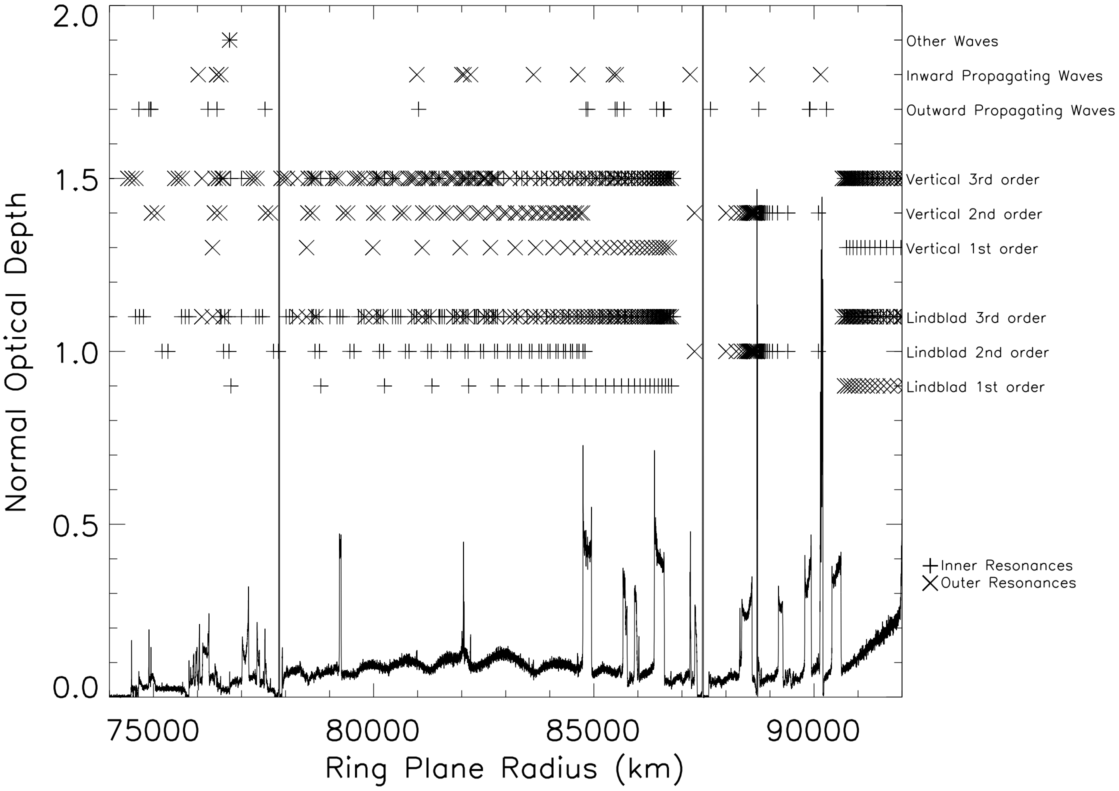

Figure 2.42: Normal optical depth of the C ring. Lindblad and vertical first, second and third order resonances positions with the Bond gap are represented together with the positions of the reported waves.

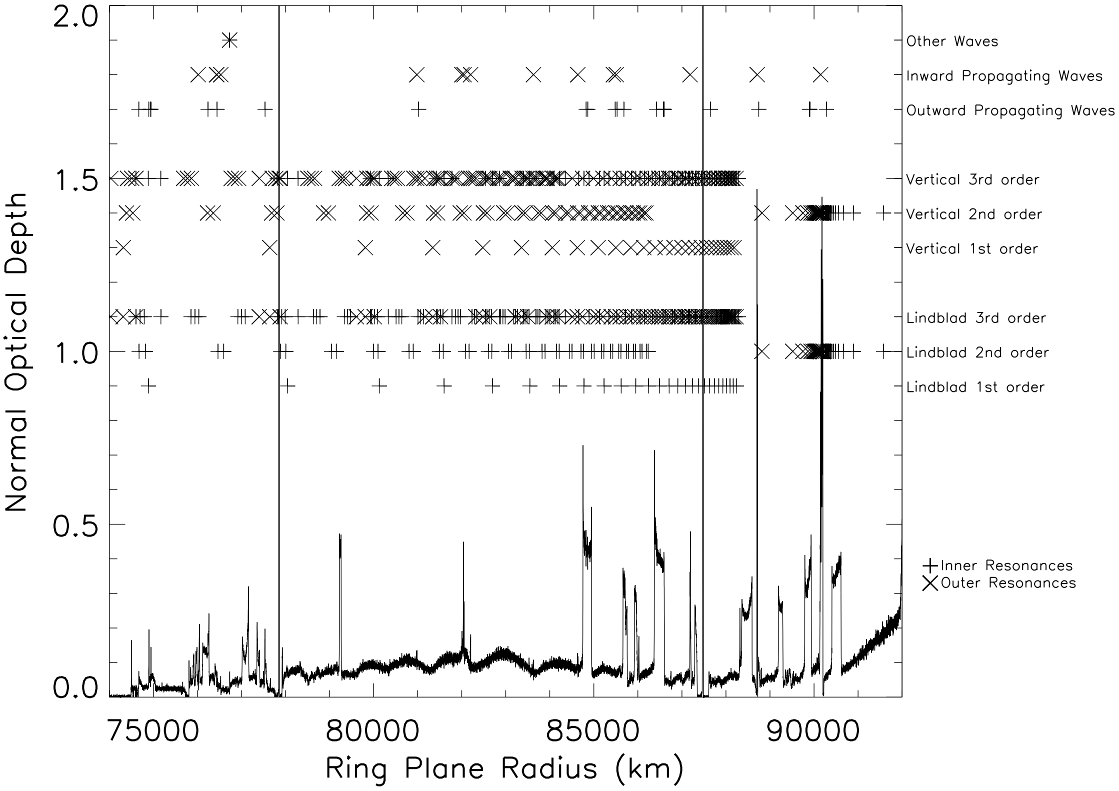

Figure 2.43: Normal optical depth of the C ring. Lindblad and vertical first, second and third order resonances positions with the Dawes gap are represented together with the positions of the reported waves.

2.4.3 Resonance Strengths

Goldreich and Tremaine (1979) provided a complete derivation of the torque $T_{l,m}$ exerted by a satellite at a resonance on a uniform fluid disk in the case of inner Lindblad resonances and corotation resonances.

2.4.3.1 Inner Lindblad Resonances

Considering a $j_1 : -j_2$ inner Lindblad resonance, we have $m = j_1 + j_3 = -j_2 - j_4$. Therefore, adopting the notation of Goldreich and Tremaine (1979), we define $l = j_1$, and consider the $l : (m-1)$ inner Lindblad resonance. We then define D_L for a Lindblad resonance and the equivalent D_V for a vertical one

$$D_L(r) = \kappa(r)^2 - m^2(n(r) - \Omega^P_{l,m})^2 \tag{2.23}$$

$$D_V(r) = \mu(r)^2 - m^2(n(r) - \Omega^P_{l,m})^2 \tag{2.24}$$

The torque can then be expressed as in Goldreich and Tremaine (1979):

$$T^L_{l,m} = -m\pi^2 \left[\sigma \left(\frac{rdD_L}{dr} \right)^{-1} \left(\frac{rd\phi^s_{l,m}}{dr} + \frac{2n(r)\phi^s_{l,m}}{n(r) - \Omega^P_{l,m}} \right)^2 \right]_{r_L} \tag{2.25}$$

where the Fourier components $\phi^s_{l,m}$ are evaluated from Brouwer and Clemence (1961) (ch. 15, p. 490) and Murray and Dermott (1999) (eq 6.244–6.246) using the Keplerian approximation of $n \approx \kappa$:

$$\begin{aligned}
\phi^s_{1,1} &= -\frac{GM_s}{a_s}[b^m_{1/2}(\beta) - \beta] && (2.26)\\
\phi^s_{m,m} &= -\frac{GM_s}{a_s} b^m_{1/2}(\beta),\ m > 1 && (2.27)\\
\phi^s_{m+1,m} &= -\frac{GM_s e_s}{a_s}\left(\frac{1}{2} + m + \frac{\beta}{2}\frac{d}{d\beta}\right) b^m_{1/2}(\beta),\ m > 1 && (2.28)\\
\phi^s_{m+2,m} &= -\frac{GM_s e_s^2}{8a_s}\left((4m^2 + m + 4) + (4m + 6)\beta\frac{d}{d\beta}\right. && (2.29)\\
&\left. +\beta^2\frac{d^2}{d\beta^2}\right) b^m_{1/2}(\beta),\ m > 1\\
\phi^s_{m+3,m} &= -\frac{GM_s e_s^3}{48a_s}\left((8m^3 + 42m^2 + 65m + 27)\right. && (2.30)\\
&+(12m^2 + 51m + 51)\beta\frac{d}{d\beta}\\
&\left. +(6m + 15)\beta^2\frac{d^2}{d\beta^2} + \beta^3\frac{d^3}{d\beta^3}\right) b^m_{1/2}(\beta),\ m > 1.
\end{aligned}$$

In these expressions, a_s and e_s are the semimajor axis and eccentricity of the perturbing satellite, $\beta = \frac{r}{a_s}$ and $b^m_{1/2}(\beta)$ is the Laplace coefficient defined in Equation 2.31, that is estimated numerically.

$$b^m_{1/2}(\beta) = \frac{2}{\pi}\int_0^\pi \frac{cos(m\theta)\,\mathrm{d}\theta}{(1 - 2\beta cos\theta + \beta^2)^{1/2}} \qquad (2.31)$$

Even though the resonance locations have been calculated up to 8^{th}-order, the previous development only allows the estimation of resonance strengths up to 3^{rd}-order. In addition, Shu (1970a) showed that in the absence of damping, the amplitude of a density wave grows linearly near the resonance. Lissauer and Cuzzi (1982) suggested evaluating the strength of a resonance by using the distance from resonance (located at r_L) at which the wave becomes non-linear:

$$r_L X_{NL} = \frac{2\pi^2}{dD/dr}\left(-\frac{m\sigma}{r_L T^L_{l,m}}\right)^{1/2}(G\sigma)^{3/2} r_L. \tag{2.32}$$

In the case where the surface mass density is unknown, we compare values of $T^L_{l,m}/\sigma$ and $X_{NL}\sigma^{-3/2}$. Strengths of main inner Lindblad resonances in the C ring are presented in Table 2.7. We should then consider possible associations with the strongest ones. Indeed, we do see some structures at the locations of the eight strongest resonances. It appears that we are only seeing structures for waves stronger than approximately the strength of the Pandora 4:2 ILR. That tends to invalidate tentative resonance association with, for example, Pan 4:2 ILR, whereas it reinforces our belief that the Mimas 4:1 ILR, the Atlas 2:1 ILR, the Mimas 6:2 ILR and the Pandora 4:2 ILR excite density waves seen respectively in structures 2, 33, 36 and 37.

For the tentative resonance associations based on the coincidence of wave feature and resonance locations (Table 2.7), we present the estimated values of $r_L X_{NL}$ in Table 2.8. Within $r_L X_{NL}$ of the wave source, undamped density waves are characterized by linear growth of the amplitude of surface mass density fluctuations, which become of order unity when $r_L X_{NL} = 1$ (Shu (1970a) and Goldreich and Tremaine (1978b)). Damping can reduce wave amplitude, but does not increase it, so the perturbation amplitude at a given distance from resonance should not exceed the fraction of $r_L X_{NL}$ that this distance represents. For the relatively strong Mimas 4:1 ILR, the expected distance to nonlinearity is comparable to the wavelength of the first cycle. The relative amplitudes stay below 0.1 but can reach up to 0.4 later (7 km away from the wave source i.e. 4 km away from the theoretical resonance location), suggesting significant damping but reinforcing the association of the resonance with the observed wave. For the Mimas 6:2 ILR ($r_L X_{NL} = 66.2$ km), we measure a relative perturbation amplitude of 0.21 at the location corresponding to 0.02 $R_L X_{NL}$. The excitation of the Mimas 6:2 ILR alone could not explain this amplitude, and our confidence in this association is weakened. The Pandora 4:2 ILR overlaps the Mimas 6:2 ILR, preventing us from evaluating amplitudes due to this wave alone. For the Atlas 2:1 ILR ($r_L X_{NL} = 2.79$ km), the predicted distance to non-linearity is comparable to the wavelength. The maximum observed relative amplitude is 0.13, which could be explained by damping.

Depending on the physical characteristics of the middle where they are located, Inner Lindblad Resonances will excite different types of waves (Meyer-Vernet and Sicardy (1987) and Sicardy (2006)), as visible in Figure 2.44. Self-gravity and viscosity are competing in the rings and can generate strongly different responses.

2.4.3.2 Other Resonances

For a self-gravitating disk, Goldreich and Tremaine (1979) also derived a torque expression for a corotation resonance:

$$T_c = \frac{m\pi^2}{2} \left[\frac{\phi_1^2}{dn(r)/dr} \frac{d}{dr} \left(\frac{\sigma}{n(r) + \frac{r}{2}\frac{dn(r)}{dr}} \right) \right]_{r_c} \tag{2.33}$$

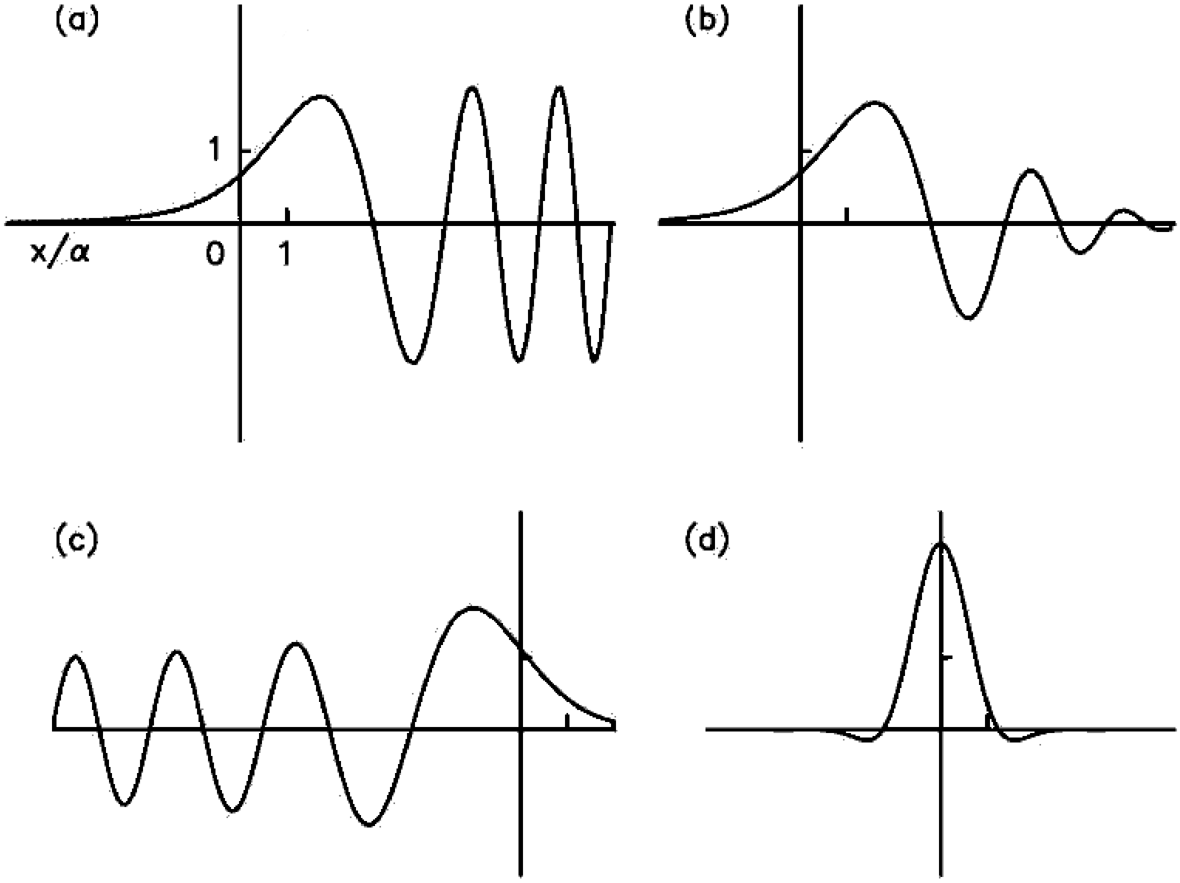

Figure 2.44: Various responses of a disk near an inner Lindlad resonance (located at $x = 0$). (a) A disk dominated by self-gravity. The wave is launched at $x = 0$ and propagates to the right of the resonance, while remaining evanescent on the left side. (b) A self-gravity wave damped by viscosity. (c) A wave in a disk dominated by pressure. The propagating and evanescent sides are inverted with respect to the self-gravity case. (d) Response in a disk dominated by viscosity. The wave is now evanescent on both sides of the resonances. Figure and caption from Sicardy (2006).

where ϕ_1 is an external perturbation potential. The dependence in the radial gradient of surface mass density prevents us from estimating the corotation resonance strengths and comparing them with Lindblad resonances.

Similar torque estimations for vertical resonances were done by Shu et al. (1983). However, no obvious association can be done between our observed structures and locations of vertical resonances in the C ring.

Table 2.7: Strongest Inner Lindblad Resonances in the C ring.

Resonance	r_L (km)	$X_{NL}\sigma^{-3/2}$ ($\mathrm{cm}^3/\mathrm{g}^{3/2}$)	T^L_{lm}/σ ($\mathrm{cm}^4/\mathrm{s}^2$)	Structures around
Mimas 3:1 ILR	90198.0	$2.00\ 10^{-6}$	$-2.00\ 10^{16}$	ER16 - struct 39
Prometheus 2:1 ILR	88712.9	$1.40\ 10^{-5}$	$-3.94\ 10^{14}$	R4 - struct 34 (Figure 2.34)
Pandora 2:1 ILR	90167.6	$1.60\ 10^{-5}$	$-2.99\ 10^{14}$	Structure 38 (Figure 2.30)
Mimas 4:1 ILR	74891.8	$5.60\ 10^{-5}$	$-6.88\ 10^{12}$	Structure 2 (Figure 2.9)
Atlas 2:1 ILR	87646.5	$3.09\ 10^{-4}$	$-6.91\ 10^{11}$	Structure 33 (Figure 2.11)
Pan 2:1 ILR	85105.8	$3.76\ 10^{-4}$	$-3.79\ 10^{11}$	Structure 22 (Figure 2.14)
Mimas 6:2 ILR	89883.3	$4.91\ 10^{-4}$	$-1.26\ 10^{11}$	Structure 36 (Figure 2.12)
Pandora 4:2 ILR	89894.0	$6.51\ 10^{-4}$	$-7.20\ 10^{10}$	Structure 37 (Figure 2.12)
Prometheus 4:2 ILR	88434.5	$1.02\ 10^{-3}$	$-2.60\ 10^{10}$	
Janus 5:2 ILR	82943.8	$2.43\ 10^{-3}$	$-2.91\ 10^{9}$	
Epimetheus 5:2 ILR	82969.7	$4.26\ 10^{-3}$	$-9.52\ 10^{8}$	
Daphnis 2:1 ILR	86924.0	$2.37\ 10^{-2}$	$-1.11\ 10^{8}$	
Atlas 4:2 ILR	87364.3	$4.28\ 10^{-2}$	$-1.36\ 10^{7}$	Inner edge of Maxwell Gap
Pandora 6:3 ILR	89801.6	$3.88\ 10^{-2}$	$-1.21\ 10^{7}$	Inner edge of P10
Enceladus 5:1 ILR	82542.9	$6.19\ 10^{-2}$	$-1.12\ 10^{7}$	
Pandora 5:2 ILR	77717.0	$7.24\ 10^{-2}$	$-2.07\ 10^{6}$	
Prometheus 6:3 ILR	88340.4	$1.16\ 10^{-1}$	$-1.20\ 10^{6}$	Inner edge of P8
Prometheus 5:2 ILR	76464.0	$2.17\ 10^{-1}$	$-2.05\ 10^{5}$	
Pan 4:2 ILR	84814.5	4.34	$-1.07\ 10^{3}$	
Atlas 6:3 ILR	87268.9	8.92	$-1.86\ 10^{2}$	
Atlas 5:2 ILR	75545.4	16.7	$-3.19\ 10^{1}$	

$r_L X_{NL}$ is the distance at which the wave becomes nonlinear. T^L_{lm} is the torque exerted on a fluid disk by a satellite at an Inner Lindblad Resonance. These quantities are depending on the surface mass density σ. Nearby structures are mentioned in the last column.

2.4.4 Wave Dispersion Relation

As expressed in Rosen et al. (1991a), the dispersion relation for a density wave associated with an $l : (m-1)$ Lindblad resonance can be written

$$m^2(\Omega_P - n(r))^2 = \kappa(r)^2 - 2\pi G\sigma|k(r)| \tag{2.34}$$

where $k(r)$ is the wavenumber.

Similarly, we can can write for a bending wave:

$$m^2(\Omega_P - n(r))^2 = \mu(r)^2 + 2\pi G\sigma|k(r)| \tag{2.35}$$

Defining $D_{L,V} = D_L$ for a Lindblad resonance, $D_{L,V} = D_V$ for a vertical one, and $\mathcal{D}_{LV} = \left(r\frac{dD_{L,V}}{dr}\right)_{r_{L,V}}$, Cuzzi et al. (1984) assumed that Saturn's gravity can be well-approximated as a point mass plus a J_2 harmonic, and Marley and Porco (1993) expressed

$$\mathcal{D}_{LV}(r) = \left(3(m-1)n(r)^2 + J_2\left(\frac{R_{Saturn}}{r_{LV}}\right)^2\left(\frac{21}{2} - \frac{9}{2}(m-1)\right)n(r)^2\right). \tag{2.36}$$

Then, the dispersion of the wavelength is given by Equation 2.37, from Rosen et al. (1991a).

$$\sigma = \frac{|r - r_{LV}|\lambda(r)}{4\pi^2 G r_{LV}}\,\mathcal{D}_{LV}(r) \tag{2.37}$$

where $\lambda(r) = \frac{2\pi}{k(r)}$ is the wavelength.

The azimuthal symmetry number m is known for waves that can be associated with a given resonance, but for waves whose forcing is not known, m is also unknown, and

Equation 2.37 may not be valid if the structure is not due to an inner Lindblad or vertical resonance. However, modeling outward propagating waves as density waves and inward propagating waves as bending waves allows one to determine $\frac{\sigma}{m-1}$ for which we considered r_{LV} to be the location of the beginning of the wave, and λ the wavelength of peak power. Indeed, for $m \neq 1$, Equation 2.37 becomes much simpler (see Equation 2.38) since the second term is very small compared to the first term. We assume outward propagating waves to be density waves and inward propagating waves to be bending waves, except for nodal bending waves such as the Titan -1:0 which is an outward propagating bending wave (Rosen and Lissauer, 1988). With these assumptions, we have:

$$\frac{\sigma}{m-1} \approx \frac{3|r - r_{LV}|\lambda(r)\ n(r)^2}{4\pi^2 G r_{LV}},\ m > 1. \tag{2.38}$$

In the case where $m = 1$, Equation 2.37 also becomes simpler and σ is now dominated by the term in J_2:

$$\sigma = J_2 \left(\frac{R_{Saturn}}{r_{LV}}\right)^2 \frac{21|r - r_{LV}|\lambda(r)\ n(r)^2}{8\pi^2 G r_{LV}}. \tag{2.39}$$

2.5 Discussion

2.5.1 Potential Resonance Association

Comparing the new catalog of observed wave structures (Table 2.3) with the catalog of resonance locations showed correlations at several locations. These associations are tentative and we need to verify that for a given resonance, either we observe the resonances that are supposed to have a higher strength or we have a good reason for not observing them.

2.5.2 Resonance Association Verification

By filtering the wavelength of maximum power for a given wave, and applying this filter to individual occultations, we can reconstruct the wave signal and therefore measure the phase of this signal at a given radial location. This phase is related to the mean longitude and longitude of the pericenter of the perturbing moon at the moment of the measure by Equation 2.40:

$$\phi_{LV} = \phi_0 + \xi^2/2 + \pi/4 \tag{2.40}$$

where the initial phase ϕ_0 is given by

$$\phi_0 = m\lambda - (m+k)\lambda_s + k\varpi_s \tag{2.41}$$

for an inner Lindblad resonance and by

$$\phi_0 = m\lambda - (m+p)\lambda_s + p\Omega_s \tag{2.42}$$

for an inner vertical resonance. ξ is a dimensionless radial parameter given by

$$\xi = \sqrt{\frac{\mathcal{D}_{LV} r_{LV}}{2\pi G\sigma_0}}\,\frac{r - r_{LV}}{r_{LV}} \tag{2.43}$$

Therefore, considering a simple first order inner Lindblad resonance as the Prometheus 9:8 in the A ring, we should be able to observe a pattern of measured phase with respect to the longitude relative to Prometheus. That pattern should show an m-order symmetry. This constitutes a validation method for a resonance association attempt, as shown in Figure 2.45. The $m = 9$ pattern is implicit while plotting the measured phase versus the longitude relative to Prometheus modulo 40°. The initial wavelength λ_0 of that density wave is much bigger than the uncertainty on the starting location of the wave δr_0, letting us measure the phase of the wave at a given location with an uncertainty of $2\pi\,\frac{\delta r_0}{\lambda_0}$.

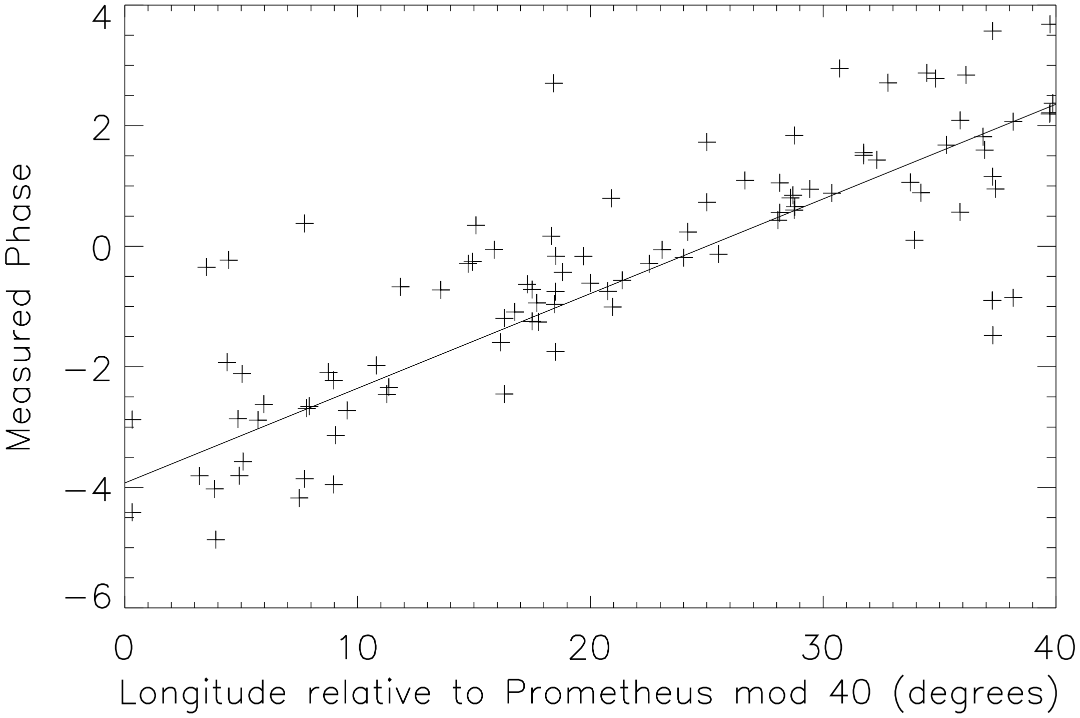

Figure 2.45: Measured phases of the Prometheus 9:8 density wave at r = 129000 km with respect to the longitude relative to Prometheus for individual occultations.

The initial wavelength and the uncertainty on the starting location of the waves in the C ring are of the same order of magnitude (about 1 km, see Section 2.3), and therefore we cannot use the phase of the wave (based on the observation of an m-periodic azimuthal pattern) to validate our resonance associations with a higher confidence. Indeed, even a realignment with presumed circular fiduciary features cannot compensate for that uncertainty: several causes are competing to prevent decreasing it, such as the actual non circularity of some of the reported fiduciary features, the distance of these features from the location of the measurement or the fact that some of these features are not sharp enough to allow a precise detection. For these reasons, our resonance associations remain tentative. For the same reasons, we have not been able to positively identify the effects of the B ring outer edge resonances in the C ring. At places where resonances with the forced mode are located, we could therefore expect a correlation between the excited wave phase and the longitude relative to Mimas, but there again, the uncertainty on the starting radial location of the wave prevents from extracting a trustable value of the phase.

Even if all our tentative resonance associations are correct, and even discounting some wave-like features that do not show the characteristic features of density and bending waves, the majority of waves cannot be associated with a known moon. Furthermore, unseen moons in any of the C ring gaps would produce many more waves than we observe. Some other mechanism is at work producing waves in the relatively low-optical-depth C ring than the classical density waves of the A ring.

Based on the idea that resonant interactions between planetary oscillation modes and ring particles orbits is similar to that between external satellites and the rings, Marley and Porco (1993) described another potential origin for wavelike feature in the rings. However, the locations of the resonances with these internal forcing perturbations do not match the pattern of the observed waves. Other possible origins of the unexplained wavelike features could reside in the existence of numerous relatively small embedded objects. These moonlets could generate wakes, but since the features we observe are not symmetrical, we should better investigate secondary waves excited by resonances with wakes. The same spatial precision argument prevents us from investigating azimuthal dependances at these wavelengths.

2.5.3 Surface Mass Density and Mass Extinction Coefficient Measurements

Rosen et al. (1991b) did not mention wave 33 but suggested that some structure could be associated with the Atlas 2:1 inner Lindblad resonance at $r_L = 87645$ km (Figure 2.11). Then, we can derive the surface mass density from the extracted wavelength of maximum power λ. Both radial and wavelength uncertainties are extracted from the wavelet profiles, allowing to estimate surface mass density and mass extinction coefficient uncertainties.

In addition to the variation of the surface mass density with the ring plane radius, we could extract a mean value for $\frac{\sigma}{m-1}$. In particular for the Atlas 2:1 ILR, since $m = 2$, we estimated a mean surface mass density $\sigma_{mean} = 0.22$ (± 0.03) g cm^{-2} and a mean mass extinction coefficient $\kappa_{mean} = \frac{\tau}{\sigma_{mean}} = 0.19$ (± 0.03) cm^2 g^{-1}.

For a differential particle size distribution[2] $n(a) = n_0 \left(\frac{a_0}{a}\right)^q$ with $a_{min} \leq a \leq a_{max}$, the mass extinction coefficient is defined by

$$\kappa = \frac{\tau}{\sigma} = \frac{\int_{a_{min}}^{a_{max}} n(a) S(a)\,\mathrm{d}a}{\int_{a_{min}}^{a_{max}} n(a) m(a)\,\mathrm{d}a} = \frac{3(4-q)}{4(3-q)} \left(\frac{a_{max}^{3-q} - a_{min}^{3-q}}{a_{max}^{4-q} - a_{min}^{4-q}} \right) \rho^{-1} \tag{2.44}$$

where ρ is the mass density of the particles. Using the power law index estimated by Zebker et al. (1985) for the C ring ($q \sim 3.1$), we find $\kappa \propto \frac{1}{a_{max}}$: the biggest particles are smaller when κ is higher. The mass extinction coefficient is an integrated property of the particle size distribution and varies across the C ring.

Thanks to the resonance associations from Section 2.3, we can also extract mean surface mass densities at these resonance locations in the C ring. Table 2.8 reports mean surface mass densities and mean mass extinction coefficients. Finally, we could estimate $\frac{\sigma}{m-1}$ in the widest wave at 86400 km and evaluate $\frac{\sigma}{m-1}$ to be about 2.35 g cm^{-2}.

Table 2.8: C ring surface-mass densities.

Resonance (order)	Figure	$r_L (r_V)$ (km)	m	(j_1, j_2, j_3, j_4, j_5, j_6)	σ (g cm^{-2})	τ	κ (cm^2 g^{-1})	ξ_d	H (m)	$r_L\ X_{NL}$ (km)
Mimas 4:1 ILR (3)	2.9	74891.8	2	(4,-1,-2,-1,0,0)	0.58 ± 0.09	0.08	0.13 ± 0.03	4.23	4.1 ± 1.0	1.85
Titan -1:0 IVR BW (3)	2.10	77511.3	1	(-1,0,1,0,1,-1)	0.60 ± 0.09	0.10	0.17 ± 0.03	5.14	5.6 ± 1.4	
Atlas 2:1 ILR (1)	2.11	87646.5	2	(2,-1,0,-1,0,0)	0.22 ± 0.03	0.04	0.19 ± 0.04	5.42	1.9 ± 0.4	2.79
Mimas 6:2 ILR (4)	2.12	89883.3	3	(6,-2,-3,-1,0,0)	1.31 ± 0.20	0.37	0.28 ± 0.06	6.61	2.4 ± 0.6	66.2
Pandora 4:2 ILR (2)	2.12	89894.0	3	(4,-2,-1,-1,0,0)	1.42 ± 0.21	0.37	0.26 ± 0.05	6.69	2.4 ± 0.6	99.0

Optical depth τ, derived surface mass densities σ, mass extinction coefficients κ, wave damping length ξ_d, and vertical thickness H of the rings of wavelike structures with associated resonance in the C ring and their resonant argument parameters (Section 2.4.1).

---

[2] The cumulative particle size distribution (number of particles with a radius greater than a) is therefore $N(a) = \int_{a_{min}}^{a_{max}} n(a)\,\mathrm{d}a$.

For the tentative resonance associations we derived values of κ between 0.13 (± 0.03) and 0.28 (± 0.06) cm^2 g^{-1}. In addition, assuming the other wavelike features are spiral density or bending waves with $m > 1$, $\frac{\sigma}{m-1}$ is a lower limit of σ while $\kappa(m-1)$ is an upper limit of κ at that location. We present these limit values in Table 2.9: values for $\kappa(m-1)$ are found between 0.004 and 0.63 cm^2 g^{-1}. We present mass extinction coefficient results in Figure 2.46. Our maximal estimated mass extinction coefficient $\kappa(m-1) = 0.63$ cm^2 g^{-1} (though κ could be smaller than this value if $m \gg 1$) is much higher than the A ring values ($0.01 - 0.02$ cm^2 g^{-1}) and the Cassini Division values ($0.07 - 0.12$ cm^2 g^{-1} from Colwell et al. (2009a)), even if in some locations the upper limit on κ may be lower than in the A ring. We notice that the highest values of mass extinction coefficient limits are mainly found in plateau regions. Therefore, by Equation 2.44, particle sizes may be smaller in these plateaus. This result is in accordance with a recent study from Colwell et al. (2010b). Finally, in contrast to the A ring and the Cassini Division where the mass extinction coefficient is fairly constant, it appears to increase with radius along the C ring. We next turn our attention to the viscosity and thickness of the ring.

Table 2.9: C ring surface mass density constraints.

r (km)	Structure	Figure	$\frac{\sigma}{m-1}$ (g cm^{-2})	τ	$\kappa \times (m-1)$ (cm^{2}g^{-1})
74666	1		5.83	0.04	0.006
74923	3	2.16	0.48	0.05	0.005
74939	4	2.16	0.28	0.13	0.46
76022	5		3.88	0.04	0.011
76234	6	2.17	0.30	0.15	0.50
76435	9	2.18	0.33	0.06	0.19
76539	10		9.21	0.03	0.004
76729	11		0.14	0.07	0.52
80988	13	2.23	1.17	0.13	0.11
81018	14		0.40	0.10	0.25
82010	15	2.24	1.42	0.14	0.10
82061	16	2.26	2.54	0.28	0.11
82209	17	2.25	1.73	0.13	0.08
83633	18		0.45	0.10	0.22
84644	19		1.35	0.11	0.08
84814	20	2.13	1.97	0.44	0.22
84857	21		1.12	0.42	0.38
85450	23		0.55	0.07	0.13
85473	24	2.20	2.77	0.07	0.03
85514	25		0.64	0.07	0.11
85677	27	2.21	0.62	0.29	0.46
86400	28	2.22	2.35	0.47	0.20
86576	29		0.59	0.38	0.63
87189	32	2.29	0.47	0.15	0.33
88736	35		1.77	0.07	0.04
90156	38	2.30	1,94	0.67	0.35
90279	40	2.15	1,14	0.06	0.06

Optical depth τ, and constraints on derived surface mass densities σ and mass extinction coefficients κ of wavelike structures with associated resonance in the C ring.

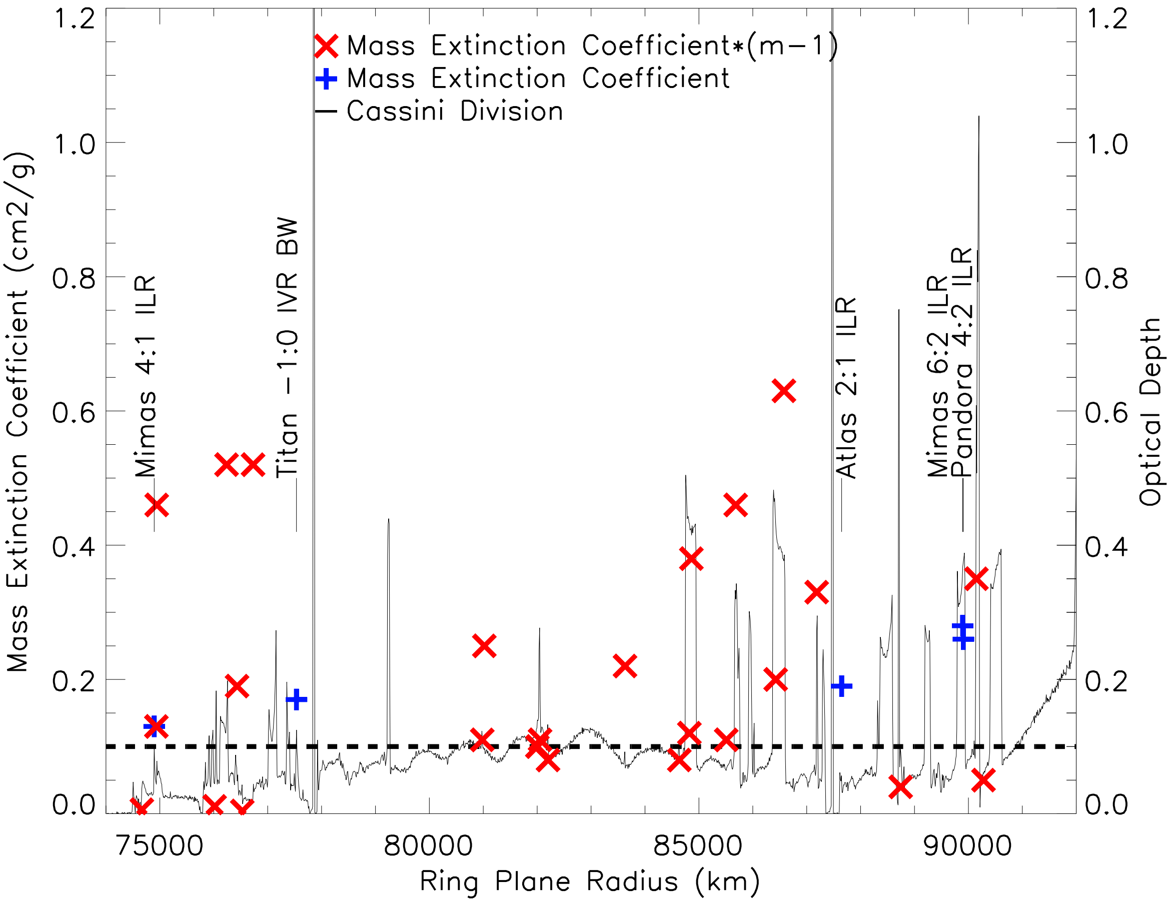

Figure 2.46: Mass extinction coefficient limit values. Actual mass extinction coefficient values, calculated at the associated resonance locations are displayed in blue while upper limits of mass extinction coefficient, estimated from κ $(m-1)$, are shown in red.

In addition, we notice that most of the resonances that are supposed to present higher strength than the ones that match the observed waves have a good reason for not being obvious. Since we are looking at wavelengths of the same order of magnitude as the uncertainty of our radial scale between two occulations, phase analysis of the waves will not be able to provide the authentication of these associations with resonances.

Using the wave damping length defined by Equation 2.43, and using the definition of the ring viscosity given by Shu (1984),

$$\eta \approx \frac{9}{7n\xi^3}\sqrt{\frac{(2\pi G\sigma)^3 r_{LV}}{\mathcal{D}_{LV}}} \tag{2.45}$$

we derive the vertical thickness of the rings H as defined by Tiscareno et al. (2007):

$$H = \frac{1}{n}\sqrt{\frac{2\eta n}{\tau}(1+\tau^2)}. \tag{2.46}$$

Values of the wave damping length and of the vertical thickness of the rings for tentative resonance associations are reported in Table 2.8. We find that the C ring has a height of 1.9 (±0.4) m to 5.6 (±1.4) m, which is consistent with the vertical thickness of the Cassini Division, between 3 and 20 m (Tiscareno et al. (2007) and Colwell et al. (2009a).

Finally, using the limits of the range of the mass extinction coefficients (derived from associated resonances), and assuming a uniform value of this coefficient along the C ring, we can constrain the mass of the C ring between 3.7 (±0.9) $\times 10^{16}$ kg and 7.9 (±2.0) $\times 10^{16}$ kg, which could be represented by a satellite (with a density of 400 kg m^{-3} close to the density of Pan and Atlas) with a radius of 28.0 (±2.3) km to 36.2 (±3.0) km (a little bigger than Pan or Atlas). For comparison, Spilker et al. (2004) estimated the A ring to be equivalent to a 110 km radius icy moon and Charnoz et al. (2010) produced numerical simulations generating a 1.5 $\times 10^{18}$ kg A ring with a similar density (equivalent to a 96 km-radius moon). Colwell et al. (2009a) estimated the Cassini Division mass to 3.1 $\times 10^{16}$ kg, ramp excluded.

2.6 Conclusions

Zebker et al. (1985) estimated values for the upper size cutoffs of the particle size distribution between 2.4 and 5.3 m in the C ring, whereas they measured 7.5 m in the Cassini Division and from 5.0 to 11.2 m in the A ring, based on differential optical depths at radio wavelengths. Colwell et al. (2009a) interpreted the higher mass extinction coefficients in the Cassini Division compared to the A ring as evidence that the upper size cutoff in the Cassini Division is 3-5 times smaller than that in the A ring. Our mass extinction coefficients from the handful of C ring waves with a reasonably firm resonance identification are more in line with those in the Cassini Division than those in the A ring. Though we do not know the wave pattern number m for most waves, taken all together the waves in the C ring suggest that the mass extinction coefficient may be larger than in the Cassini Division and that the particle size distribution has an even smaller upper limit. We can therefore imagine that the particles composing these different rings have either different origins or that their size distributions are not primordial and have evolved differently.

The highest mass extinction coefficients in the C ring appear to be in the plateaus. The plateaus themselves are of unknown origin, and the different size distributions could be a clue to their origin or evolution.

The C ring and Cassini Division are generally similar in a number of respects (color, optical depth, and, apparently, particle size distribution), but are separated by the broad and massive B ring. If they do not have the same age and origin, the C ring and Cassini

Division may have a common mode of origin that has lead to their gross overall similarities. Like the origin of the ring itself, the origins of most of the wavelike structures in the C ring remain unresolved. Although many of the waves have been observed from the Voyager epoch to the Cassini epoch and their structures appear very similar to density and bending waves, most do not appear to share the prominent association with strong resonances with Saturn's moons that characterize their counterparts in the A ring and Cassini Division. Explaining these structures and their sources is a necessary step in understanding the complexity and variety of the rings' evolution.

CHAPTER 3

WAVES IN THE B RING AND THE CASSINI DIVISION

3.1 Introduction

The methods detailed in Chapter 2 can totally be applied to other parts of the rings. In this Chapter, we are investigating the presence of waves excited by resonances with external satellites in the B ring and in the Cassini Division. Some of the waves we describe here require a few comments about similar waves in the inner A ring that we will investigate as well. We mentioned in Chapter 1 some similarities between the C ring and the Cassini Division, in optical depth, in particular: these two faint regions have the lowest optical depth of the main rings, around 0.1. The B ring however is much more opaque and presents an optical depth around 1. Despite their focus on the A ring, Rosen et al. (1991a,b) analyzed the Voyager data for some isolated waves in the other rings and provide interesting results. Tiscareno et al. (2007) and Colwell et al. (2009a) also derived some physical parameters of the rings from the analysis of density waves.

3.2 Observations

Cassini UVIS occultation data are described in Chapter 1 while the analysis techniques are the ones from Chapter 2. As stated in this previous Chapter, we will mainly focus on the α Virginis, ζ Orionis and β Centauri occultations, which provide the best signal-to-noise ratios.

3.3 Resonances

Using the previous Chapter tools, we estimate the theoretical positions of the resonances with the external satellites in the B ring (Table 3.1) and in the Cassini Division (Table 3.2). In addition to the resonance locations r_L, we present the resonance strengths and their $r_L\ X_{NL}$, distances at which the excited waves become non-linear. Resonances are displayed sorted by strength.

Table 3.1: Strongest Inner Lindblad Resonances in the B ring.

Resonance	r_L (km)	r_L X_{NL} (km)	T^L_{lm}/σ ($\mathrm{cm}^4/\mathrm{s}^2$)	Figure
Mimas 2:1 ILR	117553.7		$-3.31\ 10^{19}$	
Janus 3:2 ILR	115944.0	0.1	$-2.40\ 10^{17}$	
Mimas 4:2 ILR	117347.0	0.1	$-1.73\ 10^{17}$	3.1
Janus 2:1 ILR	96235.1	0.1	$-6.15\ 10^{16}$	3.2
Epimetheus 3:2 ILR	115980.6	0.3	$-1.90\ 10^{16}$	
Enceladus 3:1 ILR	115203.4	0.8	$-1.09\ 10^{16}$	
Epimetheus 2:1 ILR	96265.2	0.5	$-4.86\ 10^{15}$	3.2
Prometheus 4:3 ILR	115314.7	0.7	$-3.26\ 10^{15}$	
Pandora 4:3 ILR	117237.4	0.8	$-2.48\ 10^{15}$	3.3
Prometheus 3:2 ILR	106772.2	0.9	$-1.53\ 10^{15}$	
Pandora 3:2 ILR	108546.8	1.1	$-1.16\ 10^{15}$	
Mimas 6:3 ILR	117277.6	1.6	$-6.30\ 10^{14}$	3.3
Janus 6:4 ILR	115863.3	1.6	$-4.05\ 10^{14}$	
Janus 5:3 ILR	108117.2	2.4	$-1.43\ 10^{14}$	3.4
Mimas 5:2 ILR	101311.1	2.6	$-1.07\ 10^{14}$	
Epimetheus 6:4 ILR	115900.0	3.9	$-6.50\ 10^{13}$	

Resonance	r_L (km)	$r_L\ X_{NL}$ (km)	T^L_{lm}/σ (cm^4/s^2)	Figure
Janus 4:2 ILR	95980.0	3.4	$-3.88\ 10^{13}$	3.5
Epimetheus 5:3 ILR	108151.4	5.8	$-2.29\ 10^{13}$	3.4
Epimetheus 4:2 ILR	96010.2	8.4	$-6.23\ 10^{12}$	3.5

$r_L X_{NL}$ is the distance at which the wave becomes nonlinear. T^L_{lm} is the torque exerted on a fluid disk by a satellite at an Inner Lindblad Resonance. These quantities are depending on the surface mass density σ. Nearby structures are mentionned in the last column.

Two waves of the inner A ring are reported with the Cassini Division resonances: the Atlas 6:5 ILR and the Prometheus 11:9 ILR.

Table 3.2: Strongest Inner Lindblad Resonances in the Cassini Division.

Resonance	r_L (km)	$r_L\ X_{NL}$ (km)	T^L_{lm}/σ ($\mathrm{cm}^4/\mathrm{s}^2$)	Figure
Prometheus 5:4 ILR	120304.0	0.5	$-5.89\ 10^{15}$	3.6
Janus 7:5 ILR	121247.6	1.2	$-8.61\ 10^{14}$	3.8
Epimetheus 7:5 ILR	121286.0	2.9	$-1.38\ 10^{14}$	3.8
Atlas 6:5 ILR	122063.4	8.9	$-1.56\ 10^{13}$	3.15
Pan 7:6 ILR	120669.3	8.5	$-1.25\ 10^{13}$	3.9
Atlas 5:4 ILR	118831.1	11.3	$-1.03\ 10^{13}$	3.10
Pan 6:5 ILR	118454.1	10.9	$-8.52\ 10^{12}$	3.11
Pandora 9:7 ILR	120036.9	11.8	$-5.45\ 10^{12}$	3.12
Prometheus 11:9 ILR	122073.8	11.4	$-5.03\ 10^{12}$	3.15
Prometheus 10:8 ILR	120278.2	14.2	$-3.37\ 10^{12}$	3.13
Pandora 9:7 ILR	118065.6	18.7	$-1.97\ 10^{12}$	3.12

$r_L X_{NL}$ is the distance at which the wave becomes nonlinear. T^L_{lm} is the torque exerted on a fluid disk by a satellite at an Inner Lindblad Resonance. These quantities are depending on the surface mass density σ. Nearby structures are mentionned in the last column.

These strength Tables present all the resonances that excite stronger torques than the weakest features we observe in our analysis. Practically, we truncate the tables for torque values above $-2 \times 10^{12} \mathrm{cm}^4/\mathrm{s}^2$.

3.4 Results

Our wavelet analysis produced a list of observable features that we will describe as we detail the resonance list. For the resonances for which we will be able to confirm a wave association, we will determine a surface mass density value and a mass extinction coefficient, leading to a measure of the vertical thickness of the rings at the feature location.

3.4.1 B Ring Resonances

- The Mimas 2:1 ILR is supposed to be the strongest resonance around the B ring outer edge. This resonance is shaping the abrupt outer edge of the B ring (Porco et al. (1984a) and Spitale et al. (2008)).
- The second strongest resonance, the Janus 3:2 ILR, is located in a very opaque region of the B ring. The photon counts are very close to zero in these regions, preventing us from observing any wave. Some other resonances from Table 3.1 are in similar locations: the Epimetheus 3:2 ILR, the Enceladus 3:1 ILR, the Prometheus 4:3 ILR,

the Prometheus and Pandora 3:2 ILRs, the Janus and Epimetheus 6:4 ILRs and the Mimas 5:2 ILR.

- The Mimas 4:2 ILR coincides with a visible signature in the α Virginis, rev. 34, occultation (Figure 3.1). However, that wave might be perturbed by possible reflections on the close outer edge of the B ring. In addition, the wave source location seems quite interior to the theoretical resonance location. These uncertainties will not allow a determination of a surface mass density value with a good confidence.
- The Janus 2:1 ILR is certainly the clearest and longest wave in the B ring, propagating in the outward direction (Figure 3.2). It has been analyzed from Voyager data by Rosen et al. (1991b). The Epimetheus 2:1 ILR is just 30 km exterior to it, and therefore most of the wave is a superposition of the resonances due to these two coorbital satellites that are swapping their orbits every 4 years (see Chapter 2, Lissauer et al. (1985) and Spitale et al. (2006)). The Janus 2:1 ILR wave is clearly visible in every occultations. While applying the dispersion relation to this wave, we will consider that the Epimetheus contribution does not perturb the Janus 2:1 ILR derived surface mass density.
- The Pandora 4:3 ILR is just a few kilometers away interior to the B ring outer edge, at 117237 km, while the Mimas 6:3 ILR is located just 40 km farther, perturbing the Pandora 4:3 ILR wave (Figure 3.3) and preventing us from estimating a reliable surface mass density.

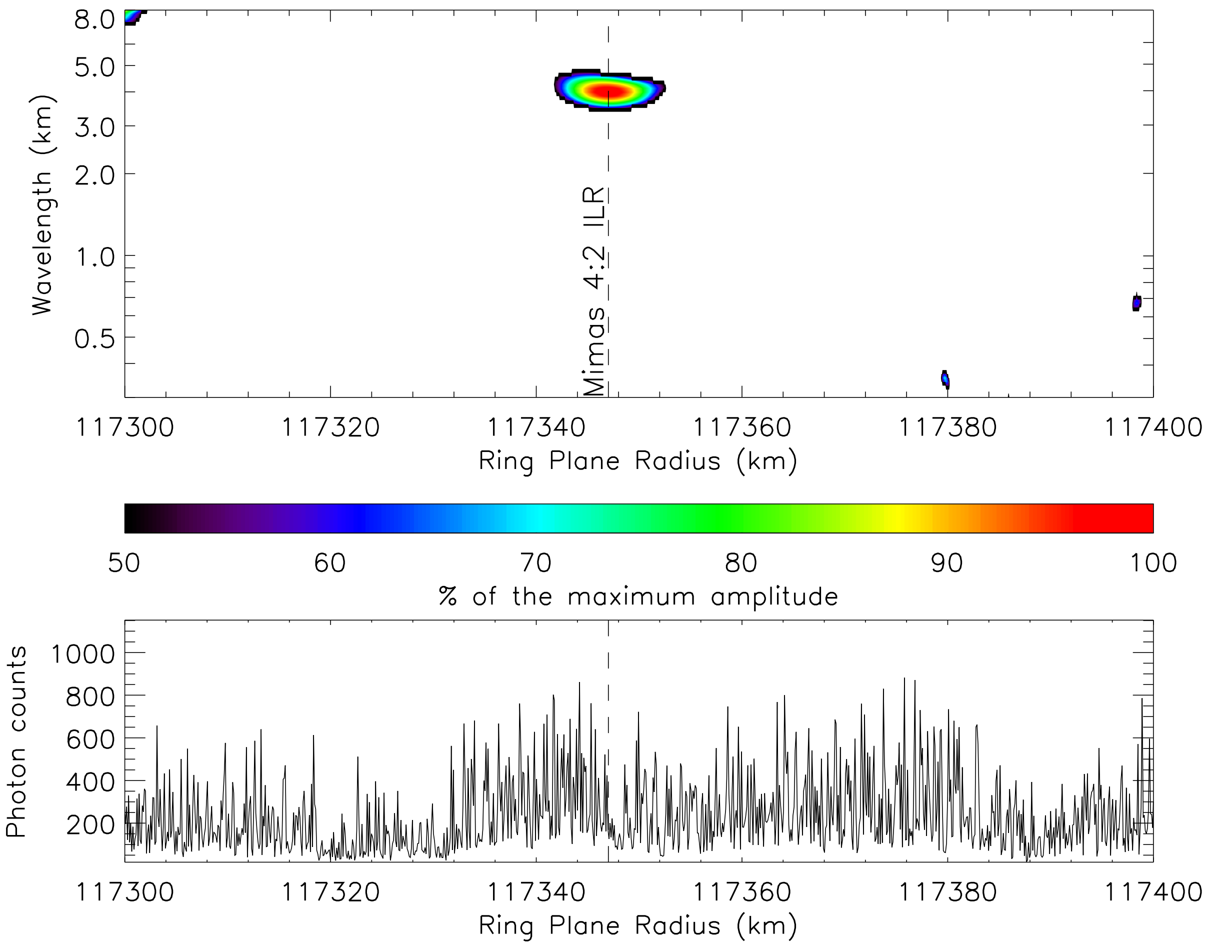

Figure 3.1: WWZ wavelet power profile computed from the α Virginis, rev. 34, occultation of the Mimas 4:2 ILR region. The lower panel shows the photon count rates.

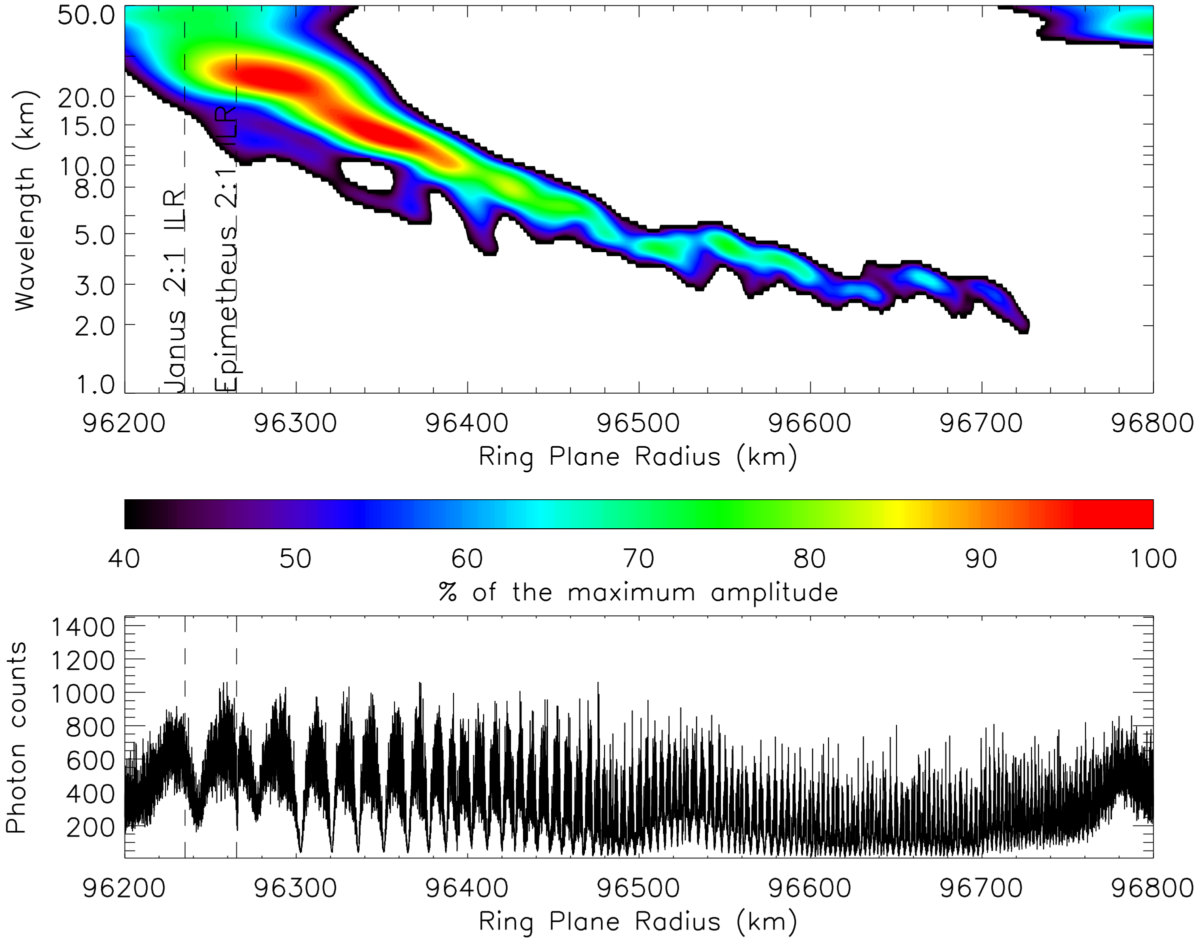

Figure 3.2: Co-added WWZ wavelet power profile computed from individual occultation profiles of α Virginis and β Centauri occultations of the Janus 2:1 ILR. The lower panel shows the α Virginis, rev. 34 photon count rates.

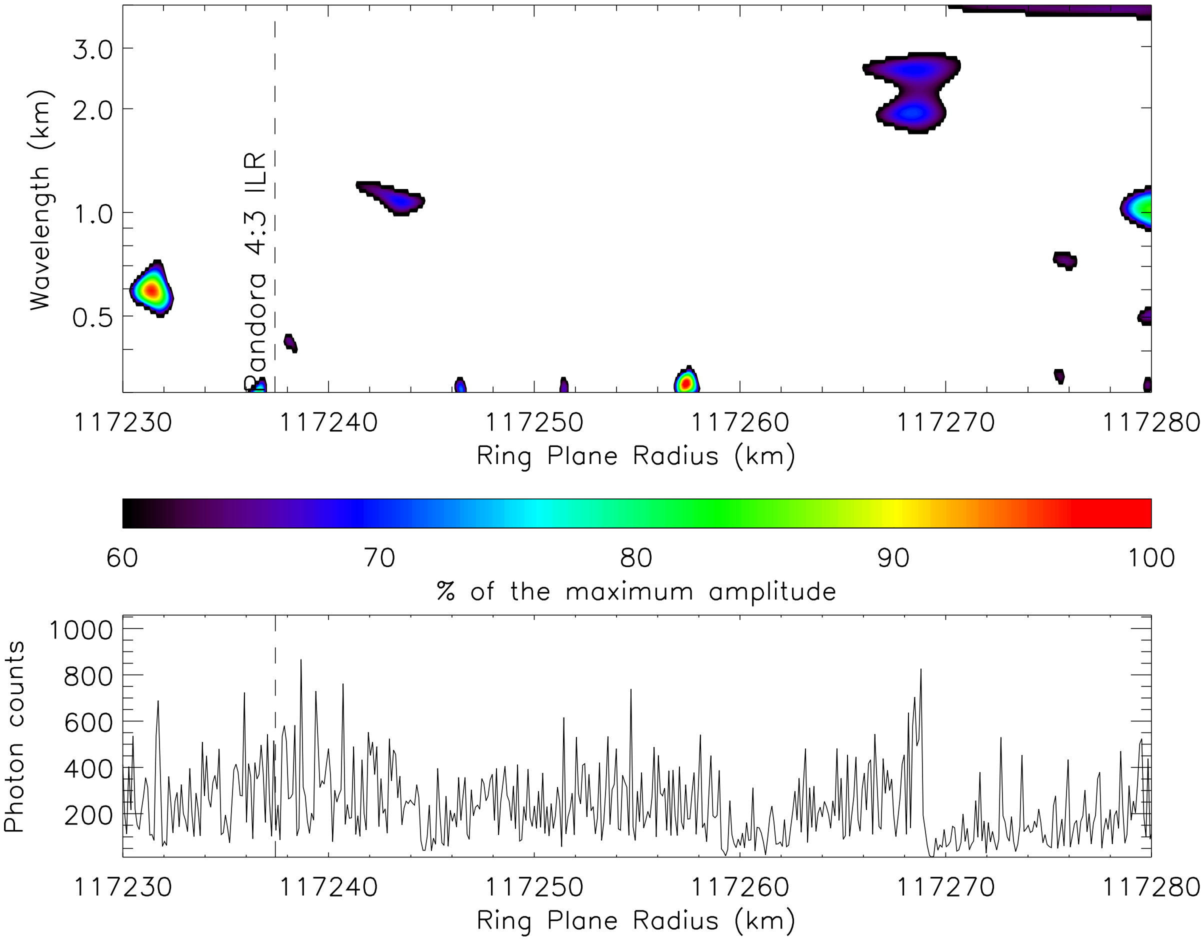

Figure 3.3: WWZ wavelet power profile computed from the α Virginis, rev. 34, occultation of the Pandora 4:3 ILR region. The lower panel shows the photon count rates.

- The Janus 5:3 ILR is located in an opaque region and becomes visible a few kilometers away (likely propagating in the outward direction). The Epimetheus 5:3 ILR is located 34 km further and perturbs the reading of the wavelength associated to the Janus 5:3 ILR (Figure 3.4).

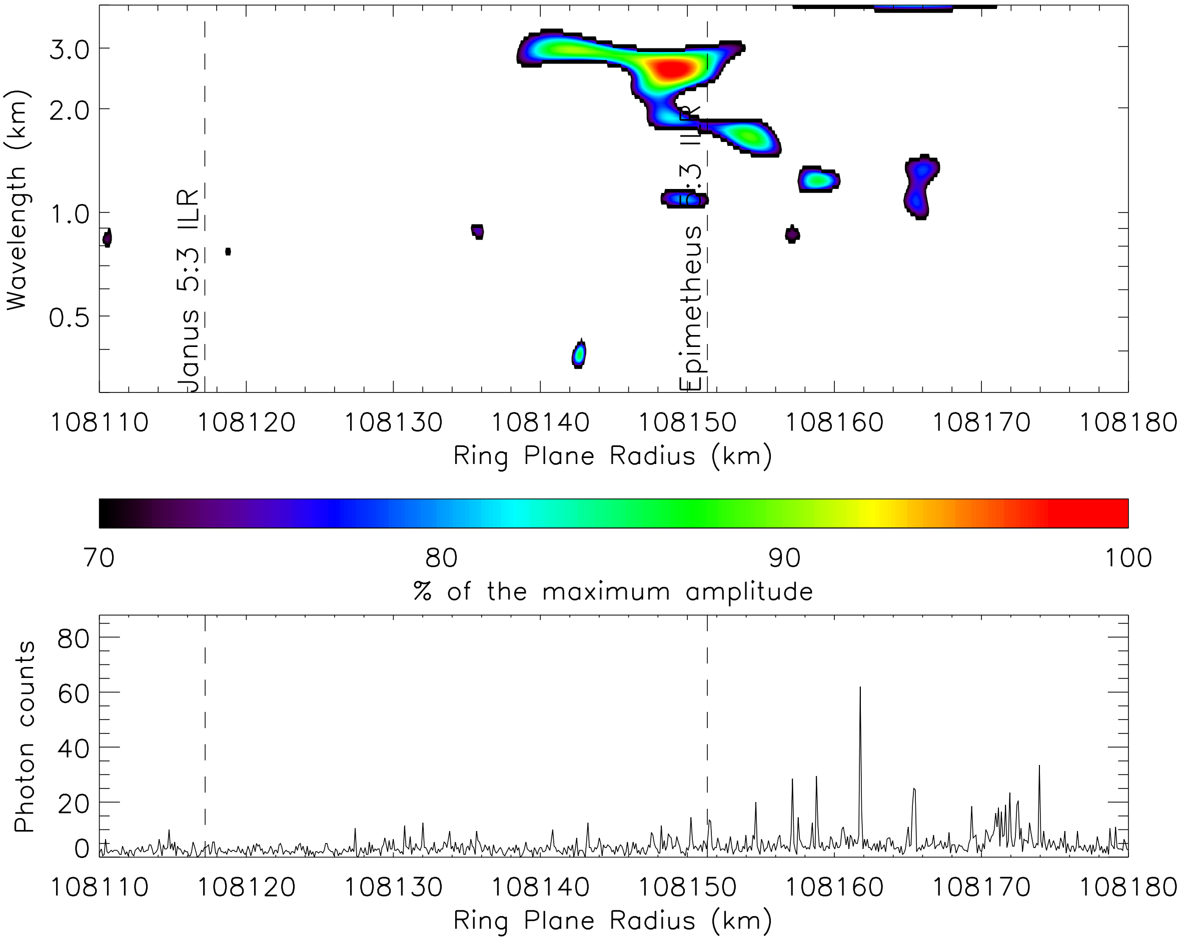

Figure 3.4: WWZ wavelet power profile computed from the α Virginis, rev. 34, occultation of the Janus 5:3 ILR region. The lower panel shows the photon count rates.

- The Janus and Epimetheus 4:2 ILR wavelet profiles show some features that cannot be further analyzed in order to derive surface mass density estimates, despite an outward trend (Figure 3.5).

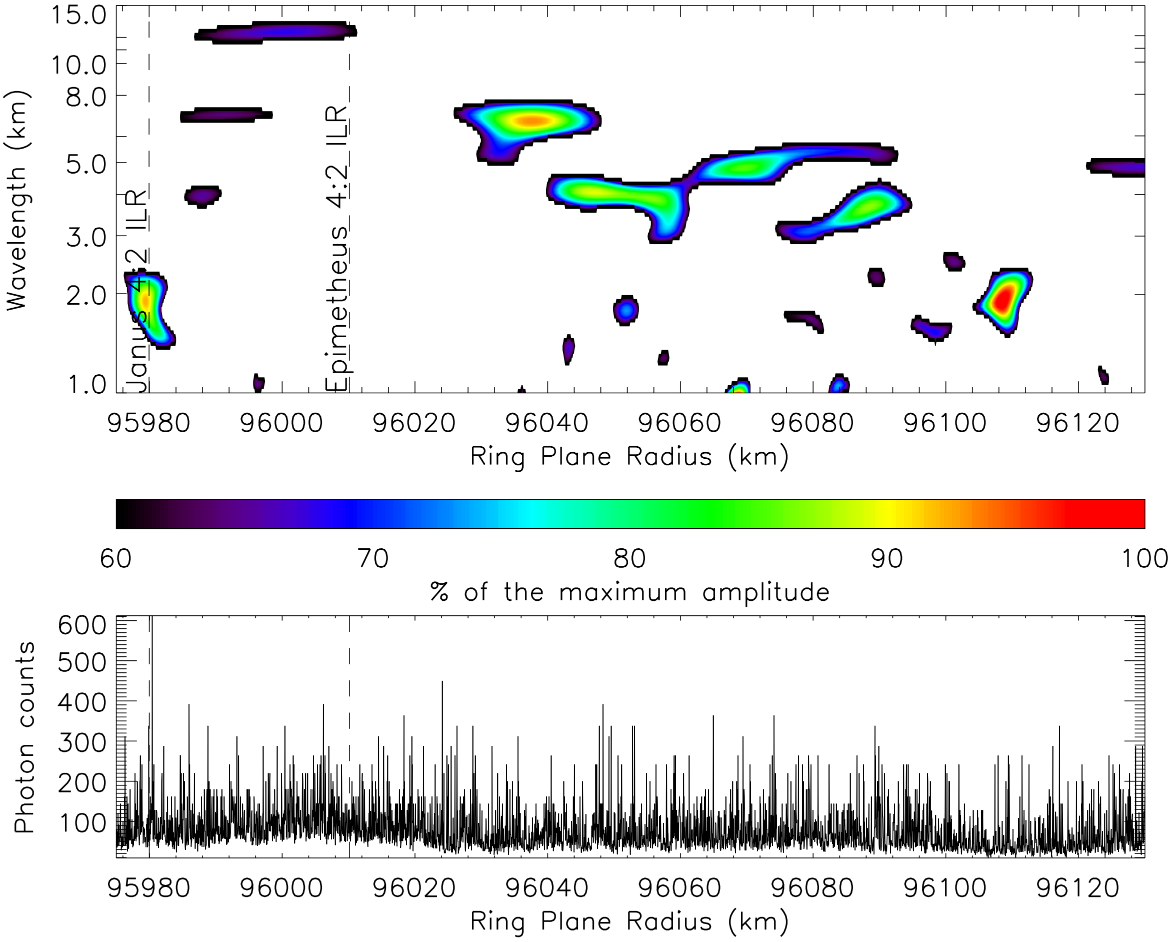

Figure 3.5: WWZ wavelet power profile computed from the α Virginis, rev. 30, occultation of the Janus 4:2 ILR region. The lower panel shows the photon count rates.

The Janus 2:1 ILR provides the only surface mass density estimation that we can get for the B ring.

3.4.2 Cassini Division Resonances

However, the Cassini Division, very similar to the C ring in terms of optical depth, allows us to observe more waves excited by associated resonances. Most of these Cassini Division waves are studied in detail in Colwell et al. (2009a), providing estimates of the physical properties of the Cassini Division. In particular, Colwell et al. (2009a) estimated the surface mass density to be between 0.98 and 15.4 g cm^{-2}. In the inner A ring, the Pandora 5:4 ILR (Porco et al., 2005) also excites a clear outward propagating density wave.

- The Prometheus 5:4 ILR is the strongest visible wave in the Cassini Division. Though the associated feature is not the clearest (Figure 3.6), we note that the Pandora 5:4 ILR is one of the brightest signature in the inner A ring, just outside the Cassini Division ramp (Figure 3.7). We can explain this difference in behavior by an environmental difference: the Prometheus 5:4 ILR coincides with the inner edge of the Barnard Gap: therefore, the excited wave is propagating in a medium where the ring material is more disperse.

- The Janus and Epimetheus 7:5 ILRs are separated by 38 km and located in the Cassini Division ramp (Figure 3.8). It appears that the wave source cannot coincide with the Epimetheus 7:5 ILR resonance.

- The Pan 7:6 ILR presents a clear outward direction of propagation (Figure 3.9). Its wave source corresponds to the theoretical value and its calculated r_L X_{NL} = 10.9

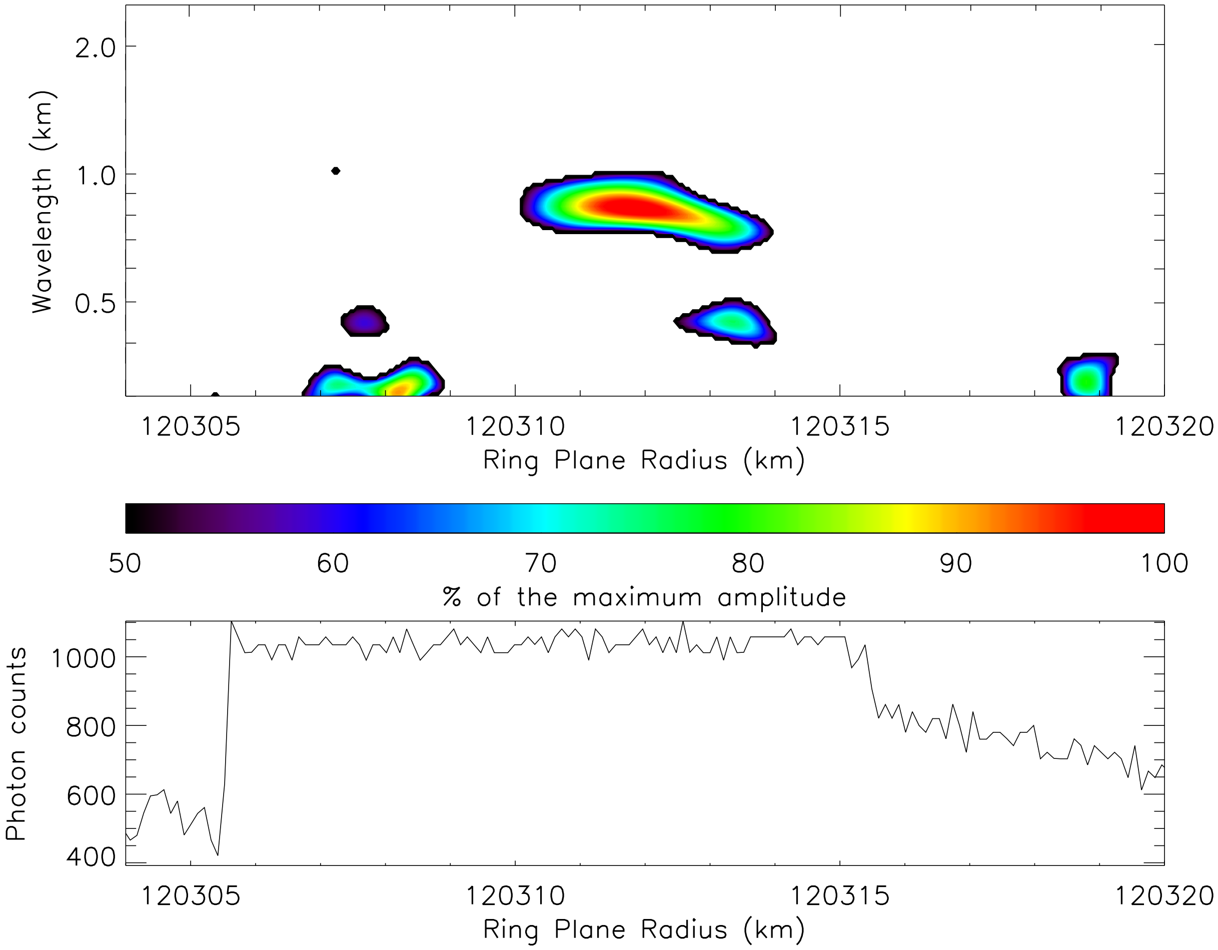

Figure 3.6: WWZ wavelet power profile computed from the α Virginis, rev. 34, occultation of the Prometheus 5:4 ILR region in the Barnard Gap. The lower panel shows the photon count rates.

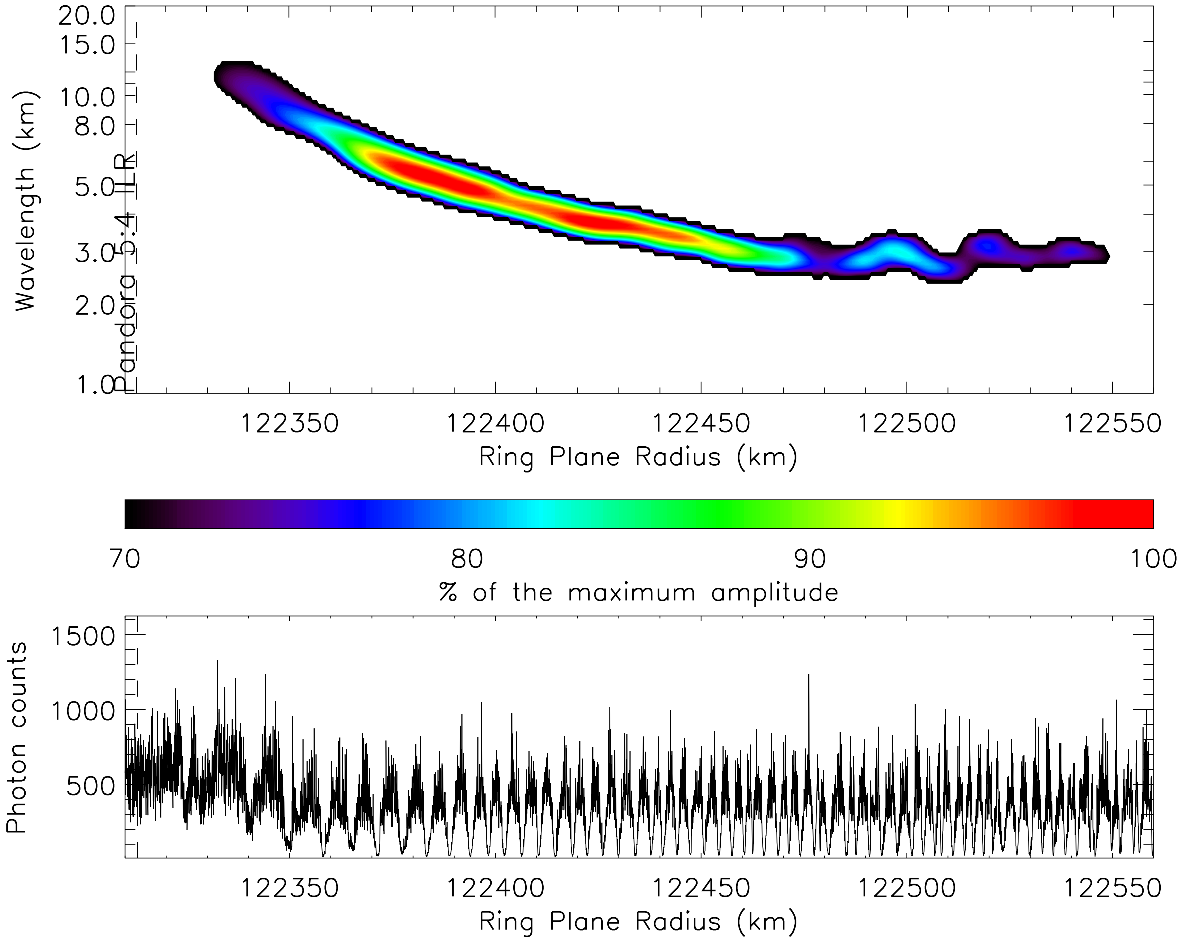

Figure 3.7: WWZ wavelet power profile computed from the α Virginis, rev. 34, occultation of the Pandora 5:4 ILR region (inner A ring). The lower panel shows the photon count rates.

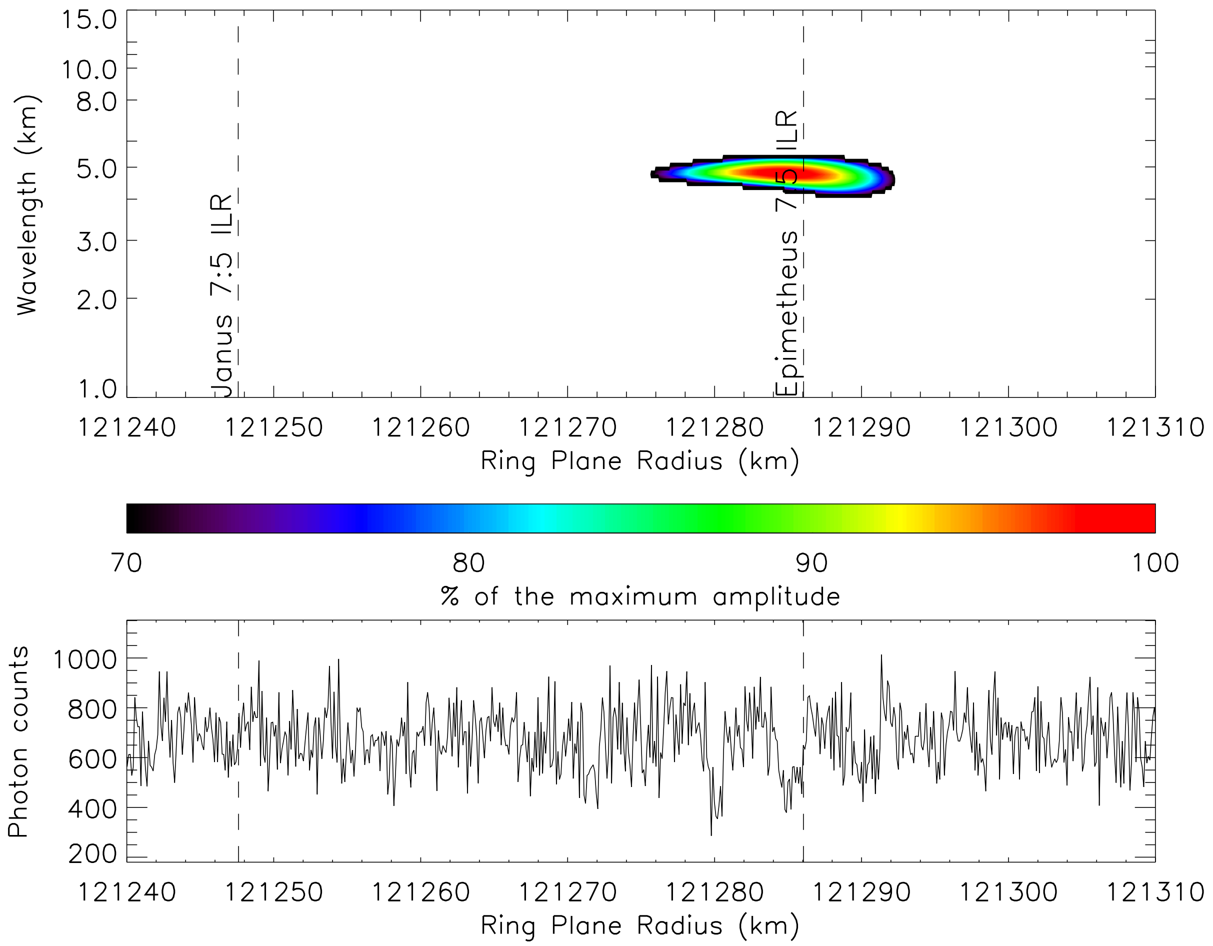

Figure 3.8: WWZ wavelet power profile computed from the α Virginis, rev. 34, occultation of the Janus 7:5 ILR region. The lower panel shows the photon count rates.

km-value corresponds to the observed distance at which the wave becomes non-linear.

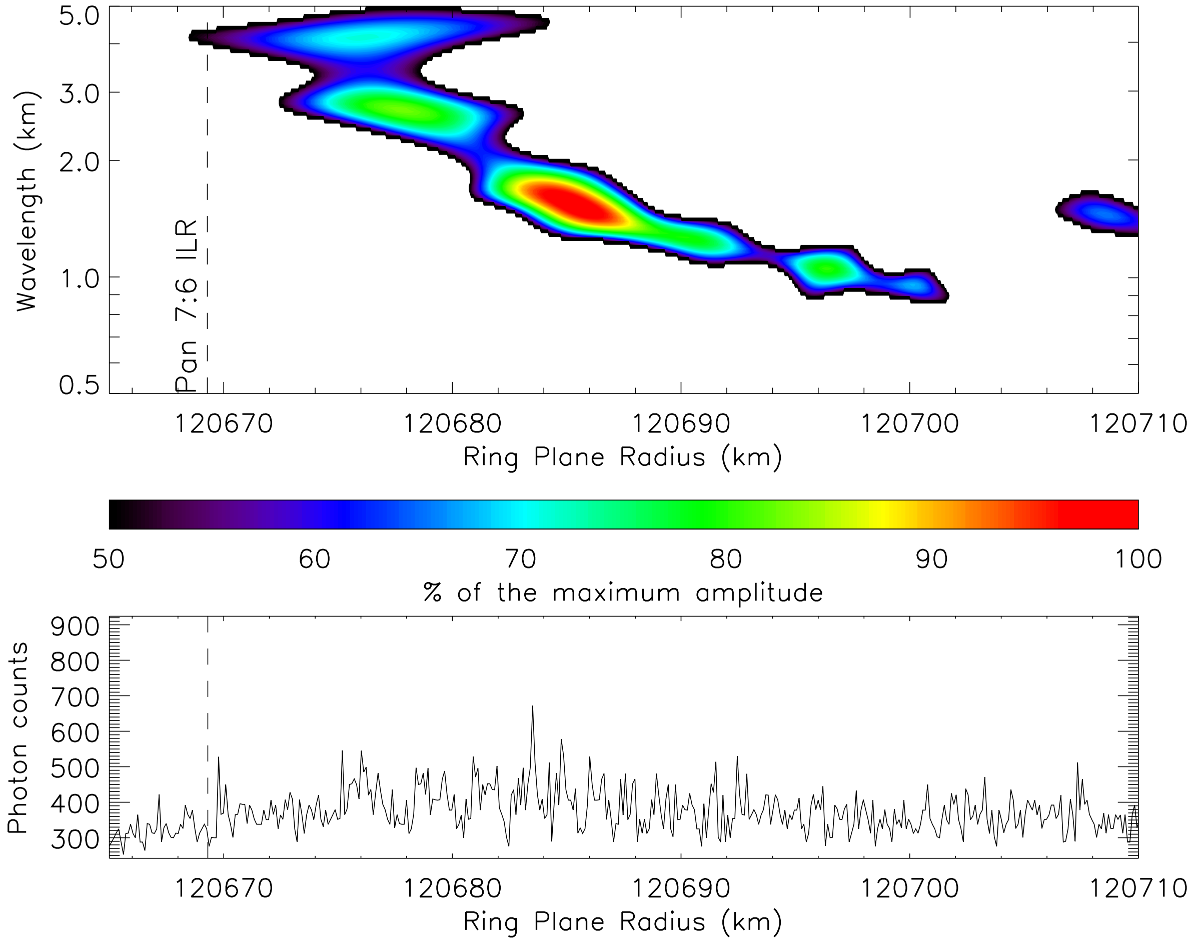

Figure 3.9: Co-added WWZ wavelet power profile computed from individual occultation profiles of α Virginis and β Centauri occultations of the Pan 7:6 ILR. The lower panel shows the α Virginis, rev. 34 photon count rates.

- The Atlas 5:4 ILR also propagates outward (Figure 3.10) and has an expected $r_L\, X_{NL} =$ 2.9 km, consistent with the data.

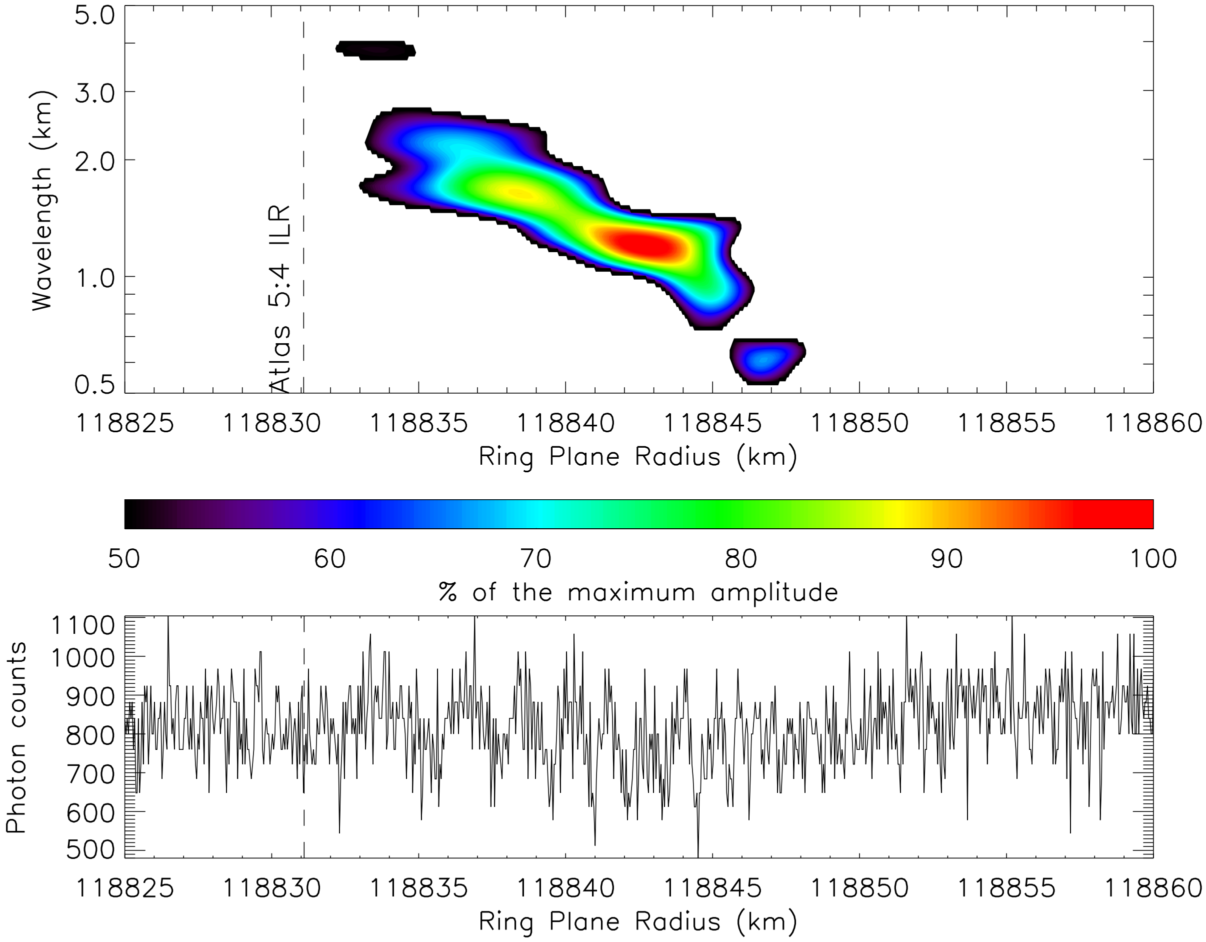

Figure 3.10: Co-added WWZ wavelet power profile computed from individual occultation profiles of α Virginis and β Centauri occultations of the Atlas 5:4 ILR. The lower panel shows the α Virginis, rev. 34 photon count rates.

- The Pan 6:5 ILR is propagating outward (Figure 3.11) and has an expected $r_L\ X_{NL} = 1.2$ km, consistent with the data.

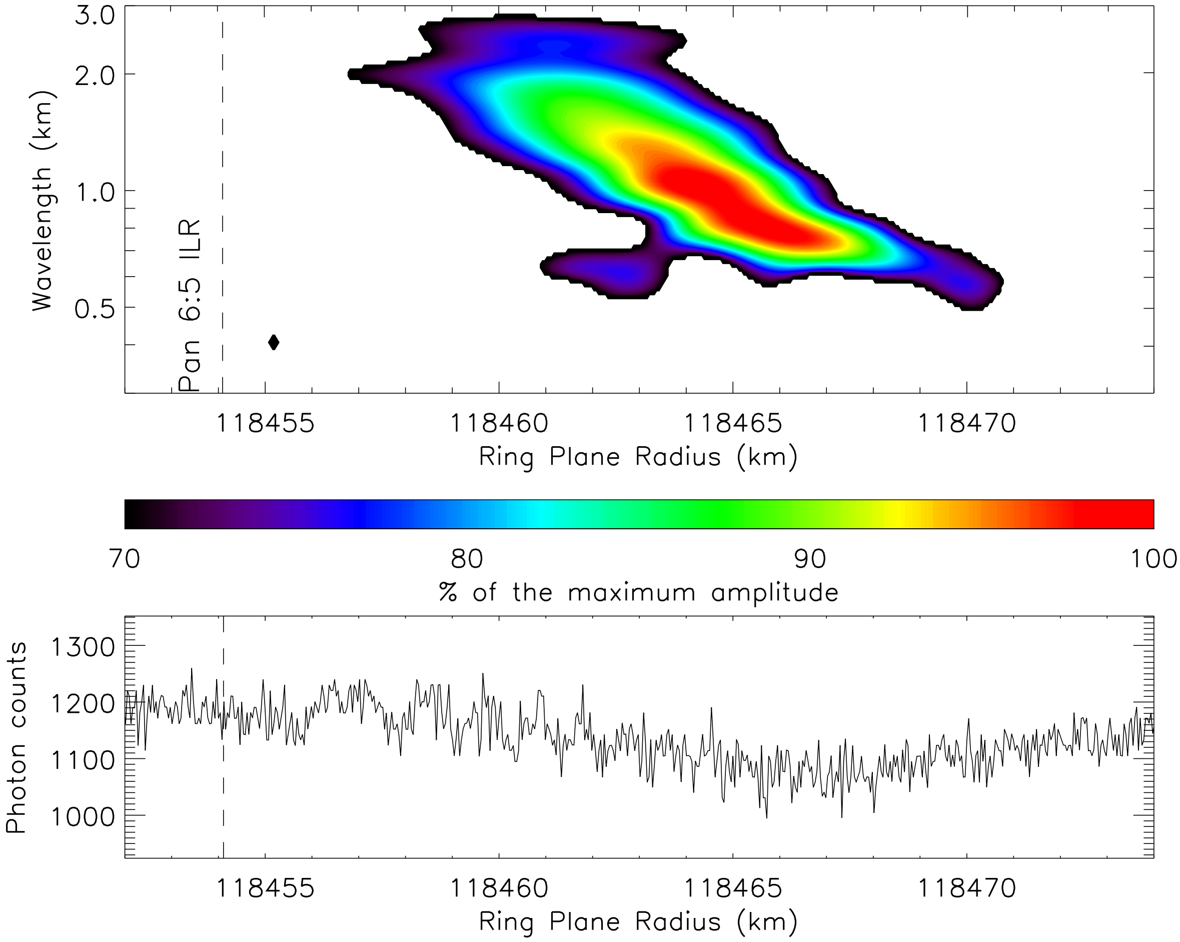

Figure 3.11: Co-added WWZ wavelet power profile computed from individual occultation profiles of α Virginis and β Centauri occultations of the Pan 6:5 ILR. The lower panel shows the α Virginis, rev. 34 photon count rates.

- The Pandora 9:7 ILR is located in the R10 ringlet in the Laplace Gap (Figure 3.12). The resonance theoretical location seems to coincide with a ramp at the inner edge of the ringlet. Its $r_L\ X_{NL}$ is about 8.9 km.

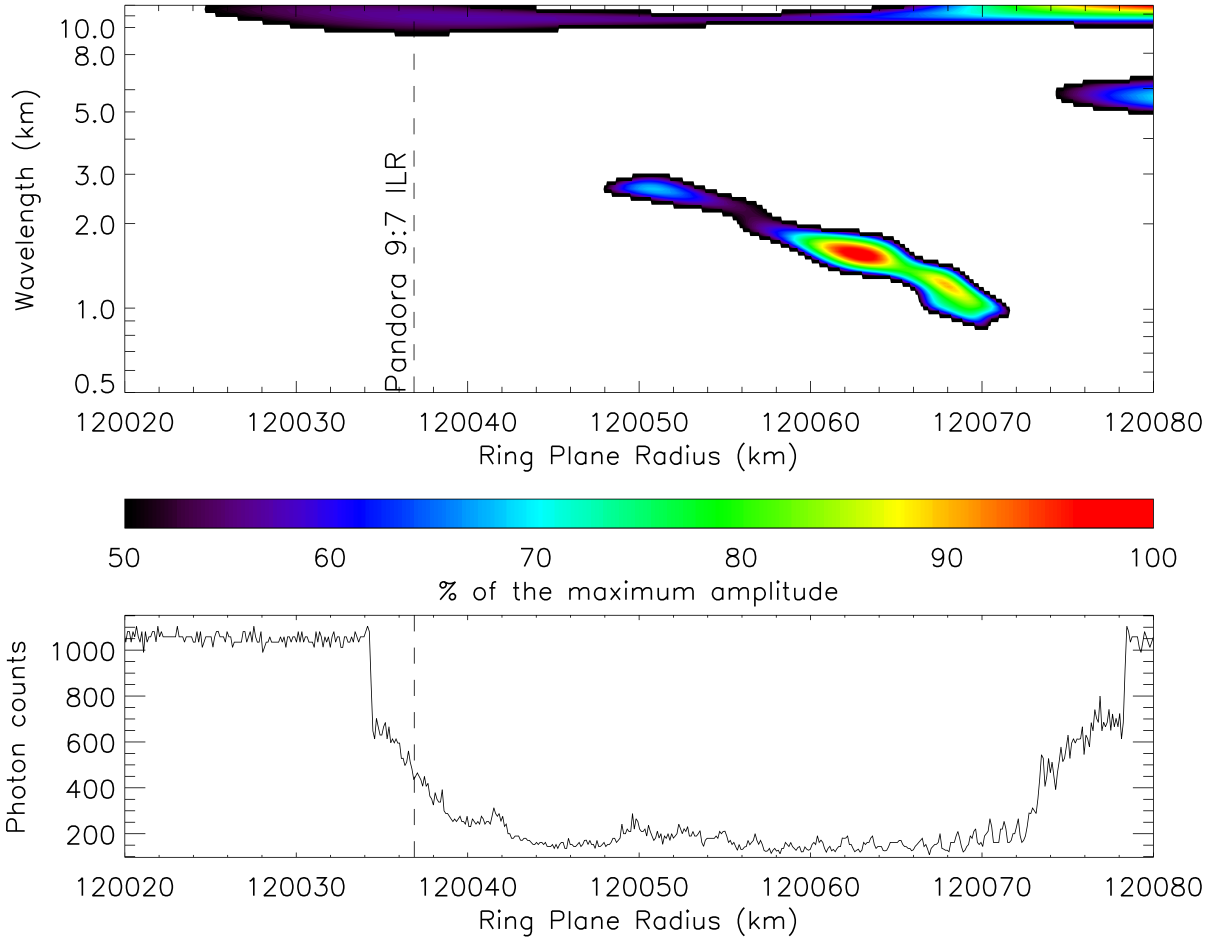

Figure 3.12: Co-added WWZ wavelet power profile computed from individual occultation profiles of α Virginis and β Centauri occultations of the Pandora 9:7 ILR. The lower panel shows the α Virginis, rev. 34 photon count rates.

- The Prometheus 10:8 ILR presents a double signature with an outward trend (Figure 3.13). Something is apparently perturbing the excitement of that wave. However, the predicted $r_L\ X_{NL} = 8.5$ km seems consistent with the observed feature.

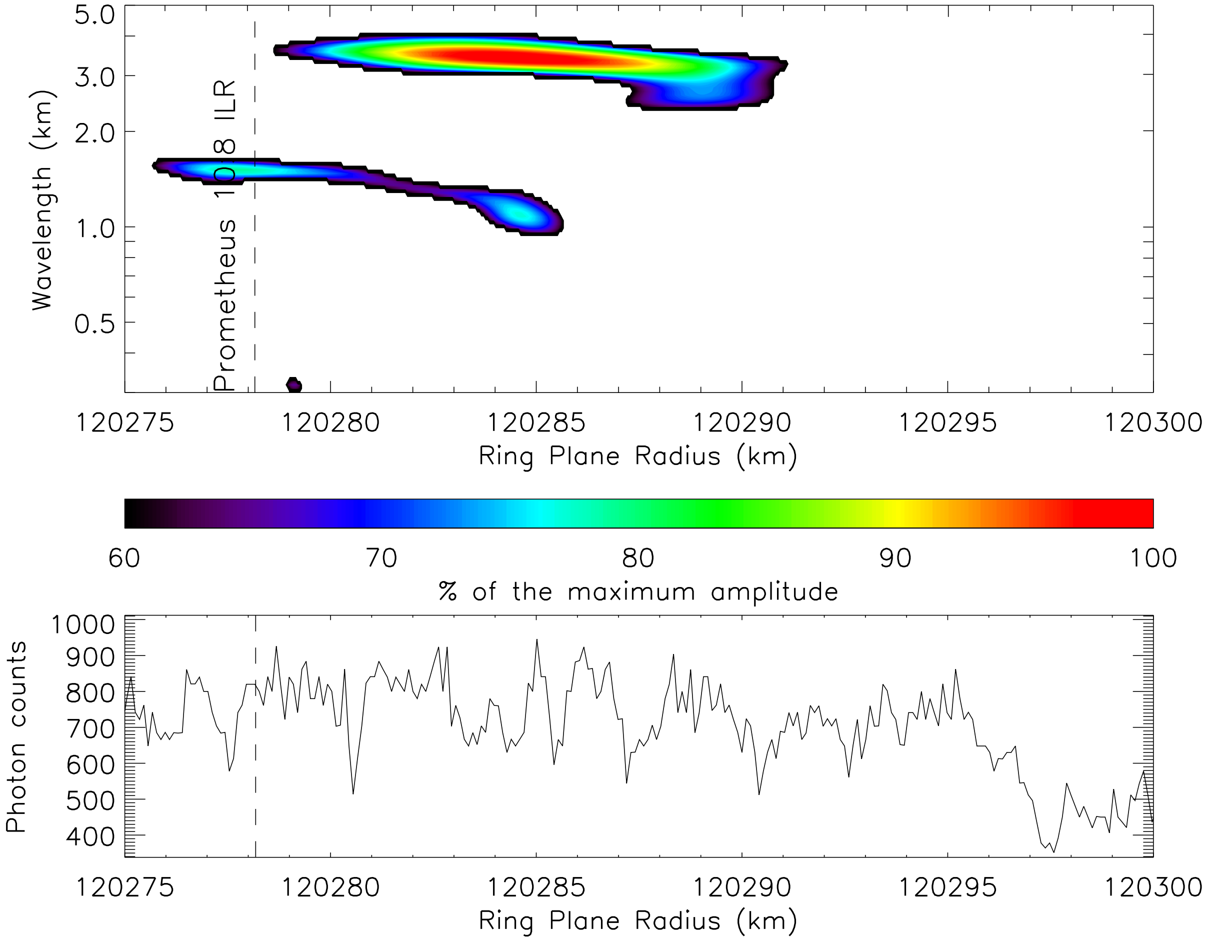

Figure 3.13: WWZ wavelet power profile computed from the α Virginis, rev. 34, occultation of the Prometheus 10:8 ILR region. The lower panel shows the photon count rates.

- The Prometheus 9:7 ILR presents an outward propagating signature with $r_L\ X_{NL} = 0.5$ km, matching the observed wave (Figure 3.14).

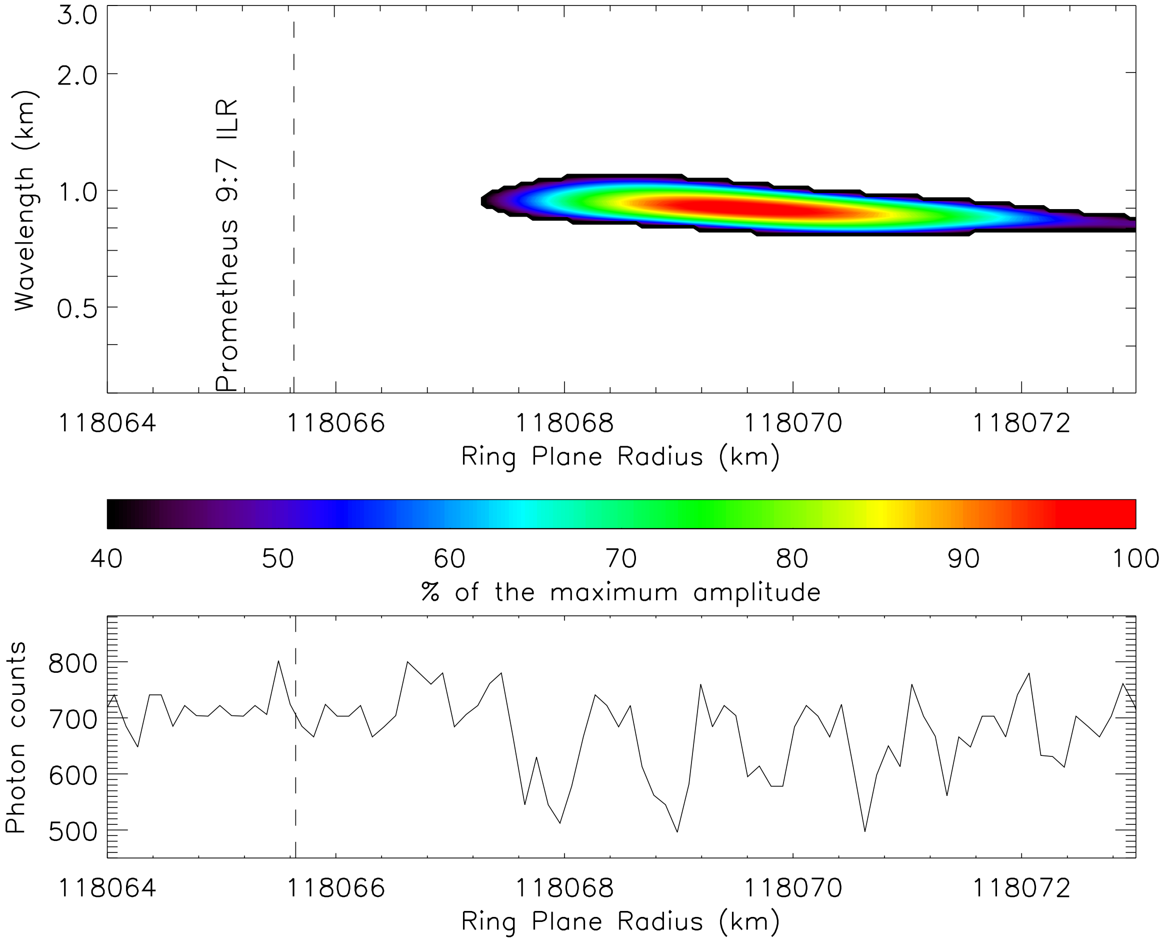

Figure 3.14: WWZ wavelet power profile computed from the α Virginis, rev. 34, occultation of the Prometheus 9:7 ILR region. The lower panel shows the photon count rates.

Just at the A ring inner border, we observed a very strong signature in the region of the Atlas 6:5 ILR and Prometheus 11:9 ILR (Figure 3.15), separated by 11 km. However, the fact that $r_L\ X_{NL}$ is greater than 14 km for both these resonances is more in favor of an association with the Atlas 6:5 ILR.

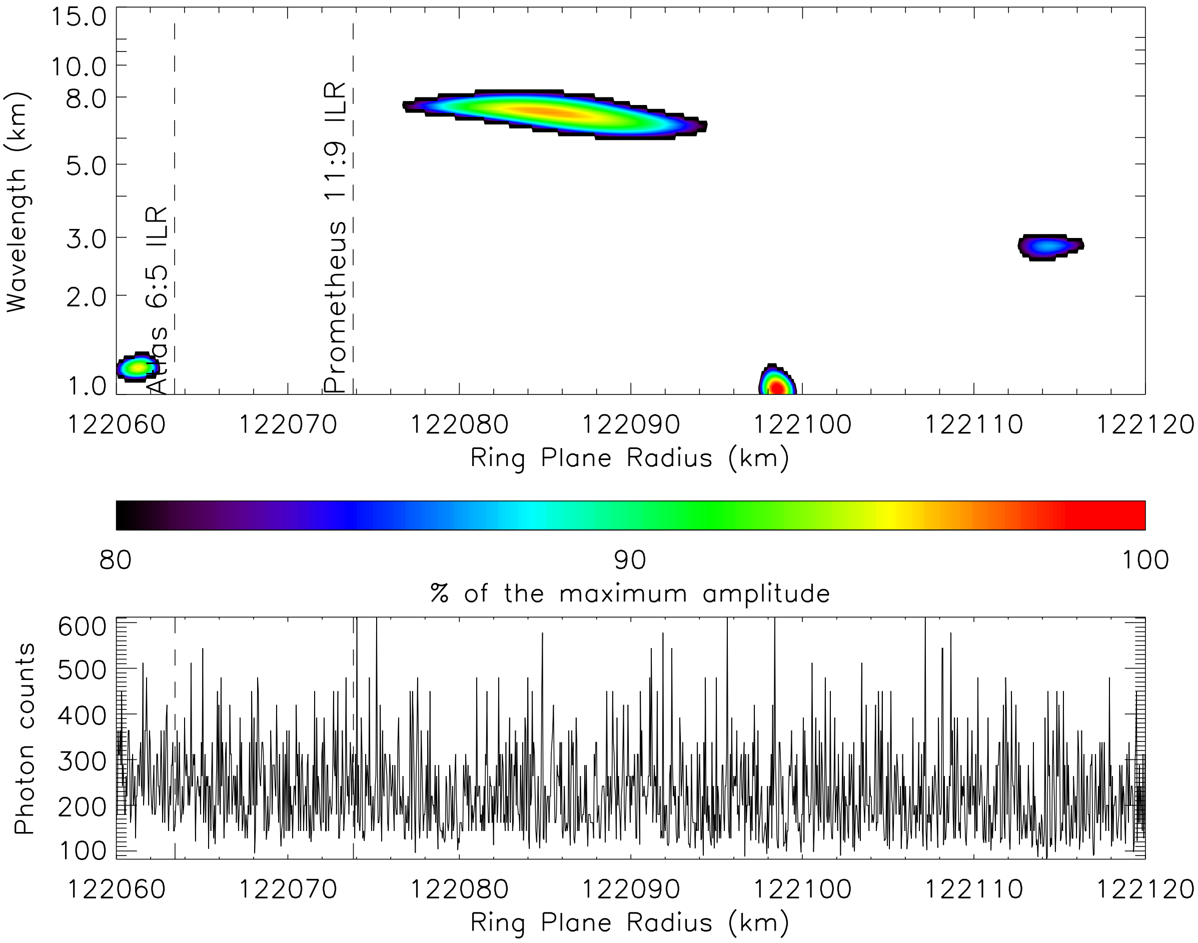

Figure 3.15: WWZ wavelet power profile computed from the α Virginis, rev. 34, occultation of the Atlas 6:5 ILR region. The lower panel shows the photon count rates.

3.4.3 Associated Waves

Associated waves with resonances and derived physical parameters are displayed in Table 3.3. The comparison of the theoretical and observed waves sources is a good indicator of the validity of an association (though in the case of the Janus 2:1 ILR, this measure might be perturbed by the close Epimetheus 2:1 ILR). Surface mass densities, mass extinction coefficients and vertical thickness of the rings are presented in that Table.

Table 3.3: Surface-mass densities.

Resonance	Region	r_{th} (km)	r_L (km)	σ (g cm^{-2})	τ	κ (cm^2 g^{-1})	H (m)
Janus 2:1 ILR	B ring	96235.1	96274.0 (±45)	62.1 (±9.3)	0.95 (±0.1)	0.02 (±0.004)	9.5 (±3)
Prometheus 9:7 ILR	CD	118065.6	118042.7 (±20)	0.72 (±0.12)	0.13 (±0.02)	0.18 (±0.04)	12.1 (±4)
Pan 6:5 ILR	CD	118454.1	118456.9 (±5)	0.91 (±0.15)	0.14 (±0.02)	0.15 (±0.03)	5.5 (±1.5)
Atlas 5:4 ILR	CD	118831.1	118824.6 (±9)	0.85 (±0.15)	0.07 (±0.01)	0.08 (±0.02)	22.2 (±6)
Pandora 9:7 ILR	CD ramp	120036.9	120052.8 (±21)	5.6 (±0.9)	0.64 (±0.07)	0.11 (±0.03)	11.6 (±3)
Pan 7:6 ILR	CD ramp	120669.3	120662.0 (±8)	2.9 (±0.5)	0.34 (±0.04)	0.12 (±0.03)	13.2 (±3.5)
Atlas 6:5 ILR	A ring	122063.4	122047.5 (±19)	12.7 (±2.0)	0.82 (±0.08)	0.04 (±0.01)	52.9 (±13)
Pandora 5:4 ILR	A ring	122313.0	122301.4 (±17)	26.5 (±4.0)	1.42 (±0.15)	0.05 (±0.01)	67.9 (±17)

Optical depth τ, derived surface mass densities σ, mass extinction coefficients κ, and vertical thickness H of the rings are provided for waves associated to known resonances, as well as the theoretical resonance location r_{th} and the observed wave source location r_L. CD: Cassini Division.

3.5 Discussions and Conclusions

Surface mass densities are much higher in the B ring (62.1 g cm^{-2}), consistently with Rosen et al. (1991b)'s values (69.8 g cm^{-2}). Then, A ring values are almost an order of magnitude greater than in the Cassini Division. Colwell et al. (2009a) found a surface mass density of 15.4 g cm^{-2} where we have 12.7 g cm^{-2} in the inner A ring and 0.98–1.31 g cm^{-2} in the Cassini Division, where we found 0.72–0.91 g cm^{-2}. Tiscareno et al. (2007) provides estimates for the further regions of the A ring: between 32.6 and 50.6 g cm^{-2}. We can also see a clear difference between the Cassini Division ramp surface mass densities (2.94 and 5.6 g cm^{-2}) and the rest of the Cassini Division. Our surface mass density estimates are consistent with previous works, though slightly lower in the Cassini Division, where the values are quite close to the C ring values: 0.22–1.42 g cm^{-2} (Chapter 2).

The values derived in the Cassini Division ramp from the Pandora 9:7 ILR are quite similar also: we found 5.6 g cm^{-2} where Colwell et al. (2009a) had 5.76 g cm^{-2}. The Pan 7:6 ILR derived surface mass densities are equally consistent: between 2.94 g cm^{-2} (our work) and 3.51 g cm^{-2} (Colwell et al., 2009a).

Mass extinction coefficients are also very close: we found lower coefficients in the A and B rings (0.02–0.05 cm^2 g^{-1}) than in the Cassini Division (0.08–0.18 cm^2 g^{-1}) where Colwell et al. (2009a) had 0.03 cm^2 g^{-1} for the Atlas 6:5 ILR in the A ring and between 0.07 and 0.12 cm^2 g^{-1} in the Cassini Division.

In addition, we derived vertical thickness values between 5.5 and 22.2 m in the Cassini Division, where Colwell et al. (2009a) values range from 3 to 20 m. The A ring's thickness is found between 52 and 67 m.

From the mass extinction coefficients, we can estimate the ring masses (with a global relative uncertainty around 0.25) by following the same methodology than in Chapter 2. We find that the Cassini Division mass lies between 3.0×10^{16} and 6.8×10^{16} kg (equivalent to a

20.4 – 26.8 km-radius icy moon with a density of 850 kg m^{-3}). Colwell et al. (2009a) found a mass of 3.1×10^{16} kg for the Cassini Division, ramp excluded.

From the only Janus 2:1 ILR density wave, we find a B ring mass of 2.8×10^{19} (a 200 km-radius moon), which is slightly lower than the previous estimates (Esposito et al., 1983, 2008; Robbins et al., 2010): 4–7 $\times 10^{19}$ kg.

Our mass extinction coefficients of the inner A ring provide masses between 1.7×10^{18} and 2.1×10^{18} kg (equivalent to a 78.3 – 84.3 km-radius moon). Spilker et al. (2004) evaluated the mass of the A ring around 0.5 – 0.7 $\times 10^{19}$ kg, while Charnoz et al. (2010) found 1.5×10^{18} kg. The relatively small difference between our estimates and the previous studies might be explained by the fact that our study is only based on density waves located in the inner A ring.

CHAPTER 4

SATELLITE WAKES

4.1 Introduction

Our previous study of the C ring structures (Baillié et al., 2011) found numerous wavelike features in the C ring and could only explain 5 of them by the excitation of density waves or bending waves, excited by inner Lindblad resonances with Mimas (4:1), Atlas (2:1), Mimas (6:2), Pandora (4:2) and vertical resonance with Titan (nodal -1:0 resonance). Most of the remaining structures do not present any resonance association. We now investigate the possibility that some of these wavy signatures could be due to the presence of embedded moonlets in the C ring. Previous studies of the Encke gap in particular have provided an interesting model for these satellite "wakes".

After Cuzzi and Scargle (1985) observed wavy edges in several Voyager images of the Encke gap, confirmed by observations of quasi-periodic optical depth variations in the Voyager stellar (PPS) and radio occultation profiles, Showalter et al. (1986) modeled the gravitationnal "wakes" that would be created after the passage of a moonlet orbiting the gap. Showalter et al. (1986) then derived dynamical and physical properties of the Encke Gap moonlet 1981S13 which would be named Pan in 1991 after Showalter (1991) detected it visually in Voyager 2 images and showed that the moonlet was following the predicted orbit. Showalter (1991) also described Pan's shepherding role in keeping the Encke gap open and its probable contribution in creating a narrow ringlet within the gap, as observed in Cassini images later (Figure 4.1). Marouf and Tyler (1986) tried to apply the same model to regions of the Cassini Division where similar quasi-periodic features appear in the Voyager occultation data, and determined the positions of two satellites shepherding a ringlet and creating the observed "wakes". However, depsite the predicted orbits of these satellites, no moonlet has been observed so far (nov 2010) in the Cassini Division, even from the Cassini mission.

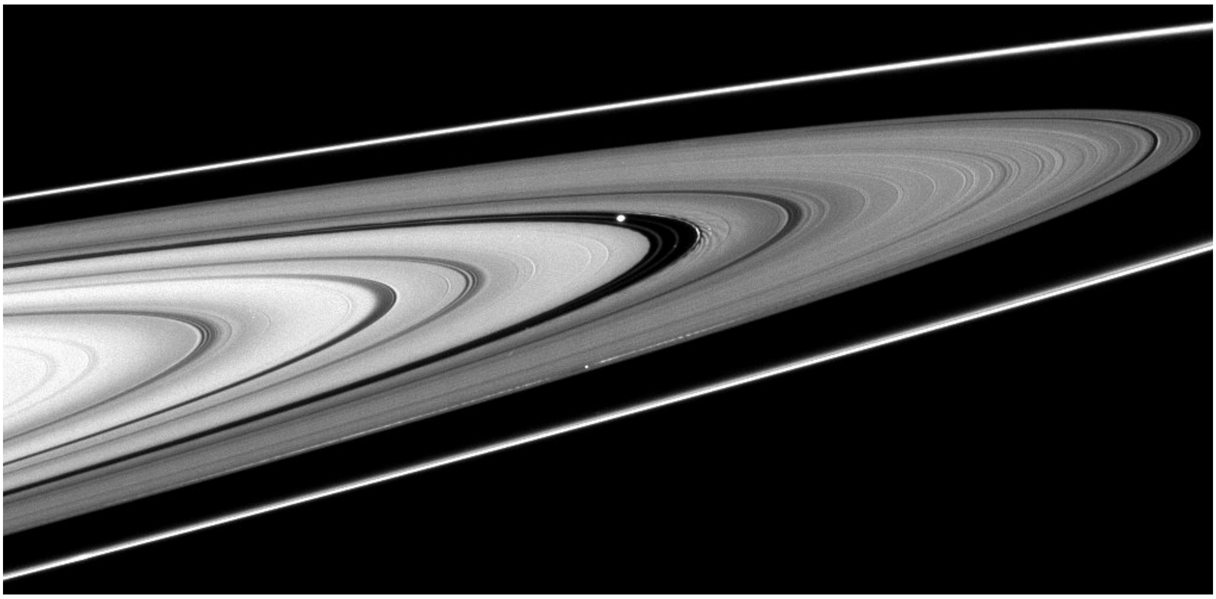

Figure 4.1: Image: NASA/JPL/Space Science Institute. Cassini ISS images revealing Pan orbiting in the Encke gap. The narrow ringlet coorbiting with Pan is also visible, together with wakes just ouside the Encke gap.

We will first describe the observed wavy regions (Section 4.2), then we will detail the "wake" model (Section 4.3) and validate it using a WWZ wavelet analysis as we described in Baillié et al. (2011). Then, we will try to apply it to other regions (Section 4.4) such as the ones described in Marouf and Tyler (1986), the Huygens ringlet or the C ring and finally draw conclusions about the likelyness to find embedded moonlets in these ringlets (Section 4.5).

4.2 Observations

From Cassini UVIS occultation data, we measure the photon counts as the line of sight crosses the Encke gap (Figure 4.2). Wavy features are visible a couple hundred kilometers inner and outer the Encke gap.

Using a similar wavelet analysis that detailed in our C ring study (Chapter 2), we could generate WWZ profiles for the regions immediately inside and outside the Encke gap (Figure 4.3). We observe very clear periodic signatures with wavelengths increasing away from the Encke gap.

In the inner Cassini Division, interior to the Huygens Gap, the Huygens ringlet sometimes presents wavy structures as seen on Figures 4.4-4.11. However, the WWZ wavelet profile does not allow do identify a clear shape for this signature. The occultation of κ Centauri presents a relatively long and horizontal signature at 1-km wavelength (Figure 4.4).

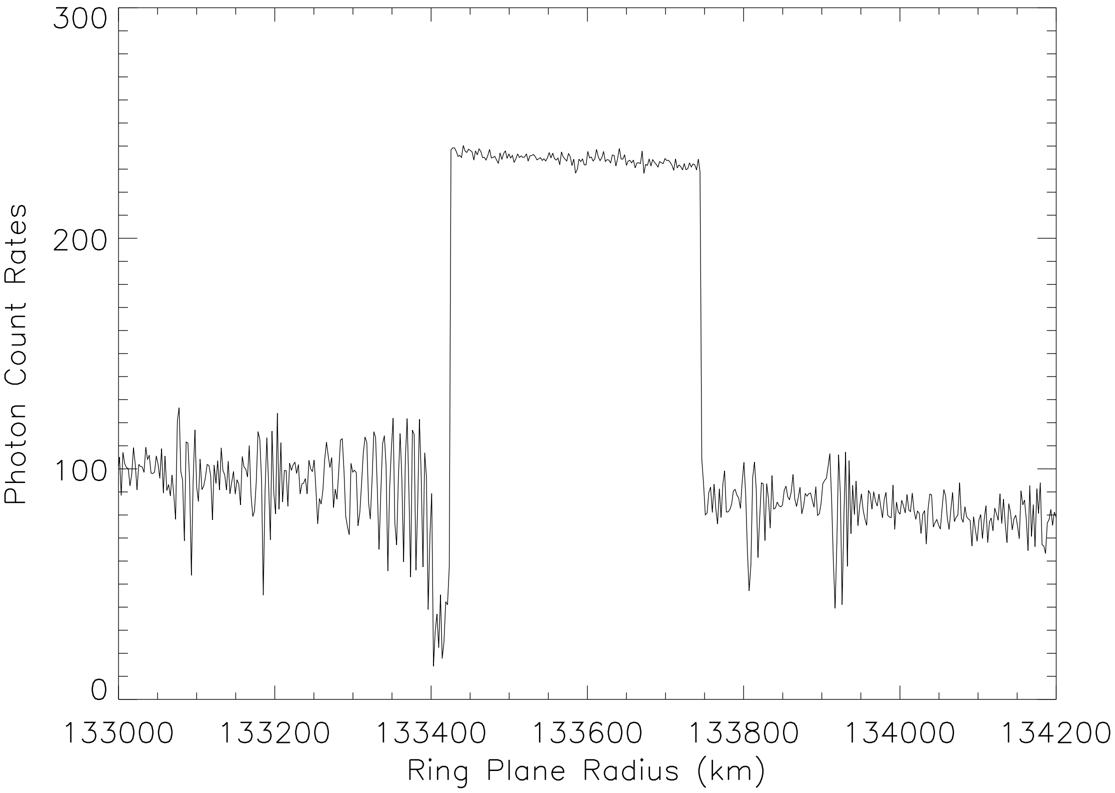

Figure 4.2: Photon counts from the occultation of σ Sagitarii (Rev 11) showing the Encke gap region and wavy features inner and outer to the gap.

The occultation of α Arae, rev. 63, also shows some structures in the photon count profile (Figure 4.5), while the wavelet profile identifies recurrent wavelength around 1 km. However, no specific shape or trend can be clearly identified.

The occultation of γ Cassiopeiae, rev. 64, also presents a horizontal signature centered on the middle of the Huygens ringlet, but at slightly higher wavelength, around 1.8 km (Figure 4.6).

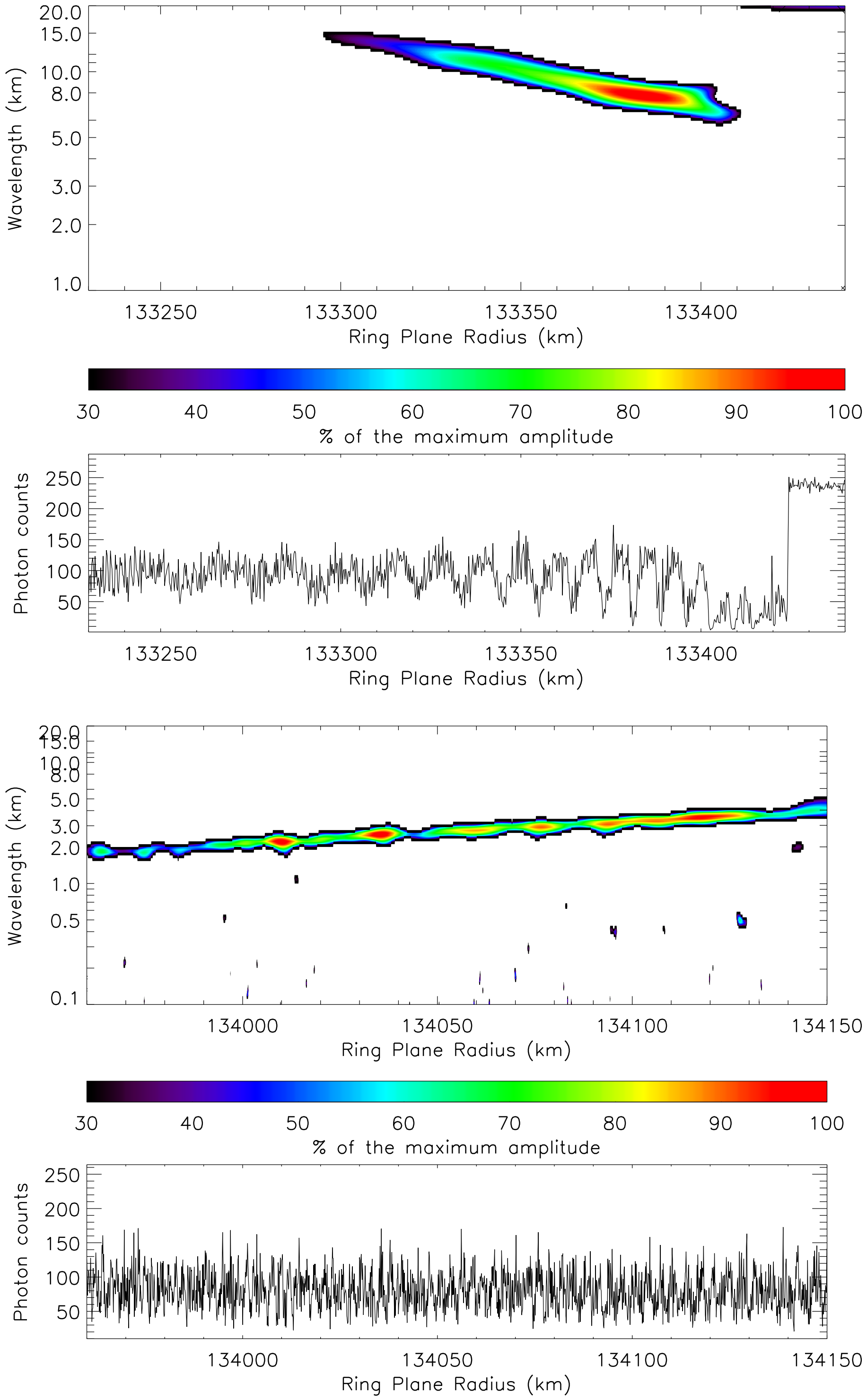

Figure 4.3: WWZ wavelet power profiles of the Cassini Division around the Encke gap from individual occultation profile of σ Sagitarii, rev 11.

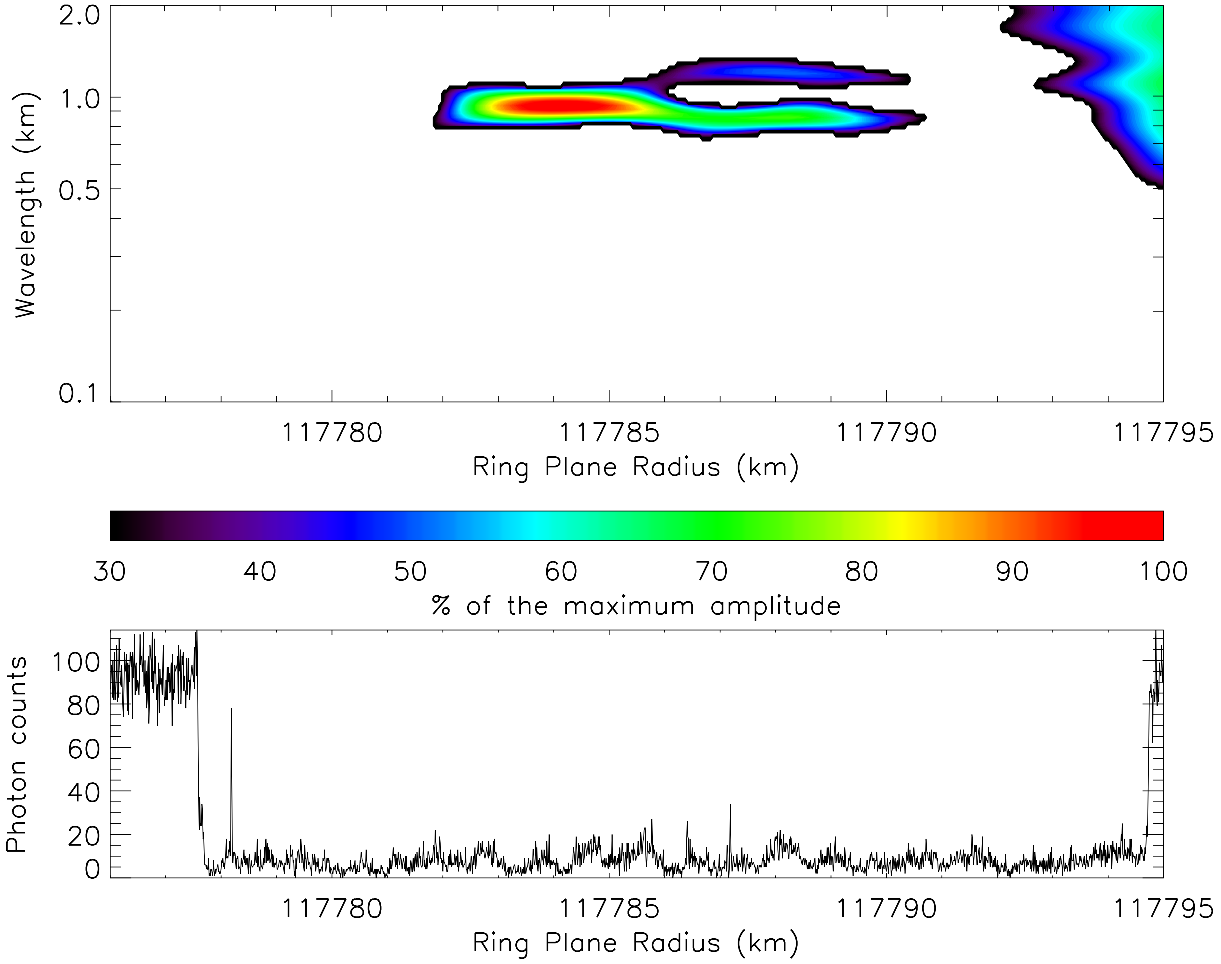

Figure 4.4: WWZ wavelet power profile of the Huygens ringlet from individual occultation profile of κ Centauri, rev 35. Lower panel shows the corresponding occultation profile.

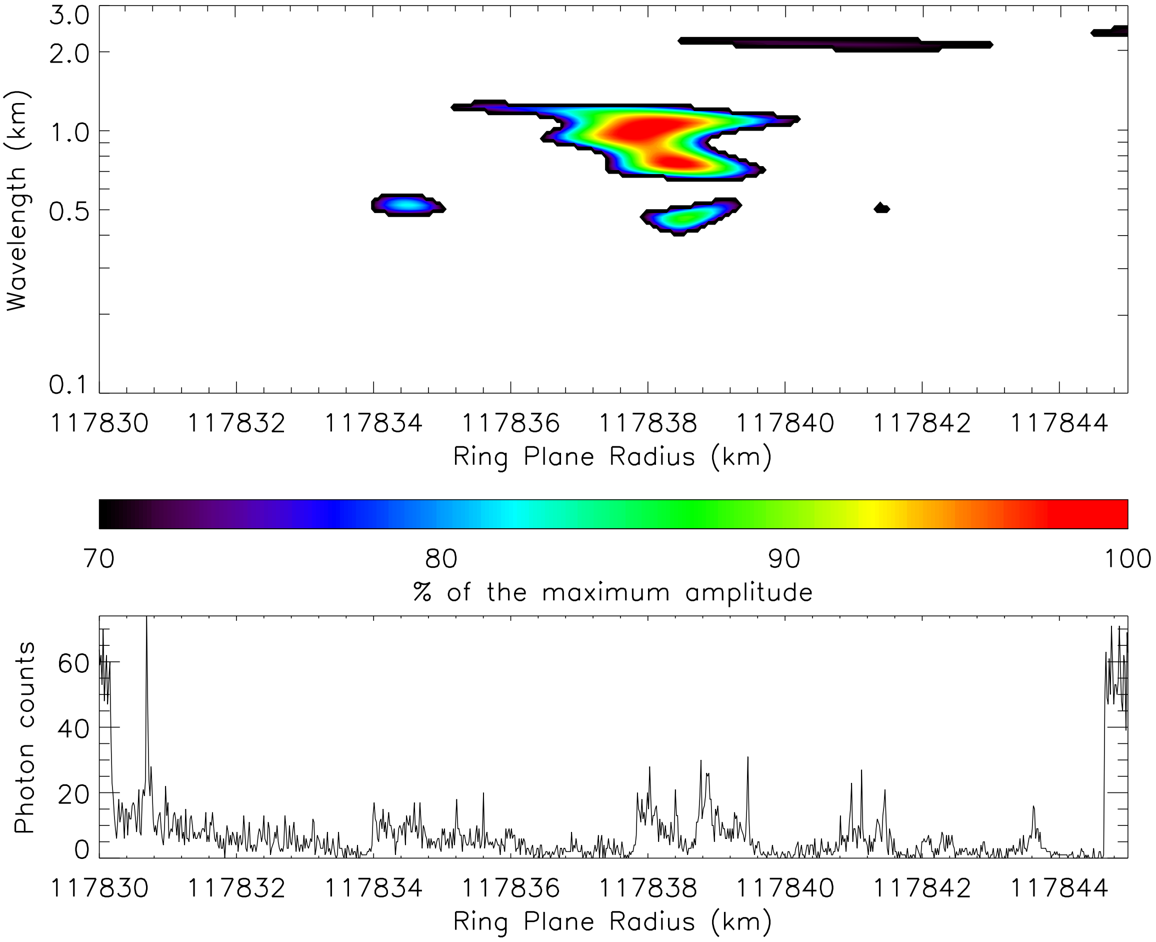

Figure 4.5: WWZ wavelet power profile of the Huygens ringlet from the occultation of α Arae, rev 63. Lower panel shows the corresponding occultation profile.

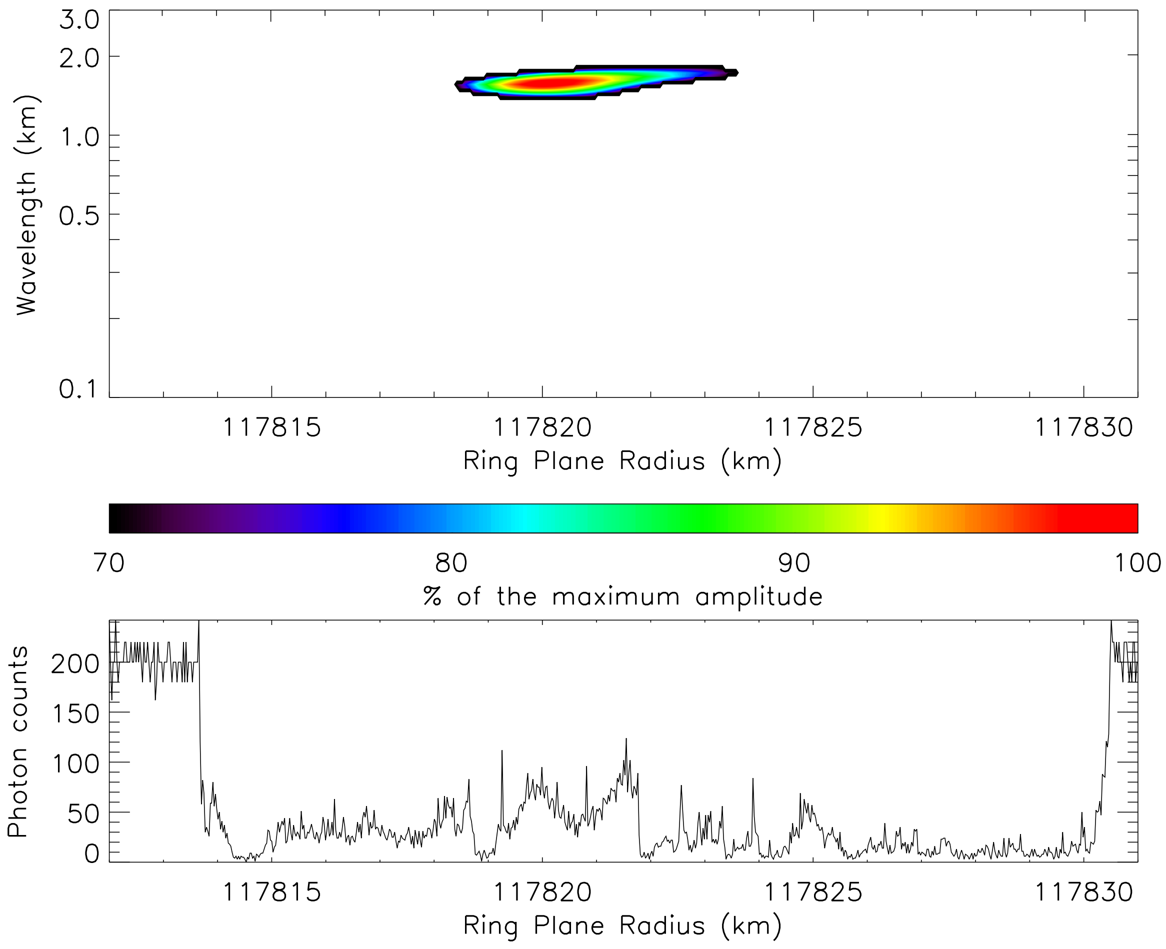

Figure 4.6: WWZ wavelet power profile of the Huygens ringlet from the occultation of γ Cassiopeiae, rev. 64. The lower panel shows the actual structures in the photon counts.

Figure 4.7 shows the Huygens ringlet structures observed during the α Virginis, rev. 30, occultation. A different signature, though around the same wavelength, appears clearly. The structures from the photon count profile do not seem correlated with the observed ones in other occultations.

The γ Gruis, rev. 41, occultation presents the usual centered signature at 1-km wavelength Figure 4.8. Its profile shows a slightly depleted zone around the center of the Huygens ringlet.

Figure 4.9 presents the occultation profile of σ Sagitarii, rev. 11. The 1-km wavelength signature is more interior in the Huygens ringlet than in the previous observations, and shows a slightly increasing trend with increasing radius.

The δ Lupi, rev. 57, occultation shows an interesting superposition of two signatures (Figure 4.10) that we have already observed separately, around 1 km and 1.8 km. However, no trend or specific structure is obvious in that occultation.

Finally, Figure 4.11 shows the occultation profile of α Virginis, rev. 116. Here we can identify two signatures, different than the previous observations: an inner signature around 0.5 km in wavelength and a centered 2-km wavelength feature.

However, most of the occultations do not show any particular signature in the Huygens Ringlet. Though we estimate that our data show evidence of actual structures in the Huygens Ringlet for some occultations, we cannot state that a specific pattern is being repeated,

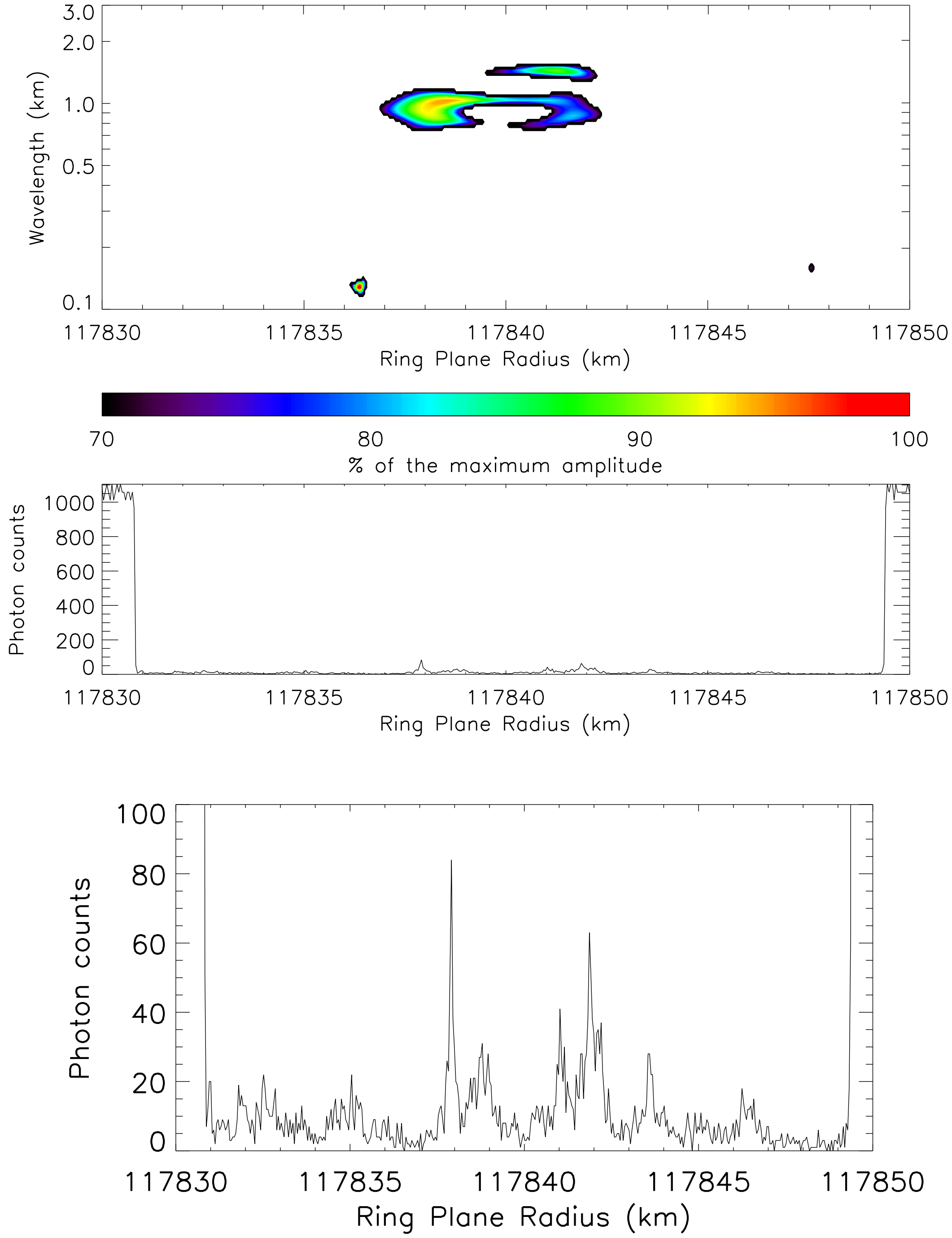

Figure 4.7: WWZ wavelet power profile of the Huygens ringlet from the occultation of α Virginis, rev. 30. The intermediate panel shows the corresponding occultation profile and the lower panel zooms in to show the actual structures in the photon counts.

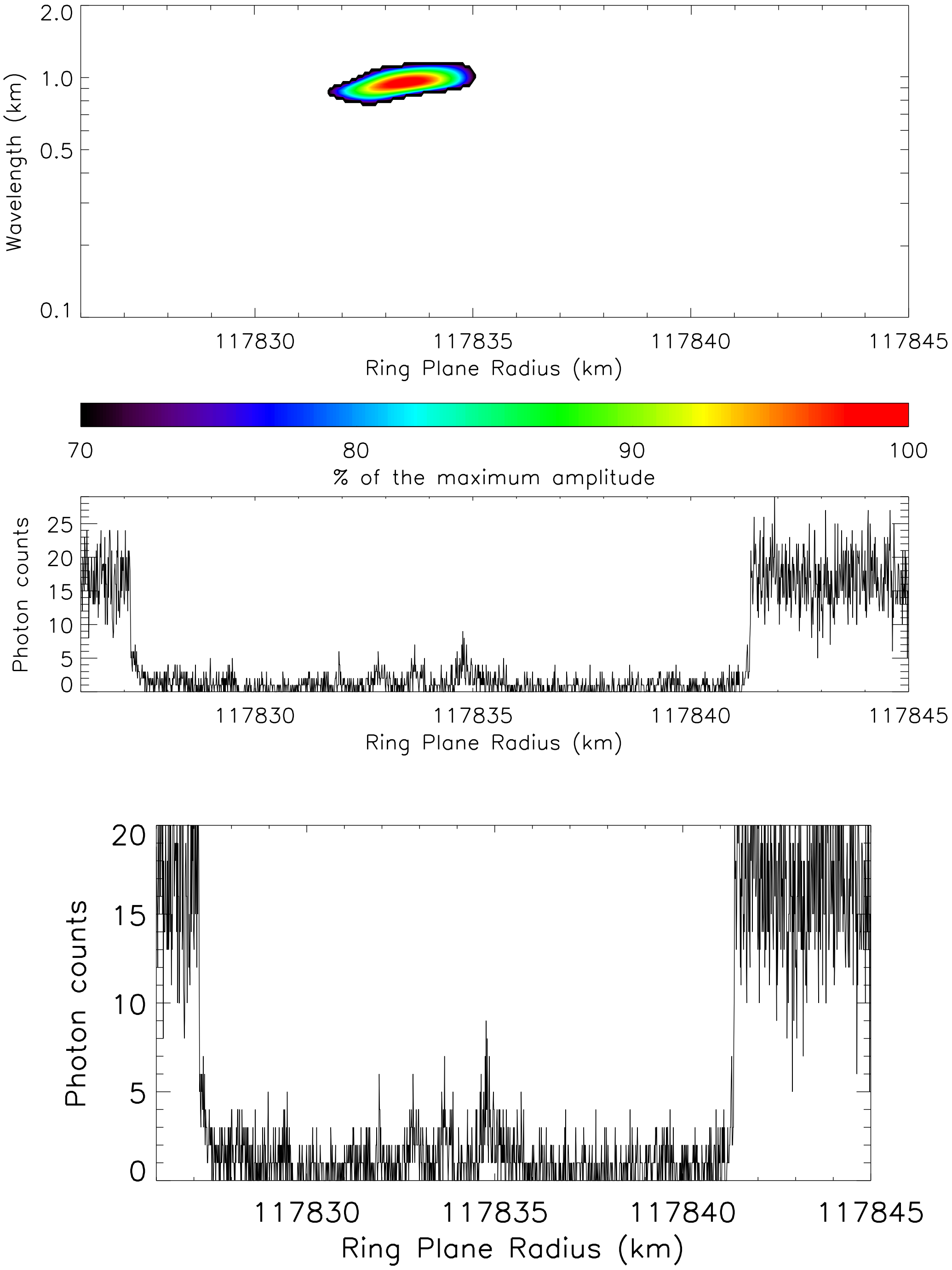

Figure 4.8: WWZ wavelet power profile of the Huygens ringlet from the occultation of γ Gruis, rev. 41. The intermediate panel shows the corresponding occultation profile and the lower panel zooms in to show the actual structures in the photon counts.

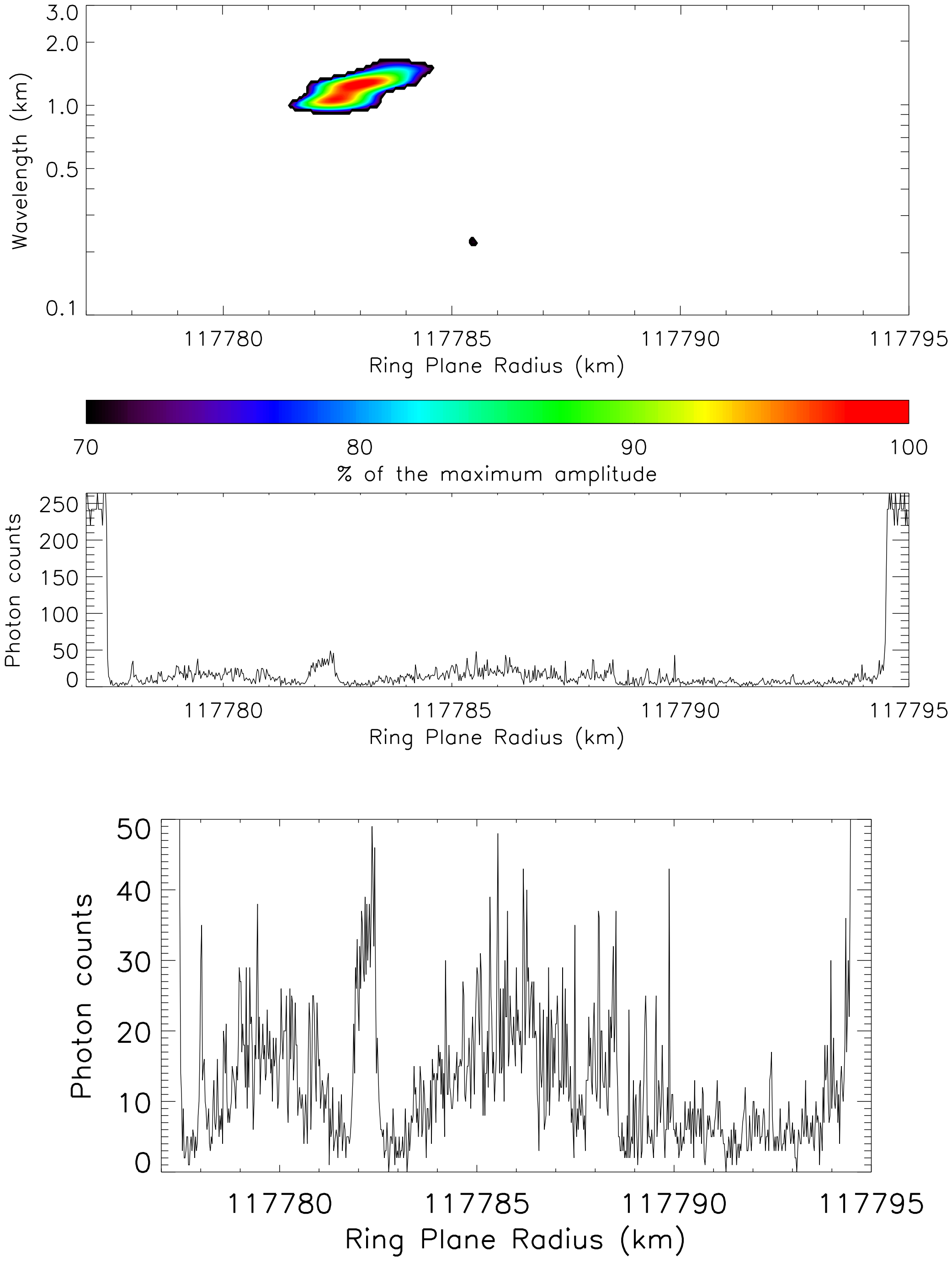

Figure 4.9: WWZ wavelet power profile of the Huygens ringlet from the occultation of σ Sagitarii, rev. 11. The intermediate panel shows the corresponding occultation profile and the lower panel zooms in to show the actual structures in the photon counts.

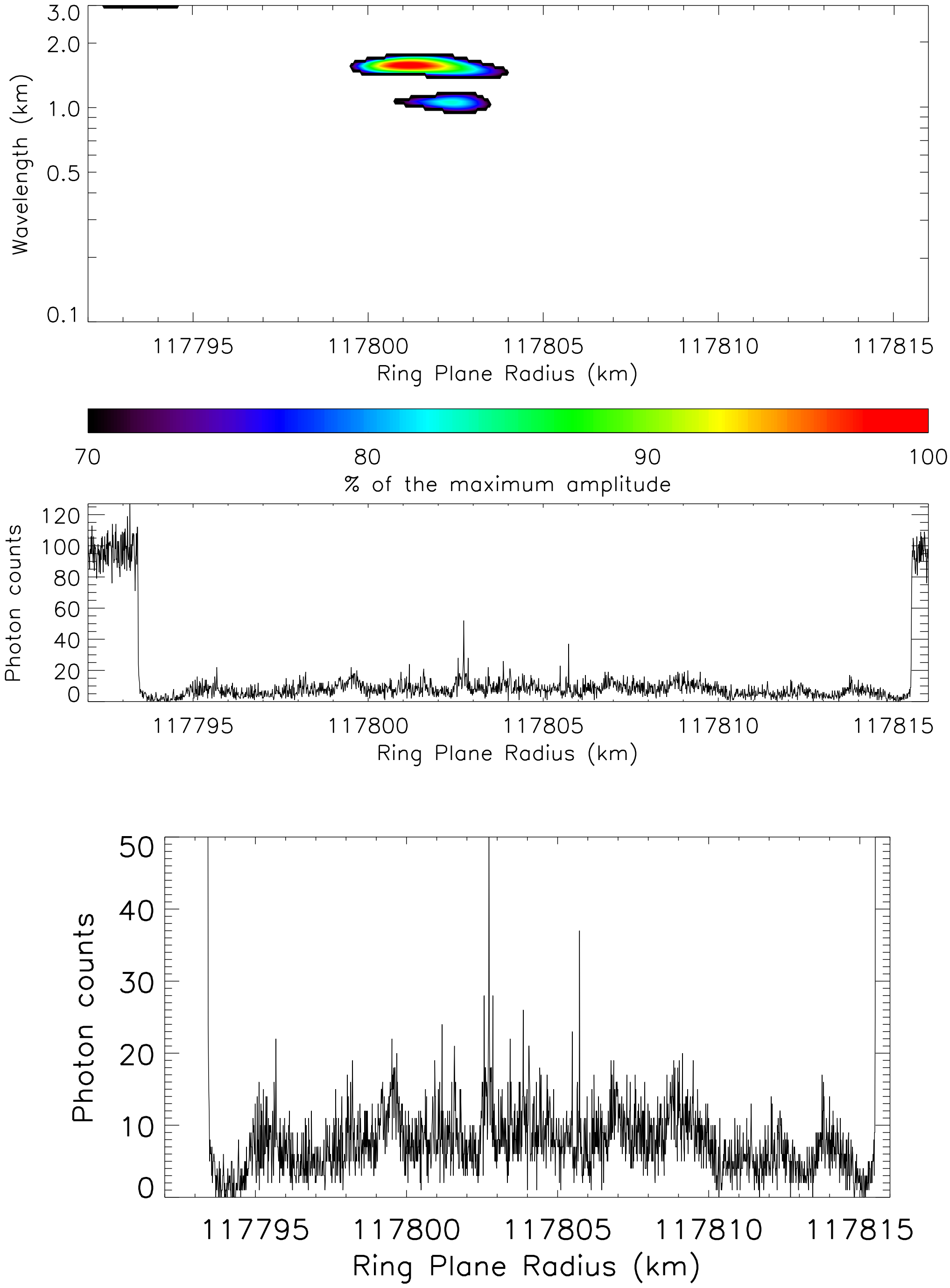

Figure 4.10: WWZ wavelet power profile of the Huygens ringlet from the occultation of δ Lupi, rev. 57. The intermediate panel shows the corresponding occultation profile and the lower panel zooms in to show the actual structures in the photon counts.

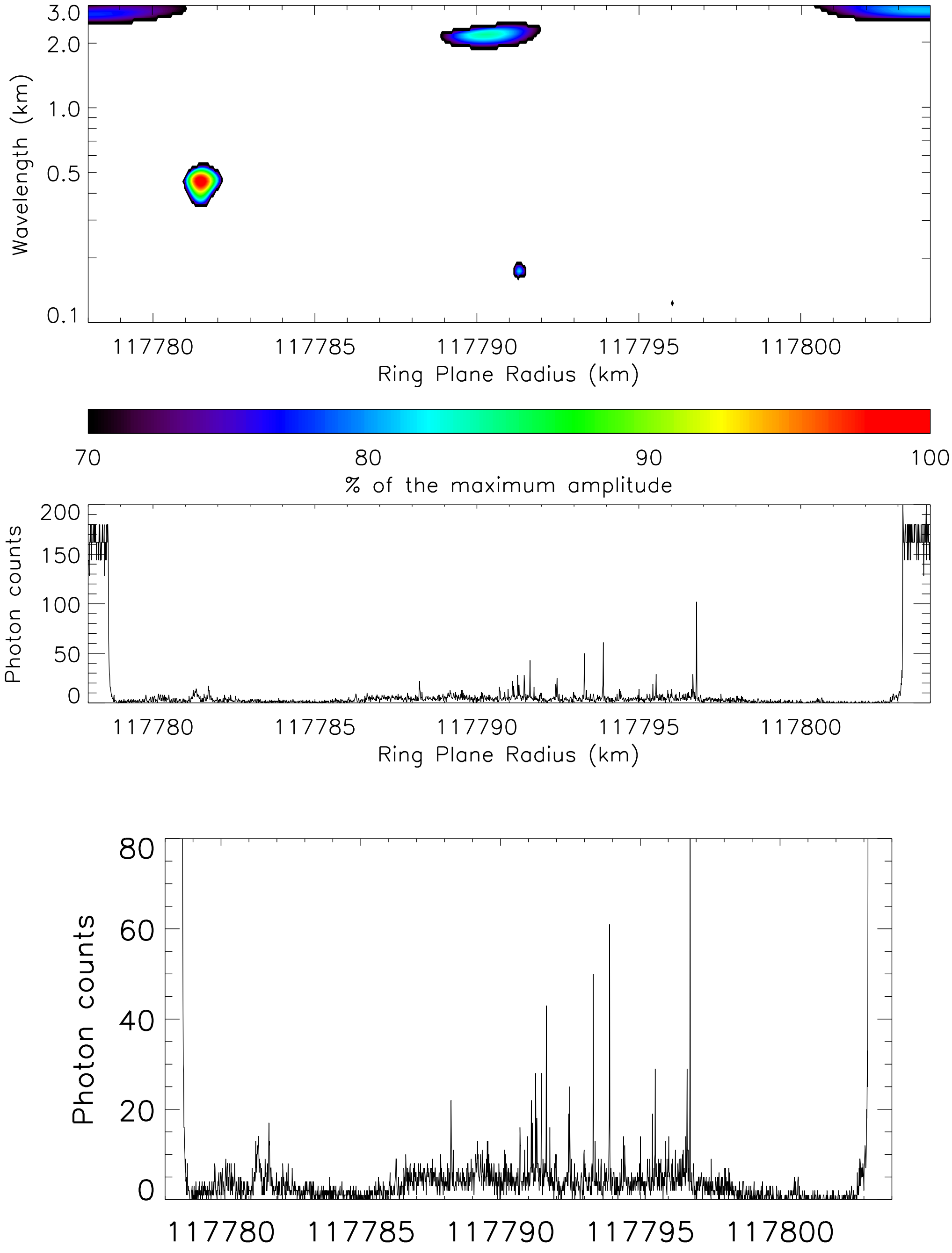

Figure 4.11: WWZ wavelet power profile of the Huygens ringlet from the occultation of α Virginis, rev. 116. The intermediate panel shows the corresponding occultation profile and the lower panel zooms in to show the actual structures in the photon counts.

nor can we explain why some other occultations do not seem to present such wavelength signatures.

4.3 Satellite Wakes

Showalter et al. (1986) described a model for the ring-moonlet interaction. As seen in Figure 4.12, in the rotating frame with the moonlet, an inner particle will move leftward while an outer particle moves rightward. The perturbation in their orbits is similar to a sinusoidal signal with period λ_θ and amplitude ae where a is the semimajor axis of the particle and e its eccentricity.

Therefore, using a streamlines approach that consists in following several particles evenly spaced in semimajor axis, Showalter et al. (1986) produced another sketch (Figure 4.13) showing the packing of streamlines that has been observed very clearly later with the Cassini mission and the ISS observations of the Encke gap (Figure 4.14).

If α is the scan angle, a the semimajor axis of a particle and a_S the satellite's semimajor axis, we can define $s = a - a_S$ and $\delta = \frac{a-a_S}{a_S}$. With these definitions, Showalter et al. (1986) derived expressions for the radial (Equation 4.1) and azimuthal wavelengths (Equation 4.2).

$$\lambda_r(a) \approx 3\pi a_S \frac{\delta^2}{|\theta|} \left(1 - \left|\frac{\delta}{\theta}\right| \tan(\alpha)\right) \tag{4.1}$$

$$\lambda_\theta(a) \approx 3\pi |s| \tag{4.2}$$

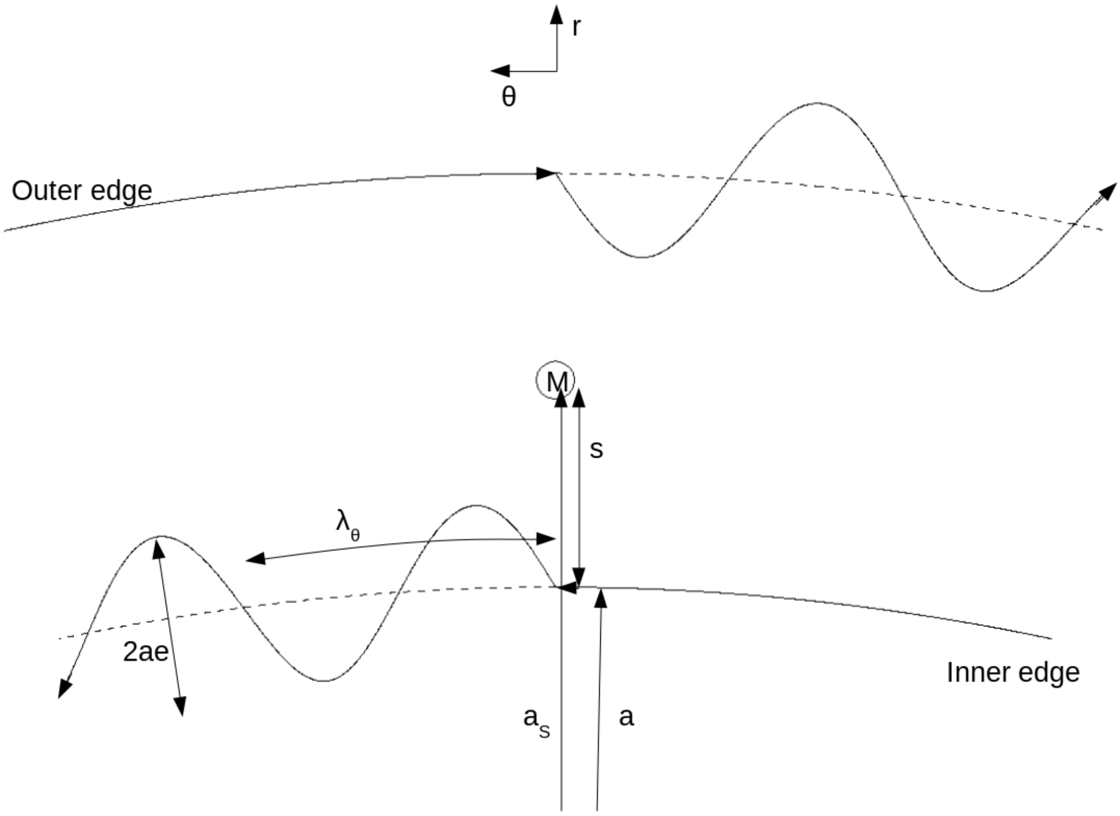

Figure 4.12: Ring-satellite interaction. Since we are in the rotating frame with the moonlet, inner particles (down) are moving to the left and outer particles (up) are moving to the right. Each encountering particle receives a gravitational "kick" as it passes close to the moonlet, and then proceeds on a more eccentric orbit. The overall direction of rotation is toward the left and the planet is toward the bottom. The radial scale is highly expanded compared to the azimuthal scale. Based on Figure 1.1 from Showalter et al. (1986).

The wavelength increases quadratically with the radial distance to the moon while it decreases inversely with the azimuthal distance. We define the first order wake as the wake

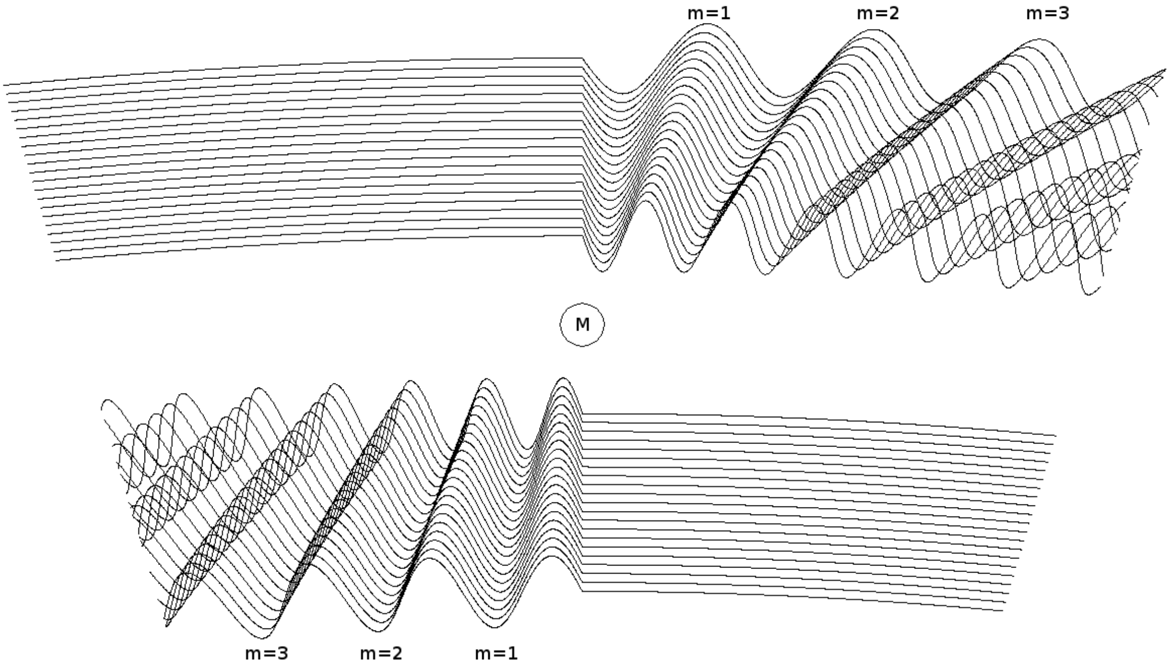

Figure 4.13: Satellite wakes. Uniformly spaced semimajor axes particles are followed in the rotating frame with the satellite. Radial scans in the generated pattern presents an increasing wavelength and a decreasing amplitude when the distance to the moonlet is increasing. Though the particles start oscillating in phase, the wavelength varies and causes the trajectories to pile-up a few periods downstream. The index m numbers the density oscillation periods, starting with $m = 0$ at the moonlet azimuthal position. Farther, the pattern of streamlines is modified by collisions and the wakes pattern fades. The radial scale is highly expanded compared to the azimuthal scale. Based on Figure 1.2 from Showalter et al. (1986).

created by the satellite during its last orbit. Thus, an n^{th} order wake was created n orbits ago.

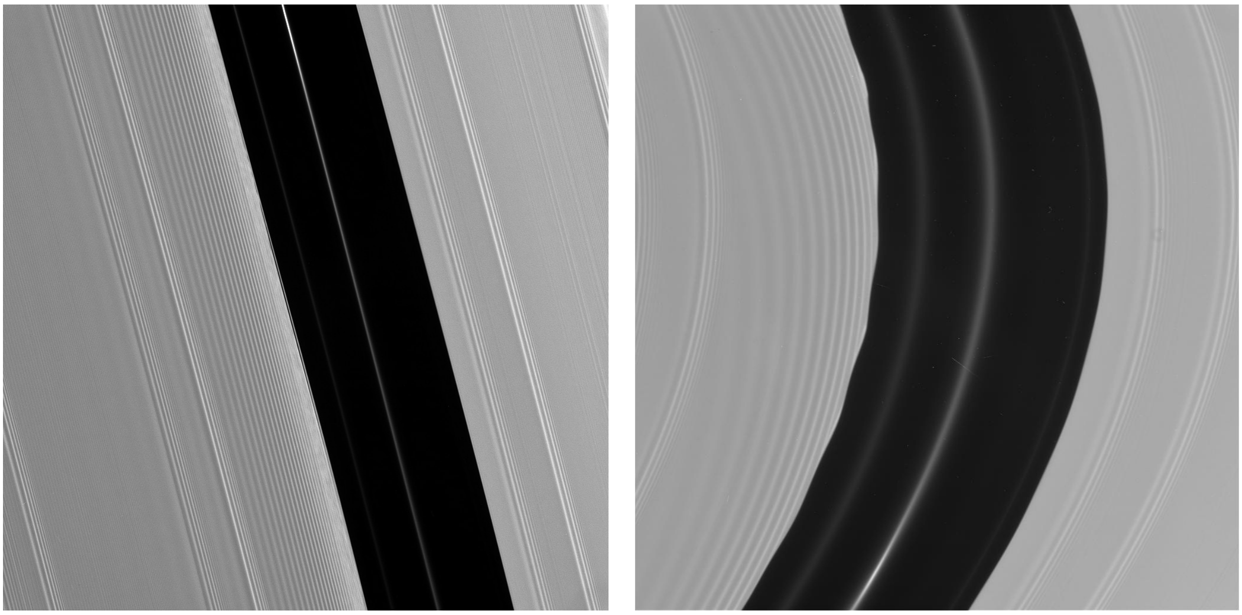

Figure 4.14: Images: NASA/JPL/Space Science Institute. Cassini ISS images of the Encke gap. Pan's orbit leaves a narrow ringlet visible inside the Encke gap. Increasing wavelengths with radial distance from Pan's orbit are clearly visible. Azimuthal wavelengths appear one order of magnitude bigger than radial wavelengths as expected from Equations 4.1 and 4.2.

4.4 Results

Longitude fitting might be necessary in order to fit Equation 4.1 on our data around the Encke gap, thus validating that the observed features are indeed Pan's wakes, as seen on Figure 4.15.

Figure 4.16 shows the first order wakes created by a satellite for particles at different longitudes relative to the satellite, evenly spaced every 10°. Thus, assuming that an observed feature is created by a given satellite wakes, we can link the observed wavelength to the

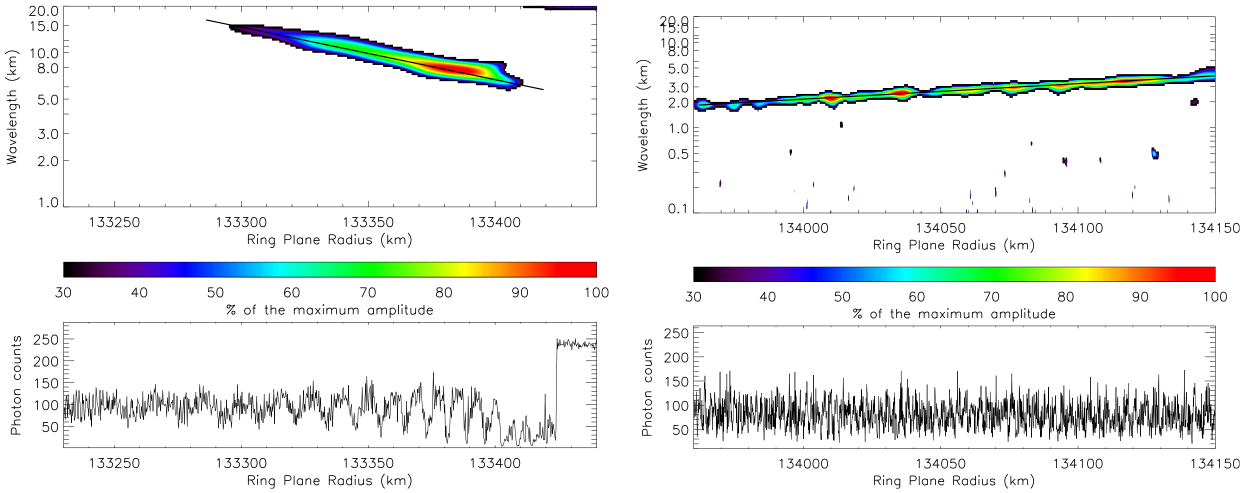

Figure 4.15: WWZ wavelet power profiles of the Cassini Division around the Encke gap from individual occultation profile of σ Sagitarii, rev 11. Lower panel shows the corresponding occultation profile. Black lines correspond to theoretical wavelength from Equation 4.1.

position of the satellite. In the case of the Huygens ringlet, we mainly observe a signature around a wavelength of 1 km. According to Figure 4.16, we should expect a satellite to be between 150 km and 350 km away from the observed signature.

4.5 Discussions and Conclusions

At these distances from the Huygens ringlet, we are close to the inner edge of the Huygens Gap on one side and outside the Huygens Gap, in the Cassini Division on the other side. No moonlets have yet been observed in these regions, though the low density of these locations should have helped their detection. The hypothesis of a moonlet in the Huygens Gap gener-

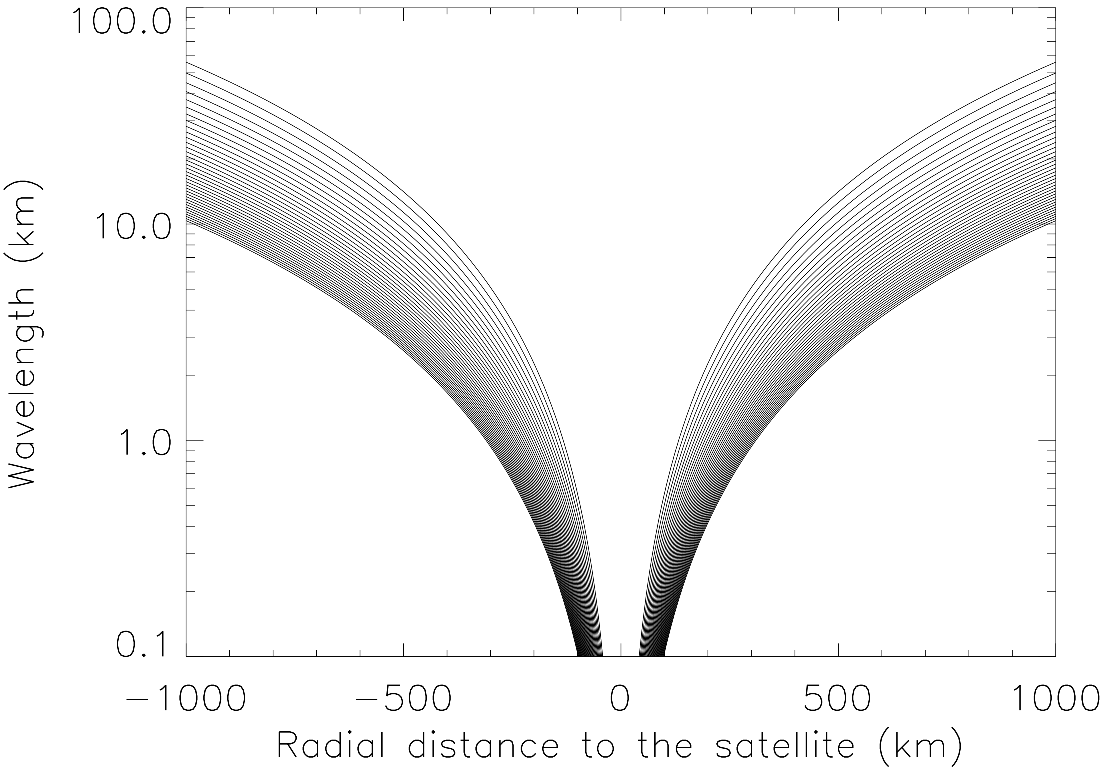

Figure 4.16: Wavelength with respect to the radial distance to the satellite are plotted for longitudes relative to the moon evenly spaced every 10°.

ating features in the Huygens ringlet is therefore very unlikely. The Huygens ringlet is very close in shape and width to the R4 ringlet in the C ring. We can draw the same conclusions about the possible presence of moonlets around it in the Bond Gap. As far as the other waves of the C ring are concerned, no symmetry is being observed between the observed structures, and that symmetry appears necessary if features are due to satellite wakes.

CHAPTER 5

GHOSTS IN THE RINGS

5.1 Introduction

Cassini UVIS stellar occultations provide the best ring plane radius resolution for the examination of fine structures. These data make possible the detection and analysis of structures of a few tens of meters wide. Zebker et al. (1985) estimated that the particles in the C ring and the Cassini Division had sizes, a, between 10 cm and a couple tens of meters, and followed power-law distributions $n(a)\mathrm{d}a = n_0 a^{-q}\mathrm{d}a$ with a differential power-law index $q = 3.1$ in the C ring and $q = 2.75$ in the Cassini Division, where $n(a)$ is the density of particles of radius a and n_0 a normalization factor. No boulder with a size between a couple tens of meters and the size of Daphnis (4 km radius) was known in the main rings until Tiscareno et al. (2006) reported the first observations of 100 m-objects in the A ring (Figure 5.1), verifying the "propellers" models developed by Petit and Henon (1988), Spahn and Wiebicke (1989) and Sremčević et al. (2002).

Scanning the ring system, we could observe isolated and unexpected high photon counts in different places. These can be explained by cosmic rays when the photon counts are higher than the star background level, whereas in optically thick regions, places where the photon

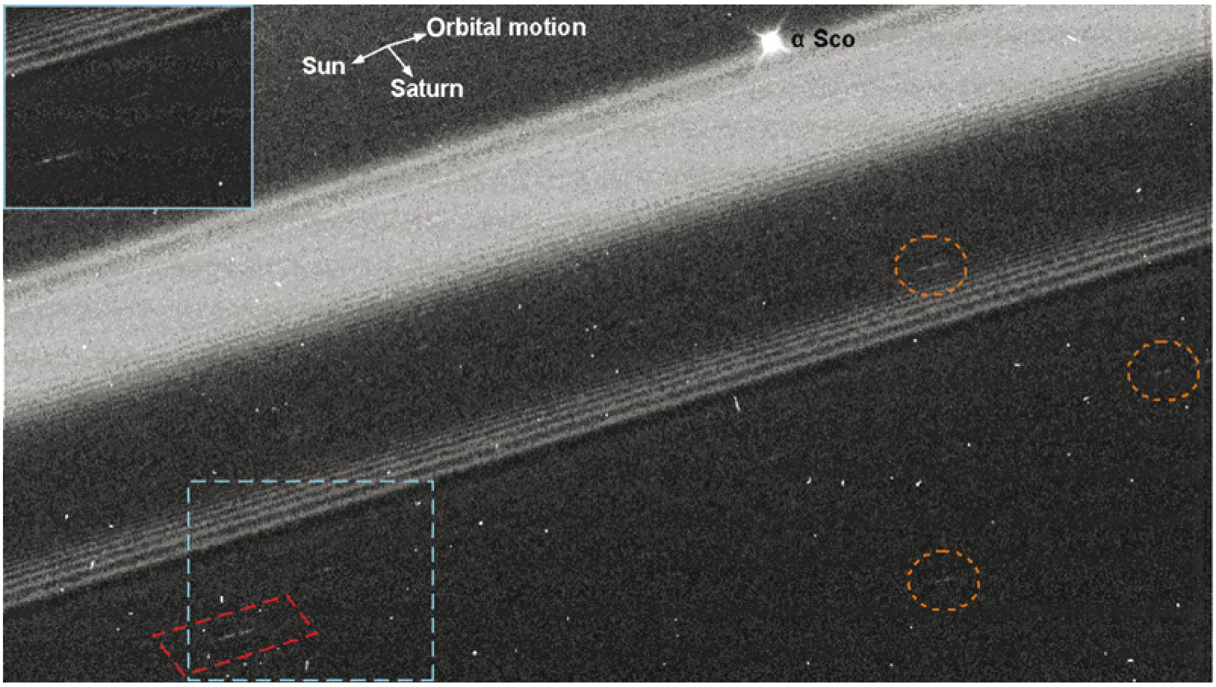

Figure 5.1: From Sremčević et al. (2007). Propellers as seen by Cassini NAC, with a 1-km/pixel resolution in radius and a 0.5-km/pixel resolution in azimuth.

counts reach the brightness of the occulted star define a new type of structure that Colwell et al. (2010a) named "ghosts". These ghosts, that we can interpret as holes in optically thick regions of tenuous rings, can be explained by some boulders creating propeller structures. Estimating the width of these ghosts ($5.4-46.7$ m in the C ring and $1.7-277$ m in the Cassini Division) provides constraints on the radii of the boulders at their origins ($1.5-14.5$ m in the C ring and $0.36-58.1$ m in the Cassini Division). Then, from numerical simulations using the N-body code described in Lewis and Stewart (2009), we can draw conclusions about the particle size distribution in these regions and provide new estimates for upper limits on the size of the largest particles in the particle size distribution (from 0.49 to 4.7 m in the C ring and from 0.12 to 18.7 m in the Cassini Division). Section 5.2 describes Cassini UVIS stellar occultation data, the regions of interest, the observed features and details the detection and identification process. Section 5.3.1 explains the propeller model and Section 5.4.1.1 studies qualitatively and quantitatively these ghosts before Section 5.4.1.2 draws conclusions about the neighbor ring properties.

5.2 Observations

5.2.1 Cassini UVIS Data

Occultations from 2007 and earlier are detailed in Colwell et al. (2007) and in Table 1.3, and a description of calibration procedures applied to all occultations is presented in Colwell et al. (2010b), documenting viewing geometries and star brightnesses. While some stars like γ Grus (Rev 40) are faint, others such as β Centauri (Rev 64, 75, 77, 78, 81, 85, 89, 92, 96, 102, 104, 105) produce photon count rates 10 to 100 times higher. We analyze star occultations presenting significant background photon counts (usually higher that 20). We call background photon count rate of a stellar occultation the average photon count rate that the instrument measures in the absence of ring material in the line of sight between the Cassini spacecraft and the star. In order to match this threshold, we exclude the following occultations from our present study: α Sextantis (rev. 63), β Lupi (rev. 58), δ Aquarii (rev. 8), γ Cancri (rev. 75), π Orionis (rev. 117), θ Hyades (rev. 94 and 104). We also exclude the occultation of α Virginis that occurred in rev. 134 for which the combination of a low inclination and low photon count rates is making the identification of actual ghosts more complicated.

The resolution of our data is of the order of 1 ms, which corresponds to about 1 to 10 m, depending on the geometry of the occultations. Though our occultations can cover the entire ring system, we will focus mainly on two optically thin regions: the C ring and the Cassini Division (Figure 1.9). As we expect self-gravity wakes to create lots of ephemeral holes in the A and B rings that would interfere with the detection of isolated ghosts, we exclude them from our study in order to focus on actual ghosts. In addition, we do not consider the C ring low-optical-depth regions since the probability of having a photon count close to the star brightness by chance is too important.

Within these regions, we focus on regions of relatively high optical depth (corresponding to low photon count rates) such as the C ring and Cassini Division ringlets and we avoid regions presenting local disturbances from known waves or structures reported in Chapter 2. Figure 5.2-a shows raw data for the Cassini Division and Figure 5.2-b presents a zoom in on the Huygens Gap.

Figures 5.3, 5.4 and 5.5 show the same kind of isolated and narrow structures in regions of relatively high optical depth inside optically thin regions.

Some stars, such as β Centauri, κ Centauri or α Crucis, are actually binary stars. Depending on the resolution of the binary, we can observe a more or less wide step at edges in the rings as explained in Figure 5.6. For these binary stars, background photon count levels

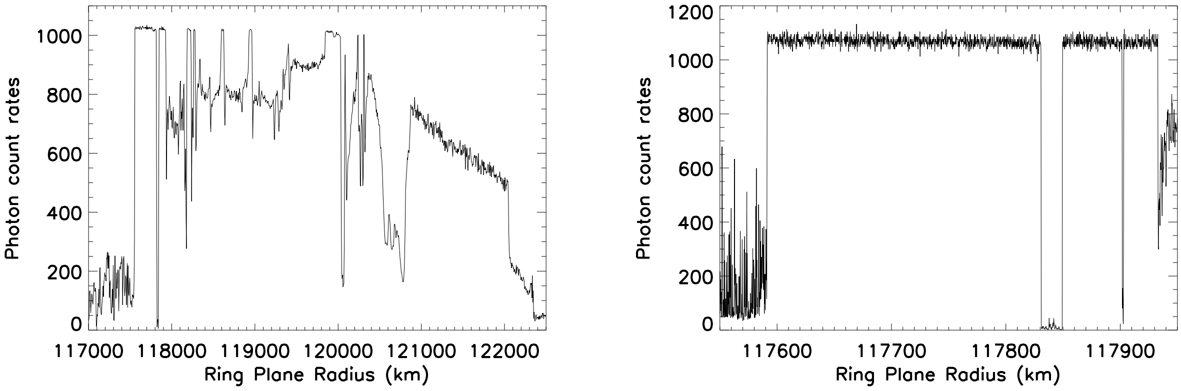

Figure 5.2: Photon count rates of the occultation of α Virginis, rev. 34 showing the Cassini Division (left) and α Virginis, rev. 30 showing the Huygens Gap (right).

are additive and it can happen that one star of the two is occulted while the other is not. The two different background levels can be estimated by the height of the edge step.

A hole could actually produce a photon count rate whose height matches one of the steps but not the total brightness of the two stars together (Figure 5.7). Assuming that the binary orbital period is small compared to the integration time of an occultation (a couple hours at most), the two stars will be occulted in the same order in the ingress and the egress intervals, but since the variation of ring plane radius are inversed and the edges have a non-zero thickness, we will observe differences in the step lengths between the two branches of an occultation (as visible in Figure 5.7).

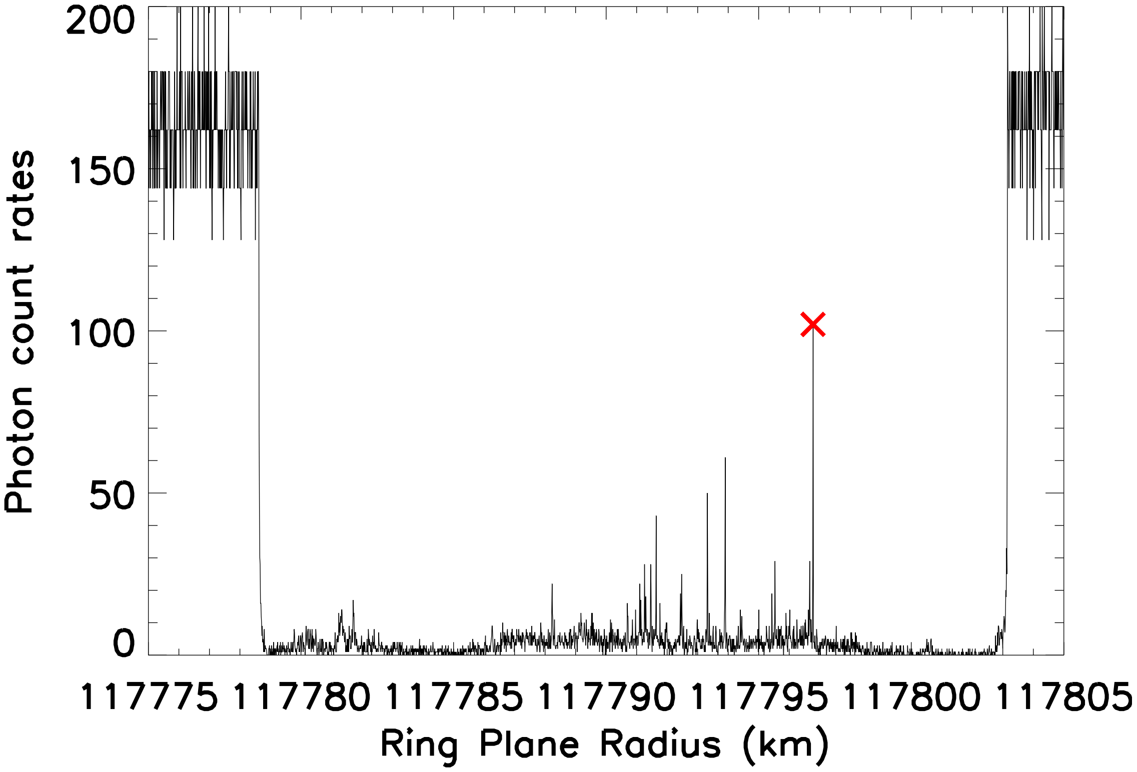

Figure 5.3: Photon count rates in the Huygens ringlet from the occultation of α Virginis, rev. 116. The red cross identifies the position of the detected ghost. Its height matches the background level of one of the stars that compose the α Virginis binary.

5.2.2 Ghosts Identification

5.2.2.1 Detection and Identification Criteria

Ghosts behave like holes in a ringlet or plateau through which we directly observe a star: it is therefore characterized by an isolated peak in photon counts with a height equal to the

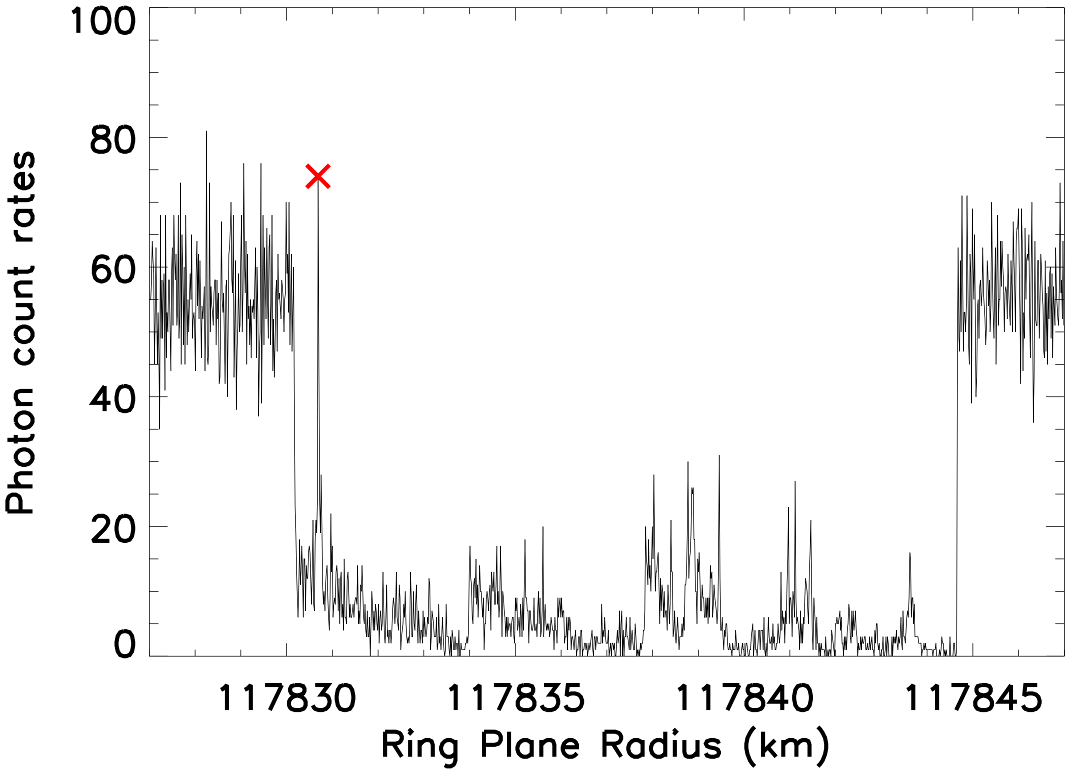

Figure 5.4: Photon count rates in the Huygens ringlet from the occultation of α Arae, rev. 63. The red cross identifies the position of the detected ghost. Its height matches the background level of the star.

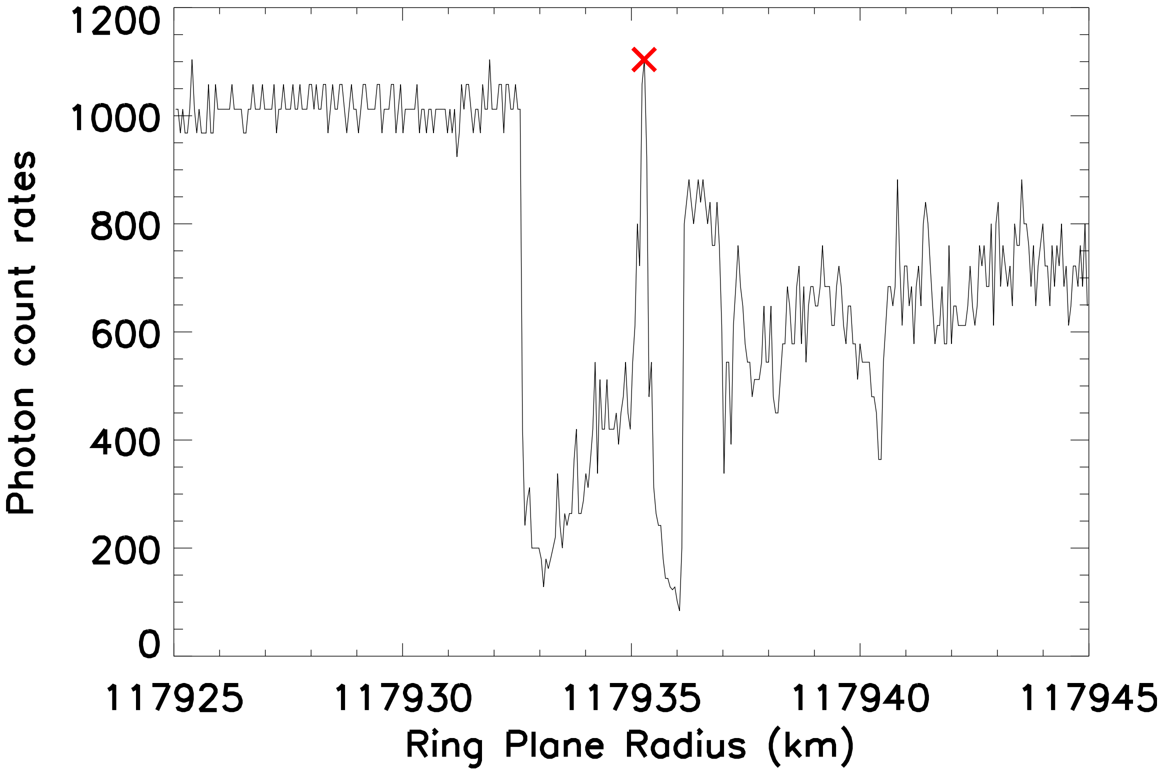

Figure 5.5: Photon count rates outside the Huygens Gap from the occultation of α Virginis, rev. 34. The red cross identifies the position of the detected ghost. Its height matches the background level of the star.

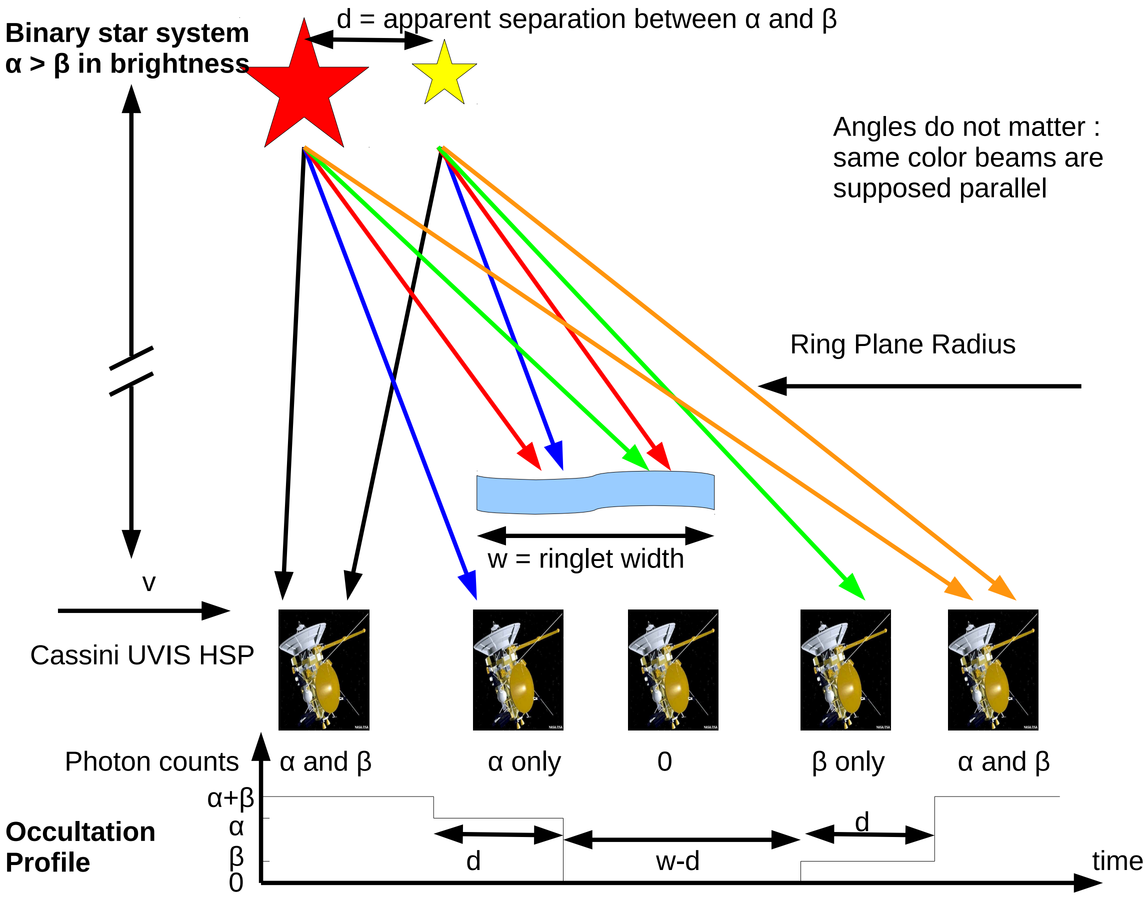

Binary star system
α > β in brightness
d = apparent separation between α and β
Angles do not matter : same color beams are supposed parallel
Ring Plane Radius
w = ringlet width
v
Cassini UVIS HSP
Photon counts
α and β
α only
0
β only
α and β
α+β
α
β
0
Occultation Profile
d
w-d
d
time

Figure 5.6: While Cassini UVIS is moving along the rings and a structure (edge, ringlet...) comes in between the target binary stars and the spacecraft, we will observe steps in the measured photon count rates. The heights of these steps are proportional to the brightness of the binary components and are additive when both components are unocculted. The radial widths of the steps are function of the apparent separation between the binary stars, as seen from the instrument.

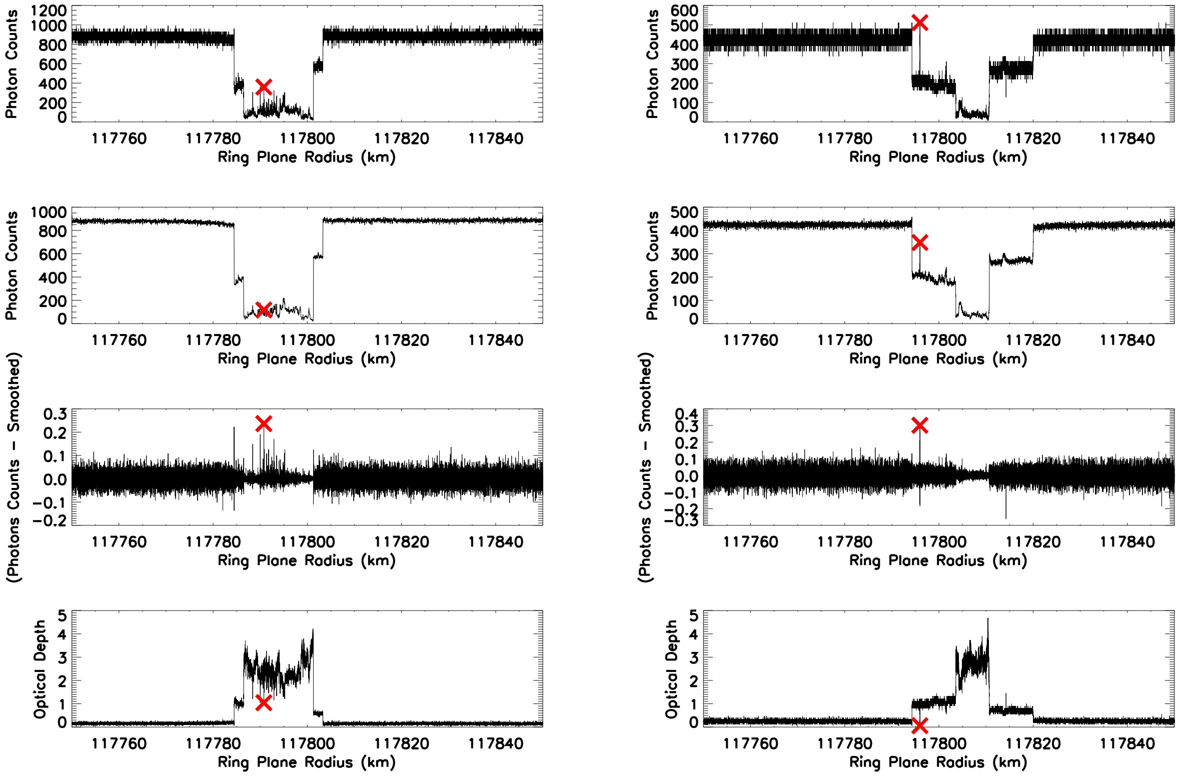

Figure 5.7: Upper panels show raw photon count rates versus ring plane radius for the occultation of the binary star α Cru (Rev 100), ingress (left) and egress (right). We observe the two rate levels due to the binary star. The central peak matches the level of one of the stars. The three lower panels for each direction of occultation provide details about the detection process steps: smoothing, subtracting and filtering on optical depth levels.

star photon counts in places without ring material. In order to detect these ghosts, we focus on the plateaus in the Cassini Division and in the C ring (the A ring contains too many clumps and therefore too many potential ghosts for a first approach). Baillié et al. (2011) reported the presence of waves in the plateaus P5, P6, P7 and P10 (according to the plateaus zoology defined by Colwell et al. (2009b)): these regions are excluded from our present study in order to avoid false-positive detections of ghosts. For similar reasons, we exclude the part of the Cassini Division between 120770 km and 120900 km.

In order to detect the points that present a much higher photon counts than their direct neighbor environment, we start by smoothing the occultation data by 10 points and subtracting it from the original signal (Figure 5.8). Then, looking for drops in optical depth that are bigger than a threshold of 0.94 (validated by a series of test runs on a pre-set of visually identified ghosts) allows detecting isolated high counts features. We then identify the features that present a photon count rate close to the background level of the star (or to one of the background levels of one of the stars of a binary star system). Finally, in order to identify their environment, and make the difference between ghosts and cosmic rays, we compare the median level of photon counts immediately around the peak with the median value of the photon counts in a known gap area from which we extract an average photon count rate for the given occultation.

Then, binning the original signal and reproducing the same process as described previously on the new data set allows the identification of wider structures. We binned our data by every number of points up to 20 before removing redundant detections. This whole procedure permitted the identification of 300 ghost structures, 35 located in the C ring and 265 in the Cassini Division. However, we note that structures that are wider than 8 points appear to be different than previously analyzed narrower ghosts (we would refer to them as gaplets). The structures' widths in number of data points are reported in Table 5.1.

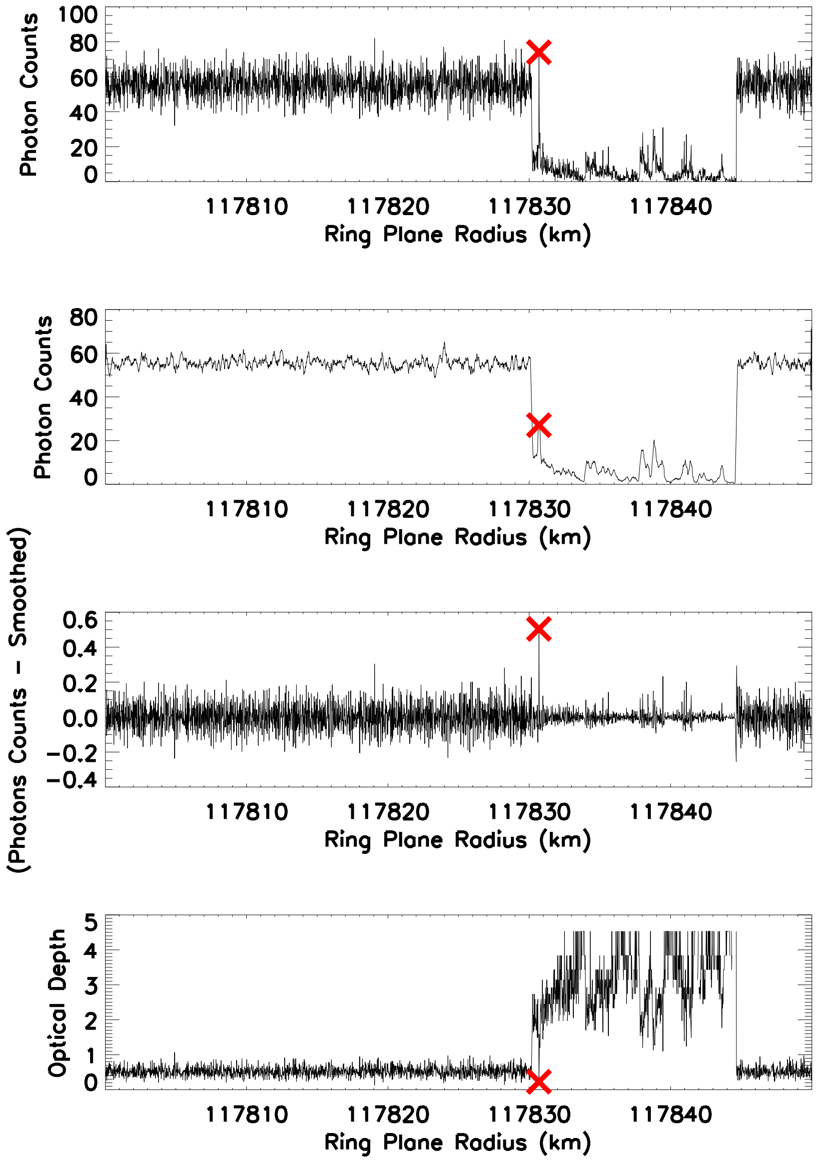

Figure 5.8: Photon count rates of the Huygens ringlet from the occultation of α Arae, rev. 63. The corresponding smoothed data is shown in the second plot. After subtracting the smoothed data from the raw data, the third plot (c) identifies the exact position of isolated features that might be a potential ghost (the structure around 117831 km is flagged as a potential ghost). The optical depth is also represented (d).

Table 5.1: Detected ghost rates and widths.

Width N	C ring		Cassini Division	
(in data points)	Number of ghosts	Width W (m)	Number of ghosts	Width W (m)
1	17	5.4 - 46.7	105	1.7 - 82.6
2	11	6.7 - 41.8	61	2.4 - 94.3
3	5	10.4 - 15.6	32	3.8 - 193
4	0	-	11	5.2 - 184
5	2	18.8 - 26.5	8	5.0 - 277
6	0	-	7	27.9 - 149
7	0	-	5	37.4 - 85.8
8	0	-	5	53.5 - 60.1
$\geqslant 9$	0	-	31	63.4 - 375

Widths are provided in equivalent data points N (number of data points with higher photon counts than the width at half height of the ghost) and converted in meters (W), using the occultation resolution. Considering a width-uncertainty of one data point on our measure of the ghost's width, this corresponds to an uncertainty of W/N meters or a relative uncertainty of $1/N$.

Figure 5.9 presents the cumulative distribution of these widths in terms of number of data points.

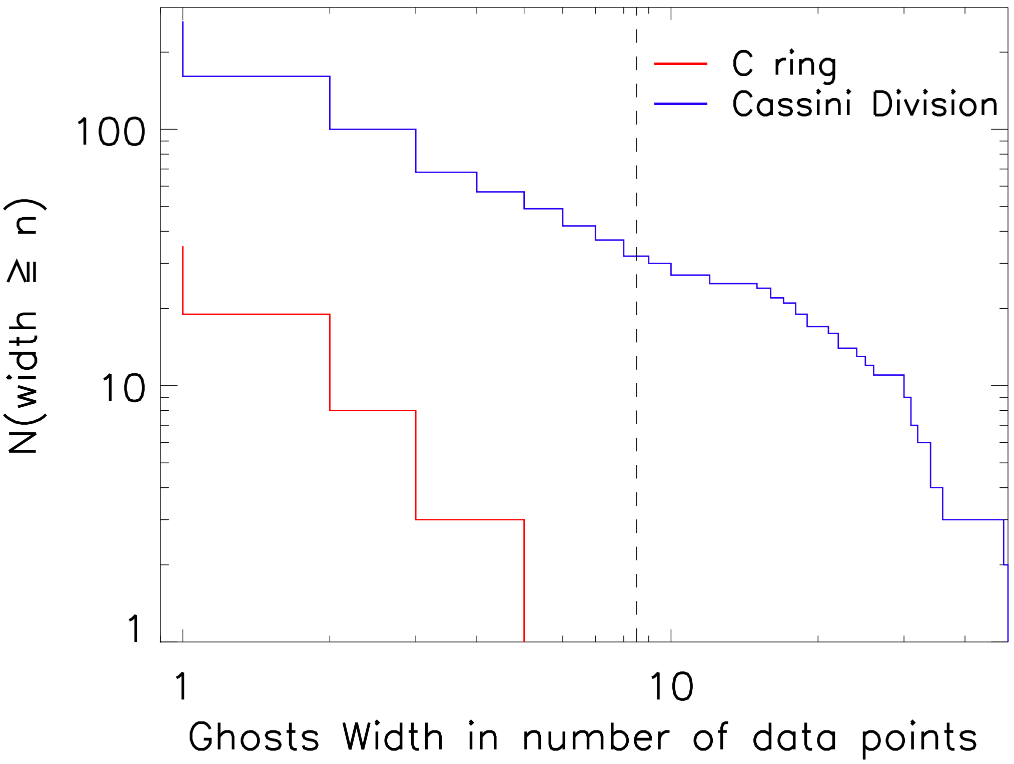

Figure 5.9: Cumulative width distribution of the detected ghosts in number of data points. The zone at the left of the vertical dashed line delimits the structures that we consider as ghosts with a high confidence. Larger structures (wider than 8 data points) that can correspond to other phenomena are excluded from the following study.

5.2.2.2 Chance Detection

Cassini UVIS-HSP is also subject to measure artifacts such as cosmic rays that are characterized by localized high photon count rates and that can occur randomly at any moment and therefore at any ring plane radius. They usually saturate the photometer detector and we can expect counts to reach at least the background level of the stars in optically thick regions. As these counts do not reflect actual structures, we want to verify that cosmic rays are not counted in our detections.

In regions of low optical depth, we expect the photon counts to be close to the background level of the star: we can actually model our data as a Poisson-like distribution with a mean equal to the signal mean. Therefore, we can estimate the probability that significantly higher counts than this level belong to this distribution. If they appear unlikely to belong to this distribution, we count them as cosmic rays.

We focus on the regions detailed in Table 5.2.

Table 5.2: Reference gaps for the identification of cosmic rays.

Structure	r_{min}	r_{max}
Huygens Gap	117515	117932
Encke Gap	133423	133745
Roche Division	136774	139380

For each occultation, and for each of these gaps, we define a mean photon count rate. We identify potential cosmic rays as previously done for ghosts. We verify that our signal in this region can be considered as a Poisson distribution by estimating the difference between the mean of the signal and the square of the standard deviation, as seen on Figure 5.10.

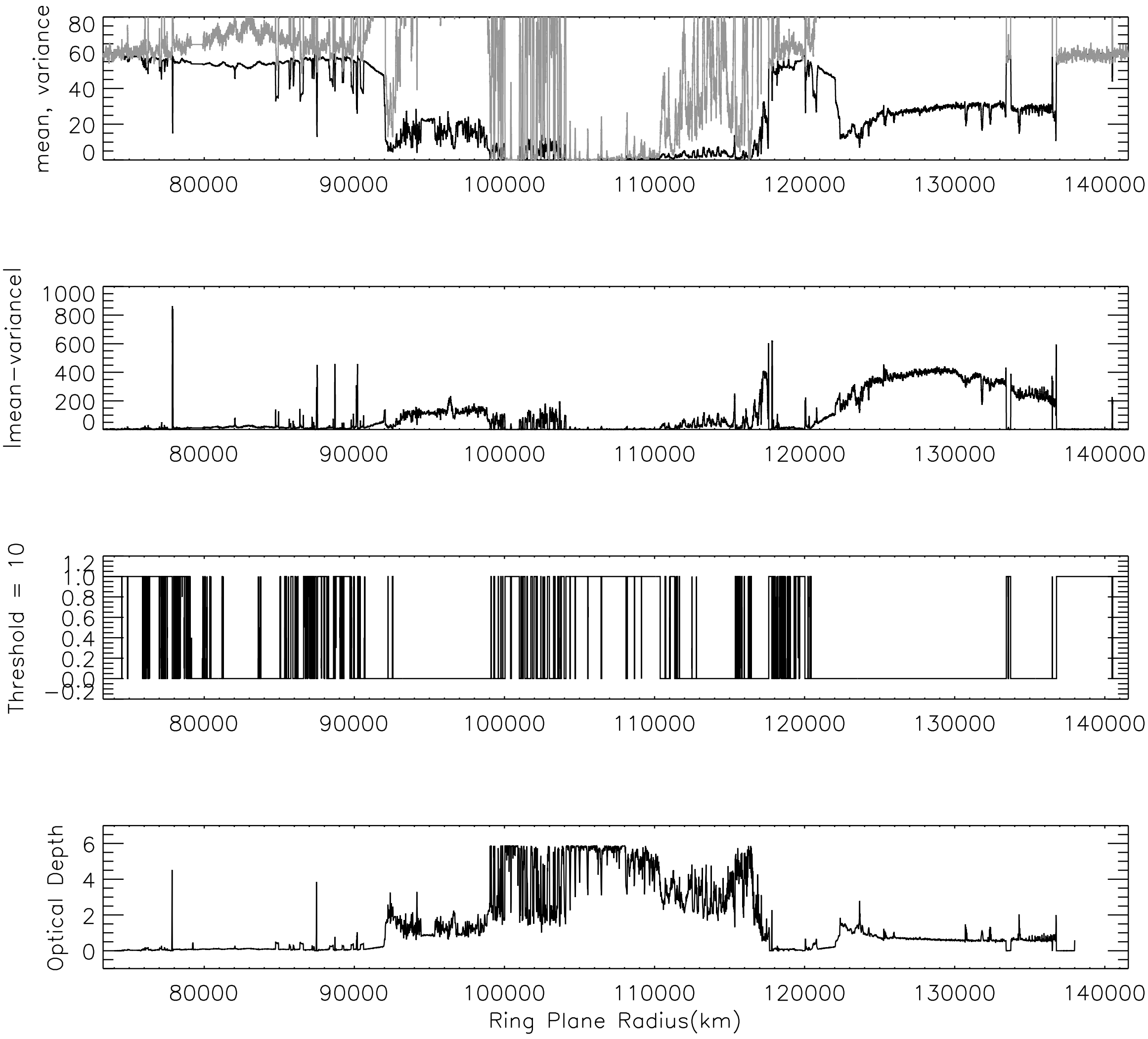

Figure 5.10: Top panel shows the mean of the signal in black and the variance of the signal in grey. Second panel presents the absolute difference between the mean and the variance, while third panel extracts the regions that can be considered "Poisson-like". Last panel shows the corresponding optical depth of the rings.

Then, considering a Poisson distribution, we estimate $p(k, \mu)$, the probability of obtaining a detection rate $d = k$, as shown in Equation 5.1.

$$p(k, \mu) = \frac{e^{-\mu}\mu^k}{k!} \tag{5.1}$$

Thus, the probability of having a rate at least equal to k is:

$$P(k, \mu) = 1 - \sum_{x=0}^{k-1}(p(x, \mu)) \tag{5.2}$$

and, the number m of points at this level, that can be expected in a Poisson distribution of N points, is given by Equation 5.3:

$$m(k, \mu) = N\ P(k, \mu) = N\ \left(1 - \sum_{x=0}^{k-1}(p(x, \mu))\right). \tag{5.3}$$

We considered a potential cosmic ray to be an actual cosmic ray if $m < 0.01$ expected actual points. Applying this process to all our identified potential cosmic rays allowed us to clearly identify 17 validated cosmic rays out of 84379588 measured points. Therefore we derived a density of cosmic rays of 1 cosmic ray per 4963505 points. We have to compare this density with the number of identified ghosts that are 1 data point wide: 122 1-data point wide ghosts were found out of 70 million scanned points. According to our measured cosmic ray frequency, we should expect to find 14 cosmic rays in our data set if we had not already been filtering our ghosts detection by matching the background level of the star (and therefore excluding all potential cosmic rays for which counts would be significantly higher than the background level of the star). This number is therefore over-estimating the number of our ghosts that would be actual cosmic rays. Chambers et al. (2008) estimated that the HSP would be hit by at most one cosmic ray in 71.8 hours (i.e. 1.3 $\times 10^8$ data points). According to that estimation, the actual number of our ghosts being cosmic rays should be negligible and we can state with a good confidence that our observed ghosts that are one data point wide are actual structures in the rings. In addition, wider ghosts cannot statistically be explained by the coincidence of two or more cosmic rays consecutive in the data set: the probability of two consecutive measures being perturbed by cosmic rays is indeed $\frac{2\times(14-1)}{70372391} = 3.7 \times 10^{-7}$. Therefore, only 2.7×10^{-5} of our 72 2-points wide ghosts can be explained by cosmic rays. Wider ghosts are also definitely corresponding to actual structures.

As mentioned in Figure 5.9, we decide to focus our study on ghosts that are between 1 and 8 points wide in order to avoid the structures that are so wide that internal structures can be distinguished.

5.3 Forming Ghosts

5.3.1 The Propeller Model

In order to understand the interactions between a moonlet and the ring particles, we evaluate the radius of the Hill sphere of a given moonlet of mass $M_{moonlet}$ and of semi-major axis $a_{moonlet}$:

$$r_H = a_{moonlet} \left(\frac{M_{moonlet}}{3(M_{Saturn} + M_{moonlet})} \right)^{1/3} \tag{5.4}$$

where M_{Saturn} is Saturn's mass. The Hill sphere of a moonlet is the region in which its attraction dominates Saturn's attraction.

Numerical simulations of the interactions between ring particles and a moonlet showed the apparition of a depletion in surface mass density in the neighborhood of the moonlets (Petit and Henon, 1988). The chaotic depletion zone where particles are cleared out by the moonlet presents two different lobes due to Keplerian shear: the inner one is carried forward while the outer one is trailing behind. Spahn and Wiebicke (1989) and Spahn et al. (1992) showed that smaller moonlets will only create localized S-shaped density modulations which radial width scales as r_H for moonlet diameters lower than 3 km and as r_H^2 for larger moonlets (Petit and Henon, 1988). Moonlets larger than 2 km in diameter can lead to the formation of complete circumferential structures: diffusion is not strong enough to close the depletion before/after the moonlet, stretching it around the entire ring system. The depletion becomes a gap although the wakes are still visible close to the moonlet. Even larger moonlets (larger than 5 km in diameter) can lead to the formation of an inner ringlet, flanked by gaps. Beyond these gaps, satellite wakes are formed as described in Showalter et al. (1986). Sremčević et al. (2002) estimated that it requires a moonlet with a radius larger than 840 m to open a gap in the B ring. The S-shape of this density modulation, called "propeller" has been described quantitatively by Spahn and Sremčević (2000) and Sremčević et al. (2002) using a viscous fluid model of the rings. They provided analytical expressions for the overall azimuthal L_ϕ and radial L_r extensions of the propeller feature:

$$L_\phi \approx \frac{50\Omega_0 r_H^3}{(1+\beta)\nu_0} \tag{5.5}$$

$$L_r \approx 10 r_H \tag{5.6}$$

where r_H is the Hill radius, $\Omega_0 = \sqrt{\frac{GM_{Saturn}}{a^3_{moonlet}}}$, ν_0 is the kinematic viscosity ($\nu_0 \approx 10\mathrm{cm}^2\ \mathrm{s}^{-1}$), $\beta = \frac{dln(\nu)}{dln(\sigma)} = 1.25$ and σ is the surface mass density.

Tiscareno et al. (2008) showed that these gap extensions may not be accurate and suggested that the observed propeller-shaped features are due to moonlet wakes rather than propeller-shaped gaps and Lewis and Stewart (2009) determined from numerical simulations that propellers can form only if the mass of the moonlet is at least 30 times higher than the mass of the largest particle in the nearby ring. Indeed, for bigger particles, self-gravity tends to accelerate the damping of the propeller-shaped gaps and prevent the formation of moonlet wakes. Therefore, calling a_{max} the radius of the largest particle in the vicinity of a moonlet, and assuming an identical density (the density of dirty ice: 1000 $kg\ m^{-3}$) for the moonlets and the particles around, we have:

$$a_{max} = \frac{r_{moonlet}}{30^{1/3}} \tag{5.7}$$

Latest numerical simulations from Tiscareno et al. (2008) use numerical integration of the classical Hill problem (massless test particles orbiting a large central body and deflected in the vicinity of a perturbing mass) in order to recreate propellers (Figure 5.11). This figure is generated with initial particles on circular orbits with semi-major axis uniformly distributed around the moonlet. Particles with a semi-major axis difference Δa with the moonlet lower than 2 r_H follow horseshoe orbits.

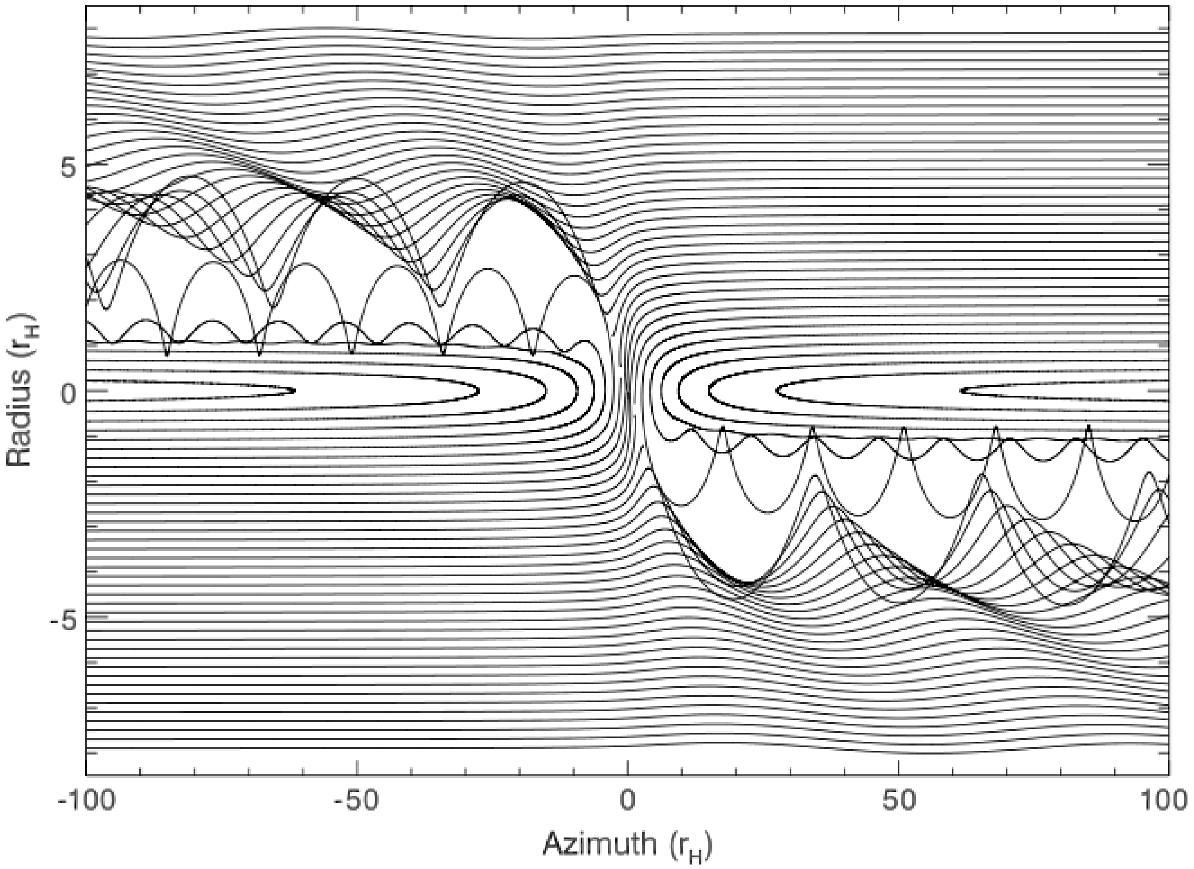

Figure 5.11: Propeller-shaped depletion zones created around a central moonlet. Orbital direction is towards the right and the planet is towards the bottom. Figure from Tiscareno et al. (2008).

Further particles are still perturbed and receive a kick in eccentricity proportional to $1/(\Delta a)^2$. In addition, the phases of these particles' orbits are roughly aligned (Showalter and Burns, 1982). These now eccentric particles will leave an open space on the outer trailing side and inner leading side of the moonlet. This primary depletion zone has a radial extension of a few Hill radii while its azimuthal extension can be much larger as confirmed in numerical simulations (Figure 5.12). After a few orbits, the oldest and farthest depletion zones are destroyed by the combined effects of collisions and inter-particle gravitational forces provoking either a damping of the eccentricity, a randomizing of the phases or a scattering of the eccentric particles in the depletion zones. The compression of the streamlines will form the satellite wakes. With the combined effects of collisions and self-gravity, the eccentricity of the wake particles will decrease and the structure will fade. More realistic models involve inter-particle collisions and self-gravity wakes; the latter usually accelerates the damping of the propeller shaped gaps and generally prevents the formation of moonlet wakes.

Tiscareno et al. (2008) suggested a propeller model based on Equation 5.8 providing the contours of the depletion zones.

$$\begin{aligned} f(l,r) &= A_0 + A_1 \left[\exp -\frac{1}{2} \left(\left[\frac{l - l_0 + \Delta l/2}{a/2} \right]^2 + \left[\frac{r - r_0 - \Delta r/2}{b/2} \right]^2 \right) \right. \\ & \left. + \exp -\frac{1}{2} \left(\left[\frac{l - l_0 - \Delta l/2}{a/2} \right]^2 + \left[\frac{r - r_0 + \Delta r/2}{b/2} \right]^2 \right) \right] \end{aligned} \tag{5.8}$$

where the radial and azimuthal extensions of one lobe (b and a), and the radial and azimuthal separations of the lobes (Δ_r and Δ_l) are shown in Figure 5.13.

This Equation described the gaps as two Gaussian peaks of azimuthal extension a and radial extension b, with their centers separated by Δl azimuthally and Δr radially, as represented in Figure 5.13. This model was mainly used to estimate the size parameters of the A ring propellers from their brightness measurements (the background brightness is A_0 and the brightness amplitude is A_1).

From numerical studies, Sremčević et al. (2002) could estimate $L_r = \Delta_r + b \approx 10 r_H$, where the radial separation between the two lobes was evaluated by Seiß et al. (2005) in

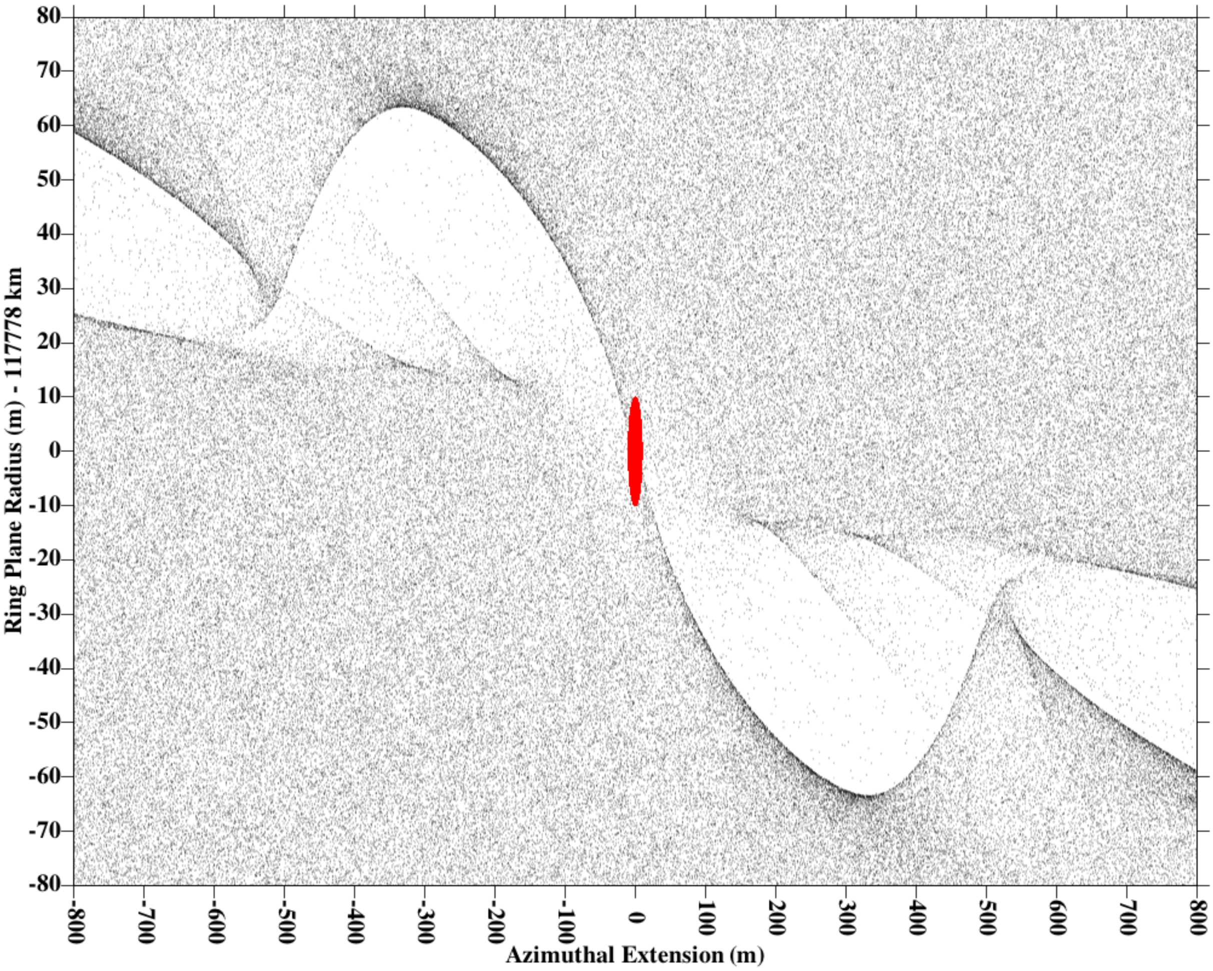

Figure 5.12: Primary lobes of the propellers created by the interaction of 20-cm radius particles with a 10-m radius boulder. Optical depth is 0.1 and Saturn's direction is towards the bottom.

collisional N-body simulation using uniform particle sizes and no self-gravity between the ring particles, and supported by Tiscareno et al. (2008): $\Delta_r \approx 4r_H$. This approximation was confirmed by recent observations of propellers in the A ring (Tiscareno et al. (2008), Lewis and Stewart (2009) and Tiscareno et al. (2010b)). This would therefore provide $b \approx 3r_H$.

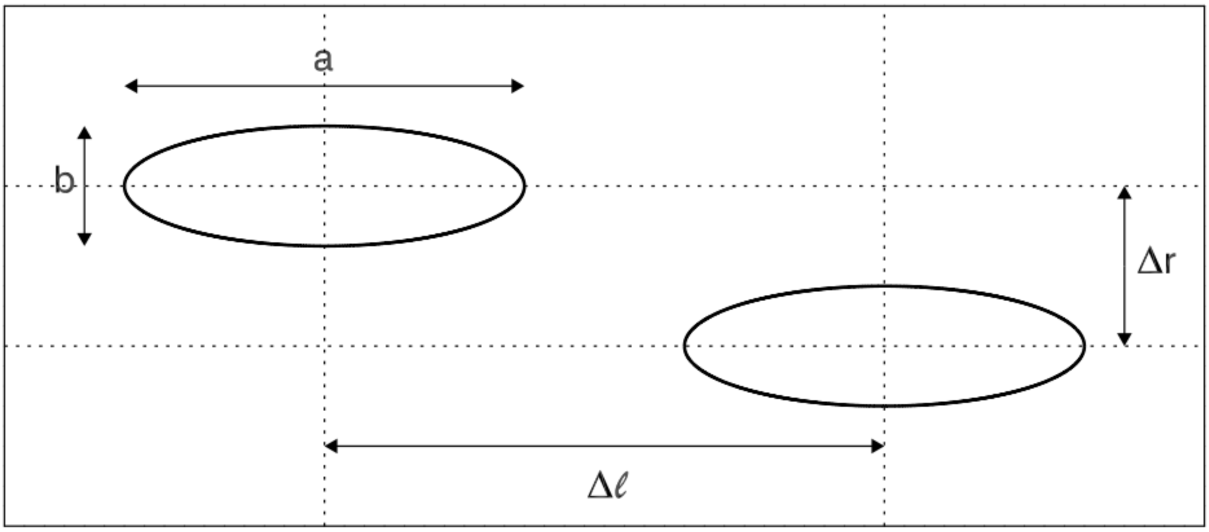

Figure 5.13: The propeller model described by Equation 5.8. The coordinate system is a radius-azimuth grid, in which the direction toward Saturn is down (-r) and the orbital direction is to the right (+). From Tiscareno et al. (2008).

Previous observations of propellers showed bright regions around the gaps (Figure 5.14). These bright strands were both seen on the lit and unlit sides, validating that it is not a scattering effect. However, these bright regions cannot be fully explained by our numerical simulations. Sremčević et al. (2007) suggested that collisions could dislodge the particles regolith, increasing the reflectivity and therefore showing as brighter in Cassini images, whereas Tiscareno et al. (2008) described that bright regions could be due to the disruption of self-gravity wakes and the spreading of the material in the self-gravity wakes, increasing the reflectivity.

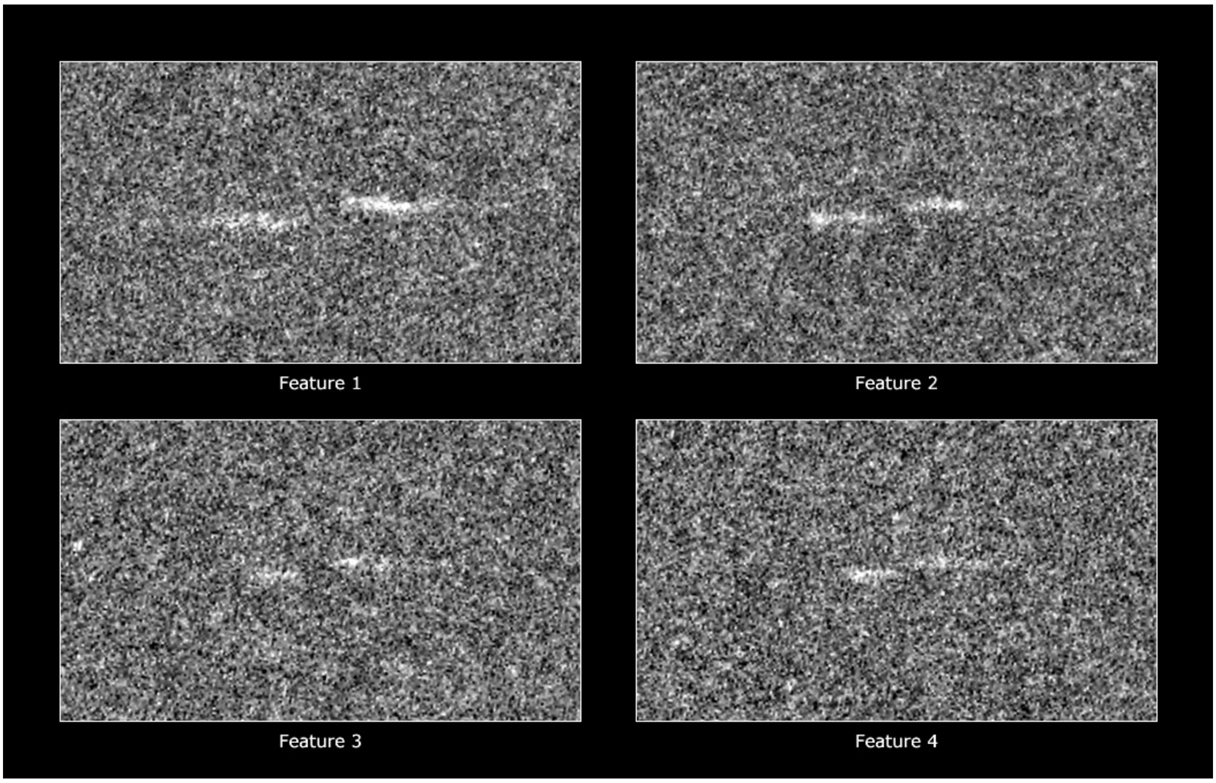

Figure 5.14: Credit: NASA/JPL/Space Science Institute. Four propellers were identified in two images taken from Saturn Orbit Insertion on July 1, 2004 with the narrow angle camera on-board Cassini. These propellers are located in the A ring. They are about 5 kilometers long overall and have a total radial extension around 300 meters. Images are reprojected: Saturn is up and orbital motion is toward left.

5.3.2 Numerical Simulations

5.3.2.1 The Numerical Code

We adapted the N-body numerical code described in Lewis and Stewart (2009). This code assumes the particles are smooth, inelastic, hard spheres. Using Hill's approximation (Murray and Dermott (1999) and Stewart (1991)), the particle motions are described using a rotating pseudo-cartesian coordinate system referred to as "guiding center variables" in Lewis and Stewart (2009). And additional details on the numerical methods are provided in Appendix A. Our simulations used periodic conditions for the azimuthal direction: therefore we made sure that our evolution times verified that no excited particle would cycle to get involved in a second close encounter with the moonlet in order to comply with reality where perturbations from a close encounter with the moonlet have been damped for a long time when a second close encounter happens.

5.3.2.2 Forming S-Shaped Depletion Zone

First considering a limited box, propeller signatures are presented in Figure 5.15. We can see clear open zones on the outer trailing side and inner leading side of the moonlet. Higher order open zones are degrading as the close encounter of the particles surrounding it gets older. We can also observe the formation of satellite wakes in the prolongation of the peaks of the open gaps. Considering only a few orbits will be equivalent to set up a fixed damping length, and therefore the structures farther from the moonlet than the open gaps will show the packing of the streamlines creating the satellite wakes. Such patterns can be observed in Figure 5.15, in the upper left and lower right corners. Features in the upper right and lower left corners are actually artifacts generated by the azimuthal cyclic boundary conditions of our simulation.

A zoom in the primary outer trailing depletion zone (Figure 5.16) allows us to estimate the variation of the radial extension with respect to the azimuthal distance to the boulder. We can numerically interpolate a scaled shape of this primary depletion zone for later purposes.

5.3.2.3 Parameters

5.3.2.3.1 Time Steps

For our initial set of parameters, it appears that the computation time is optimized for timesteps between 10^{-4} orbital period and 10^{-2} orbital period at 117778 km. For lower values, the computation time explodes while the resulting positions of the particles starts showing some variations for timesteps longer than 10^{-1} orbital period. As a precaution, we set the timestep at 10^{-3} orbital period.

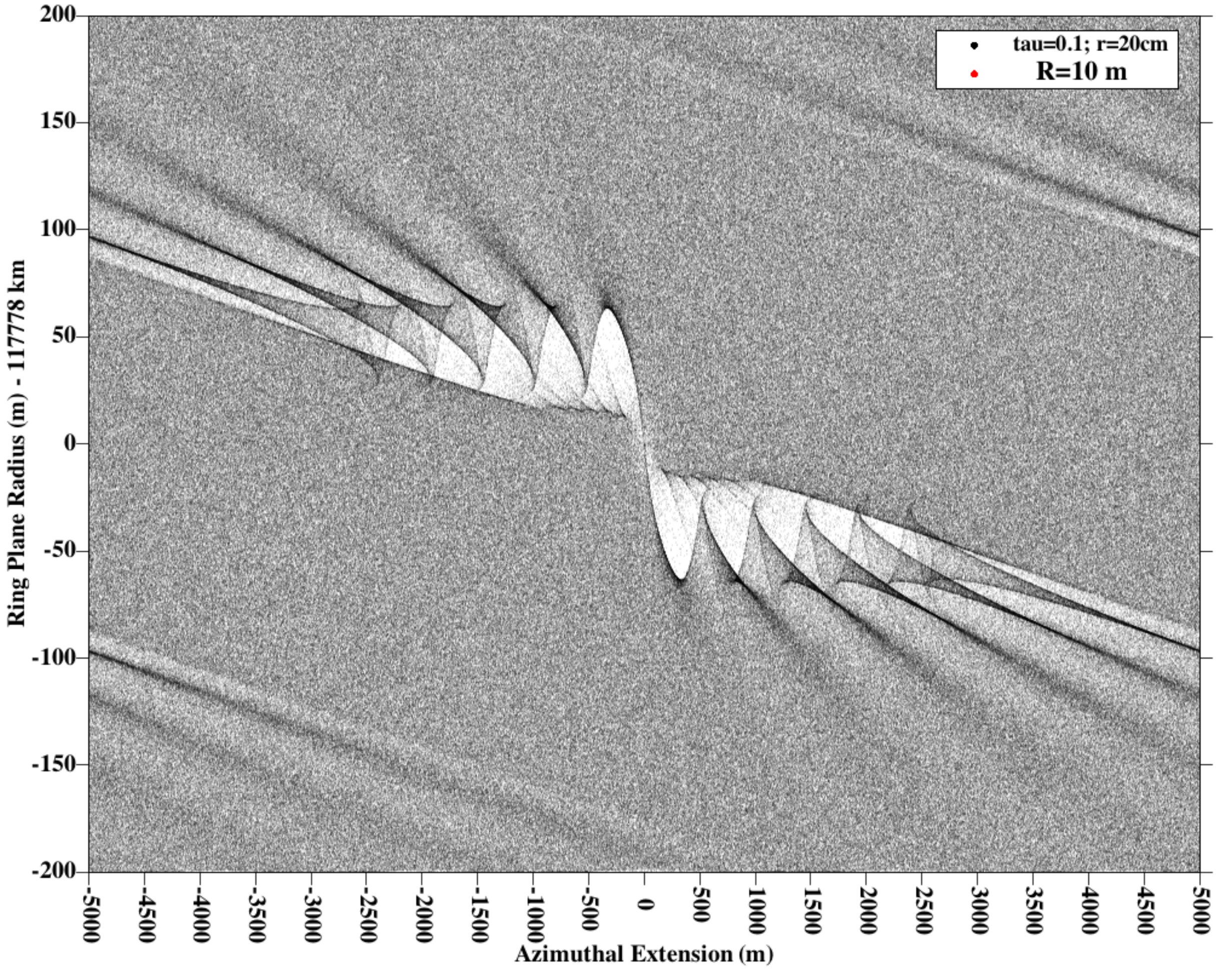

Figure 5.15: Propeller signature after 6 orbits for a 10-m radius boulder (represented in red in the center of the figure) and 20-cm radius ring particles. Enough particles were simulated to reach an optical depth of 0.1. Saturn's direction is towards the bottom.

5.3.2.3.2 Particle Population

The radial and azimuthal positions of the particles guiding centers are randomly set with uniform probabilities in the box. However, we center the box around the ring plane radius of the Huygens ringlet in the Cassini Division at 117778 km. Eccentricities are also uniformly

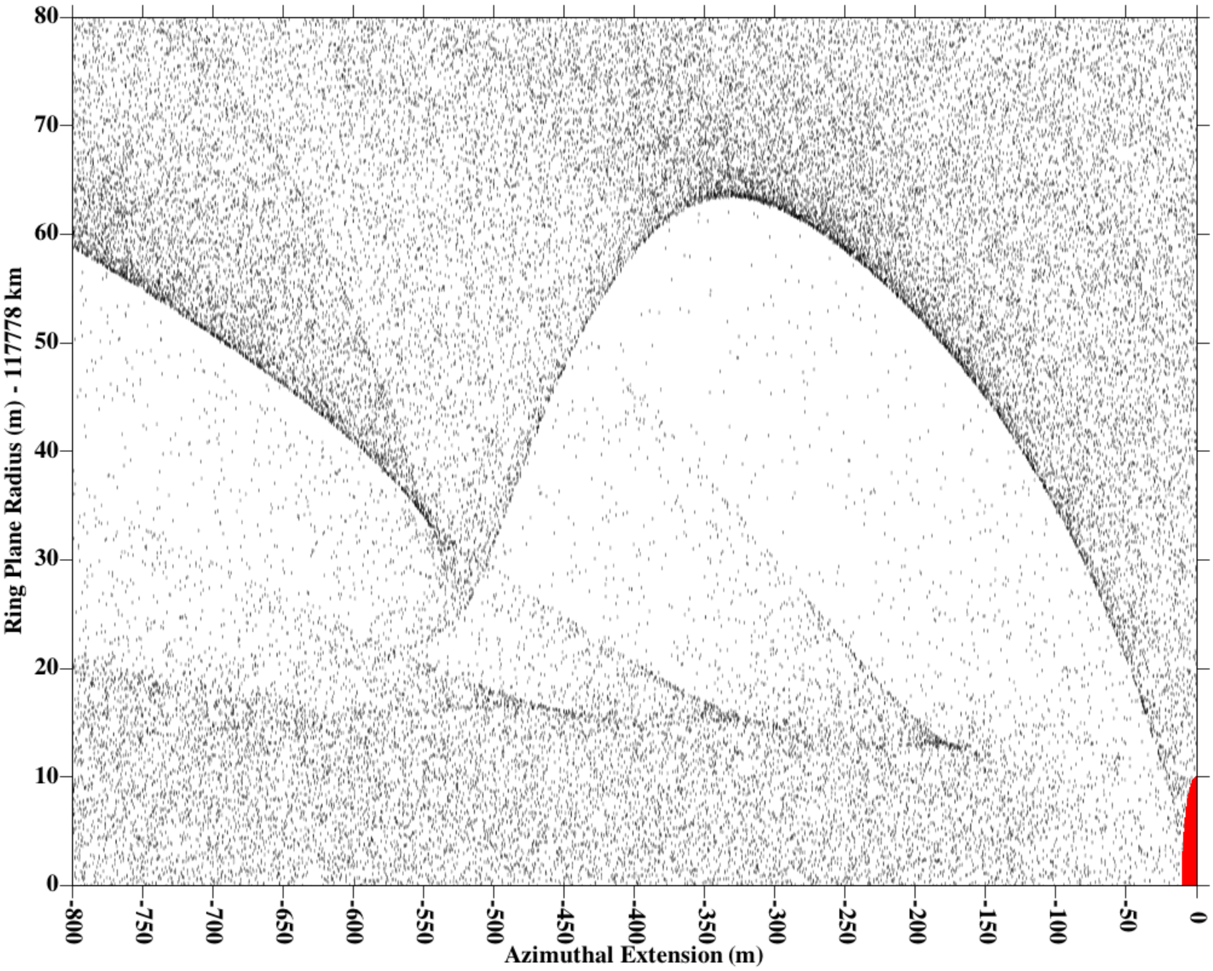

Figure 5.16: Primary lobe of the propellers created by the interaction of 20-cm radius particles with a 10-m radius boulder. This zoom in is showing the primary trailing outer lobe of the depletion zone. Particles around this zone had a close encounter with the boulder less than one orbit ago.

randomly distributed between 0 and 10^{-8}, as well as inclinations between 0 and 2×10^{-8} (the larger inclination range aims at reducing the probability of finding overlapping particles) and epicyclic phases between $-\pi$ and π. However, we can have a rough estimate of the optical depth if we consider the rings as mono-layered. In that approximation, and considering a box of radial extension h and azimuthal extension w, we can establish the following relation between the number of particles N, their radii r_p (supposed uniform) and the optical depth τ:

$$\tau = \frac{N\ \pi\ r_p^2}{h\ w} \tag{5.9}$$

Since we are focusing on relatively high optical depth regions in the C ring and the Cassini Division, we can set $\tau = 0.1$ for a start. For larger simulations involving tens of millions of particles and more, the run time can be very long and it becomes necessary to decrease the number of particles. However, we want to conserve the optical depth and the particles mass m. Therefore, we change the density of the particles (conserving the density of the boulder) in order to match the conservation of the optical depth and particle mass. Dividing the number of particles by a factor 4, for example, will multiply the particles radii by a factor 2, and the mass by a factor 8. We then have to divide the particles density by 8 and the surface mass density will become one-quarter of what it was. Figure 5.17 compares the shapes and sizes of the primary open gaps for different sets of [particle radius - number of particles - particle density] that all have the same optical depth and particle masses. No real difference can be seen in the sizes and in the shapes of the depletion zones. Such a process can therefore be used to decrease the number of particles or consider bigger simulation boxes.

Another possibility would be to conserve the surface mass density instead of the particle masses. Following the same example, we would need to divide the density by a factor 2

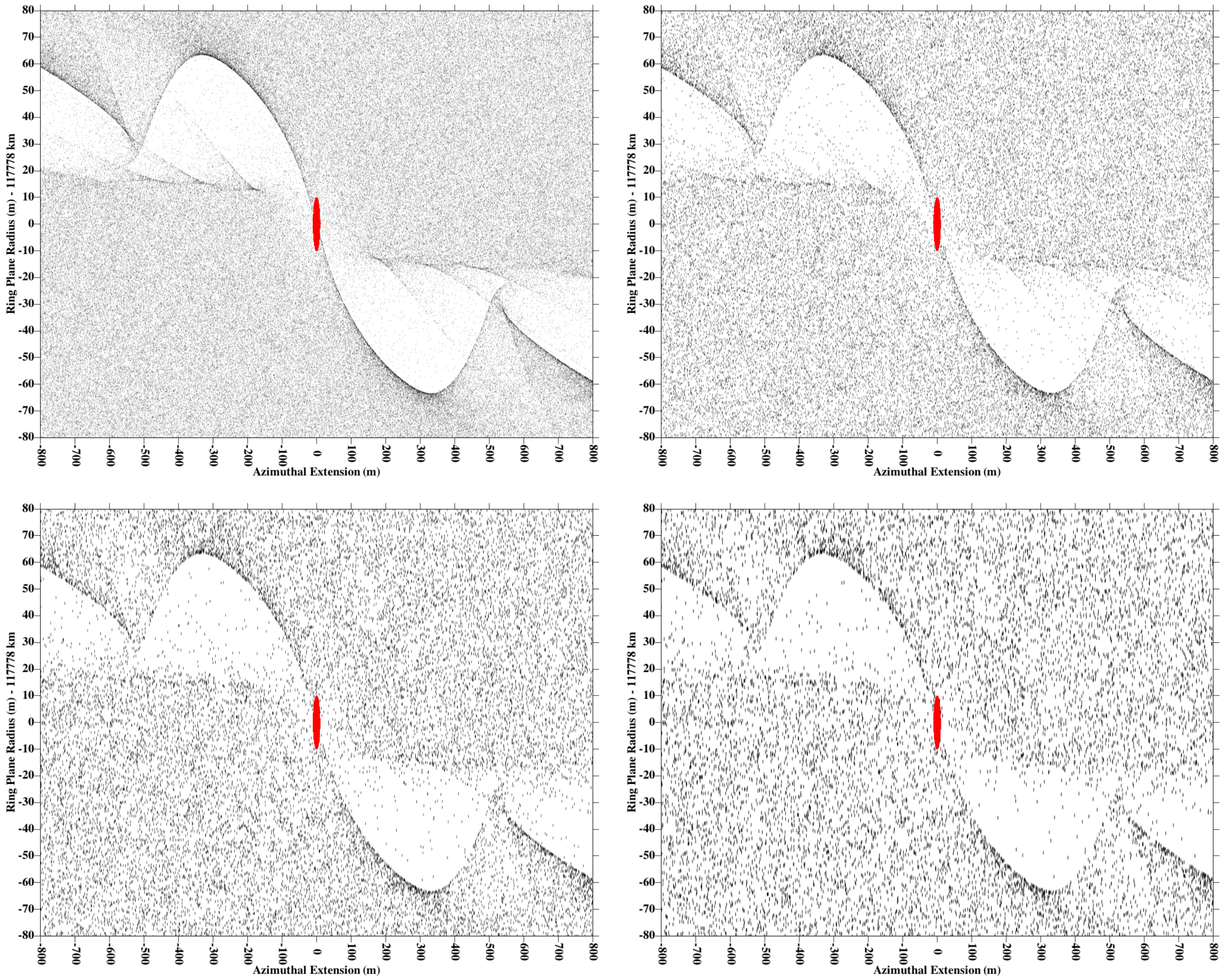

Figure 5.17: Propeller signature for a 10-m radius boulder (represented in red). Particles radii are 20 cm (upper left), 40 cm (upper right), 60 cm (lower left) and 80 cm (lower right). In each case, the optical depth and the particle masses are kept constant. Saturn's direction is towards the bottom.

instead but in that case, each particle mass would be multiplied by 4 and the particles motion would be changed and no longer physically realistic.

5.3.2.3.3 Forcings

We are mainly interested in the gravitational forcing of a central boulder. The density of this boulder is taken by default equal to the density of the particles: $\rho = 850\ kg\ m^{-3}$. Inter-particle gravity and collisions are numerically very time-consuming given the number of particles that we had to consider in order to reach an optical depth around 0.1. Some tests were conducted to estimate the importance of the collisions and of the inter-particle gravity. For a given optical depth τ, we can estimate a typical collision timescale of $t_{coll} \approx \frac{t_{orb}}{\tau}$, where t_{orb} is the orbital period at that location. Therefore, collisional dependencies can only be estimated after a few orbits. Figure 5.18 shows the exact same initial conditions with different forcing configurations involving collisions and self-gravity. It appears that self-gravity is not playing an important role in the shaping of the propellers and wakes. However, propellers are damped by collisions, even though the S-shape remains. The gap radial width is somehow lowered by the faster presence of particles filling the depletions. No adhesion forces are implemented in our simulations.

In our simulations, the boulder stays stable at the center of the simulated box as long as particles are not big enough to change its orbital elements (we verified that this does not happen as long as the particle size radius condition of existence of the depletion zones is respected (see Section 5.3.1)). It appears that collisions and self-gravity are not playing a key role in the formation of primary propeller signature zones for the initial particle populations described by Zebker et al. (1985) in our regions of interest. However, Lewis and Stewart (2009) showed that self-gravity will generally prevent boulder wakes from forming and will

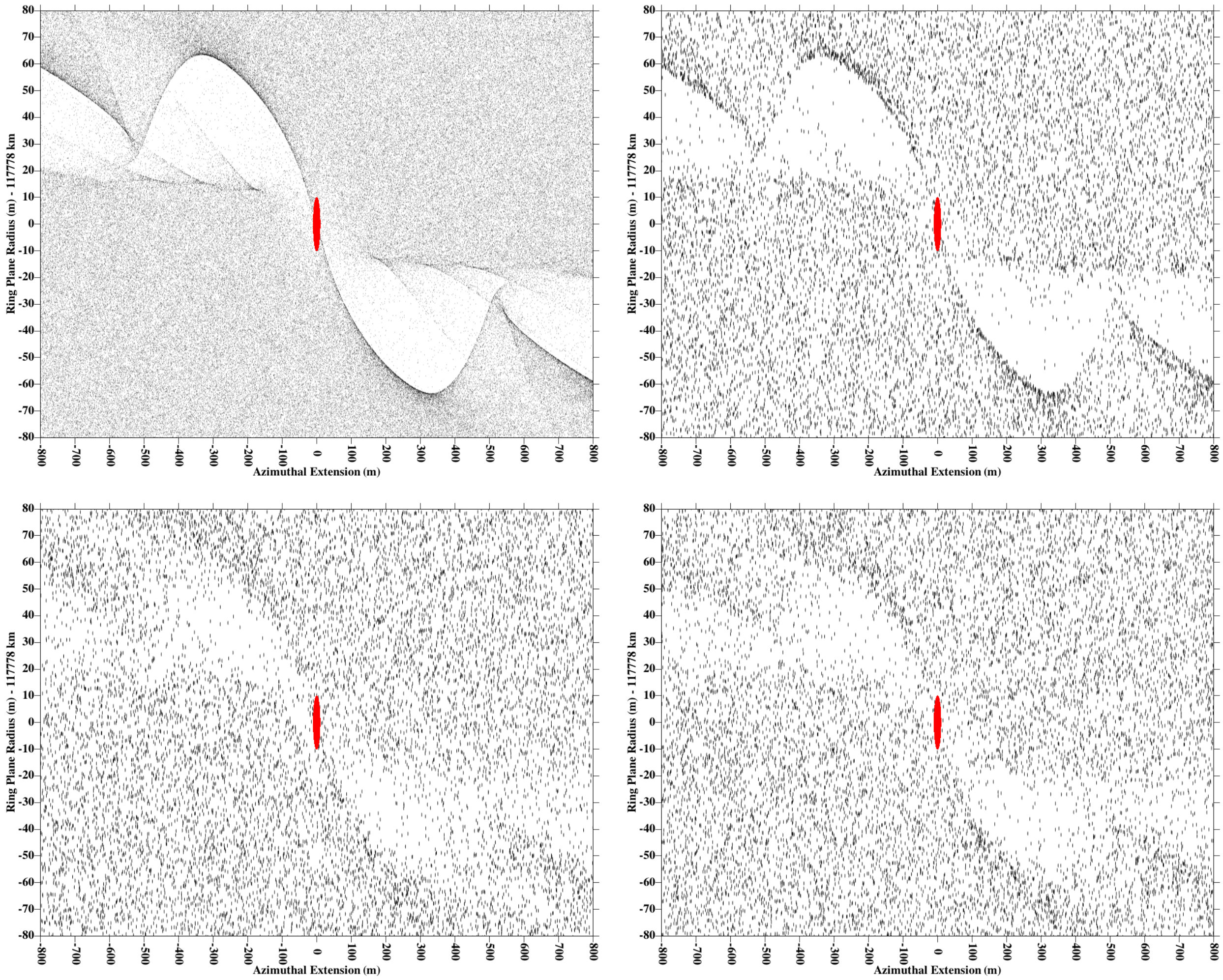

Figure 5.18: Propeller signature for a 10-m radius boulder (represented in red) and equivalent 20-cm radius ring particles (in agreement with results from Section 5.3.2.3.2, we consider 80-cm radius particles with a density of 13.3 $kg\ m^{-3}$). Enough particles were simulated to reach an optical depth of 0.1. Saturn's direction is towards the bottom. Upper figures do not consider collisional effects whereas lower figures do. Self-gravity is taken into account only in right figures.

rapidly damp the higher order propeller-shaped gaps. Inputting particles sizes close to the boulder radius will have a similar effect.

5.4 Results

5.4.1 Quantitative Results

5.4.1.1 Observational Results

We identified 35 ghosts in the C ring plateaus and 265 ghosts in the Cassini Division ringlets and plateaus (mainly in the Huygens Ringlet, the Triple Band and the Cassini Division ramp). No real meaningful spatial distribution can be drawn from our observations since we already selected the places where we were observing. However, we notice that ghosts do not appear in similar locations between occultations. We therefore conclude that these features are not complete circular gaps. In addition, we could estimate an observed radial width W for each of the observed ghosts. As shown in Figure 5.19, the ghosts are a few data points wide, and we can estimate their width by taking the width at half-height of the interpolation of the occultation scan.

The observed W is necessarily lower than the modeled quantity b since the instrument was scanning an rounded hole (according to the model detailed in Figure 5.13), probably not at the precise location where the scanned width is equal to b. We are therefore estimating

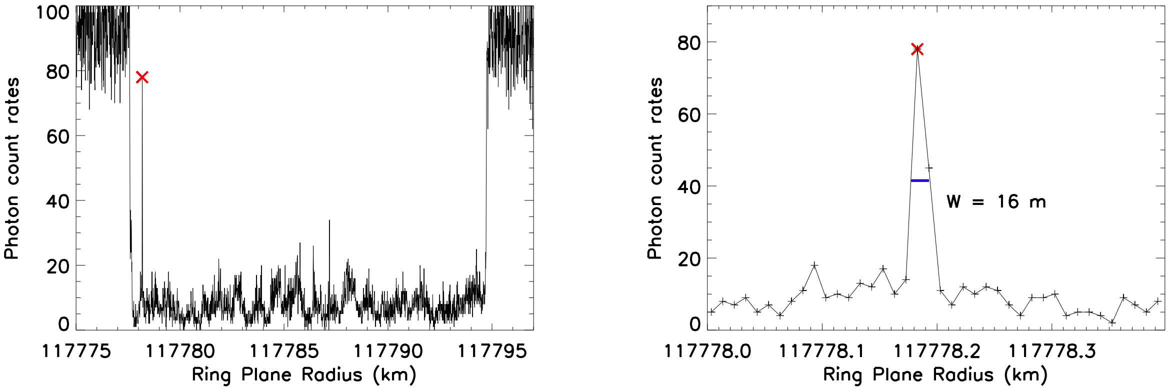

Figure 5.19: Photon count rates from the occultation of κ Centauri, rev. 35 across the Huygens Ringlet (left). We measure the width of the isolated peak (here defined by two data points) by estimating the width at half-height of the interpolation of the data (16 m) - (right).

lower limits on the sizes of the ghosts. However, in first approximation, we considered $W = b$ and measured width ranges for the observed ghosts from 5.4 m to 46.7 m in the C ring and from 1.7 m to 277 m in the Cassini Division. Cumulative distributions of the ghost widths in the C ring and Cassini Division are presented in Figure 5.20.

Assuming that these ghosts are part of propellers created by boulders orbiting in the rings, we estimate the Hill radii for these boulders and therefore derive the boulder radii. From those, we could evaluate the azimuthal extension of the corresponding propellers and also the size constraints on the largest particles in the vicinity of the ghost from Equation 5.7 (Table 5.3). Recent estimates of the vertical thickness of the C ring (from Baillié et al. (2011)) and Cassini Division (from Colwell et al. (2009a)) are provided for comparison.

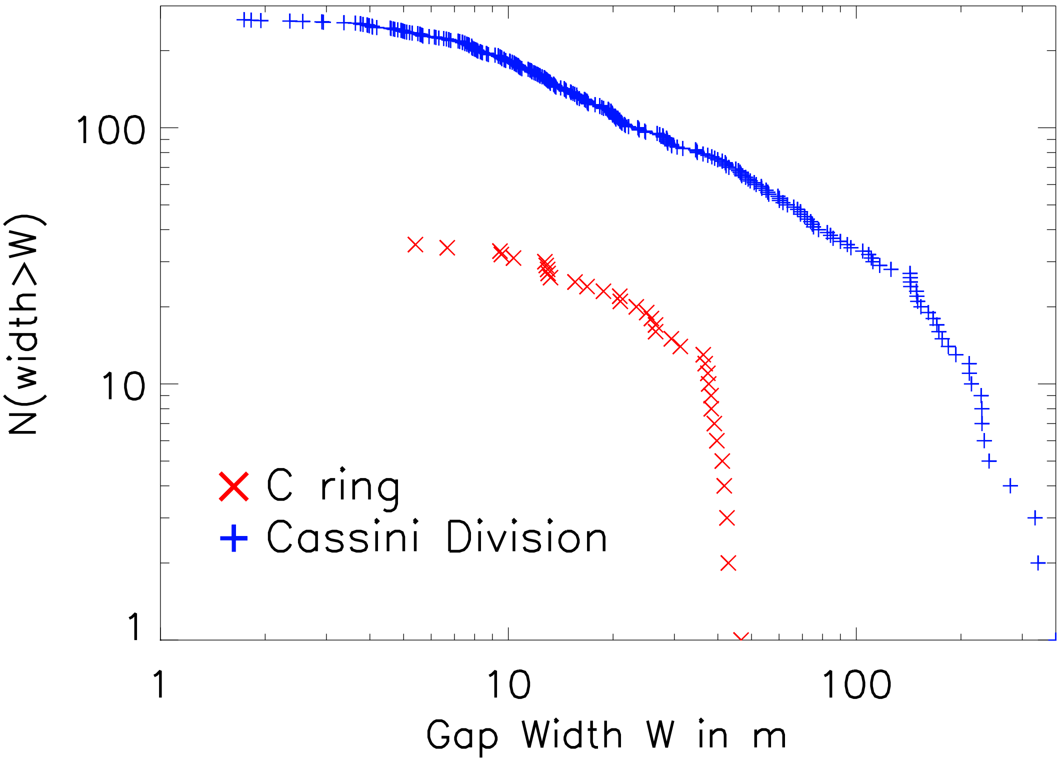

Figure 5.20: Cumulative distribution of the ghosts widths in the C ring and in the Cassini Division. Though figure clarity prevents us from displaying them, we estimate the relative uncertainty on our width measures to be about $1/N$, N being the number of points in the ghost.

Table 5.3: Derived boulder radii.

	C ring	Cassini Division
W	5.4 – 46.7 m	1.7 – 277 m
$r_{boulder}$	1.5 – 14.5 m	0.36 – 58.1 m
Δ_{ϕ}	152 m – 115 km	3.3 m – 13300 km
a_{max}	0.49 – 4.7 m	0.12 – 18.7 m
H	1.9 – 7.5 m	3.0 – 20 m

Derived boulder radii from the application of the propeller model to the width distribution of observed ghosts in the C ring and the Cassini Division. Inferred azimuthal extensions of the propellers and constraints on the particle size distribution in the vicinity of the ghosts are also presented together with recent estimates of the rings vertical thickness. If N is the number of data points in a ghost, the relative uncertainty is about $1/N$ for widths, boulder radii and maximal particle sizes and around $3/N$ for azimuthal extensions.

5.4.1.2 Removing the Resolution Bias

The UVIS instrument has a constant integration time. However, each occultation has a specific navigation and geometry configuration that changes the spatial resolution in the ring plane. The fact that each occultation has its own resolution introduces a bias in our ghost width measures. In order to estimate the impact of this variability and in order to model the difference between the observable widths and the observed widths, we use a Monte Carlo algorithm designed to model the statistical impact of our occultation resolution variations. This algorithm will evaluate the modeled observed ghost widths from a known particle size distribution. We assume that the particle size distribution in the Cassini Division can be modeled as a power-law. Such a differential distribution will be described by the following equation:

$$n(a)\mathrm{d}a = n_0 a^{-q}\mathrm{d}a \tag{5.10}$$

where a is the particle radius, $n(a)$ the number of particles with a radius equal to a, n_0 is a normalization factor and q is the differential power-law index. Then, we can define a cumulative power-law distribution: $N(\geq a)$, the number of particles with a radius larger than a is provided by the following equations.

$$N(\geq a_0) = \int_{r=a}^{\infty} n(r)\mathrm{d}r = \frac{n_0 a^{1-q}}{q-1} = N_0 a^{-Q}, \tag{5.11}$$

where $Q = q - 1$ defines the cumulative power-law index. More precisely, n_0 is related to the total number or particles N_{tot} defined by:

$$N_{tot} = \int_{r=a_{min}}^{a_{max}} n(r)\mathrm{d}r = \frac{n_0(a_{min}^{1-q} - a_{max}^{1-q})}{q-1} \tag{5.12}$$

where a_{min} and a_{max} are the boundaries of the considered size distribution.

From an arbitrary proportion of the total number of particles, we estimate the corresponding particle radius and model the Hill radius of the boulder and then the width of the ghost that would be created. We assume that this ghost is on a random occultation track, at a random azimuthal distance from the boulder (within the range of the primary open gap) and we estimate what would be measured for its width, given the occultation resolution and based on our interpolated model of the ghost width with respect to the distance from the boulder: this observable width can be zero if the resolution of the occultation is larger than the ghost width. The statistical repetition of this process allows us to determine a cumulative size distribution of the theoretically observed ghost widths. By comparing this distribution with the ones in Figure 5.20, we adjust the initial particle size distribution index in order to match the observable distribution with the observed distribution (by matching both the number of the particles and the shape of the distribution). We estimate that a cumulative power-law index of 0.6 in the C ring and 0.8 in the Cassini Division for the initial particle size distribution will generate ghost-width distributions close to the observed ones (Figure 5.21). This process happens to provide quite close values between the C ring and the Cassini Division. The difference between these indices is of the same order of magnitude as the difference between the distributions of smaller particles by Zebker et al. (1985): $Q_{Cring} = 2.1$ and $Q_{CD} = 1.75$. From these derived indices, we can estimate that the actual boulder population, that generated our observations, follows a cumulative size distribution not in the prolongation of the one for smaller particles.

5.4.2 Qualitative Results

5.4.2.1 Boulder Radius

For an initial 20-cm radius particle population giving an optical depth of 0.1, we run several simulations with different boulder radii from 50 centimeters to 50 meters and measure the extensions of the primary outer trailing depletion zone. Following the tests detailed in Section 5.3.2.3.3, the simulations do not include any other forcing than the boulder gravitational force. We present the primary gaps on the outer trailing side in Figure 5.22. We notice that the propeller structure becomes less and less defined as the boulder radius decreases and gets closer to the particles radii. Gaps are hardly visible in the 1-m radius boulder run (upper left panel) but could not be identified in runs with smaller boulders. The propeller signature is disappearing for good reasons when the boulder is not significantly larger the particles and the threshold in the radii ratio was estimated by Lewis and Stewart (2009) around 3. This is actually respected by our runs with 50-cm and 1-m boulders: the gaps are only visible in the second one.

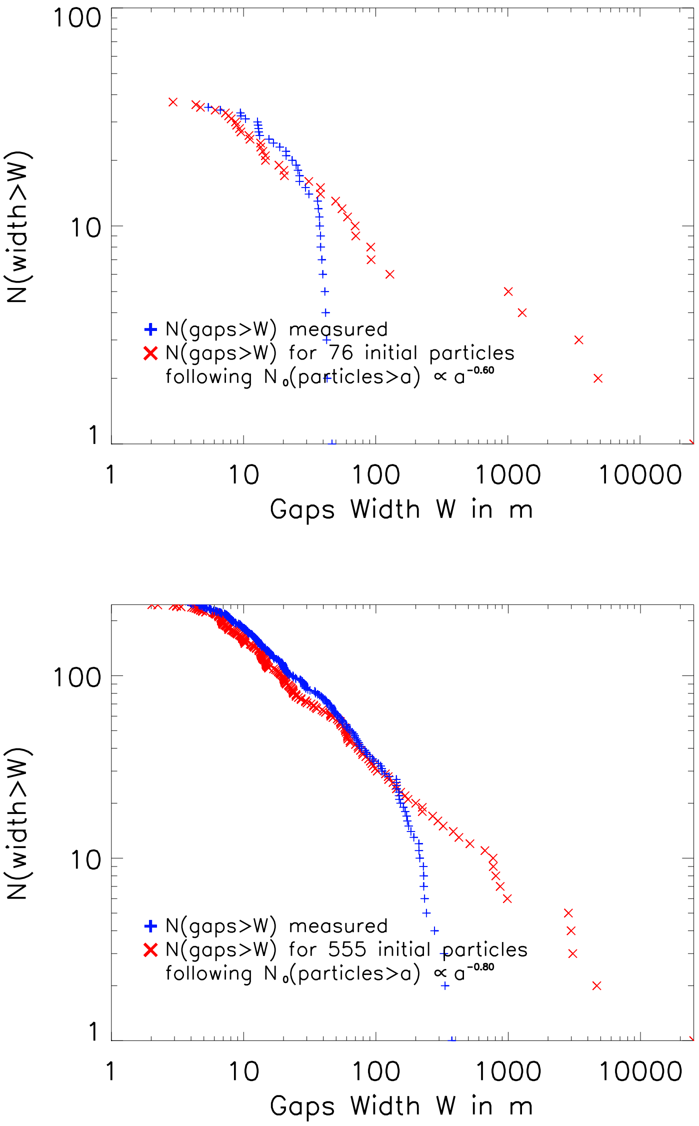

Figure 5.21: Cumulative distribution of the modeled ghosts widths in the C ring (upper panel) and in the Cassini Division (lower panel) for an initial particle size distribution power-law index of 0.6 for the C ring and 0.8 for the Cassini Division. Due to the logarithmic scales, matching the last few scattered points is less important than matching the left part: statistics cannot be applied for such small numbers of the biggest particles.

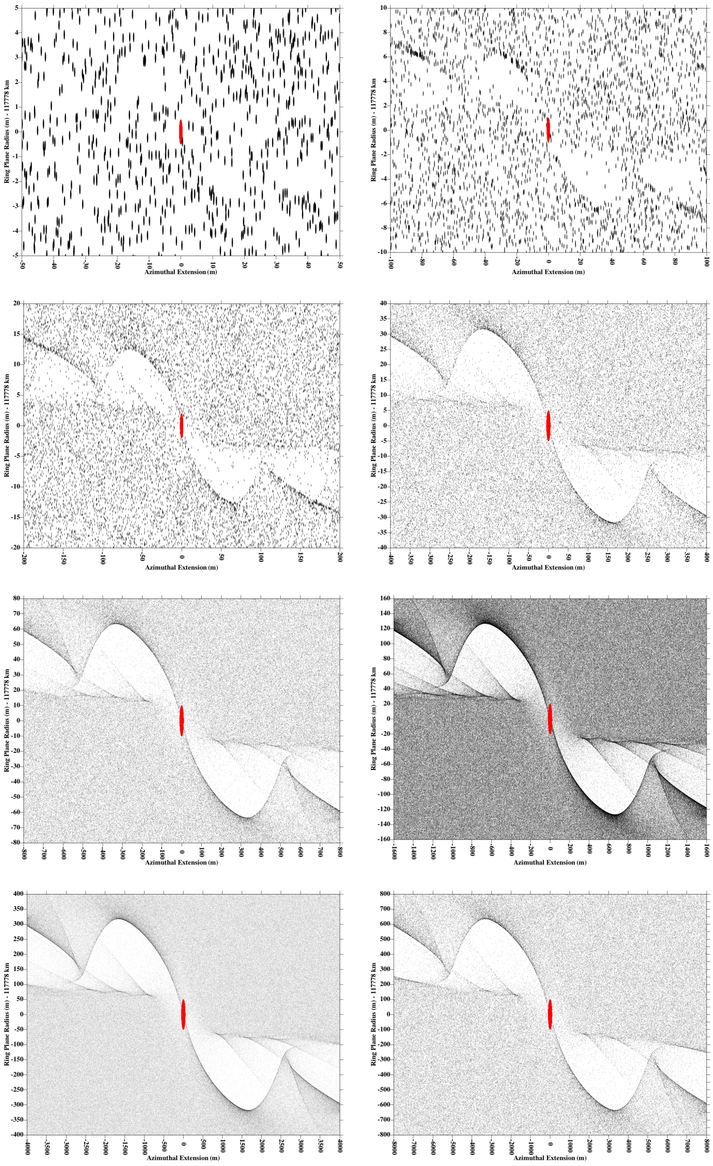

Figure 5.22: Outer trailing propeller signature for a perturbing boulder (represented in red) in an environment of 20-cm particles (50-cm for the 50-m and 100-m boulders) providing an optical depth around 0.1. Saturn's direction is towards the bottom. The boulder is drawn to scale in red. From left to right and top to bottom, boulder radii are 1 m, 2 m, 5 m, 10 m, 20 m, 50 m and 100 m. The extended size of the 100-m boulder simulation required to adapt the number of particles and the density as detailed in Section 5.3.2.3.2: we considered 2-m particles with a density of 13.3 $kg\ m^{-3}$ in that case.

Table 5.4: Radial extension of the outer trailing primary lobe of the propeller signatures.

r_{boulder} (m)	$r_{\text{particles}}$ (cm)	Radial Extension W (m)	Azimuthal Extension $a\Delta\phi$ (m)	Hill Radius r_H (m)	W/r_H	$a\Delta\phi/r_H^3$ (m^{-2})	$a\Delta\phi/r_H$
0,5	20			0,75			
1	20	3 ± 0.2	30 ± 1.5	1,51	$1{,}99 \pm 0.10$	$8{,}79 \pm 0.44$	19.9 ± 1.0
2	20	8 ± 0.4	95 ± 5.0	3,01	$2{,}66 \pm 0.13$	$3{,}48 \pm 0.18$	31.5 ± 1.6
5	20	24 ± 1.2	230 ± 12	7,53	$3{,}19 \pm 0.16$	$0{,}54 \pm 0.03$	30.6 ± 1.6
10	20	50 ± 2.5	520 ± 26	15,06	$3{,}32 \pm 0.17$	$0{,}15 \pm 0.008$	34.5 ± 1.7
20	20	105 ± 5.0	1030 ± 50	30,11	$3{,}49 \pm 0.18$	$0{,}038 \pm 0.002$	34.2 ± 1.7
50	50	250 ± 12	2600 ± 130	75,28	$3{,}32 \pm 0.17$	$0{,}006 \pm 3 \times 10^{-4}$	34.5 ± 1.7
100	50	490 ± 25	5300 ± 270	150,56	$3{,}25 \pm 0.16$	$0{,}0016 \pm 8 \times 10^{-5}$	35.2 ± 1.8

All simulations considered enough particles to have an optical depth of 0.1. The simulated box is centered at 117778 km from Saturn's center. Boulder and particle densities are 850 $kg\ m^{-3}$. For numerical purposes, the last two runs used 50-cm particles instead of 20-cm particles. Radial and azimuthal extensions are provided together with their ratio over the Hill radius of the boulder.

We notice that both radial and azimuthal extensions of the primary lobe seem to grow linearly with the boulder radius. Values in Table 5.4 verify the relation between the radial extension b and the Hill radius r_H that was previously reported by Sremčević et al. (2002); Tiscareno et al. (2008):

$$b \approx 3\ r_H. \tag{5.13}$$

However, Spahn and Sremčević (2000); Sremčević et al. (2002) calculated that the azimuthal extension was supposed to grow as the cube of the Hill radius of the boulder. We find no evidence of such a relation but our simulations suggest the following relation for the azimuthal extension $r\ \Delta\phi$:

$$r\ \Delta\phi = (33.4 \pm 2.0) r_H \tag{5.14}$$

5.4.2.2 Particle Radii

We investigated the possible influence of the particle sizes over the formation and size of the depletion zones. Considering for granted that particles have to be at least three times smaller than the boulder to create a propeller signature (see Section 5.4.2.1), we vary the particles radii for lower values. As Figure 5.23 shows, no real difference is visible between simulations for 10-cm particles and 40-cm particles.

In the case of non-uniform sized particles, the estimation of the optical depth is numerical (Equation 5.15 replaces Equation 5.9) and the number of particles is determined by the code.

$$\tau = \frac{\int\limits_{particles} \pi r^2 \mathrm{d}r}{h\ w}, \tag{5.15}$$

where h and w define the simulation box size as previously.

We investigated the propeller signatures for initial particles following power-law size distributions with the indices estimated by Zebker et al. (1985) from the Voyager radio occultation data at different wavelengths. Figure 5.23 also shows the propeller signatures for $q = 2.75$, which is supposed to be the Cassini Division value. No significant difference can be observed in the propeller pattern than with uniform particle sizes. This is however the most realistic simulation of the Cassini Division that we can make. Yet, the important number of small particles in such a distribution makes it very heavy numerically.

5.5 Discussion

In both the C ring and the Cassini Division, we have been able to identify a population of boulders that would be able to create the ghosts we have observed in UVIS occultation data. These boulders follow less steep power-law distributions than smaller particles, and with similar indices between the C ring and the Cassini Division: $0.6-0.8$. For these derived boulder distributions, we estimate N_0 from the number of observed ghosts. However, in the case of particle distribution, N_0 has to be determined using Equation 5.11, and the integral definition of the optical depth (Equation 5.16).

$$\tau = \int_{a_{\min}}^{a_{\max}} n(r) \pi r^2 \mathrm{d}r, \tag{5.16}$$

where we set $a_{\min} = 10$ cm as a lower bouldary and $a_{\max}$ is provided by Zebker et al. (1985) (5.3 m in the C ring, 7.5 m in the Cassini Division and 11.2 m in the A ring). Then, we have:

$$N_0 = \frac{\tau\ (3-q)}{\pi\ (q-1)\ (a_{\max}^{3-q} - a_{\min}^{3-q})}. \tag{5.17}$$

Figure 5.24 compares particle size distributions and boulder size distributions for the C ring and the Cassini Division. Zebker et al. (1985) values for submeter particles were determined with a good accuracy while suprameter particles and in particular upper limits

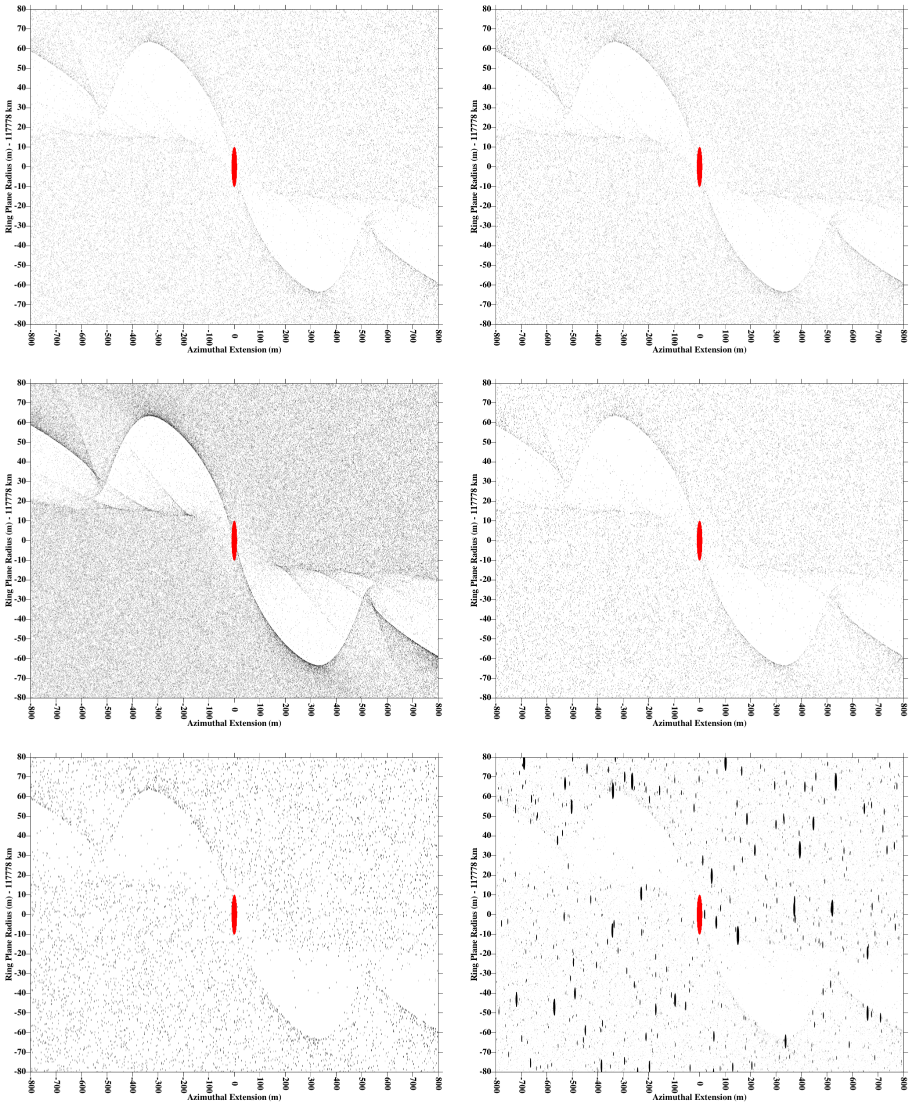

Figure 5.23: Propeller signature for a 10-m radius boulder (represented in red). For left to right and top to bottom, particles radii are 5 cm, 10 cm, 20 cm, 50 cm, 1 m and following a power-law distribution with an index $q = 2.75$ reflecting the estimated Cassini Division particle distribution, between 10 cm and 1 m in the lower right panel. Optical depth is 0.1. Saturn's direction is towards the bottom. Simulations involving 5-cm and 10-cm particles are too heavy and required being adapted as detailed in Section 5.3.2.3.2: we considered 40-cm particles instead with densities of 1.66 $kg\ m^{-3}$ in the first case and 13.3 $kg\ m^{-3}$ in the second one.

of the distributions were probably overestimated. The boulders appear to not follow the previous trend of the particle size distributions. This is consistent with recent conclusions from Baillié et al. (2011) according to which particles tends to be smaller in the C ring plateaus.

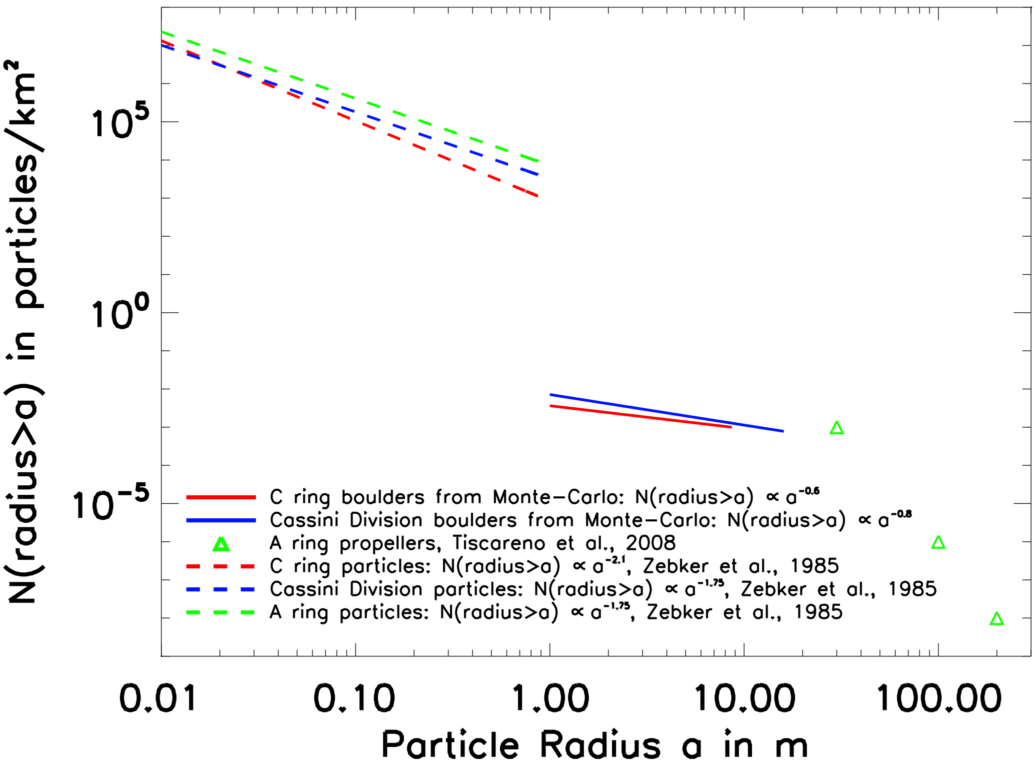

Figure 5.24: Cumulative particle size distribution for the C ring (red), Cassini Division (blue) and the A ring (green). Submeter particle populations from Zebker et al. (1985) are displayed with dashed lines while the source distribution estimated from the Monte-Carlo algorithm for suprameter particles is displayed in solid lines.

Pre-Cassini radio-occultation observations (Zebker et al., 1985) estimated that ring particles were smaller than a couple tens of meters in radius at most. Since Cassini's arrival in Saturn's orbit, the particle size distribution had to be extended to larger sizes: recent observations of the A ring propellers (Tiscareno et al. (2006), Sremčević et al. (2007), Tiscareno et al. (2008), Lewis and Stewart (2009) and Tiscareno et al. (2010b)) lead to a steeper distribution of the largest particles, modeled as a power-law distribution with a cumulative index $Q \sim 5$ (Tiscareno et al., 2010b). This distribution is also steeper than our C ring and Cassini Division results. Recent work (Lewis and Stewart, 2009) introduced the idea of a break in the power-law distribution and suggested that the boulder population could be a bump in the particle size distribution, formed by accretion (Canup and Ward, 2006a) inside the planet Roche radius.

Our results actually present more similarities with the F ring clumps and moonlets observations (Esposito et al. (2008) and Meinke et al. (2011)): UVIS occultations showed a flatter particle-size-distribution extension to larger sizes than estimated from radio-occultations. However, though the presence of the F ring moonlets could be interpreted as an evidence for the evolutionary models involving accretion and disruption mechanisms (Barbara and Esposito, 2002), neither the F ring clumps distribution nor our C ring and Cassini Division results look similar to the bimodal distribution that is supposed to characterize this model. The results from Esposito et al. (2008) also differ from the expectations of Barbara and Esposito (2002): the number of kitten features is orders of magnitude greater than predicted. These F ring structures, interpreted as temporary aggregation clumps of multiple smaller particles, should still create gravitational disturbances clearing gaps around them. It is worth noting that objects inferred in the C ring are smaller than the ones in the Cassini Division, which is consistent with stronger tidal forces closer to Saturn, therefore making accretion more difficult closer to the planet.

Our boulders constitute evidence of a distinct population of bigger particles (reaching 5 m in the C ring and up to 20 m in the Cassini Division) that cannot be obtained by extrapolation of the previous particle size distribution models. This raises the question of a possible different origin between the particles and the boulders. The largest particles flatter distribution origin could involve fragmentation or accretion. We further detail the two possible scenarios and their limitations for the present study observations.

A unique progenitor, big enough to generate the boulder population, would have to be at least 800-m wide for the C ring and at least 2.8-km wide for the Cassini Division. Such small boulders should be able to survive tidal disruption well inside the Roche limit (Goldreich and Tremaine, 1982). However, catastrophic disruptions involving cometary collisions would generate a secondary particle population. In such a scenario, the minor accretion effects would not have allowed the formation of the progenitors in situ. These boulders would have more likely formed outside the main rings and then spiraled inwards by gas drag (Mosqueira and Estrada, 2003b). They could also be the results of another bigger fragmentation. In addition, we would expect the resulting particle size distribution from a fragmentation process to be steeper than our derived estimations, closer to a power-law distribution with a cumulative index around 3.4 (which is the index obtained for the ejecta of a hammer-destruction of a glacial boulder (Hartmann (1969), Dohnanyi (1969) and Dohnanyi (1972))). However, a disruption event involving a comet would result in many fragments being created, following a very shallow size distribution with a cumulative index around 1 (Fuse et al. (2007), Reach et al. (2009) and Fernández (2009)). However, the origin of these events remains mainly unknown, only a very small fraction being caused by tidal disruption. The rest may be due to thermal stresses in the nucleus, or possibly gas pressure build-up in the interior, leading to possible new formation scenarios for the ghosts.

Considering aggregation as the principal effect, it is possible to form temporary aggregates inside the Roche limit (Karjalainen and Salo, 2004), which would disturb the encountering particles and clear depletion zones. However, the accretion effects are not predominant in tenuous rings like the C ring or the Cassini Division. In addition, we do not observe any trend in the distribution of our boulder sizes with respect to their distance to Saturn that would strengthen the confidence in this scenario.

Finally, we ruled out another scenario, based on recent studies of density waves in the C ring. The C ring plateaus present higher mass extinction coefficients than other locations in the C ring (Baillié et al., 2011), leading to a lower limit for the smallest particles in the plateaus. Our present results suggest the existence of a secondary population of particles in these same plateaus. Applying a pairwise-coagulation process on the largest particles of the initial particle population (derived from radio-occultations) could lead to a deficit in the largest part of the primary population and create a secondary population of larger particles. However, coagulation effects should affect all the particles similarly, not regarding their size, and therefore, such a scenario would require a segregation process of the initial particles so that coagulation would affect only the largest particles.

Propellers observed in the A ring are much larger than the ones we report here. However, the only detection effort in the A ring was made on Cassini images, whose resolution does not reach the one from the UVIS instrument. Analyzing occultation ghosts in the A ring might be difficult due to the numerous structures. Collected information so far do not concern the same size of objects in the C ring or Cassini Division and in the A ring: we cannot infer any smaller boulder distribution in the A ring. However, we consider that imaging observations and the optical depth of the faint rings bring evidence that bigger objects than the one described here are very unlikely to exist in the C ring and in the Cassini Division.

Tiscareno et al. (2010b) described propellers in the A ring, such as the Blériot Propeller Object for example (Figure 5.25). We can estimate the radius of the Blériot Propeller Object around 83 m ($a_{max} \sim 26$ m), which corresponds to a lower estimate from images from Tiscareno et al. (2010b). We can explain the variations with their other measures by the fact that it is highly unprobable that we scanned the propeller at the azimuth where it was the largest. These objects appear, in Figure 5.24, below the trend of the particle size distribution which seems in contradiction with the accretion model from Barbara and Esposito (2002) in the F ring. Either conclusions of the F ring cannot be used in the main rings, or we could imagine a less simple particle size distribution inflecting above a certain particle size.

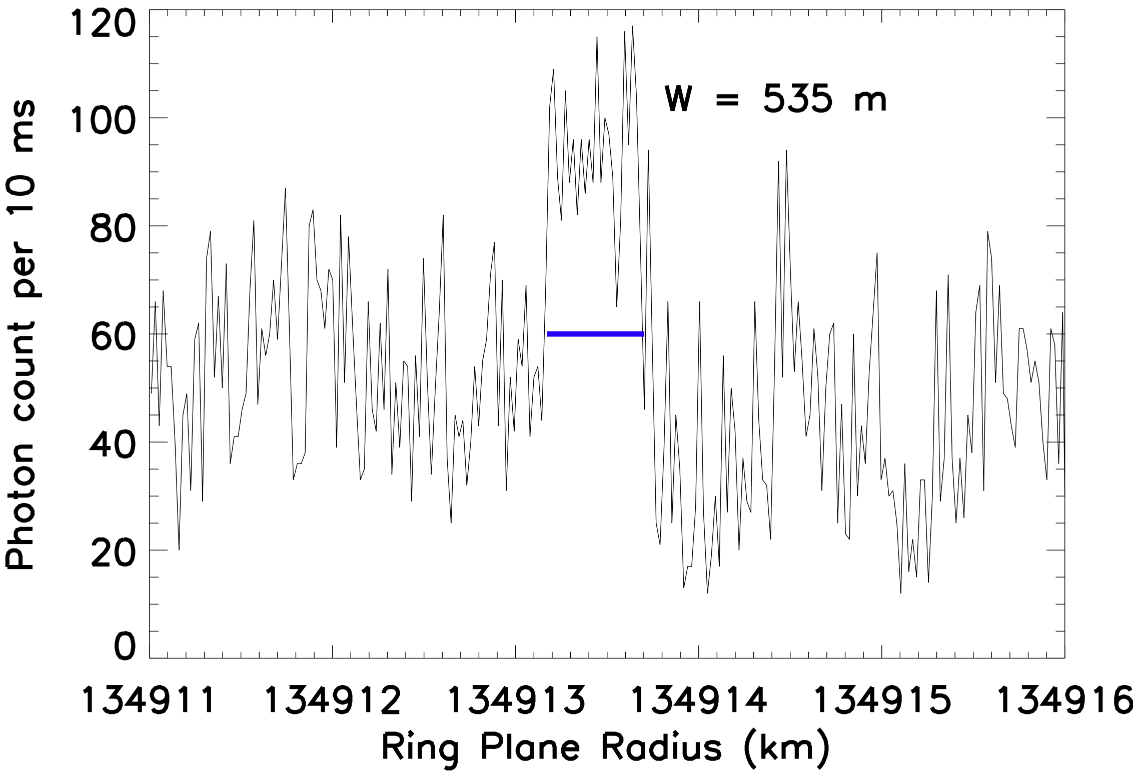

Figure 5.25: Photon count rates from the ζ Orionis, rev. 42 occultation showing the Blériot Propeller Object. We measure a width of 535 m.

In this study, we focused on narrow holes, corresponding to 8 data points at most. We notice that larger ghosts present important similarities with the observed signature of the Blériot propeller Object. Analyzing these wider structures might provide complementary information for boulders with larger radii, and in this case, the varying-resolution issue would be obsolete as the gap zone would definitely be larger than the occultation resolution. Identically, other regions could be scanned such as the B ring or the A ring for larger ghosts but extra care should be used to avoid similar signatures due to wavy structures such as density waves, bending waves, satellite wakes or self-gravity wakes. In addition, though previous works in the A ring experienced difficulties estimating the dependency of the observed radial and azimuthal extensions with respect to the Hill radii of the boulders (due to the uncertainty of the association of the observed bright features with either wakes of propeller-shaped gaps), our observations did not suffer the same worries as we are observing the gaps rather than the brightness of the structures.

5.6 Conclusions and Perspectives

5.6.1 Conclusions

Taking advantage of the highest resolution available to study Saturn's rings, we were able to increase our knowledge of the objects size distribution in the faint ring regions such as the C ring and the Cassini Division. A different population of boulders seem to emerge, not connected to the previously known particle size distribution. These boulder are following power-law size distribution with cumulative indices between 0.6 and 0.8. Objects up to 15 m were found in the C ring and up to 60 meters in the Cassini Division.

5.6.2 Perspectives

Such objects are already four to five times larger than the thickness of the rings. Therefore, inclination effects are probably not negligible, probably generating three dimensional structures in the rings. The question of the formation of these boulders inside the Roche limit is tricky: can accretion allow the growth of long-lived structures or are these boulders ephemeral? In addition, propellers have been observed in regions where collisional effect are more or less important. What is the actual influence of the collisions on the lifetime of a boulder? Is it possible, as it is question for Pan and Daphnis, that these boulders were formed further (possibly outside the Roche zone) by fragmentation of a more important body and migrated inward in the rings? We can hope that Cassini extended mission will bring some answers to these questions.

CHAPTER 6

CONCLUSIONS

6.1 Conclusions and Discussion

The Cassini mission is already one of the greatest achievements for NASA in the spatial exploration of our solar system. Following the first discoveries of the Pioneer and Voyager space probes, Cassini allowed great progress in our understanding of the Saturnian system, either concerning the rings, or about the satellites and their interactions. Thanks to the variety of instruments onboard, we were able to detect and analyze finer and finer structures. The UVIS instrument, with a spatial resolution of a few meters depending on stellar occultations, enabled the detection of structures around this order of magnitude in size and the derivation of physical parameters for the rings.

In our study, we have detailed the new structures that we observed in some of the most tenuous main rings: the C ring and the Cassini Division. A fine detection of periodic radial structures in the C ring allowed to identify more than 30 wavelike features, four of which being spiral density waves associated with Inner Lindblad Resonances with the external satellite Mimas (twice), Atlas and Pandora, and one of those being a spiral bending wave excited by the Titan -1:0 nodal resonance. Though the great majority remains unexplained, the associated structures enabled the derivation of physical parameters for the rings. From the spiral density wave model in the spiral galaxies, adapted to the density waves in Saturn's rings, we were able to estimate the C ring surface mass density between 0.22 (±0.03) and 1.42 (±0.21) g cm^{-2}, and the mass extinction coefficients from 0.13 (±0.03) to 0.28 (±0.06) cm^{2} g^{-1}. This allowed the estimation of the vertical thickness of the C ring (between 2 and 6 m) and its mass, equivalent to an 30-km radius icy porous satellite (slightly bigger than Pan and Atlas with a similar composition). From that, we could infer that the upper limit in the particle size distribution is smaller in the C ring than in the A ring or in the Cassini Division, while it is also smaller in the C ring plateaus than in the other regions. These plateaus themselves are of unknown origin, and the differences in size distributions could provide hints to their origin or evolution. If they do not have the same age and origin, the C ring and Cassini Division may have a common mode of origin that has lead to their gross overall similarities.

The rings total masses that we have derived are summarized in Figure 6.1. However, it is worth noting that the B ring mass is still highly uncertain.

Inner satellites like Pan and Daphnis can also shape the rings. Though some recurrent structures were observed in the Huygens Ringlet of the Cassini Division, the constraints on the potential moons, that could actually create such structures, require that such moons are located in places where observations make it quite confident that no moon can be embedded.

Recent observations of the A ring showed the existence of a whole population of moonlets at the origin of the observed propellers. The fragmentation scenario of the formation of

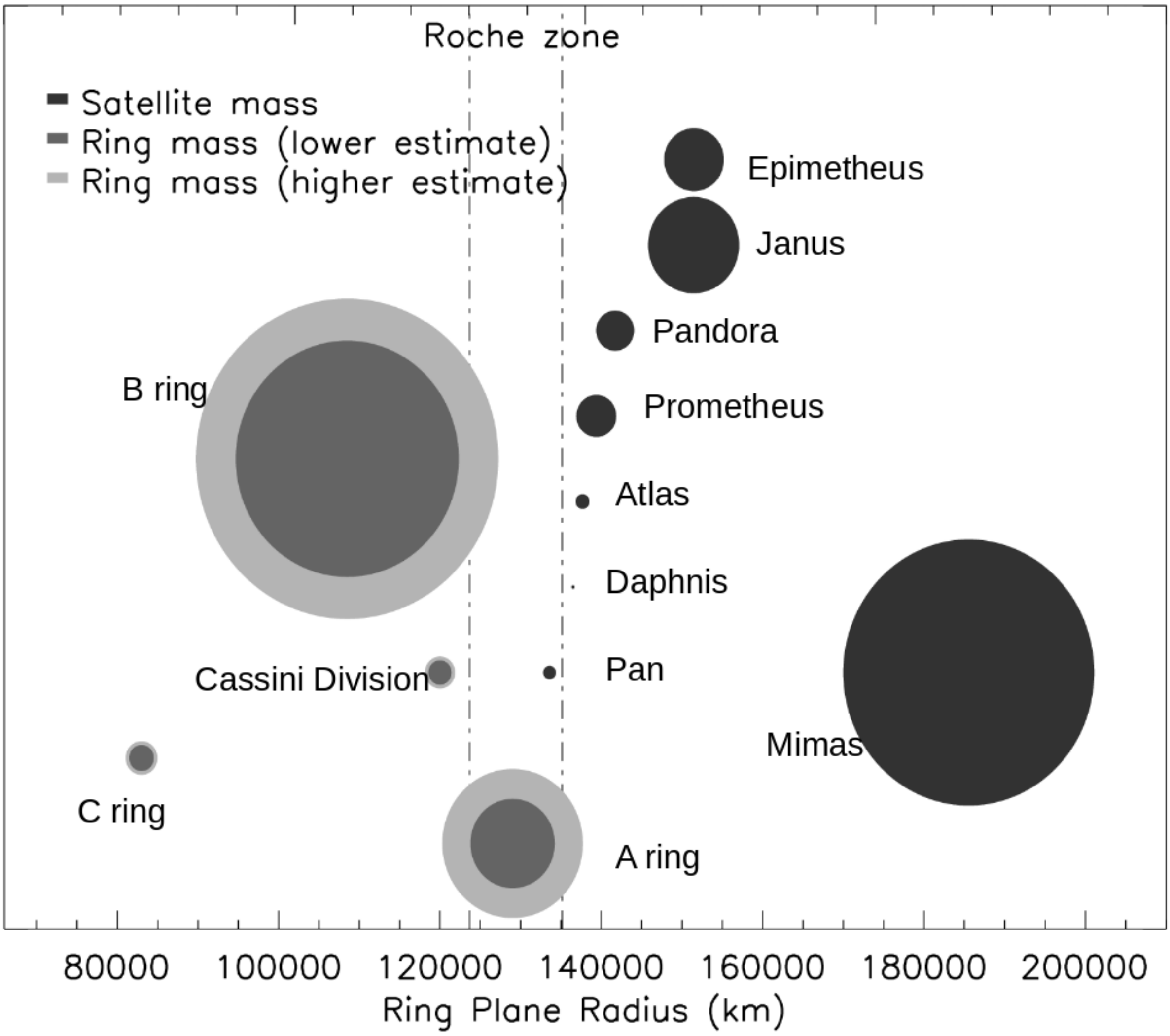

Figure 6.1: Relative masses of Saturn's inner satellites and rings as a function of their distance to the planet center. The masses are represented by circles of radius proportional to the cubic root of the mass.

small embedded satellites and moonlets would suggest a possible common origin between intermediate-size satellites and big boulders orbiting within the rings. We believe that the narrow holes, called "ghosts", observed by UVIS in the C ring and the Cassini Division can be related to propeller signatures. Measuring these ghost widths helped constraining the radii of the moonlets creating them ($1.5 - 14.5$ m in the C ring and $0.36 - 58.1$ m in the Cassini Division). Numerical models estimate that there is an actual population of boulders following a much shallower power-law in size distribution than the smaller particles. Whether these two distributions are forming a bimodal distribution or are connected remains unknown.

6.2 Perspectives

6.2.1 Saturn's Rings

The origin of these boulders is also uncertain. Whether they formed by accretion in the main rings is quite possible but complicated by the fact that the main rings are entirely inside the Roche limit of the planet. And the fragmentation scenario in which a 100ish-km satellite is fragmented in smaller parts (including possibly Pan and Daphnis) that start migrating inward in the rings does not seem to respect the expected power-law size distribution for collisional fragmentation (hitting a glacial boulder with a hammer would generates a particle size distribution with an index of 3.4 while we determined an index of 1.8 in the Cassini Division and 1.6 in the C ring). Complementary hints such as the surprisingly high porosity of Pan and Daphnis or the ages of the equatorial ridges of these moons might help finding the true origin of this boulder population. Finally, it could be possible that the two populations evolved differently after a common origin.

The origins and age of the rings are still unanswered questions. Though some formation scenarios invoke the necessity of a higher cometary flux than presently, a possible solution has been proposed based on the Late Heavy Bombardment and the possibility that it has been triggered during the chaotic event modeled in the "Nice model". On the contrary, invoking the "sub-nebula" formation scenario of the rings asks the question of the conservation of Saturn's sub-nebula in the eventuality of a brutal migration such as presented in that model. In addition these scenarios do not provide precise and complete explanation on the disappearance of silicates in the ring particles, on the apparent diversity of the rings, or on the uniqueness of Saturn's rings system.

At the end of the Cassini mission in 2017, the spacecraft will crash on the planet after crossing the ring plane between the D ring and the planet. That might be a good opportunity to have a closer look at particles, though we suspect mainly dust to constitute the D ring. Further investigations could provide useful information about the formation scenarios of the biggest particles if accretion bulges could be observed at equatorial regions of the boulders initiating the ghosts (therefore validating a possible accretion scenario).

6.2.2 Other Disks

Though the giant planets faint rings may present similarities in their formation process, it is more unlikely that dense rings and tenuous rings can share a common origin: the predominant effects on dust are not the ones that govern bigger particles.

Considering the formation scenario of dense rings by tidal disruption or catastrophic collision of a satellite, we could assimilate the main rings to a debris disk containing satellite fragments instead of material from a disrupted binary for example, though the compositions are quite different. As far as other disks are concerned, β Pictoris is the most famous example of a circumstellar disk: its primary and secondary disks, its exoplanet, the asymmetry of the disk contribute to make it a very original system. The exoplanet hunt might provide chances to observe more of these distant disks. The recent models of accretion, migration and fragmentation might present a lot of similarities between proto-planetary disks and ring systems.

Finally, since four planets are hosting rings in our solar system, we can imagine that a good proportion of the detected exoplanets so far could have a ring system. These exorings would be very interesting to provide information about the planet age, about its Roche radius (and therefore the planet mass and density), or about the possibility that a chaotic event like the "Nice model" happened. They can also increase the detection possibilities by increasing the observed cross-section. Ringed super-Earths can also be considered, though the formation inside the frost line will change the composition of the rings: they will contain more silicates and therefore be denser, decreasing the Roche radius. Exorings can tell a distant system history as Saturn's rings are telling us about our own solar system history.

APPENDIX

THE NUMERICAL CODE

The numerical code (described in Lewis and Stewart (2009)) that we used to model the propellers formation relies on an N-body numerical simulation. Particles are assumed to be spherical, smooth and inelastic. Ring particles are studied in a rotating pseudo-Cartesian coordinate system. Considering the gravitational potential of the moonlet V_M and the gravitational potential of the other particles self-gravity, V_{SG}, particle motions are governed by the following equations:

$$\begin{aligned}
\frac{\mathrm{d}^2x}{\mathrm{d}t^2} - 2\Omega\frac{\mathrm{d}y}{\mathrm{d}t} - 3\Omega^2 x &= -\frac{\partial V_M}{\partial x} - \frac{\partial V_{SG}}{\partial x} \\
\frac{\mathrm{d}^2y}{\mathrm{d}t^2} + 2\Omega\frac{\mathrm{d}x}{\mathrm{d}t} &= -\frac{\partial V_M}{\partial y} - \frac{\partial V_{SG}}{\partial y} \\
\frac{\mathrm{d}^2x}{\mathrm{d}t^2} + \Omega^2 z &= -\frac{\partial V_M}{\partial z} - \frac{\partial V_{SG}}{\partial z},
\end{aligned} \tag{1}$$

where (x, y, z) are the cylindrical coordinates derivated from r_0, the distance to Saturn's center, and Ω, the angular velocity at that distance r_0.

$$\begin{aligned}
x &= r - r_0 \\
y &= r_0(\theta - \Omega t) \\
z &= z
\end{aligned} \tag{2}$$

Each time step is divided into two parts. First, Equations 1 are solved without the right hand sides and particles are moved following that non-perturbed analytical solution given by:

$$\begin{aligned}
\frac{x}{r_0} &= X - e\cos\phi \\
\frac{y}{r_0} &= Y + \beta e \sin\phi
\end{aligned}$$

$$\frac{z}{r_0} = i\cos\zeta, \tag{3}$$

where the unperturbed motion constants X (the scaled semi-major axis), e, i and the linear functions of time $Y(t)$ (the mean anomaly in the rotating reference frame), $\phi(t)$ and $\zeta(t)$ defined in Equations 3 and 4 are the "guiding center variables".

$$\begin{aligned} Y(t) &= Y_0 - \frac{3}{2}X\Omega t \\ \phi(t) &= \phi_0 + \Omega t \\ \zeta(t) &= \zeta_0 + \Omega t \end{aligned} \tag{4}$$

Saturn's oblateness is not taken into account in the conversion from Cartesian coordinates to guiding center coordinates as this effect is very minor on local perturbations.

In a second time, the code calculates the gravitational interactions of each particle with the moonlet and the other particles. Self-gravity is implemented using the tree method detailed in Barnes and Hut (1986) in which the octree is replaced by a k-D tree from Bentley (1975). Our simulated box is divided in 2-dimensions cells, themselves subdivided in cells recursively until cells contain just a few particles. For each particle, the code evaluates the opening angle β at which it sees the other cells. For cells seen with $\beta < 0.3$, a gravitation monopole is evaluated for the whole cell and its force applied. For cells seen wider than this threshold, the same process is iterated one level lower in the tree. If the lowest level is reached, the gravitation of each particle is applied manually. This whole process allows to decrease the number of operations by a ratio of N^2 to $N\ ln(N)$, where N is the number of particles involved. Trajectories are then modified before collisions are treated.

The code uses a similar k-D tree method to find particles that are close enough to collide. Then these particle trajectories are checked for actual collisions. Actual colliding particles will be moved to the collision point, and have their velocities updated using a restitution coefficient ϵ defined as $\epsilon(v^{\perp}) = min(0.34\ v_{\perp}^{-0.234}, 1)$ (Bridges et al., 1984), where $v_{\perp}$ is the velocity perpendicular to the contact plane in cm/s. The other particles supposed to be on the track of the colliding particles are then removed from the list of collisions which is updated for the rest of the timestep after new trajectories recalculations.

REFERENCES

A. F. O. Alexander. *The planet Saturn: a history of observation, theory, and discovery.* 1962.

K. Baillié, J. E. Colwell, L. W. Esposito, M. Sremčević, and J. J. Lissauer. Waves in Cassini UVIS stellar occultations. 2. The C ring. *Icarus in press*, 2011.

J. M. Barbara and L. W. Esposito. Moonlet Collisions and the Effects of Tidally Modified Accretion in Saturn's F Ring. *Icarus*, 160:161–171, November 2002. doi: 10.1006/icar.2002.6962.

J. Barnes and P. Hut. A hierarchical O(N log N) force-calculation algorithm. *Nature*, 324: 446–449, December 1986. doi: 10.1038/324446a0.

Jon Louis Bentley. Multidimensional binary search trees used for associative searching. *Commun. ACM*, 18(9):509–517, 1975.

E. T. Bradley, J. E. Colwell, L. W. Esposito, J. N. Cuzzi, H. Tollerud, and L. Chambers. Far ultraviolet spectral properties of Saturn's rings from Cassini UVIS. *Icarus*, 206:458–466, April 2010. doi: 10.1016/j.icarus.2009.12.021.

A. Brahic. The formation of disks by inelastic collisions of gravitating particles - Applications to the dynamics of the Saturn's ring and to the formation of the solar system. In

A. A. Wyller, editor, *Stability of the Solar System and of Small Stellar Systems*, volume 62 of *IAU Symposium*, pages 83–93, 1974.

A. Brahic. A numerical study of a gravitating system of colliding particles - Applications to the dynamics of Saturn's rings and to the formation of the solar system. *Icarus*, 25: 452–457, July 1975. doi: 10.1016/0019-1035(75)90010-X.

A. Brahic. Systems of colliding bodies in a gravitational field. I - Numerical simulation of the standard model. *Astronomy and Astrophysics*, 54:895–907, February 1977.

F. G. Bridges, A. Hatzes, and D. N. C. Lin. Structure, stability and evolution of Saturn's rings. *Nature*, 309:333–335, May 1984. doi: 10.1038/309333a0.

D. Brouwer and G. M. Clemence. *Methods of celestial mechanics.* New York: Academic Press, 1961, 1961.

R. M. Canup. Origin of Saturn's rings and inner moons by mass removal from a lost Titan-sized satellite. *Nature*, 468:943–926, December 2010. doi: 10.1038/nature09661.

R. M. Canup and W. R. Ward. Accretion of large satellites of gas planets. In *European Planetary Science Congress 2006*, pages 465–+, 2006a.

R. M. Canup and W. R. Ward. A common mass scaling for satellite systems of gaseous planets. *Nature*, 441:834–839, June 2006b. doi: 10.1038/nature04860.

L. S. Chambers, J. N. Cuzzi, E. Asphaug, J. Colwell, and S. Sugita. Hydrodynamical and radiative transfer modeling of meteoroid impacts into Saturn's rings. *Icarus*, 194:623–635, April 2008. doi: 10.1016/j.icarus.2007.11.017.

S. Charnoz, C. C. Porco, E. Déau, A. Brahic, J. N. Spitale, G. Bacques, and K. Baillié. Cassini Discovers a Kinematic Spiral Ring Around Saturn. *Science*, 310:1300–1304, November 2005. doi: 10.1126/science.1119387.

S. Charnoz, A. Brahic, P. C. Thomas, and C. C. Porco. The Equatorial Ridges of Pan and Atlas: Terminal Accretionary Ornaments? *Science*, 318:1622–, December 2007. doi: 10.1126/science.1148631.

S. Charnoz, A. Morbidelli, L. Dones, and J. Salmon. Did Saturn's rings form during the Late Heavy Bombardment? *Icarus*, 199:413–428, February 2009. doi: 10.1016/j.icarus.2008.10.019.

S. Charnoz, J. Salmon, and A. Crida. The recent formation of Saturn's moonlets from viscous spreading of the main rings. *Nature*, 465:752–754, June 2010. doi: 10.1038/nature09096.

R. N. Clark, J. M. Curchin, R. Jaumann, D. P. Cruikshank, R. H. Brown, T. M. Hoefen, K. Stephan, J. M. Moore, B. J. Buratti, K. H. Baines, P. D. Nicholson, and R. M. Nelson. Compositional mapping of Saturn's satellite Dione with Cassini VIMS and implications of dark material in the Saturn system. *Icarus*, 193:372–386, February 2008. doi: 10.1016/j.icarus.2007.08.035.

R. N. Clark, J. M. Curchin, T. M. Hoefen, and G. A. Swayze. Reflectance spectroscopy of organic compounds: 1. Alkanes. *Journal of Geophysical Research (Planets)*, 114(13): E03001, March 2009. doi: 10.1029/2008JE003150.

J. E. Colwell, L. J. Horn, A. L. Lane, L. W. Esposito, P. A. Yanamandra-Fisher, S. H. Pilorz, K. E. Simmons, M. D. Morrison, C. W. Hord, R. M. Nelson, B. D. Wallis, R. A. West, and B. J. Buratti. Voyager photopolarimeter observations of Uranian ring occultations. *Icarus*, 83:102–125, January 1990. doi: 10.1016/0019-1035(90)90009-X.

J. E. Colwell, L. W. Esposito, and M. Sremčević. Self-gravity wakes in Saturn's A ring measured by stellar occultations from Cassini. *Geophysics Research Letters*, 33:L07201, April 2006. doi: 10.1029/2005GL025163.

J. E. Colwell, L. W. Esposito, M. Sremčević, G. R. Stewart, and W. E. McClintock. Self-gravity wakes and radial structure of Saturn's B ring. *Icarus*, 190:127–144, September 2007. doi: 10.1016/j.icarus.2007.03.018.

J. E. Colwell, J. H. Cooney, L. W. Esposito, and M. Sremčević. Density waves in Cassini UVIS stellar occultations. 1. The Cassini Division. *Icarus*, 200:574–580, April 2009a. doi: 10.1016/j.icarus.2008.12.031.

J. E. Colwell, P. D. Nicholson, M. S. Tiscareno, C. D. Murray, R. G. French, and E. A. Marouf. *The Structure of Saturn's Rings*, pages 375–412. In Dougherty et al. (2009), 2009b. doi: 10.1007/978-1-4020-9217-6_13.

J. E. Colwell, K. Baillié, and L. W. Esposito. Seeing Ghosts in Saturn's Rings: Ephemeral Gaps in Cassini UVIS Stellar Occultations. *38th COSPAR Scientific Assembly, Bremen Germany, Paper B03-0031-10*, July 2010a.

J. E. Colwell, L. W. Esposito, R. G. Jerousek, M. Sremčević, D. Pettis, and E. T. Bradley. Cassini UVIS Stellar Occultation Observations of Saturn's Rings. *Astronomical Journal*, 140:1569–1578, December 2010b. doi: 10.1088/0004-6256/140/6/1569.

J. Cuzzi, R. Clark, G. Filacchione, R. French, R. Johnson, E. Marouf, and L. Spilker. *Ring Particle Composition and Size Distribution*, pages 459–509. In Dougherty et al. (2009), 2009. doi: 10.1007/978-1-4020-9217-6_15.

J. N. Cuzzi and J. D. Scargle. Wavy edges suggest moonlet in Encke's gap. *Astrophysical Journal*, 292:276–290, May 1985. doi: 10.1086/163158.

J. N. Cuzzi, J. J. Lissauer, L. W. Esposito, J. B. Holberg, E. A. Marouf, G. L. Tyler, and A. Boishchot. *Saturn's rings - Properties and processes*, pages 73–199. In Greenberg and Brahic (1984), 1984.

J. N. Cuzzi, R. G. French, and L. Dones. HST Multicolor (255-1042 nm) Photometry of Saturn's Main RingsI: Radial Profiles, Phase and Opening Angle Variations, and Regional Spectra. *Icarus*, 158:199–223, July 2002. doi: 10.1006/icar.2002.6851.

J. S. Dohnanyi. Collisional Model of Asteroids and Their Debris. *Journal of Geophysics Research*, 74:2531–+, May 1969. doi: 10.1029/JB074i010p02531.

J. S. Dohnanyi. Interplanetary objects in review: Statistics of their masses and dynamics. *Icarus*, 17:1–48, August 1972. doi: 10.1016/0019-1035(72)90044-9.

L. Dones. A recent cometary origin for Saturn's rings? *Icarus*, 92:194–203, August 1991. doi: 10.1016/0019-1035(91)90045-U.

L. Dones, P. D. Nicholson, C. A. McGhee, J. J. Lissauer, M. R. Showalter, R. G. French, S. M. Larson, P. Seitzer, B. Sicardy, and G. E. Danielson. HST WFPC2 Observations of Small Saturnian Satellites During the 1995 Ring-Plane Crossings. In *AAS/Division of Dynamical Astronomy Meeting #27*, volume 28 of *Bulletin of the American Astronomical Society*, pages 1184–+, June 1996.

M. K. Dougherty, L. W. Esposito, and S. M. Krimigis, editors. *Saturn from Cassini-Huygens*. 2009.

R. H. Durisen, N. L. Cramer, B. W. Murphy, J. N. Cuzzi, T. L. Mullikin, and S. E. Cederbloom. Ballistic transport in planetary ring systems due to particle erosion mechanisms. I - Theory, numerical methods, and illustrative examples. *Icarus*, 80:136–166, July 1989. doi: 10.1016/0019-1035(89)90164-4.

R. H. Durisen, P. W. Bode, J. N. Cuzzi, S. E. Cederbloom, and B. W. Murphy. Ballistic transport in planetary ring systems due to particle erosion mechanisms. II - Theoretical models for Saturn's A- and B-ring inner edges. *Icarus*, 100:364–393, December 1992. doi: 10.1016/0019-1035(92)90106-H.

J. L. Elliot, E. Dunham, and D. Mink. The rings of Uranus. *Nature*, 267:328–330, May 1977. doi: 10.1038/267328a0.

L. W. Esposito. *Planetary rings*, volume 65. December 2002. doi: 10.1088/0034-4885/65/12/201.

L. W. Esposito and J. E. Colwell. Creation of the Uranus rings and dust bands. *Nature*, 339:605–607, June 1989. doi: 10.1038/339605a0.

L. W. Esposito, M. Ocallaghan, and R. A. West. The structure of Saturn's rings - Implications from the Voyager stellar occultation. *Icarus*, 56:439–452, December 1983. doi: 10.1016/0019-1035(83)90165-3.

L. W. Esposito, C. C. Harris, and K. E. Simmons. Features in Saturn's rings. *Astrophysical Journal Supplement Series*, 63:749–770, March 1987. doi: 10.1086/191181.

L. W. Esposito, J. E. Colwell, and W. E. McClintock. Cassini UVIS observations of Saturns rings. *Planetary Space Science*, 46:1221–1235, October 1998.

L. W. Esposito, C. A. Barth, J. E. Colwell, G. M. Lawrence, W. E. McClintock, A. I. F. Stewart, H. U. Keller, A. Korth, H. Lauche, M. C. Festou, A. L. Lane, C. J. Hansen, J. N. Maki, R. A. West, H. Jahn, R. Reulke, K. Warlich, D. E. Shemansky, and Y. L. Yung. The Cassini Ultraviolet Imaging Spectrograph Investigation. *Space Science Reviews*, 115: 299–361, December 2004. doi: 10.1007/s11214-004-1455-8.

L. W. Esposito, B. K. Meinke, J. E. Colwell, P. D. Nicholson, and M. M. Hedman. Moonlets and clumps in Saturn's F ring. *Icarus*, 194:278–289, March 2008. doi: 10.1016/j.icarus.2007.10.001.

Y. R. Fernández. That's the way the comet crumbles: Splitting Jupiter-family comets. *Planetary and Space Science*, 57:1218–1227, August 2009. doi: 10.1016/j.pss.2009.01.003.

G. Foster. Wavelets for period analysis of unevenly sampled time series. *Astronomical Journal*, 112:1709, October 1996. doi: 10.1086/118137.

R. G. French and P. D. Nicholson. Saturn's Rings II. Particle sizes inferred from stellar occultation data. *Icarus*, 145:502–523, June 2000. doi: 10.1006/icar.2000.6357.

R. G. French, P. D. Nicholson, M. L. Cooke, J. L. Elliot, K. Matthews, O. Perkovic, E. Tollestrup, P. Harvey, N. J. Chanover, M. A. Clark, E. W. Dunham, W. Forrest, J. Harrington, J. Pipher, A. Brahic, I. Grenier, F. Roques, and M. Arndt. Geometry of the Saturn system from the 3 July 1989 occultation of 28 SGR and Voyager observations. *Icarus*, 103:163–214, June 1993. doi: 10.1006/icar.1993.1066.

R. G. French, J. Cuzzi, L. Dones, and J. Lissauer. High-resolution imaging of Saturn's G Ring from the Hubble Space Telescope. In M. F. Bietenholz, N. Bartel, M. P. Rupen, A. J. Beasley, D. A. Graham, V. I. Altunin, T. Venturi, G. Umana, & J. E. Conway, editor, *Bulletin of the American Astronomical Society*, volume 29 of *Bulletin of the American Astronomical Society*, pages 1097–+, September 1997.

R. G. French, D. Graham, J. Cuzzi, L. Dones, and J. J. Lissauer. Hubble Space Telescope Observations of Saturn's Rings: The Opposition Effect. In *Bulletin of the American Astronomical Society*, volume 30 of *Bulletin of the American Astronomical Society*, pages 1045–+, September 1998.

R. G. French, L. Dones, and H. Salo. HST Observations of the Azimuthal Brightness Asymmetry in Saturn's Rings. In *AAS/Division of Dynamical Astronomy Meeting*, volume 32 of *Bulletin of the American Astronomical Society*, pages 864–+, May 2000.

T. Fuse, N. Yamamoto, D. Kinoshita, H. Furusawa, and J.-I. Watanabe. Observations of Fragments Split from Nucleus B of Comet 73P/Schwassmann-Wachmann 3 with Subaru Telescope. *Publications of the Astronomical Society of Japan*, 59:381–386, April 2007.

P. Goldreich and S. Tremaine. The excitation and evolution of density waves. *Astrophysical Journal*, 222:850–858, June 1978a. doi: 10.1086/156203.

P. Goldreich and S. Tremaine. The excitation of density waves at the Lindblad and corotation resonances by an external potential. *Astrophysical Journal*, 233:857–871, November 1979. doi: 10.1086/157448.

P. Goldreich and S. Tremaine. Disk-satellite interactions. *Astrophysical Journal*, 241:425–441, October 1980. doi: 10.1086/158356.

P. Goldreich and S. Tremaine. The dynamics of planetary rings. *Annual Review of Astronomy and Astrophysics*, 20:249–283, 1982. doi: 10.1146/annurev.aa.20.090182.001341.

P. Goldreich and S. D. Tremaine. The formation of the Cassini division in Saturn's rings. *Icarus*, 34:240–253, May 1978b. doi: 10.1016/0019-1035(78)90165-3.

D. A. Golimowski, D. R. Ardila, J. E. Krist, M. Clampin, H. C. Ford, G. D. Illingworth, F. Bartko, N. Benítez, J. P. Blakeslee, R. J. Bouwens, L. D. Bradley, T. J. Broadhurst, R. A. Brown, C. J. Burrows, E. S. Cheng, N. J. G. Cross, R. Demarco, P. D. Feldman, M. Franx, T. Goto, C. Gronwall, G. F. Hartig, B. P. Holden, N. L. Homeier, L. Infante, M. J. Jee, R. A. Kimble, M. P. Lesser, A. R. Martel, S. Mei, F. Menanteau, G. R. Meurer, G. K. Miley, V. Motta, M. Postman, P. Rosati, M. Sirianni, W. B. Sparks, H. D. Tran, Z. I. Tsvetanov, R. L. White, W. Zheng, and A. W. Zirm. Hubble Space Telescope ACS Multiband Coronagraphic Imaging of the Debris Disk around β Pictoris. *Astronomical Journal*, 131:3109–3130, June 2006. doi: 10.1086/503801.

R. Gomes, H. F. Levison, K. Tsiganis, and A. Morbidelli. Origin of the cataclysmic Late Heavy Bombardment period of the terrestrial planets. *Nature*, 435:466–469, May 2005. doi: 10.1038/nature03676.

R. Greenberg and A. Brahic, editors. *Planetary rings*. 1984.

E. Grün, B. A. S. Gustafson, S. Dermott, and H. Fechtig. *Interplanetary Dust*. 2001.

K. C. Hansen, J. T. Clarke, F. J. Crary, D. L. de Zeeuw, M. K. Dougherty, D. A. Gurnett, T. I. Gombosi, G. B. Hospodarsky, W. S. Kurth, A. J. Ridley, J. H. Waite, and D. T. Young. Saturn's Magnetosphere During the January, 2004 Cassini and HST Observations. *AGU Spring Meeting Abstracts*, pages A7+, May 2004.

W. K. Hartmann. Terrestrial, Lunar, and Interplanetary Rock Fragmentation. *Icarus*, 10: 201–+, March 1969. doi: 10.1016/0019-1035(69)90022-0.

W. K. Hartmann, G. Ryder, L. Dones, and D. Grinspoon. *The Time-Dependent Intense Bombardment of the Primordial Earth/Moon System*, pages 493–512. 2000.

C. Hayashi, K. Nakazawa, and I. Adachi. Long-Term Behavior of Planetesimals and the Formation of the Planets. *Publications of the Astronomical Society of Japan*, 29:163–196, 1977.

M. M. Hedman, J. A. Burns, M. R. Showalter, C. C. Porco, P. D. Nicholson, A. S. Bosh, M. S. Tiscareno, R. H. Brown, B. J. Buratti, K. H. Baines, and R. Clark. Saturn's dynamic D ring. *Icarus*, 188:89–107, May 2007a. doi: 10.1016/j.icarus.2006.11.017.

M. M. Hedman, J. A. Burns, M. S. Tiscareno, C. C. Porco, G. H. Jones, E. Roussos, N. Krupp, C. Paranicas, and S. Kempf. The Source of Saturn's G Ring. *Science*, 317: 653–, August 2007b. doi: 10.1126/science.1143964.

M. M. Hedman, P. D. Nicholson, H. Salo, B. D. Wallis, B. J. Buratti, K. H. Baines, R. H. Brown, and R. N. Clark. Self-Gravity Wake Structures in Saturn's A Ring Revealed by Cassini VIMS. *Astronomical Journal*, 133:2624–2629, June 2007c. doi: 10.1086/516828.

M. M. Hedman, J. A. Burns, M. S. Tiscareno, and C. C. Porco. Organizing some very tenuous things: Resonant structures in Saturn's faint rings. *Icarus*, 202:260–279, July 2009. doi: 10.1016/j.icarus.2009.02.016.

M. M. Hedman, P. D. Nicholson, K. H. Baines, B. J. Buratti, C. Sotin, R. N. Clark, R. H. Brown, R. G. French, and E. A. Marouf. The Architecture of the Cassini Division. *Astronomical Journal*, 139:228–251, January 2010. doi: 10.1088/0004-6256/139/1/228.

J. K. Hillier, S. F. Green, N. McBride, J. P. Schwanethal, F. Postberg, R. Srama, S. Kempf, G. Moragas-Klostermeyer, J. A. M. McDonnell, and E. Grün. The composition of Saturn's E ring. *Monthly Notices of the Royal Astronomical Society*, 377:1588–1596, June 2007. doi: 10.1111/j.1365-2966.2007.11710.x.

W. B. Hubbard, A. Brahic, P. Bouchet, L. R. Elicer, R. Haefner, J. Manfroid, F. Roques, B. Sicardy, and F. Vilas. Occultation detection of a Neptune ring segment. *Journal of Geophysical Research Supplement*, 90:35–37, November 1985.

R. A. Jacobson, P. G. Antreasian, J. J. Bordi, K. E. Criddle, R. Ionasescu, J. B. Jones, R. A. Mackenzie, M. C. Meek, D. Parcher, F. J. Pelletier, W. M. Owen, Jr., D. C. Roth, I. M. Roundhill, and J. R. Stauch. The Gravity Field of the Saturnian System from Satellite Observations and Spacecraft Tracking Data. *Astronomical Journal*, 132:2520–2526, December 2006. doi: 10.1086/508812.

R. A. Jacobson, J. Spitale, C. C. Porco, K. Beurle, N. J. Cooper, M. W. Evans, and C. D. Murray. Revised Orbits of Saturn's Small Inner Satellites. *Astronomical Journal*, 135: 261–263, January 2008. doi: 10.1088/0004-6256/135/1/261.

D. Jewitt and N. Haghighipour. Irregular Satellites of the Planets: Products of Capture in the Early Solar System. *Annual Review of Astronomy and Astrophysics*, 45:261–295, September 2007. doi: 10.1146/annurev.astro.44.051905.092459.

G. H. Jones, E. Roussos, N. Krupp, U. Beckmann, A. J. Coates, F. Crary, I. Dandouras, V. Dikarev, M. K. Dougherty, P. Garnier, C. J. Hansen, A. R. Hendrix, G. B. Hospodarsky, R. E. Johnson, S. Kempf, K. K. Khurana, S. M. Krimigis, H. Krüger, W. S. Kurth, A. Lagg, H. J. McAndrews, D. G. Mitchell, C. Paranicas, F. Postberg, C. T. Russell, J. Saur, M. Seiß, F. Spahn, R. Srama, D. F. Strobel, R. Tokar, J.-E. Wahlund, R. J. Wilson, J. Woch, and D. Young. The Dust Halo of Saturn's Largest Icy Moon, Rhea. *Science*, 319:1380–, March 2008. doi: 10.1126/science.1151524.

P. Kalas, J. Larwood, B. A. Smith, and A. Schultz. Rings in the Planetesimal Disk of β Pictoris. *Astrophysical Journal Letters*, 530:L133–L137, February 2000. doi: 10.1086/312494.

P. Kalas, J.-M. Deltorn, and J. Larwood. Stellar Encounters with the β Pictoris Planetesimal System. *Astrophysical Journal*, 553:410–420, May 2001. doi: 10.1086/320632.

R. Karjalainen and H. Salo. Gravitational accretion of particles in Saturn's rings. *Icarus*, 172:328–348, December 2004. doi: 10.1016/j.icarus.2004.05.022.

W. S. Kurth, T. F. Averkamp, D. A. Gurnett, J. B. Groene, and A. Lecacheux. An update to a Saturnian longitude system based on kilometric radio emissions. *Journal of Geophysical Research (Space Physics)*, 113(12):5222, May 2008. doi: 10.1029/2007JA012861.

J. D. Larwood and P. G. Kalas. Close stellar encounters with planetesimal discs: the dynamics of asymmetry in the β Pictoris system. *Monthly Notices of the Royal Astronomical Society*, 323:402–416, May 2001. doi: 10.1046/j.1365-8711.2001.04212.x.

M. C. Lewis and G. R. Stewart. Features around embedded moonlets in Saturn's rings: The role of self-gravity and particle size distributions. *Icarus*, 199:387–412, February 2009. doi: 10.1016/j.icarus.2008.09.009.

J. J. Lissauer and J. N. Cuzzi. Resonances in Saturn's rings. *Astronomical Journal*, 87: 1051–1058, July 1982. doi: 10.1086/113189.

J. J. Lissauer and R. G. French. HST High-Resolution Backscatter Image of Saturn's G Ring. *Icarus*, 146:12–18, July 2000. doi: 10.1006/icar.2000.6386.

J. J. Lissauer, P. Goldreich, and S. Tremaine. Evolution of the Janus-Epimetheus coorbital resonance due to torques from Saturn's rings. *Icarus*, 64:425–434, December 1985. doi: 10.1016/0019-1035(85)90066-1.

M. S. Marley and C. C. Porco. Planetary acoustic mode seismology - Saturn's rings. *Icarus*, 106:508, December 1993. doi: 10.1006/icar.1993.1189.

E. A. Marouf and G. L. Tyler. Detection of two satellites in the Cassini division of Saturn's rings. *Nature*, 323:31–35, September 1986. doi: 10.1038/324031a0.

E. A. Marouf, R. French, N. Rappaport, K. Wong, C. McGhee, and A. Anabtawi. Physical Properties of Saturn's Rings from Cassini Radio Occultations. In *AAS/Division for Plane-*

tary Sciences Meeting Abstracts #40, volume 40 of *Bulletin of the American Astronomical Society*, pages 429–+, September 2008.

J. C. Maxwell. Abstract of Professor Maxwell's paper on the Stability of Saturn's Rings. *Monthly Notices of the Royal Astronomical Society*, 19:297–304, June 1859.

C. A. McGhee and R. G. French. HST Observations of Spokes in Saturn's B Ring. In *AAS/Division for Planetary Sciences Meeting Abstracts #34*, volume 34 of *Bulletin of the American Astronomical Society*, pages 899–+, September 2002.

C. A. McGhee, P. D. Nicholson, R. G. French, and K. J. Hall. HST Observations of Saturnian Satellites during the 1995 Ring Plane Crossings. *Icarus*, 152:282–315, August 2001. doi: 10.1006/icar.2001.6635.

C. A. McGhee, R. G. French, L. Dones, J. N. Cuzzi, H. J. Salo, and R. Danos. HST Observations of Spokes in Saturn's B Ring. In *AAS/Division for Planetary Sciences Meeting Abstracts #36*, volume 36 of *Bulletin of the American Astronomical Society*, pages 1110–+, November 2004.

C. A. McGhee, R. G. French, L. Dones, J. N. Cuzzi, H. J. Salo, and R. Danos. HST observations of spokes in Saturn's B ring. *Icarus*, 173:508–521, February 2005. doi: 10.1016/j.icarus.2004.09.001.

B.K. Meinke, L. W. Esposito, N. Albers, M. Sremčević, and C. Murray. Classification of F ring features observed in Cassini UVIS occultations. *Submitted to Icarus*, 2011.

N. Meyer-Vernet and B. Sicardy. On the physics of resonant disk-satellite interaction. *Icarus*, 69:157–175, January 1987. doi: 10.1016/0019-1035(87)90011-X.

R. L. Millis and L. H. Wasserman. The occultation of BD -15 deg 3969 by the rings of Uranus. *Astronomical Journal*, 83:993–998, August 1978. doi: 10.1086/112281.

E. D. Miner, R. R. Wessen, and J. N. Cuzzi. *Planetary Ring Systems.* 2007.

A. Morbidelli, H. F. Levison, K. Tsiganis, and R. Gomes. Chaotic capture of Jupiter's Trojan asteroids in the early Solar System. *Nature*, 435:462–465, May 2005. doi: 10.1038/nature03540.

I. Mosqueira and P. R. Estrada. Formation of the regular satellites of giant planets in an extended gaseous nebula I: subnebula model and accretion of satellites. *Icarus*, 163:198–231, May 2003a. doi: 10.1016/S0019-1035(03)00076-9.

I. Mosqueira and P. R. Estrada. Formation of the regular satellites of giant planets in an extended gaseous nebula II: satellite migration and survival. *Icarus*, 163:232–255, May 2003b. doi: 10.1016/S0019-1035(03)00077-0.

O. Muñoz, F. Moreno, A. Molina, D. Grodent, J. C. Gérard, and V. Dols. Study of the vertical structure of Saturn's atmosphere using HST/WFPC2 images. *Icarus*, 169:413–428, June 2004. doi: 10.1016/j.icarus.2003.12.018.

C. D. Murray and S. F. Dermott. *Solar system dynamics.* Berlin: Springer, 2009, 1999.

C. D. Murray and S. M. Giuliatti Winter. Periodic collisions between the moon Prometheus and Saturn's F ring. *Nature*, 380:139–141, March 1996. doi: 10.1038/380139a0.

C. D. Murray, M. K. Gordon, and S. M. Giuliatti Winter. Unraveling the Strands of Saturn's F Ring. *Icarus*, 129:304–316, October 1997. doi: 10.1006/icar.1997.5774.

C. D. Murray, C. Chavez, K. Beurle, N. Cooper, M. W. Evans, J. A. Burns, and C. C. Porco. How Prometheus creates structure in Saturn's F ring. *Nature*, 437:1326–1329, October 2005. doi: 10.1038/nature04212.

P. D. Nicholson. Saturn Ring Profiles from the August 1995 HST Data. In *AAS/Division for Planetary Sciences Meeting Abstracts #29*, volume 29 of *Bulletin of the American Astronomical Society*, pages 998–+, July 1997.

P. D. Nicholson and C. C. Porco. A new constraint on Saturn's zonal gravity harmonics from Voyager observations of an eccentric ringlet. *Journal of Geophysical Researc*, 93: 10209–10224, September 1988. doi: 10.1029/JB093iB09p10209.

P. D. Nicholson, M. L. Cooke, and E. Pelton. An absolute radius scale for Saturn's rings. *Astronomical Journal*, 100:1339–1362, October 1990. doi: 10.1086/115601.

P. D. Nicholson, M. M. Hedman, and Cassini VIMS Team. A Crack in the C Ring? In *AAS/Division for Planetary Sciences Meeting Abstracts #42*, volume 42 of *Bulletin of the American Astronomical Society*, page 981, October 2010.

M. E. Ockert-Bell, J. A. Burns, I. J. Daubar, P. C. Thomas, J. Veverka, M. J. S. Belton, and K. P. Klaasen. The Structure of Jupiter's Ring System as Revealed by the Galileo Imaging Experiment. *Icarus*, 138:188–213, April 1999. doi: 10.1006/icar.1998.6072.

J.-M. Petit and M. Henon. A numerical simulation of planetary rings. III - Mass segregation, ring confinement, and gap formation. *Astronomy and Astrophysics*, 199:343–356, June 1988.

J. B. Pollack, A. S. Grossman, R. Moore, and H. C. Graboske, Jr. A calculation of Saturn's gravitational contraction history. *Icarus*, 30:111–128, January 1977. doi: 10.1016/0019-1035(77)90126-9.

C. Porco, G. E. Danielson, P. Goldreich, J. B. Holberg, and A. L. Lane. Saturn's nonaxisymmetric ring edges at 1.95 R(s) and 2.27 R(s). *Icarus*, 60:17–28, October 1984a. doi: 10.1016/0019-1035(84)90135-0.

C. Porco, P. D. Nicholson, N. Borderies, G. E. Danielson, P. Goldreich, J. B. Holberg, and A. L. Lane. The eccentric Saturnian ringlets at 1.29 R(s) and 1.45 R(s). *Icarus*, 60:1–16, October 1984b. doi: 10.1016/0019-1035(84)90134-9.

C. C. Porco, E. Baker, J. Barbara, K. Beurle, A. Brahic, J. A. Burns, S. Charnoz, N. Cooper, D. D. Dawson, A. D. Del Genio, T. Denk, L. Dones, U. Dyudina, M. W. Evans, B. Giese, K. Grazier, P. Helfenstein, A. P. Ingersoll, R. A. Jacobson, T. V. Johnson, A. McEwen, C. D. Murray, G. Neukum, W. M. Owen, J. Perry, T. Roatsch, J. Spitale, S. Squyres, P. Thomas, M. Tiscareno, E. Turtle, A. R. Vasavada, J. Veverka, R. Wagner, and R. West.

Cassini Imaging Science: Initial Results on Saturn's Rings and Small Satellites. *Science*, 307:1226–1236, February 2005. doi: 10.1126/science.1108056.

C. C. Porco, P. Helfenstein, P. C. Thomas, A. P. Ingersoll, J. Wisdom, R. West, G. Neukum, T. Denk, R. Wagner, T. Roatsch, S. Kieffer, E. Turtle, A. McEwen, T. V. Johnson, J. Rathbun, J. Veverka, D. Wilson, J. Perry, J. Spitale, A. Brahic, J. A. Burns, A. D. Del Genio, L. Dones, C. D. Murray, and S. Squyres. Cassini Observes the Active South Pole of Enceladus. *Science*, 311:1393–1401, March 2006. doi: 10.1126/science.1123013.

F. Poulet, J. N. Cuzzi, R. G. French, and L. Dones. A Study of Saturn's Ring Phase Curves from HST Observations. *Icarus*, 158:224–248, July 2002. doi: 10.1006/icar.2002.6852.

F. Poulet, D. P. Cruikshank, J. N. Cuzzi, T. L. Roush, and R. G. French. Compositions of Saturn's rings A, B, and C from high resolution near-infrared spectroscopic observations. *Astronomy and Astrophysics*, 412:305–316, December 2003. doi: 10.1051/0004-6361:20031123.

W. T. Reach, J. Vaubaillon, M. S. Kelley, C. M. Lisse, and M. V. Sykes. Distribution and properties of fragments and debris from the split Comet 73P/Schwassmann-Wachmann 3 as revealed by Spitzer Space Telescope. *Icarus*, 203:571–588, October 2009. doi: 10.1016/j.icarus.2009.05.027.

S. J. Robbins, G. R. Stewart, M. C. Lewis, J. E. Colwell, and M. Sremčević. Estimating the masses of Saturn's A and B rings from high-optical depth N-body simulations and stellar occultations. *Icarus*, 206:431–445, April 2010. doi: 10.1016/j.icarus.2009.09.012.

P. A. Rosen and J. J. Lissauer. The Titan-1:0 nodal bending wave in Saturn's Ring C. *Science*, 241:690–694, August 1988. doi: 10.1126/science.241.4866.690.

P. A. Rosen, G. L. Tyler, and E. A. Marouf. Resonance structures in Saturn's rings probed by radio occultation. I - Methods and examples. *Icarus*, 93:3–24, September 1991a. doi: 10.1016/0019-1035(91)90160-U.

P. A. Rosen, G. L. Tyler, E. A. Marouf, and J. J. Lissauer. Resonance structures in Saturn's rings probed by radio occultation. II - Results and interpretation. *Icarus*, 93:25–44, September 1991b. doi: 10.1016/0019-1035(91)90161-L.

J. Salmon, S. Charnoz, A. Crida, and A. Brahic. Long-term and large-scale viscous evolution of dense planetary rings. *Icarus*, 209:771–785, October 2010. doi: 10.1016/j.icarus.2010.05.030.

H. Salo, R. G. French, C. McGhee, and L. Dones. Photometric modeling of Saturn ring's opposition effect: extracting the mutual shadowing contribution from HST observations. In *AAS/Division for Planetary Sciences Meeting Abstracts #37*, volume 37 of *Bulletin of the American Astronomical Society*, pages 772–+, August 2005.

P. K. Seidelmann, B. A. Archinal, M. F. A'Hearn, A. Conrad, G. J. Consolmagno, D. Hestroffer, J. L. Hilton, G. A. Krasinsky, G. Neumann, J. Oberst, P. Stooke, E. F. Tedesco, D. J. Tholen, P. C. Thomas, and I. P. Williams. Report of the IAU/IAG Working Group on cartographic coordinates and rotational elements: 2006. *Celestial Mechanics and Dynamical Astronomy*, 98:155–180, July 2007. doi: 10.1007/s10569-007-9072-y.

M. Seiß, F. Spahn, M. Sremčević, and H. Salo. Structures induced by small moonlets in Saturn's rings: Implications for the Cassini Mission. *Geophysical Research Letters*, 32: 11205, June 2005. doi: 10.1029/2005GL022506.

M. R. Showalter. Visual detection of 1981S13, Saturn's eighteenth satellite, and its role in the Encke gap. *Nature*, 351:709–713, June 1991. doi: 10.1038/351709a0.

M. R. Showalter and J. A. Burns. A numerical study of Saturn's F-ring. *Icarus*, 52:526–544, December 1982. doi: 10.1016/0019-1035(82)90013-6.

M. R. Showalter and J. J. Lissauer. The Second Ring-Moon System of Uranus: Discovery and Dynamics. *Science*, 311:973–977, February 2006. doi: 10.1126/science.1122882.

M. R. Showalter, J. N. Cuzzi, E. A. Marouf, and L. W. Esposito. Satellite 'wakes' and the orbit of the Encke Gap moonlet. *Icarus*, 66:297–323, May 1986. doi: 10.1016/0019-1035(86) 90160-0.

M. R. Showalter, J. A. Burns, J. N. Cuzzi, and J. B. Pollack. Jupiter's ring system - New results on structure and particle properties. *Icarus*, 69:458–498, March 1987. doi: 10.1016/0019-1035(87)90018-2.

M. R. Showalter, J. N. Cuzzi, and S. M. Larson. Structure and particle properties of Saturn's E Ring. *Icarus*, 94:451–473, December 1991. doi: 10.1016/0019-1035(91)90241-K.

F. H. Shu. On the Density-Wave Theory of Galactic Spirals. II. The Propagation of the Density of Wave Action. *Astrophysical Journal*, 160:99, April 1970a. doi: 10.1086/150410.

F. H. Shu. On the Density-Wave Theory of Galactic Spirals. I. Spiral Structure as a Normal Mode of Oscillation. *Astrophysical Journal*, 160:89, April 1970b. doi: 10.1086/150409.

F. H. Shu. *Waves in planetary rings*, pages 513–561. In Greenberg and Brahic (1984), 1984.

F. H. Shu, J. N. Cuzzi, and J. J. Lissauer. Bending waves in Saturn's rings. *Icarus*, 53: 185–206, February 1983. doi: 10.1016/0019-1035(83)90141-0.

B. Sicardy. Dynamics of Planetary Rings. In J. Souchay, editor, *Dynamics of Extended Celestial Bodies and Rings*, volume 682 of *Lecture Notes in Physics, Berlin Springer Verlag*, pages 183–+, 2006.

B. A. Smith, L. A. Soderblom, T. V. Johnson, A. P. Ingersoll, S. A. Collins, E. M. Shoemaker, G. E. Hunt, H. Masursky, M. H. Carr, M. E. Davies, A. F. Cook, J. M. Boyce, T. Owen, G. E. Danielson, C. Sagan, R. F. Beebe, J. Veverka, J. F. McCauley, R. G. Strom, D. Morrison, G. A. Briggs, and V. E. Suomi. The Jupiter system through the eyes of Voyager 1. *Science*, 204:951–957, June 1979. doi: 10.1126/science.204.4396.951.

B. A. Smith, L. A. Soderblom, R. Beebe, D. Bliss, R. H. Brown, S. A. Collins, J. M. Boyce, G. A. Briggs, A. Brahic, J. N. Cuzzi, and D. Morrison. Voyager 2 in the Uranian system - Imaging science results. *Science*, 233:43–64, July 1986. doi: 10.1126/science.233.4759.43.

F. Spahn and M. Sremčević. Density patterns induced by small moonlets in Saturn's rings? *Astronomy and Astrophysics*, 358:368–372, June 2000.

F. Spahn and H.-J. Wiebicke. Long-term gravitational influence of moonlets in planetary rings. *Icarus*, 77:124–134, January 1989. doi: 10.1016/0019-1035(89)90012-2.

F. Spahn, A. Saar, S. Schmidt, and U. Schwarz. The influence of various moonlets on the optical depth profile in planetary rings. *Icarus*, 100:143–153, November 1992. doi: 10.1016/0019-1035(92)90025-3.

F. Spahn, J. Schmidt, N. Albers, M. Hörning, M. Makuch, M. Seiß, S. Kempf, R. Srama, V. Dikarev, S. Helfert, G. Moragas-Klostermeyer, A. V. Krivov, M. Sremčević, A. J. Tuzzolino, T. Economou, and E. Grün. Cassini Dust Measurements at Enceladus and Implications for the Origin of the E Ring. *Science*, 311:1416–1418, March 2006. doi: 10.1126/science.1121375.

L. J. Spilker, S. Pilorz, A. L. Lane, R. M. Nelson, B. Pollard, and C. T. Russell. Saturn A ring surface mass densities from spiral density wave dispersion behavior. *Icarus*, 171: 372–390, October 2004. doi: 10.1016/j.icarus.2004.05.016.

J. N. Spitale and C. C. Porco. Detection of Free Unstable Modes and Massive Bodies in Saturn's Outer B Ring. *Astronomical Journal*, 140:1747–1757, December 2010. doi: 10.1088/0004-6256/140/6/1747.

J. N. Spitale, R. A. Jacobson, C. C. Porco, and W. M. Owen, Jr. The Orbits of Saturn's Small Satellites Derived from Combined Historic and Cassini Imaging Observations. *Astronomical Journal*, 132:692–710, August 2006. doi: 10.1086/505206.

J. N. Spitale, C. C. Porco, J. E. Colwell, and J. M. Hahn. Kinematics of the Outer Edges of Saturn's A and B Rings. In *AAS/Division of Dynamical Astronomy Meeting #39*, volume 39 of *AAS/Division of Dynamical Astronomy Meeting*, pages #18.03–+, May 2008.

M. Sremčević, F. Spahn, and W. J. Duschl. Density structures in perturbed thin cold discs. *Monthly Notice of the Royal Astronomical Society*, 337:1139–1152, December 2002. doi: 10.1046/j.1365-8711.2002.06011.x.

M. Sremčević, J. Schmidt, H. Salo, M. Seiß, F. Spahn, and N. Albers. A belt of moonlets in Saturn's A ring. *Nature*, 449:1019–1021, October 2007. doi: 10.1038/nature06224.

G. R. Stewart. Nonlinear satellite wakes in planetary rings. I - Phase-space kinematics. *Icarus*, 94:436–450, December 1991. doi: 10.1016/0019-1035(91)90240-T.

M. S. Tiscareno, J. A. Burns, M. M. Hedman, C. C. Porco, J. W. Weiss, L. Dones, D. C. Richardson, and C. D. Murray. 100-metre-diameter moonlets in Saturn's A ring from observations of "propeller" structures. *Nature*, 440:648–650, March 2006. doi: 10.1038/nature04581.

M. S. Tiscareno, J. A. Burns, P. D. Nicholson, M. M. Hedman, and C. C. Porco. Cassini imaging of Saturn's rings. II. A wavelet technique for analysis of density waves and other radial structure in the rings. *Icarus*, 189:14–34, July 2007. doi: 10.1016/j.icarus.2006.12.025.

M. S. Tiscareno, J. A. Burns, M. M. Hedman, and C. C. Porco. The Population of Propellers in Saturn's A Ring. *Astronomical Journal*, 135:1083–1091, March 2008. doi: 10.1088/0004-6256/135/3/1083.

M. S. Tiscareno, M. M. Hedman, J. A. Burns, J. W. Weiss, and C. C. Porco. Saturn's A Ring Has No Inner Edge. In *AAS/Division for Planetary Sciences Meeting Abstracts #41*, volume 41 of *AAS/Division for Planetary Sciences Meeting Abstracts*, page #25.04, September 2009.

M. S. Tiscareno, J. A. Burns, J. N. Cuzzi, and M. M. Hedman. Cassini imaging search rules out rings around Rhea. *Geophysical Research Letters*, 37:L14205, July 2010a. doi: 10.1029/2010GL043663.

M. S. Tiscareno, J. A. Burns, M. Sremčević, K. Beurle, M. M. Hedman, N. J. Cooper, A. J. Milano, M. W. Evans, C. C. Porco, J. N. Spitale, and J. W. Weiss. Physical Characteristics and Non-Keplerian Orbital Motion of "Propeller" Moons Embedded in Saturn's Rings. *Astrophysical Journal*, 718:L92–L96, August 2010b. doi: 10.1088/2041-8205/718/2/L92.

C. Torrence and G. P. Compo. A practical guide to wavelet analysis. *Bulletin of the American Meteorological Society*, 79:61–78, 1998.

K. Tsiganis, R. Gomes, A. Morbidelli, and H. F. Levison. Origin of the orbital architecture of the giant planets of the Solar System. *Nature*, 435:459–461, May 2005. doi: 10.1038/nature03539.

W. R. Ward. Density waves in the solar nebula - Differential Lindblad torque. *Icarus*, 67: 164–180, July 1986. doi: 10.1016/0019-1035(86)90182-X.

H. A. Zebker, E. A. Marouf, and G. L. Tyler. Saturn's rings - Particle size distributions for thin layer model. *Icarus*, 64:531–548, December 1985. doi: 10.1016/0019-1035(85)90074-0.